EXPLORING THE FACTORS MODULATING THE SOLUBILIZATION OF *β*-CAROTENE IN DIETARY MIXED MICELLES THROUGH COMPUTER SIMULATIONS

A Thesis Submitted to
the Graduate School of Engineering and Sciences of
İzmir Institute of Technology
in Partial Fulfillment of the Requirements for the Degree of

DOCTOR OF PHILOSOPHY

in Food Engineering

by
Esra TUNÇER

December 2018
İZMİR

We approve the thesis of **Esra TUNÇER**

Examining Committee Members:

_____
Assist. Prof. Dr. Beste BAYRAMOĞLU
Department of Food Engineering, İzmir Institute of Technology

_____
Prof. Dr. Nuran ELMACI IRMAK
Department of Chemistry, İzmir Institute of Technology

_____
Assist. Prof. Dr. Şükrü GÜLEÇ
Department of Food Engineering, İzmir Institute of Technology

_____
Prof. Dr. Sibel KARAKAYA
Department of Food Engineering, Ege University

_____
Prof. Dr. Mine ÇAPAR
Department of Physics, Ege University

26 December 2018

_____
Assist. Prof. Dr. Beste BAYRAMOĞLU
Supervisor, Department of Food Engineering,
İzmir Institute of Technology

_____   _____
Prof. Dr. Figen KOREL   **Prof. Dr. Aysun SOFUOĞLU**
Head of the Department of   Dean of the Graduate School of
Food Engineering   Engineering and Sciences
İzmir Institute of Technology   İzmir Institute of Technology

ACKNOWLEDGMENTS

ABSTRACT

EXPLORING THE FACTORS MODULATING THE SOLUBILIZATION
OF β-CAROTENE IN DIETARY MIXED MICELLES THROUGH
COMPUTER SIMULATIONS

β-carotene is one of the major carotenoids beneficial to human health in the prevention of a variety of diseases. However, due to its hydrophobic nature, the bioavailability of β-carotene is very low. The solubilization of β-carotene in the duodenal mixed micelles is considered as a key step in their bioavailability. Therefore, understanding the factors and the molecular mechanisms behind their solubilization within the dietary mixed micelles are of great importance. Based on this motivation, the aim of this dissertation was to systematically investigate this phenomenon via extensive coarse-grained molecular dynamics simulations in three steps: (i) the characterization of the self-assembly and structure of the mixed micelles of bile salts and phospholipids at fasted and fed state conditions, (ii) determination of the effects of addition of the fatty acids with different chain lengths and degrees of unsaturation ,(iii) solubilization of different amounts of β-carotene in the selected mixed micelles. As it would be computationally too expensive to equilibrate the systems with full atomistic resolution, the MARTINI force field, which is a well-established model for lipid systems, was used. All the simulations were carried out using the GROMACS simulation package. Validations of results were made by comparison of the micellar properties with experimental data in the literature when available. The knowledge gained by this study provides important information to be utilized in the design of effective nutraceutical delivery systems that optimize the bioaccessibility of β-carotene.

ÖZET

BESİDÜZENSEL KARMA MİSELLERİNDE β-KAROTENİN ÇÖZÜLMESİNİ ETKİLEYEN FAKTÖRLERİN BİLGİSAYAR BENZETİMLERİ İLE ARAŞTIRILMASI

β-karoten çeşitli hastalıkların önlenmesinde rol oynayarak insan sağlığı üzerine olumlu etkiler gösteren temel karotenoidlerden birisidir. Ancak, hidrofobik doğası nedeniyle β-karotenin biyoyararlanımı oldukça düşüktür. β-karotenlerin ince bağırsak karma misellerinde çözünmeleri biyoyararlanımlarına etki eden anahtar basamak olarak düşünülmektedir. Bu nedenle β-karotenlerin besidüzensel karma misellerdeki çözünmelerini etkileyen faktörleri ve moleküler mekanizmaları anlamak büyük önem taşımaktadır. Bu tez çalışmasının amacı kaba ölçekli moleküler dinamik simülasyonlar ile karotenoidlerin ince bağırsak karma misellerinde çözülme mekanizmasını ve çözülmeyi etkileyen faktörleri sistematik olarak üç basamak altında incelemektir: (i) açlık ve tokluk durumlarını temsil eden konsantrasyonlarda safra asitleri ve fosfolipidlerin öztoplaşımı ve oluşan karma misel yapılarının tanımlanması, (ii) farklı zincir uzunlukları ve doymamışlık derecelerindeki yağ asitlerinin öztoplaşım ve misel yapılarına etkilerinin belirlenmesi, (iii) farklı miktarlardaki β-karoten moleküllerinin seçilen karma miseller içerisinde çözündürülmesi. Bütün sistemin atomik çözünürlükte dengeye gelmesi işlemsel olarak çok maliyetli olacağından lipid sistemler için tasarlanmış kaba ölçekli bir model çeşidi olan Martini Modeli kullanılmıştır. Tüm simülasyonlar GROMACS simülasyon paketi kullanılarak gerçekleştirilmiştir. Elde edilen sonuçların doğrulaması, çeşitli misel özelliklerinin literatürde yer alan mevcut deneysel verilerle karşılaştırılması ile gerçekleştirilmiştir. Bu çalışma β-karotenlerin biyoerişilebilirliğini optimize etmeye yarayan etkin iletim sistemlerin geliştirilmesi için kullanılmak üzere önemli bilgiler sağlamaktadır.

TABLE OF CONTENTS

LIST OF FIGURES

LIST OF TABLES

CHAPTER 1

BACKGROUND AND MOTIVATION

1.1. Introduction

Carotenoids are widely spread molecules in nature and are natural colorants. They are responsible for the yellow to red color of fruits and vegetables. β-carotenes are one of the most common carotenoids and are extensively used in scientific studies and industry as a colorant or nutraceutical. They are known as the precursors of vitamin A, and have many known health promoting effects such as having antioxidant activity and being effective on some types of cancer, etc. However, the highly hydrophobic nature of them reduces their bioavailability after consumption. Considering the digestion of lipophilic food materials, their solubilization within the dietary mixed micelles of the small intestine (bioaccessibility) is recognized as a key step affecting their bioavailability. It is believed that the rate and extent to which carotenoids are solubilized in dietary mixed micelles is directly related to the rate and extent of their absorption by the intestinal cells. Therefore, the poorly understood molecular-scale mechanisms by which they are taken up in the mixed micelles need to be clarified in the first place. Unfortunately, current experimental methods are incompetent in this regard due to the highly dynamic nature of micellar structures. Understanding these mechanisms requires molecular-scale models of the various components of mixed micelles as well as a good understanding of the molecular-scale behavior of mixed micelle constituents. Computer simulations at molecular level provide a powerful tool in this respect. In particular, molecular dynamics (MD), which calculate the time dependent behavior of a system, can reliably simulate the structure and dynamics of self-assembly systems.

In this perspective, the aim of this study is to systematically investigate the mechanism of solubilization of β-carotene in duodenal mixed micelles and the factors modulating this phenomenon through extensive molecular dynamics simulations. As it would be computationally too expensive to equilibrate the whole system with full atomistic resolution, the MARTINI force field, which is a well-established coarse-

grained model for lipid systems, is used. The study is divided into three main parts. In the first part, mixed micelle formation is investigated from a model upper intestinal medium composed of bile salts (cholate) and phospholipids (POPC) at physiological fasted and fed state conditions. Validation of the model and the results are made by comparison of the micellar properties with the available experimental data in the literature. In the second part, the effects of additional lipid digestion products (fatty acids) to the micelle formation and structure are investigated. The chain length and the saturation degree of the fatty acids are the studied factors. For this purpose, lauric (12:0), stearic (18:0), oleic (18:1) and linoleic (18:2) acid are used. Finally, in the last stage, the solubilization of β-carotene in the selected pre-assembled micelles from the second stage is studied. All the simulations were carried out using the GROMACS simulation package. Overall, the outcomes of this study provide valuable information to be utilized in the design of effective nutraceutical delivery systems that optimize the bioaccessibility of carotenoids.

1.2. *β*-carotene

Carotenoids are natural colorants and more than 700 carotenoids are identified in nature so far (Maiani et al., 2009). One of the best-known carotenoids is β-carotene and it is widely found in nature. Therefore, it is chosen as a representative carotenoid to study in the present thesis project.

1.2.1. Structure of *β*-carotene

Carotenoids are responsible for the color range from light yellow to deep red. They are synthesized by photosynthetic and some non- photosynthetic bacteria, algae, fungi, yeasts, and higher plants. The color of some marine invertebrates, insects, and birds are originated from the carotenoids which consumed through the diet (Namitha & Negi, 2010). Food carotenoids are mainly found in yellow and orange fruits and vegetables. Besides, leafy vegetables with dark green color are also rich in carotenoids. Almost 50 of carotenoids are consumed in the human diet and can be metabolized by the human body and the 95% of the total carotenoids in blood are β-carotene, β-

cryptoxanthin, α-carotene, lycopene, lutein and zeaxanthin (Maiani et al., 2009; O'Neill et al., 2001).

Carotenoids are fat-soluble pigments and most of them have the $C_{40}H_{56}O_n$ formula where n changes between 0 and 6. If there is no oxygen in the carotenoid structure (n = 0) they are named as "*carotenes*" while in presence of oxygen they are called as "*xanthophylls*". Carotenoids are symmetrical molecules formed by isoprene units linked covalently in head to head or tail to tail fashion (Elbe & Schwartz, 1996). Carotenoids may have no, one or two rings in their structures and may be acyclic (lycopene), monocyclic (γ-carotene), or dicyclic (β-carotene), respectively. Carotenoids are conjugated molecules and mostly found in the all-trans form in nature (Socaciu, 2008). One of the best-known carotenoids is β-carotene ($C_{40}H_{56}$) and it is widely found in nature and extensively used as a colorant and nutritional supplement also (Figure 1.1.). Therefore, it is chosen as a representative carotenoid to study in the present thesis project.

Carotenoids are reported to have many health benefits. Therefore, in many studies, the amounts of carotenoids in widely consumed foods are investigated to form a database. For example, Holden et al. (1999) reported a database named "The Carotenoid Content of US foods" including the portion of carotenoids in raw, processed and cooked forms of foods. Similarly, databases are described by O'neill et al. (2001) for most commonly consumed foods in five European countries: UK, Ireland, Spain, France, and The Netherlands and by Murkovic et al. (2000) for Austrian foods. In the studies of Holden et al. (1999) and O'neill et al. (2001), β-carotene is reported to be the most widespread carotenoid among the studied ones. Dark orange and green fruits and vegetables like mango, tomatoes, carrots, red peppers, pumpkin, sweet potatoes, broccoli and leafy greens like spinach are described as the primary sources.
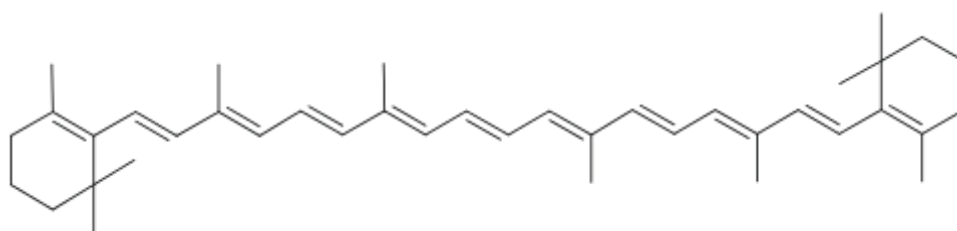
Figure 1.1. Structure of β-carotene

1.2.2. Health Effects

The β-ionone rings in the carotenoids structure make them a precursor of provitamin A. β-carotene, α-carotene and β-cryptoxanthin are some example carotenoids with provitamin A activity. β-carotene has the highest provitamin A activity due to its two β-ionone rings. Carotenoids may be split into the preformed vitamin A compounds, named as retinoids, by intestinal 15-15/-dioxygenase and monooxygenase enzymes after ingestion (Nagao, During, Hoshino, Terao, & Olson, 1996). The unconverted carotenoids may be transported to body tissues like bone marrow, blood cells, muscles, kidney and liver and some of them may be converted to retinoids in liver (Smolin & Grosvenor, 2007). Deficiency of vitamin A is a serious problem, especially among children. Children deficient in vitamin A have poor appetites and higher susceptibility to infections. Deficiency may cause anemia, growth retardation and premature death among children. Adults deficient in vitamin A may have night blindness, xerophthalmia, immune diseases, problems in the heart and circulatory systems (Maiani et al., 2009; Namitha & Negi, 2010; Smolin & Grosvenor, 2007).

Carotenoids also have a role in human health as an antioxidant. The double bonds in their structure behave as singlet oxygen quenchers and free radical scavengers and they protect cell membranes from damages of free radicals. Therefore, they have a role in the prevention of some diseases like cancer and cardiovascular diseases (Rao & Rao, 2007; Smolin & Grosvenor, 2007). Carotenoids reported to have an effect on certain types of cancers like lung, prostate, cervical, stomach, pancreatic and colorectal (Betz, Blackman, & Levine, 2010; Namitha & Negi, 2010) Besides, their intake prevents weakening of vision due to macular degeneration and cataracts which are caused by blue-light mediated free radical damage to the retina. Additionally, 300 mg/day β-carotene intake reported improving resistance to skin photosensitivity in Erythropoietic protoporphyria patients who are extremely sensitive to sunlight inborn (Betz et al., 2010).

Overconsumption of β-carotene is reported to cause hypercarotenemia or carotenodermia which causes to skin turn into yellow-orange color. The storage of excess β-carotene in plasma and adipose tissue cause the color change. This situation does not have any known harm to body and color turns back to normal by the time when β-carotene intake is discontinued (Betz et al., 2010; Smolin & Grosvenor, 2007). On the

4

other hand, high doses of β-carotene may increase the risk of lung cancer among smokers and asbestos workers (Betz et al., 2010; Rao & Rao, 2007; Socaciu, 2008).

Although having many health effects on the human body, carotenoids are not classified as essential nutrients and therefore they do not have a dietary reference intake (DRI) (Rao and Rao 2007). They neither have an upper limit in usage except for current good manufacturing practices according to FDA (U.S. Food and Drug Administration) while the European Expert Group on Vitamins and Minerals defined the safe upper limit as 7 mg/ day. On the other hand, vitamin A is essential for human and recommended dietary allowance (RDA) is equal to 700 and 900 µg per day for men and women, respectively. Vitamin A deficiency is common in some countries like Africa, India, Latin America, and the Caribbean. Also, the studies showed that many Americans do not meet the recommended daily intake values (Smolin and Grosvenor 2007). According to the WHO (World Health Organization), vitamin A deficiency is a moderate problem among preschool-aged children in Turkey. To fight with the deficiency of vitamin A, it is proposed to use food-based solutions like fortification of foods or introducing new plant cultivars with enhanced provitamin A activity (Namitha and Negi 2010).

1.2.3. Bioavailability

Due to the positive health effects and provitamin A activity of β-carotene, it is important to take it into the body by foods or supplements. But the hydrophobic nature of β-carotene reduces its bioavailability. Bioavailability of β-carotene refers to the fraction of it becomes available for utilization in normal physiological functions or for storage in the body. There are many factors affecting the bioavailability of carotenoids and they are listed under the mnemonic "SLAMENGHI", i.e.:

- **S**pecies of carotenoids

- Molecular **l**inkage

- **A**mount of carotenoids consumed in a meal

- **M**atrix in which the carotenoid is incorporated

- **E**ffectors of absorption and bioconversion

5

- **N**utrient status of the host

- **G**enetic factors

- **H**ost-related factors

- **I**nteractions (Borel, 2003; Castenmiller & West, 1998).

The bioavailability is directly related to the digestion process of β-carotene. During the digestion, the consumed food follows the organs of the gastrointestinal tract: mouth, pharynx, esophagus, stomach, small intestine, large intestine, and anus. The small intestine has a great role in the digestion of hydrophobic molecules. The secretion of lipase takes place in small intestine and bile including bile acids and phospholipids is also secreted to small intestine from gallbladder. Bile has a key function in the small intestine by forming mixed micelles or vesicles. The mixed micelles are comprised of phospholipids, bile acids and a small amount of cholesterol. They are characterized by hydrophobic cores and hydrophobic shells. The hydrophobic core solubilizes the hydrophobic molecules in the small intestine like fatty acids, some vitamins or other lipophilic nutrients while the hydrophilic shell enables to disperse the micelle in the water phase (Rozner et al., 2010; Smolin & Grosvenor, 2007). The carotenoids become bioavailable when they are solubilized in those mixed micelles.

The process of carotenoids become bioavailable can be summarized in steps:

1. The release of carotenoids from a food matrix
2. The transfer of carotenoids to micelles
3. The uptake of carotenoids by intestinal cells
4. The incorporation of carotenoids into chylomicrons and their secretion by intestinal cells
5. The transport of carotenoids to the blood (O'Sullivan, Ryan, Aherne, & O'Brien, 2008).

Therefore, the solubilization of carotenoids in mixed micelles is a critical point that affects the bioavailability of carotenoids. There are many experimental studies in the literature that have investigated the factors affecting the micellization of carotenoids. They may be classified under three main groups. In the first group, the studies are focused on the separation of carotenoids from the ingested food matrix

which naturally contains carotenoids or has it by fortification with emulsion like structures. The processes applied, like heat treatments, mechanical processing, freezing etc., to the food effect the carotenoid micellization. They usually increase the bioavailability of carotenoids by breaking down the cell walls and increasing the release of them (Knockaert, Lemmens, Van Buggenhout, Hendrickx, & Van Loey, 2012; Liu, Bi, Xiao, & McClements, 2015; O'Sullivan et al., 2008; Rich et al., 2003; Van Buggenhout et al., 2010). Besides the formulation of food also has a great effect. If the food contains dietary fibers like pectin, the micellization level reduces because these components make carotenoids harder to leave food structure (Borel, 2003; Yonekura & Nagao, 2007). If there is lipid in the food matrix carotenoids more easily transported from the matrix to the lipid phase. Besides lipids enhance the secretion of bile and lipase, and they help the micellization and lipolysis of fats to fatty acids, respectively (Borel, 2003; Charman, Porter, Mithani, & Dressman, 1997). Here, lipid type has a crucial effect on the micellization process. It is harder to hydrolyze triglycerides then di- or monoglycerides, therefore, the presence of triglycerides slows down the micellization process and carotenoids may be trapped in lipid phase that does not involve the micelle structure and leaves the body before being absorbed (Sy et al., 2012; Xia, McClements, & Xiao, 2017).

In the second group, the studies have investigated the situation in the small intestine, where the digestion of lipophilic nutrients takes place. Here, the scientists are mainly focused on the differences born from different types of carotenoids and fatty acids. Hydrocarbon carotenoids, namely carotenes are more hydrophobic then oxygenated ones. Therefore, addition of lipids to the media usually positively affects the solubilization of carotenes within mixed micelles (Brown et al., 2004; Fernández-García, Mínguez-Mosquera, & Pérez-Gálvez, 2007; Hedrén, Diaz, & Svanberg, 2002; Hornero-Méndez & Mínguez-Mosquera, 2007; Nagao, Kotake-Nara, & Hase, 2013; Saini, Nile, & Park, 2015). The chain length, unsaturation level and amount of lipids may show different consequences. For example, the fatty acids with larger chain length were reported to increase the micellization of carotenoids. However, unsaturation level may show different effects and some of the authors conclude that unsaturation has a positive effect on the solubilization of certain type of carotenoids while the others report that there is no significant difference. This difference may be due to the differences in food matrix and type of carotenoids (Failla, Chitchumronchokchai, Ferruzzi, Goltz, &

Campbell, 2014; Huo, Ferruzzi, Schwartz, & Failla, 2007; Nagao et al., 2013; Yonekura & Nagao, 2007).

Finally, in the third group, the absorption of carotenoids from the intestinal cells is analyzed to figure out the number of mixed micelles that pass through the wall. For this purpose, the carotenoid level in the blood level is measured in some in vivo studies. The carotenoid levels in the tissues that store them like liver or eyes are analyzed in some animal studies (Arunkumar, Harish Prashanth, & Baskaran, 2013; Gorusupudi & Vallikannan, 2012; Sy et al., 2012). Caco-2 cells are used in in-vitro studies and sometimes even the mucus part of the intestinal wall is involved in the systems. The mucus layer usually prevents the passing of the particles larger than about 450 nm (Xia et al., 2017). The presence of lipids and phospholipids in the small intestine was to reported to increase the uptake of carotenoids (Marisiddaiah, Rangaswamy, & Vallikannan, 2011). The types of carotenoids have a great effect in their uptake; the absorption by Caco-2 cells was reported to depend on the hydrophobicity levels of carotenoids (Borel, 2003; Yonekura & Nagao, 2007).

All these studies give valuable information about the factors affecting the carotenoid bioavailability. The common belief for all the studies is that the micellization of carotenoids is the key step for its bioavailability. Although defining the important factors affecting this phenomenon, experimental studies remain insufficient to explain the mechanism behind the solubilization process. Therefore, in this study, it was aimed to investigate the solubilization of β-carotene in dietary mixed micelles at molecular level with the help of molecular dynamics simulations. Among a variety of possibilities, the frame of the study was restrained to investigating the effects of fatty acids with different unsaturation levels and chain lengths at fasted and fed states. For this purpose, β-carotene was chosen as a representative carotenoid due to its common presence in nature, highest vitamin A activity among other carotenoids and wide usage in experimental studies. The fatty acid chain length effect was investigated by using medium- and long- chain Lauric (12:0) and Stearic (18:0) acids, respectively. Besides, to see the effect of the double bond in the structure, saturated (Stearic acid, 18:0), monounsaturated (Oleic acid, 18:1) and polyunsaturated (Linoleic acid, 18:2) fatty acids with the same chain length were used. To avoid the complications to be born from human metabolisms and food-related differences it was assumed that all the lipids undergo complete lipolysis which results with the presence of only fatty acids in the

media. By doing so, the factors related to the release of the *β*-carotene from the lipid phase in the digestive system were eliminated.

1.3.   **Motivation and Objectives**

Experimental studies about carotenoid bioaccessibility and bioavailability have mainly focused on the factors playing role in their solubilization in the dietary mixed micelles as well as their absorption by the epithelial cells. In most of these studies, mixed micelles (and vesicles) were mainly characterized through generic physical properties such as shape, particle size distribution, polydispersity, etc. Even with more sophisticated experimental techniques - which allow working at smaller length scales - such as small angle X-ray scattering (SAXS), small angle neutron scattering (SANS), cryo-transmission electron microscopy (cryo-TEM), etc., the characterization of formed aggregates was limited to the determination of average aggregation numbers. **In other words, a detailed cluster-specific description of the structure and dynamics at the molecular level seems to be missing. This knowledge would certainly shed light onto the understanding of the molecular mechanisms involved in mixed micelle formation in the small intestine and solubilization of *β*-carotene within them**. Indeed, the experimental determination of the micellar structure on an atomic level seems impossible due to the highly dynamic nature of the aggregates and to the fact that the results are often affected by interaction effects which are difficult to disentangle from structural information and cannot be avoided by dilution since this would affect the aggregates (Madenci & Egelhaaf, 2010). At this point, computer simulations appear as a solution. When the literature is surveyed for the computational studies about this subject, it is noticed that only a few studies about the mixed micelle formation have been conducted so far while no study has been reported for the solubilization of *β*-carotene in them.

The motivation of this study comes from the fact that in order to design effective delivery systems that optimize the bioaccessibility of *β*-carotene, a good understanding of the molecular-scale mechanisms by which *β*-carotenes are taken up by the duodenal mixed micelles, the factors modulating this phenomenon and the behavior of mixed micelle constituents at molecular level are needed in the first place. Molecular dynamics simulations, which calculate the time-dependent behavior of a system, provide a

powerful tool to reliably simulate the structure and dynamics of such self-assembly systems.

Based on this motivation, the main and specific objectives of this dissertation is to systematically investigate the molecular-scale mechanisms of solubilization of β-carotene in duodenal mixed micelles, the factors modulating this phenomenon and to reveal the detailed structural and dynamic properties of the system at molecular level through extensive molecular dynamics simulations. Specifically, we aim to investigate;

1. the micellization process of bile salts and phospholipids at fasted and fed state conditions in the small intestine and to characterize the structural properties of formed aggregates

2. the effect of the addition of different fatty acids to the media on self-assembly process and characteristics of formed structures at fasted and fed state conditions. The chain length and the degree of unsaturation are the factors to be investigated.

3. the solubilization of β-carotene within these micelles in the presence of different fatty acids at different concentrations. Besides, the effects of the interactions between β-carotene molecules in the solubilization process and structural properties of the micelles are investigated.

1.4. Computer Simulations

Computer simulations were used for the first time during the Second World War to perform calculations in order to break codes and develop nuclear weapons. Then they became available for civil usage. Today, they are widely used to study the motion of many interacting bodies, which is impossible to calculate by hand (Frenkel & Smith, 2002).

Scientist used experimental data to develop theories before computer simulations. However, the validation of those theories needs more experimental analysis. Today, the validation process can be done with the help of computer simulations which help one to avoid long analysis times and the expense of experimental methods. Besides, in some cases, experimental methods are insufficient to gain more microscopic data about the systems under study. Therefore, usage of

computer simulation appears as a solution in the above-mentioned situations. Moreover, the comparison of the results of computer simulations with experimental results and theoretical predictions allow scientist to test both the model and the theories (Allen & Tildesley, 1989).

1.4.1. Molecular Dynamics Simulations

Molecular dynamics (MD) simulations represent the real dynamics of a system and help to determine the macroscopic properties of a system by using the microscopic model. This model is used in order to describe the main interactions between constituent particles (Apol et al., 2010). The positions of the particles in the systems are derived by applying Newton's equations of motion and this makes it possible to predict the properties of a system at any future time from its current situation. Therefore, MD simulations are referred as deterministic methods and can be used for determination of both static and dynamic properties of a system such as the distribution of kinetic energy or self-diffusion coefficients (Doucet & Weber, 1997).

$$V_{total} = V_{bonded} + V_{non-bonded} + V_{restraints} \tag{1.1}$$

$$V_{total} = V_{bond} + V_{angle} + V_{dihedrals} + V_{elec} + V_{vW} + V_{restraints} \tag{1.2}$$

In a molecular dynamics simulation, the behavior of a system is determined as a function of time from an algorithm that includes a starting structural model and a force field. The force field expresses the potential energy function which is formed by non-bonded and bonded interactions and restraints (if present) (Equation 1.1). Bonded interaction potentials contain bond stretching (V_{bond}), angle (V_{angle}) and dihedral angle ($V_{dihedrals}$) energy while non-bonded interaction potentials involve van der Waals (V_{LJ}) and electrostatic potentials (V_{elec}) (Equation 1.2). The restraints are special potentials that are used for limiting the motion of the system in order to avoid unrealistic deviations or to include experimental knowledge. The restraints can be defined for the positions, angles, dihedrals, distances or orientations (Apol et al., 2010; Doucet & Weber, 1997; S.-J. Marrink, Fuhrmans, Risselada, & Periole, 2009) of particles.

In MD simulations, the system is expressed as a function of the positions and momenta of the constituent particles (Frenkel & Smith, 2002). The motion of the system is determined by solving Newton's equations of motion for the system of N interacting atoms (Equations 1.3). The force on atom i along a coordinate vector r_i is given by the slope of the potential. The negative derivatives of the potential function $V(r_1, r_2 \ldots r_N)$ give the forces (Equation 1.4). In equation 1.3, F_i is the force on atom i caused by the N-1 other molecules and V is the potential function. The equations are solved for small time steps (t) (Apol et al., 2010). A particle moves in a straight line at a constant velocity if there is no force acting on it. The rate of change of the momentum equals the force acting on that particle (Leach, 2001).

$$m_i \frac{\partial^2 r_i}{\partial t^2} = F_i, \qquad i = 1 \ldots N. \tag{1.3}$$

$$F_i = -\frac{\partial V}{\partial r_i} \tag{1.4}$$

Before starting a molecular dynamics simulation, it is necessary to allow a structure to reach a locally stable energy state. But it is difficult to solve because of a large number of atoms and interactions involved. Here, energy minimization is a useful method. Energy minimization is required if a starting configuration is very far from equilibrium, i.e. the forces may be excessively large, and the MD simulation may fail. It also reduces the thermal noise in the structures and potential energies. Depending on the available energy (proportional to the temperature) the molecule may be trapped in a global or local minimum (Apol et al., 2010).

The basic steps of a molecular dynamics simulation can be listed as follows:

1. The parameters that specify the conditions of the run (e.g., number of particles, time step, and initial temperature) are read.

2. The system is initialized (i.e., initial positions and velocities are defined).

3. Energy minimization is performed if necessary (It is necessary if you are preparing the simulation for the first time).

4. The forces on all particles are computed.

5. Newton's equations of motion are integrated. This step and the previous one make up the core of the simulation. They are repeated until the time evolution of the system is computed for the desired length of time.

6. After completion of the central loop, the averages of measured quantities are computed and printed (Frenkel & Smith, 2002).

The steps of MD simulations show that they are similar to real experiments in many aspects. Both methods start with the preparation of samples. Then the experiment and the measurements take place. The details of the similarities between those two methods can be found in Table 1.1.

Table 1.1.Similarities between molecular dynamics simulations and real experiments

Real Experiments	Molecular Dynamics
Prepare a sample of the material	Prepare a sample
	• Select a model system consisting of N particles
Connect this sample to a measuring instrument	• Solve Newton's equations of motion for this system until the properties of the system no longer change with time.
Measure the property of interest during a certain time interval	After equilibration, we perform the actual measurement.
Mistakes: the sample is not prepared correctly, the measurement is too short, the system undergoes an irreversible change during the experiment, or we do not measure what we think	

1.4.2. MARTINI Force Field

The MD simulations can be performed by using different force fields. The force field may consider all-atom or united atom parameters. GROMOS, OPLS-AA/L, AMBER, CHARM, and MARTINI are the most common force fields. The difference between the force fields is born from the differences in the parameters for interactions, potentials and atom/interaction site types. The proper force field selection should be done depending on the system under study.

The MARTINI force field was developed by Marrink et al. (2007) originally to model lipid molecules in a coarser level. The model has been extended to study with

different types of biomolecules like cholesterol, sugars, amino acids, DNA, collagen, etc. (Daily, Olsen, Schlesinger, Ory, & Baker, 2014; Siewert J Marrink et al., 2007; Siewert J Marrink & Tieleman, 2013). In the Martini force filed, the systems are represented by coarser building blocks which are usually calibrated according to experimental thermodynamic data like oil/water partitioning coefficients. The building blocks are named as Martini beads or interaction sites and typically four to one mapping is used for coarsening process. Four to one mapping reduces the degrees of freedom of the system and allows an improvement in time length scale. Thus, for various biomolecular systems, it becomes possible to work with larger systems for longer simulation times with less computer power.

In the Martini force field generally, four heavy (non-hydrogen) atoms are represented by a single bead. In presence of ring structures, the mapping should be less coarse to represent the geometry and two heavy atoms are mapped to one Martini bead. Four to one mapping is also applied to water molecules, i.e. four real water molecules mapped to one Martini water bead. Ions are represented by a single Martini bead containing both the ion and its first hydration shell (Siewert J Marrink et al., 2007).

$$U_{LJ}(r) = 4\epsilon_{ij} \left[\left(\frac{\sigma_{ij}}{r}\right)^{12} - \left(\frac{\sigma_{ij}}{r_{ij}}\right)^{6} \right] \tag{1.5}$$

Martini beads have four main types according to their polarity; polar (P), nonpolar (N), apolar (C), and charged (Q). For more accurate representation of the chemical nature of the molecules, subtypes are also used. There are 9 subtypes and they are distinguishing by denoting the hydrogen bonding capability (d=donor, a=acceptor, da=both, 0=none) and degree of polarity (from 1, low polarity, to 5, high polarity). These particle types are inadequate for ring structures because of not giving geometric specificity of these structures. Therefore "S-particles" are used which result in higher resolution mapping for ring structures of aromatic components, benzene, sugars or sterol bodies (Daily et al., 2014; Siewert J Marrink et al., 2007). Ordinarily, Martini beads mass set to 72 amu, but the mass of beads in ring structures set to 45 amu for providing efficient computation (Siewert J Marrink & Tieleman, 2013; Periole & Marrink, 2013). All particle type combinations create 18 different bead types.

Non-bonded interactions are described by Lennard-Jones (LJ) and electrostatic potentials. In the Martini force field, the LJ 12-6 potential is used in the shifted form and it is calculated for particles i and j with distance r_{ij} (Equation 1.5). In Equation 1.5, ϵ_{ij} is the value of the well-depth and represents the strength of the particle interaction. Therefore, it depends on the particle type. For interactions between strongly polar groups, the value of ϵ_{ij} is 5.6 kJ/mol, whereas for polar and apolar groups interactions ϵ_{ij} is smaller to mimic the hydrophobic effect and equal to 2.0 kJ/mol. The levels of interactions between different bead types are given in Table 1.2. Here level O is the strongest polar interaction site and used for components that are solid in room temperature or particles that have strong hydration shell. Level I models strong polar interactions whereas level II and III model more volatile components. Level IV used for nonpolar interactions in aliphatic chains. The hydrophobic interactions at different levels between polar and apolar phases are showed by level V to VIII. Lastly, the interaction of charged particles and very apolar medium is represented by level IX. In the case of ring particles, ϵ_{ij} is reduced to 75% of its standard value. In Equation 1.5 σ is the LJ parameter which represents the closest distance to approach for two particles and equal to 0.47 nm for all normal particles and 0.43 nm for ring particles (Siewert J Marrink & Tieleman, 2013).

$$U_{el}(r) = \frac{q_i q_j}{4\pi\epsilon_0 \epsilon_{rel} r_{ij}} \tag{1.6}$$

In addition to LJ potential, a shifted Coulombic energy function is used to describe non-bonded interactions of charged groups (Q type). It is calculated with the help of Equation 1.6 for charged groups having charge q with relative dielectric constant value (ε_{rel}) of 15. The non-bonded interactions are used in their shifted forms in Martini force field by 1.2 nm cutoff value (r_{cut}). The LJ and electrostatic potentials are shifted from r_{shift} (0.9 and 0.0 nm, respectively) to r_{cut}. The neighbor list can be updated every 10 steps because of using shifted potentials (Siewert J Marrink & Tieleman, 2013)

Table 1.2. Interaction matrix for coarse-grained Martini beads [a] (Source: Siewert J Marrink et al., 2007)

	sub	Q				P					N				C				
		da	d	a	0	5	4	3	2	1	da	d	a	0	5	4	3	2	1
Q	da	O	O	O	II	O	O	I	I	I	I	I	I	IV	V	VI	VII	IX	IX
	d	O	I	O	II	O	O	O	I	I	I	III	I	IV	V	VI	VII	IX	IX
	a	O	O	I	II	O	O	O	I	I	I	I	III	IV	V	VI	VII	IX	IX
	0	II	II	II	IV	I	O	I	II	III	III	III	III	IV	V	VI	VII	IX	IX
P	5	O	O	O	I	O	O	O	O	O	I	I	I	IV	V	VI	VI	VII	VIII
	4	O	O	O	O	O	O	I	I	II	III	III	III	IV	V	VI	VI	VII	VIII
	3	I	O	O	I	O	I	I	I	II	II	II	II	IV	V	V	V	VI	VI
	2	I	I	I	II	O	I	I	II	II	II	II	II	III	IV	IV	V	VI	VI
	1	I	I	I	III	O	II	II	II	II	II	II	II	III	IV	IV	V	VI	VI
N	da	I	I	I	III	I	III	II	II	II	II	II	II	IV	V	VI	VI	VI	VI
	d	I	III	I	III	I	III	II	II	II	II	III	II	IV	V	VI	VI	VI	VI
	a	I	I	III	III	I	III	II	II	II	II	II	III	IV	V	VI	VI	VI	VI
	0	IV	IV	IV	IV	IV	IV	IV	III	III	IV	IV	IV	IV	IV	IV	IV	V	VI
C	5	V	V	V	V	V	V	V	IV	IV	V	V	V	IV	IV	IV	IV	V	V
	4	VI	VI	VI	VI	VI	VI	V	IV	IV	VI	VI	VI	IV	IV	IV	IV	IV	IV
	3	VII	VII	VII	VII	VI	VI	V	V	V	VI	VI	VI	IV	IV	IV	IV	IV	IV
	2	IX	IX	IX	IX	VII	VII	VI	VI	V	VI	VI	VI	V	V	V	IV	IV	IV
	1	IX	IX	IX	IX	VIII	VIII	VII	VII	VI	VI	VI	VI	VI	V	V	IV	IV	IV

[a] Level of interaction indicates the well depth in the LJ potential: O, $\epsilon = 5.6$ kJ/mol; I, $\epsilon = 5.0$ kJ/mol; II, $\epsilon = 4.5$ kJ/mol; III, $\epsilon = 4.0$ kJ/mol; IV, $\epsilon = 3.5$ kJ/mol; V, $\epsilon = 3.1$ kJ/mol; VI, $\epsilon = 2.7$ kJ/mol; VII, $\epsilon = 2.3$ kJ/mol; VIII, $\epsilon = 2.0$ kJ/mol; IX, $\epsilon = 2.0$ kJ/mol. The LJ parameter $\sigma = 0.47$ nm for all interaction levels except level IX for which $\sigma = 0.62$ nm. Four different CG sites are considered: charged (Q), polar (P), nonpolar (N), and apolar (C). Subscripts are used to further distinguish groups with different chemical nature: 0, no hydrogen-bonding capabilities are present; d, groups acting as hydrogen bond donor; a, groups acting as hydrogen bond acceptor; da, groups with both donor and acceptor options; 1-5, indicating increasing polar affinity.

Bonded interactions are calculated by Equations 1.7 to 1.10 between bonded sites *i, j, k, l* with equilibrium distance of d_b, angle φ_a, and dihedral angles θ_d and θ_{id}. In these equations, *K* symbolizes the force constants and is usually weak. This supplies flexible coarse-grained molecule that results from the collective motions at the fine-grained level. In these equations; V_b is the bonded potential of chemically bonded sites and V_a is the angle potential which represents the chain stiffness. V_d represents the proper dihedrals and only used for the secondary structure of peptide backbone. V_{id} is the improper dihedral potential and used for out-of-plane distortion prevention of planar groups. Here, LJ interactions between nearest neighbors are excluded (S.-J. Marrink et al., 2009).

$$V_b = \frac{1}{2} K_b \left(d_{ij} - d_b \right)^2 \tag{1.7}$$

$$V_a = \frac{1}{2} K_a \left[cos\left(\varphi_{ijk}\right) - cos\left(\varphi_a\right) \right]^2 \tag{1.8}$$

$$V_d = K_d \left[1 + cos\left(\theta_{ijkl} - \theta_d\right) \right] \tag{1.9}$$

$$V_{id} = K_{id} \left(\theta_{ijkl} - \theta_{id} \right)^2 \tag{1.10}$$

CHAPTER 2

MIXED MICELLES OF BILE SALTS AND PHOSPHOLIPIDS

2.1. Introduction

Bile is secreted from the gallbladder and it contains bile acids, phospholipids (PLs), and cholesterol. These secretions form dietary mixed micelles in the small intestine, which have a significant role in the lipid digestion. Lipid digestion basically takes place in the small intestine due to the lipase enzyme present here. Lipase breaks triglycerides into fatty acids and monoglycerides. These lipid digestion products, as well as other lipophilic substances such as cholesterol and fat soluble vitamins, are solubilized in the dietary mixed micelles formed by bile acids and phospholipids. Here, bile acids have a role as an emulsifier or solubilizer.
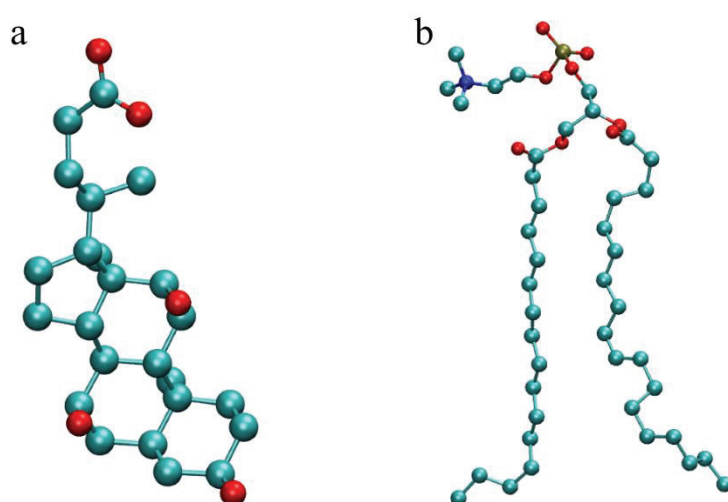
Figure 2.1. Structures of (a) cholate (CHOA) and (b) 1-palmitoyl-2-oleoyl-sn-glycero-3-phosphocholine (POPC) molecules. Red, blue and oil green atoms are representing oxygen, nitrogen, and phosphorus, respectively. Hydrogen atoms are omitted for visual clarity.

Bile acids and their salts are biosynthesized from cholesterol in the liver. They are different from ordinary surfactants which have distinct hydrophilic and hydrophobic head and tail parts. Bile acids have facial amphiphilic structure instead. This characteristic amphiphilic structure is born from the methyl and hydroxyl groups being

attached to different sides of molecules. The methyl groups on the convex *β*-face of the molecule are responsible for the hydrophobic nature while the hydroxyl groups give hydrophilic character to the opposite concave *α*-face (Figure 2.1.a). The number of methyl and hydroxyl groups change depending on the bile acid type. For instance, cholate (CHOA), which is one of the major bile acids present in the human body (and chosen to be used in this study), has three methyl and hydroxyl groups.

In human body, bile acids are usually present in the form of micelles. They form dietary mixed micelles together with phospholipids, which are the other essential components of human bile. POPC (1-palmitoyl-2-oleoyl-sn-glycero-3-phosphocholine) is one of the most common phospholipids secreted from the gallbladder and used in the present study. As in typical phosphatidylcholines, POPC has hydrophilic head groups formed by choline and phosphate groups, hydrophobic glycerol moieties and tail groups. The tail groups are formed by saturated palmitoyl and monounsaturated oleoyl chains (Figure 2.1.b).

The aggregates of bile acids have different properties compared to the aggregates of classical amphiphilic surfactants. The critical micelle concentration (CMC) of bile acids is lower than the CMC of ordinary surfactants. Also, the CMC value is given as a range instead of a single value. The reason is the highly dynamic nature of the aggregates, which continuously exchange molecules with the surrounding media. Another difference is the smaller aggregation numbers observed. Typical aggregates are composed of 2-10 molecules when their concentrations are between 10-50 mM (Jójárt, Viskolcz, Poša, & Fejer, 2014; Warren, Chalmers, Hutchison, Dang, & Pouton, 2006). However, by increasing concentration, the aggregation numbers may reach a high value like 20 (Pártay, Jedlovszky, & Sega, 2007). The concentration and number of molecules both affect the micellization behavior and micelle structure. The solutions of bile acids at different concentrations include micelles with different aggregation numbers. Therefore, they have higher polydispersities than the solutions of classical surfactants. All these differences make it more challenging to understand the formation mechanisms and the structure of mixed micelles involving bile acids.

Many biophysical studies have long been conducted in order to characterize the upper intestinal medium. Several experimental techniques such as dynamic light scattering, small angle X-ray scattering (SAXS), small angle neutron scattering (SANS),

cryo-transmission electron microscopy (cryoTEM), etc. have been used to analyze the generic physical properties such as the morphology, size distribution and dynamics of dietary mixed micelles (Aizawa, Ichikawa, Kotake-Nara, & Nagao, 2017; Arleth, Roskilde, Egelhaaf, Schurtenberger, & Pedersen, 2003; Birru et al., 2014; Cohen, Thurston, Chamberlin, Benedek, & Carey, 1998; Hildebrand, Neubert, Garidel, & Blume, 2002; R. P. Hjelm, Alkan, & Thiyagarajan, 1990; Rex P Hjelm, 1992; Khoshakhlagh et al., 2014; Lin, Chen, Gabriel, & Roberts, 1986; Madenci, Salonen, Schurtenberger, Pedersen, & Egelhaaf, 2011; Mazer, Benedek, & Carey, 1980; Rezhdo et al., 2017). Despite the rigorous efforts made, there are still persisting gaps in the knowledge of mixed micelle formation and micelle structure due to the difficulties associated with the experimental methods. For example, it is impossible to determine the micellar structure at atomic level and also on the basis of individual aggregates owing to the highly mobile and dynamic (continuously dissociating and associating) nature of the micelles (Madenci & Egelhaaf, 2010). Fortunately, the advances in the computational power and techniques have enabled the researchers to attain a deeper understanding of these systems (Prakash et al., 2012). Being a deterministic method, molecular dynamics (MD) simulations are especially considered as a powerful tool to study the structure and dynamics of self-assembly systems reliably.

The first attempt to model human bile and the dietary mixed micelles in the intestinal lumen was the prominent study of Marrink and Mark (2002). They performed a number of atomistic MD simulations on model systems composed of cholate, POPC and cholesterol, and analyzed the equilibrium structures of the mixed micelles at atomic level. Due to the limited computational power of then, their simulations were restricted to a single micelle of predetermined size based on experimental estimates. Furthermore, in order to achieve the equilibration of the systems at accessible time scales, they studied at the concentration of the human gall bladder, which is quite higher from the duodenal concentrations. Ever since, MD simulations of bile salts (BSs) and phospholipids have been of great interest to other researchers owing to their importance in many different fields of applications. Some of the earlier attempts were focused on the structure and aggregation dynamics of simple dietary micelles (composed of BS molecules only) (Pártay, Jedlovszky, et al., 2007; Pârtay, Sega, & Jedlovszky, 2008; Pártay, Sega, & Jedlovszky, 2007; Warren et al., 2006). The studies usually consisted of a certain type of bile acid and the structural characterizations of the micelles formed at

different concentrations were performed. For instance, Warren et al. (2006) carried out separate MD simulations of the spontaneous aggregation of the bile salts cholate, glycocholate, taurocholate, glycochenodeoxycholate, glycodeoxycholate and glycolithocholate in the aqueous phase to gain insight into their micellar structure. The structure and dynamics of the resulting aggregates were analyzed, compared to the existing literature models and an improved model of bile salt association was proposed. The authors indicated that the bile salt micelles are highly dynamic and the intermolecular hydrogen-bonding is one of the major factors influencing size, structure and dynamics of the micelles. Pártay et al. (2007) also obtained results, which supports the previous study. In their study, they performed molecular dynamics simulations at atomistic resolution and investigated the aggregation behavior of two widely studied bile acid salts, namely, sodium cholate and sodium deoxycholate in their aqueous solutions. They studied at three different concentrations (i.e., 30, 90, and 300 mM). The authors indicated that primary micelles were kept together by hydrophobic interactions. At low concentrations, only such hydrophobically bound primary micelles were present in the system, whereas at high concentrations, they formed larger, secondary micelles via hydrogen-bonding. This study also revealed that the observed differences in the aggregation behavior of the cholate and deoxycholate ions originate in their different hydrogen-bonding abilities. Depending on the bile acid type (di- or trihydroxy) the aggregation numbers were shown to vary in the range of 2-20 molecules (Jójárt, Viskolcz, et al., 2014; Pártay, Jedlovszky, et al., 2007; Warren et al., 2006). In those studies, maximum 10 cholate molecules were reported to self-aggregate without having a cavity inside the micelles (Madenci & Egelhaaf, 2010).

Another study showed that the concentration of the bile acids is the main factor affecting the size and shape of the micelles (Haustein, Schiller, Wahab, & Mögel, 2014). The ionic strength of the surrounding medium is another important factor, which was shown to impact the micelle formation. It was stated that the increasing ionic strength caused decreasing repulsion between the charged bile acid molecules and increased the affinity of micelle formation (Madenci & Egelhaaf, 2010). The shapes of the aggregates were found to be size dependent. More spherical geometries were adopted in smaller aggregates while more ellipsoidal shapes were observed with increasing aggregation numbers (Pártay, Sega, et al., 2007). The time dependent investigation of the shape factors showed that micelles exhibited different shapes

varying from prolate to oblate, which can be considered as an indicator of the fluid nature of micelles.

The subsequent computational studies were directed towards both the simple and mixed micelles. Sayyed-Ahmad et al. (2010a) investigated the dependence of the structure of mixed micelles composed of cholate (CHOA) and dodecylphosphocholine (DPC) on concentration. Though, the concentrations and the ratios of PL-to-BS they used were still far beyond the duodenal conditions. Turner et al. (2010a) acquired important knowledge on the intermolecular interactions involved in the micelle formation through their MD simulations of glycocholate (GCHOA) and GCHOA-oleic acid (OA) mixtures. However, they restricted the self-assembly simulations to GCHOA micelles at the gall bladder concentration and studied the incorporation of OAs into a single GCHOA micelle after its dilution to intestinal fed state concentration. Some researchers resorted to using coarse-grained force fields to probe larger length and time scales in order to gain a molecular-scale insight into the micellization process and the structural properties of simple and mixed micelles (Clulow et al., 2017; Haustein et al., 2014; SJ Marrink, 2004; Verde & Frenkel, 2010; Vila Verde & Frenkel, 2016). The BS/PL ratio was reported to be the main factor affecting micellization behavior, aggregation number and shape of the mixed micelles (Birru, Warren, Headey, et al., 2017; Clulow et al., 2017; S. J. Marrink & Mark, 2002). With the accumulation of knowledge and the advance of computational resources, recent studies have been targeted at investigating more sophisticated phenomena such as the effects of digestion products, cholesterol content, pH and inorganic salt content on the phase behavior of intestinal fluids (Birru, Warren, Headey, et al., 2017; Markina, Ivanov, Komarov, Khokhlov, & Tung, 2017; Suys et al., 2017).

The aim of the first part of this dissertation is to analyze and compare the dietary mixed micelle formation under two physiologically relevant duodenal concentrations; i.e., fasted and fed states. Besides, a detailed characterization of the structural properties and their dependence on micelle size are aimed at. For this purpose, CHOA and POPC molecules are chosen for model bile salt and phospholipid molecules in the present study. The cholesterol was excluded on the grounds of various studies showing that the concentration of cholesterol in the small intestine originating from the gall bladder is dilute (Grundy & Metzger, 1972; Wilson & Rudel, 1994), and thus its solubility in the dietary mixed micelles is very low (Coreta-Gomes, Vaz, Wasielewski, Geraldes, &

Moreno, 2016; Matsuoka, Rie, Yui, Honda, & Endo, 2012). Furthermore, it has been demonstrated that cholesterol does not have any significant effects on the micelle size, shape, structure or dynamics under dilute concentrations (SJ Marrink, 2004; Matsuoka, Maeda, & Moroi, 2004; Suys et al., 2017).   As stated before, in order to bring down the computational costs of the self-assembly simulations to affordable levels, the coarse-grained MARTINI force field was used in the simulations. The rest of the chapter is organized as follows. In the next section, the details of the system configurations in the self-assembly simulations and the simulation methodology are given. Then, the evolution of the mixed micelle formation under both fasted and fed states are analyzed, which is followed by a detailed size dependent characterization of the structural properties of the equilibrium micelles.

2.2. Methods

In the methods section, firstly the system details are given. Then the simulation procedure and the analysis methods are explained in detail.

2.2.1. System Details

The concentrations of bile salts and phospholipids in the upper intestinal fluid differ depending on the state of digestion within the body. To model the fasted (before digestion) and fed state (during digestion) conditions, widely used BS:PL concentrations in various *in vitro* studies, 5:1.25 mM and 20:5 mM, respectively, were used (Kossena, Boyd, Porter, & Charman, 2003; Sek, Porter, Kaukonen, & Charman, 2002). The ratio of BS to PL concentrations is fixed to 4 in both states as this ratio is at which they are secreted in bile (Schersten, 1973; Sek et al., 2002). In the simulated conditions, cholate molecules are assumed to be in their negatively charged forms because of having a pKa value (~5.5), which is smaller than the intestinal pH (~7). The simulation media also contain Na^+ and Cl^- ions corresponding to a concentration of 150 mM NaCl to mimic the physiological conditions. Additional Na^+ ions were added to neutralize the systems. Sufficient amounts of water molecules were added to solvate each system to the desired concentration. As one of the objectives was to explore the effects of micelle size on structural properties, three systems of different sizes were studied at fasted state. The compositional details of each system can be found in Table

2.1. The simulation of a larger system at fasted state was prohibited due to overwhelming computational costs.

Table 2.1. Number of molecules in the systems of self-assembly simulations at fasted and fed states.

	Fasted State (BS:PL=5:1.25 mM)			Fed State (BS:PL=20:5 mM)
System/	A	B	C	D
Simulation box size	8000 nm^3	16000 nm^3	20000 nm^3	16000 nm^3
CHOA	24	48	60	193
POPC	6	12	15	48
Na^+	746	1493	1867	1638
Cl^-	722	1445	1807	1445
Water	64873	129699	162178	123538

BS: bile salt, PL: phospholipid, CHOA: cholate, POPC: 1-palmitoyl-2-oleoyl-sn-glycero-3-phosphocholine.

The coarse-grained (CG) MARTINI Force Field was used in the simulations. The previously proposed models for POPC and CHOA molecules (Siewert J Marrink et al., 2007; SJ Marrink, 2004) were adopted in this study. POPC and CHOA are represented by 13 and 8 beads, respectively. There are two charged beads on the POPC head group representing the choline and the phosphate groups two beads of intermediate hydrophilicity are used to represent the glycerol ester moiety, and the remaining 9 beads are hydrophobic tail beads. CHOA is modeled by 6 beads (mapped on a 3:1 basis) forming the sterol body and 2 beads representing the short tail including the charged COO^- group. CG water molecules are comprised of four real water molecules and the CG beads of single atom ions are represented with their first hydration shell. The details of the CG structures together with their atomistic backbones are given in Figure 2.2.
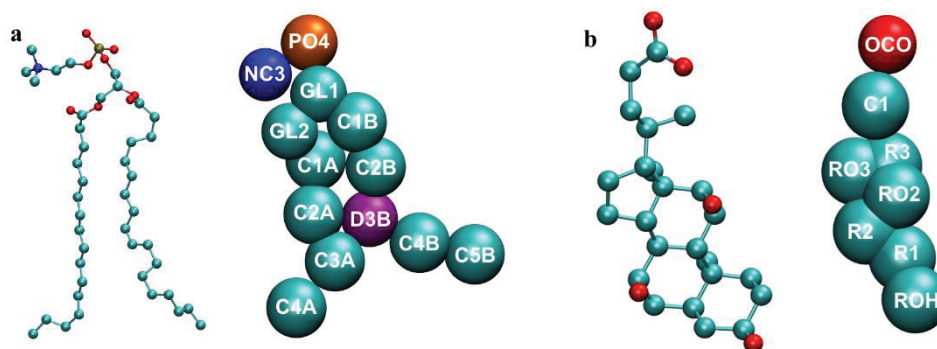
Figure 2.2. Atomistic and coarse-grained structures of (a) POPC and (b) CHOA (cholate). Hydrogen atoms are omitted in atomistic structures for visual clarity.

2.2.2. Simulation Procedure

MD simulations were performed using the GROMACS simulation package (version 5.1) (Hess, Kutzner, Van Der Spoel, & Lindahl, 2008) in cubic simulation boxes with periodic boundary conditions. The coarse-grained simulations were carried out by using standard Martini force field parameters. Lennard Jones potential was used to describe nonbonded interactions with a smooth shift to zero between 0.9 and 1.2 nm. The electrostatic interactions were defined by Coulombic potential with a relative permittivity of 15 and a shift function from 0 to 1.2 nm. Bond lengths of cholate molecules, if present, were constrained with Lincs algorithm. The Maxwell-Boltzmann distribution corresponding to 310 K was used to set the initial velocities of the interaction sites. The neighbor list was updated at every 10 steps. The temperature and pressure couplings (Equation 2.1 & 2.2) (Apol et al., 2010) were performed by Berendsen thermostat and barostat (with a time constant of 1 ps) throughout the simulations, respectively (Berendsen, Postma, Gunsteren, Dinola, & Haak, 1984).

$$\frac{dT}{dt} = \frac{T_0 - T}{\tau} \qquad (2.1)$$

T: Temperature at time t
T_0: Initial temperature
τ: time constant

$$\frac{dP}{dt} = \frac{P_0 - P}{\tau_p} \qquad (2.2)$$

P: Pressure at time t
P_0: Initial pressure

The system setup was performed by random placement of coarse-grained POPC and CHOA molecules into simulation boxes. The necessary configuration and topology files were directly taken from the Martini website (http://cgmartini.nl/index.php). Then the Na^+ and Cl^- ions were added randomly, and the systems were solvated in Martini water molecules. In order to change the initial configurations of constituent molecules and to prevent the close contacts between the molecules, energy minimization was applied by the steepest descent method with the step size of 0.01 nm. Following that, pre-equilibration runs of 10 ns (dt=40 fs) under constant pressure and temperature (NPT) at 1 bar and 310 K, were conducted to relax the systems.

The pre-equilibration and resizing of the boxes were repeated until the system volumes and the concentrations were stabilized. Then the 5 μs runs, including equilibration and production steps, were started at constant NPT with a time step of 20 fs. The attainment of the equilibrium state was monitored by the time evolution of the total energy, pressure, the number-/weight-averaged aggregation numbers of the clusters and the number of free molecules and clusters within the system. In the meantime, whenever shrinkage in size occurred during pressure coupling, simulation boxes were resized and filled with additional CG water molecules to maintain the desired concentration of bile lipids. Once the system volumes (thus, the concentrations) were stabilized, the equilibration runs were started at constant NPT with a time step of 20 fs. The attainment of the equilibrium state was monitored by the time evolution of the total energy, the number/weight-averaged aggregation numbers of the clusters and the number of free molecules within the system. The equilibration simulations were followed by the production runs (using the same parameters), which lasted for 1 to 4 μs depending on the system. The sum of both the equilibration and production runs for each system lasted for 5 μs in total.

For each system, the micelle that was observed for the longest time in the trajectory (belonging to the production runs) was chosen for detailed structural analyses. The extraction process of selected micelle from the equilibrium trajectory is computationally very costly due to the high number of molecules in the systems. Since the structural analyses were aimed to be made for only the selected equilibrium micelle, an alternative approach was followed instead. The selected micelle for each system (of which the structure has already been equilibrated) was extracted from the final frame of its original trajectory and placed in a smaller simulation box full of equilibrated Martini

water molecules. Additional CHOA molecules were added to this box to maintain the intermicellar CHOA concentration (i.e., the concentration of the free CHOAs in the aqueous solution) in the original simulation box. The 150 mM NaCl concentration with additional Na^+ ions, to neutralize the media, were also preserved. After a short re-equilibration simulation, the production run was started on these smaller simulation boxes. The equilibrium simulations on each system were extended until at least 80000 time frames were collected. The analyses of the structural properties were performed on these trajectories (over the last 150-300 ns). The global structures were analyzed through the calculations of the radii of gyration (R_g), the ratios of the principle moments of inertia and the solvent accessible surface area (SASA). The local structures were examined through the radial density distributions (RDDs). The average angles between selected vectors in a molecule and with respect to the radial vector were calculated to further analyze the internal and surface orientations of the constituent molecules.

2.2.3. Analysis Methods

In the analysis methods section, firstly the selection of the cluster criterion is explained. Then the analysis methods used for the characterization of self-assembly process and determination of the structural properties of the formed micelles are given.

2.2.3.1. Clustering

In order to analyze the clusters formed throughout the trajectories, a cluster criterion had to be decided in the first place. The cluster criterion was determined based on the inspection of the first minima of the RDFs between the individual CG beads of the CHOA and POPC molecules in a micelle. Two molecules were considered to belong to the same cluster if the distance between their closest beads was smaller than 0.6 nm. This cutoff value was also verified by analyzing the time dependent number of clusters with varying cutoff values (0.5 to 1.0 nm), and visual inspection of the snapshots of clusters. Moreover, the chosen cutoff is in agreement with similar studies conducted with different phospholipids using the MARTINI force field field (Brocos, Mendoza-Espinosa, Castillo, Mas-Oliva, & Piñeiro, 2012; Kraft, Vestergaard, Schiøtt, & Thøgersen, 2012; Sanders & Panagiotopoulos, 2010). The clustering was performed with the *gmx_clustsize* tool of GROMACS.

2.2.3.2. Weight and Number Averaged Aggregation Numbers

Time dependent weight- (N_w) and number- (N_n) averaged aggregation numbers were calculated in order to trace the aggregation behavior of the systems. The calculations were performed by the help of the Equations 2.3 and 2.4 (Sayyed-Ahmad et al., 2010) where A_n is the number of micellar aggregates consisting of n molecules.

$$N_n = \frac{\sum_{n>1} n A_n}{\sum_{n>1} A_n} \qquad (2.3)$$

$$N_w = \frac{\sum_{n>1} n^2 A_n}{\sum_{n>1} n A_n} \qquad (2.4)$$

2.2.3.3. Radius of Gyration

To gain information about micelle dimensions, the radius of gyration (R_g) was calculated for three principle directions by the *gmx_gyrate* tool of GROMACS. R_g is calculated by the help of Equation 2.5 where m_i and r_i represent the mass and the position of atom *i*, respectively, with respect to the center of mass of the micelle (Apol et al., 2010).

$$R_g = \left(\frac{\sum_i ||r_i||^2 m_i}{\sum_i m_i} \right)^{\frac{1}{2}} \qquad (2.5)$$

2.2.3.4. Principal moments of inertia

The shapes of micelles were characterized by calculating the ratios of the three principal moments of inertia I_1/I_2 and I_2/I_3 (where $I_1 < I_2 < I_3$). The ratios of I_1/I_2 and I_2/I_3 define the micelle shapes, i.e., $I_1 \approx I_2 \approx I_3$ and $I_1/I_2 \approx I_2/I_3 \approx 1$ for spherical structures, $I_1 \approx I_2 \ll I_3$ and $I_1/I_2 \approx 1$ and $I_2/I_3 \approx 0$ for disk-like structures and $I_1 \ll I_2 \approx I_3$ and $I_1/I_2 \approx 0$ and $I_2/I_3 \approx 1$ for rod-like structures. Three principal moments of inertias are calculated using Equations 2.6 to 2.8 (Apol et al. 2010) by the *gmx_gyrate* tool of GROMACS.

$$\breve{I} = \begin{matrix} I_{xx} & I_{xy} & I_{xz} \\ I_{yx} & I_{yy} & I_{yz} \\ I_{zx} & I_{zy} & I_{zz} \end{matrix} \qquad (2.6)$$

m_a: the atomic mass of atom *a*

q_{ij}: the respective atomic degree of freedom

$$I_{ii} = \sum_\alpha m_\alpha \left(q_{j \neq i}^2 + q_{k \neq i}^2 \right) \quad (2.7)$$

$$I_{ij} = -\sum_\alpha m_\alpha q_i q_j \quad (2.8)$$

2.2.3.5. Solvent Accessible Surface Area

Solvent accessible surface areas (SASA) were calculated separately for all, hydrophilic and hydrophobic moieties of the micelles. SASA is calculated by using an imaginary probe with the radius of a solvent molecule. This probe is assumed to scan the selected surface area for calculation. The radius of the probe was selected as 0.56 nm in the present study which is equal to the diameter of a Martini water bead (represents four real water molecules).

2.2.3.6. Radial Density Distributions (RDDs)

The RDDs of selected beads in a molecule with respect to center of mass (com) of the micelles were calculated to gain detailed information about the local inner structures and the distributions of water and ions around them. RDDs ($\rho(r)$) were calculated by normalizing the radial distribution functions (RDFs) with the number of selected beads and the box volume of the systems by the help of Equation 2.9. In this equation $g_{AB}(r)$ represents the RDF of particle A with respect to particle B. The RDF calculations were performed by the *gmx_rdf* tool, which uses Equation 2.10. Here, V represents the total volume of the system and $P(r)$ represents the probability of the particle B *being* distance r away from particle A (Apol et al., 2010).

$$\rho(r) = g_{AB}(r) \left(\frac{number\ of\ particles}{box\ volume} \right) \qquad (2.9)$$

$$g_{AB}(r) = \frac{V}{4\pi r^2} \sum_{i \in A}^{N_A} \sum_{i \in B}^{N_B} P(r) \qquad (2.10)$$

For RDD calculations were performed for each bead of CHOA, and head (NC3$^+$, PO4$^-$), intermediate (GL1, GL2) and tail groups (C1A, C2A, C3A, C4A, C1B, C2B, D3B, C4B, C5B) of POPC molecules. Besides, RDDs of surrounding water molecules

and Na^+ and Cl^- ions were analyzed to understand the structuring of these molecules/ions around the micelles.

2.2.3.7. Intramolecular and Intramicellar Angles

The average angles between selected vectors in a molecule were calculated to further analyze the internal and surface orientation of the constituent molecules and/or specific moieties. The calculations were performed using the *gmx_gangle* tool of GROMACS considering two different types of angles: Type I: The angle between a vector which is formed by two selected beads on a molecule and the radial vector (calculated as the vector from the com of the micelle to the midpoint of the selected beads' positions) (Figure 2.3-a); and Type II: The angle between two vectors in a molecule denoted by 3 beads in total, of which the middle bead is the origin of both vectors and the remaining ones indicate their directions (Figure 2.3-b). The latter gives information about the conformations of the molecules within the micelles.
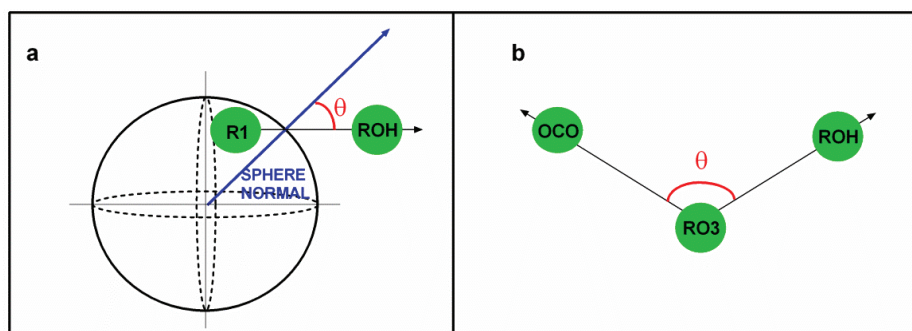
Figure 2.3. The illustrations for Type I (a) and Type II (b) angles

2.3. Results and Discussion

In the results and discussion section, firstly evolution of the micellization is explained. Following that the structural characterization of the selected mixed micelles are investigated.

2.3.1. Evolution of the Mixed Micelle Formation

The evolution of the micellization process in each system (Table 2.1) was examined separately. The clusters were determined using a cutoff of 0.6 nm as described in Section 2.2.3.1. In order to trace the aggregation behavior of the systems the time dependent number of clusters and weight- (N_w) and number- (N_n) averaged aggregation numbers were calculated. The data were also used to check whether the simulations were equilibrated.
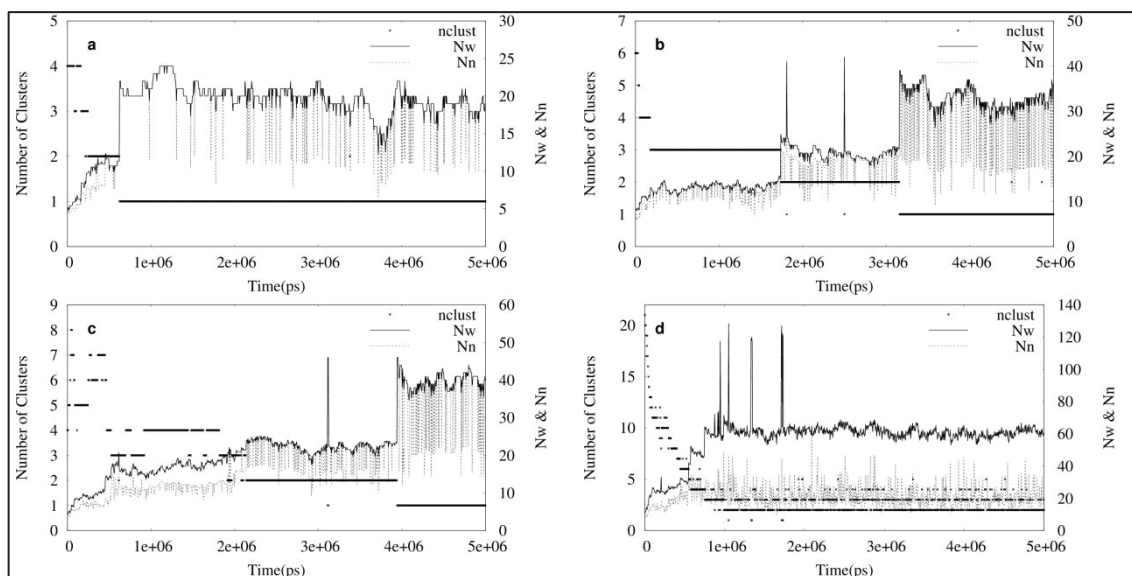
Figure 2.4. The time evolution of the number of clusters (left y-axis) and weight- (N_w) and number- (N_n) averaged aggregation numbers (right y-axis) for systems A (Fasted-8000 nm^3), B (Fasted-16000 nm^3), C (Fasted-20000 nm^3) and D (Fed-16000 nm^3). Results are given for each 5th ns of the trajectory (skipping the intermediate frames) for visual clarity. The numbers of clusters results were refined by excluding the clusters with two molecules.

The time evolution of the number of clusters, N_w and N_n are given in Figure 2.4 for each 5th ns of the trajectory for the purpose of visual clarity. The number of clusters results were refined by excluding the clusters composed of two molecules. The expected trends of decreasing number of clusters and increasing N_w and N_n with time, which indicates the evolution towards equilibrium, are exemplified in all the systems. The correspondence of the time steps at which a sudden drop in the number of clusters and a sudden jump in N_w in each system is certainly not accidental. This indicates that the smaller aggregates that were self-assembled in the earlier stages of the simulations merge together to form larger aggregates in the course of the process, finally eventuating in stable micelles. The sharp peaks in N_w observed in Figure 2.4-b,c,d also

correspond to the fusion moments of two aggregates into a single larger cluster. However, the structures formed were apparently unstable as they split into two soon. The simulation times after which no more consistent dramatic changes in the aggregation numbers and the number of clusters were observed were taken as the equilibration points for the simulations, which correspond to roughly 1, 3, 4 and 1 μs for systems A, B, C, and D, respectively. The increasing trend in the equilibration times observed in the fasted state systems (towards system C) is the expected consequence of the significant increase in system sizes. A faster equilibration was observed in the fed state system (D) compared to the fasted state system of similar size (system B), which is due to higher lipid concentrations in the former (Turner et al., 2010).

Although the mixed micelles obtained in each system were equilibrated structures as implied by Figure 2.4, the attainment of true thermodynamic equilibrium states in these systems did not seem applicable due to the limited system size and computation times imposed by the available computational sources. This is especially the case for fasted state systems as they were very dilute in bile lipids (6.25 mM in total). Each fasted state system ended up in a single mixed micelle, which grew in size with increasing number of bile lipids while the concentration was kept constant. This behavior is an indication of the above-mentioned situation; i.e., fail to attain the true thermodynamic equilibrium states. As a matter of fact, the true thermodynamic equilibrium state -at the total lipid concentration ranges (6.25-25 mM) and the PL-to-BS ratio (0.25) covered here- is expected to be composed of simple micelles coexisting with mixed micelles as shown by several experimental studies (Birru et al., 2014; Madenci et al., 2011; Mazer et al., 1980) before. The attainment of thermodynamic equilibrium states in dilute systems, in which multiple micellar structures with varying sizes in dynamic equilibrium with free unimers would be observed, requires very large system sizes and long simulation times even with CG force fields (Sanders & Panagiotopoulos, 2010; Sayyed-Ahmad et al., 2010). Although it is less likely to capture the true equilibrium states via simulations of limited system size and time windows, the results obtained from these simulations still provide valuable insight into the mechanism of micellization. Besides, each millar structure formed in different sizes can be seen as representative transient state aggregates (Lebecque, Crowet, Nasir, Deleu, & Lins, 2017), which appear during the course of digestion and are very dynamic in nature (Madenci & Egelhaaf, 2010; Phan et al., 2015; Xie et al., 2014).

These transient state structures are also believed to possess a role in the bioaccessibilities of lipophilic (Birru et al., 2014; Yao, Xiao, & McClements, 2014). The fate of lipophilic molecules within the aqueous duodenal medium under non-equilibrium conditions would certainly be of interest for further investigations.

In contrast to the fasted state systems, simulations of the fed state system reached a relatively fast equilibrium with two separate mixed micelles (Figure 2.4-d). The predicted cluster size distribution in the fed state seems to be more reliable (although not definitive) since an equilibrium phase consisting of more than a single mixed micelle coexisting with simple micelles was obtained. As mentioned above, this is the expected phase behavior of a mixture of PLs and BSs at a total lipid concentration of 25 mM and a PL/BS ratio of 0.25 (Birru et al., 2014; Madenci et al., 2011; Mazer et al., 1980). Furthermore, an additional simulation of the system performed in a half-sized simulation box resulted in the same result.

The cumulative probability distributions of the aggregation numbers are given in Figure 2.5 as block-averaged values over 1 µs increments to analyze the time dependent behaviors. Similar micellization behaviors were observed in all the systems. The initial stages of the simulations were dominated by dimers of cholates and small clusters involving mainly simple micelles, and, to lesser extent small mixed micelles. As the simulations proceeded, these small clusters merged together to form larger aggregates as evidenced by their disappearance towards equilibrium. For instance, in system C, clusters with small aggregation numbers (3 to 15) dominated the system up to 3 µs. The following 1 µs interval of the trajectory was sampled by relatively larger micelles (with aggregation numbers ranging from 17 to 27) while the smaller aggregates seen in the previous stages were no longer observable, indicating their fusion. Likewise, the largest micelles (37-44) were observed only after the equilibration point (4 µs) after which none of the small micelles were observed anymore. This finding is also supported by the time evolution of N_w and the number of clusters (Figure 2.4) values as discussed above. At equilibrium, the mixed micelles were involved in a dynamic exchange of cholates with the surrounding medium. This was observed by visual inspection of the final stages of the trajectories. It was also observed that once the hydrophobic core was formed by POPC molecules, they never left the micelles. Therefore, we infer that the broadness of the equilibrium size distributions is due to this dynamic exchange of cholates between the micelles and the aqueous phase. Another observation is that the broadness of the

equilibrium size distribution seems to increase with increasing system size. Taken all together, these observations suggest a mechanism, which is independent of the total bile lipid concentration such that once the hydrophobic core is formed by the POPC tails, cholates try to fill in the available spaces on the micelle's surface. Similar behavior was reported for the self-assembly of mixed micelles composed of cholate and sodium dodecyl sulfate (Jójárt, Poša, et al., 2014).
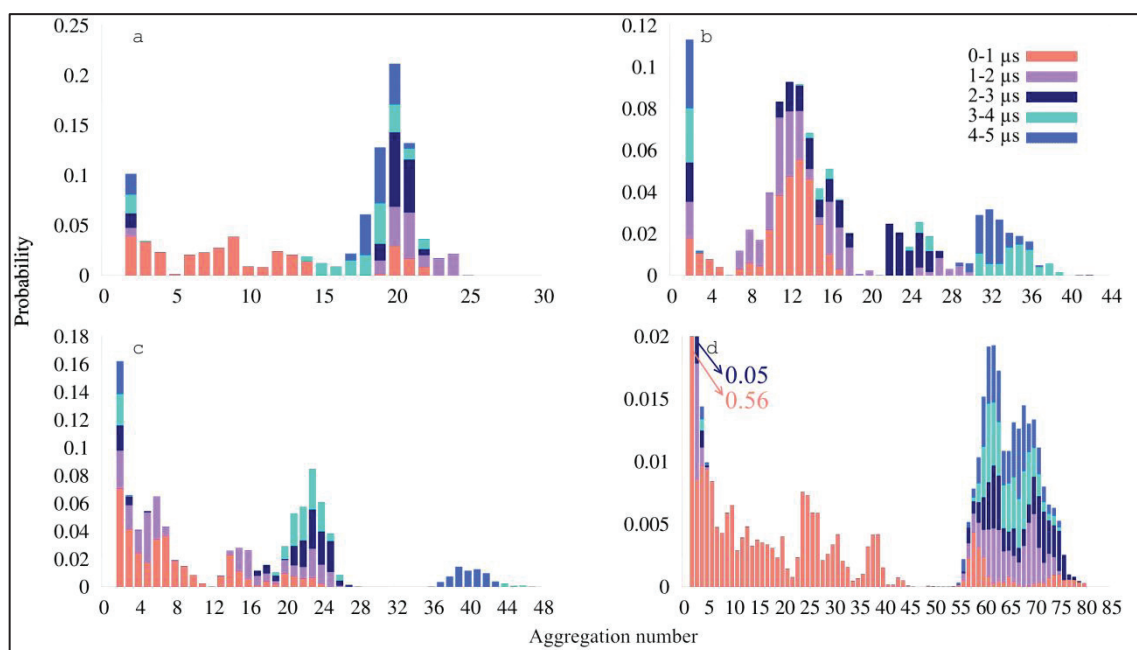
Figure 2.5. The cumulative probability distributions of aggregation numbers as a function of time (block-averaged over 1 μs intervals) for systems A (Fasted-8000 nm^3), B (Fasted-16000 nm^3), C (Fasted-20000 nm^3), and D (Fed-16000 nm^3). The regions including larger aggregation numbers in part (d) are omitted for clarity.

The evolution of micelle formation is demonstrated for the fed state system in Figure 2.6 as a collection of subsequent snapshots from the trajectory. The first snapshot (Figure 2.6-a) displays the initial configuration where all the participant molecules were randomly placed in the box. The fast self-assembly was observed beginning from the earlier stages of the simulation (Figure 2.6-b). In the course of the simulation, larger micelles were formed by the fusion of smaller clusters (Figure 2.6-c,d). Moreover, some representative aggregates/micelles formed during the simulation of system A (fasted-8000 nm^3) are given in Figure 2.7 to give some idea about the intermolecular interactions.

34
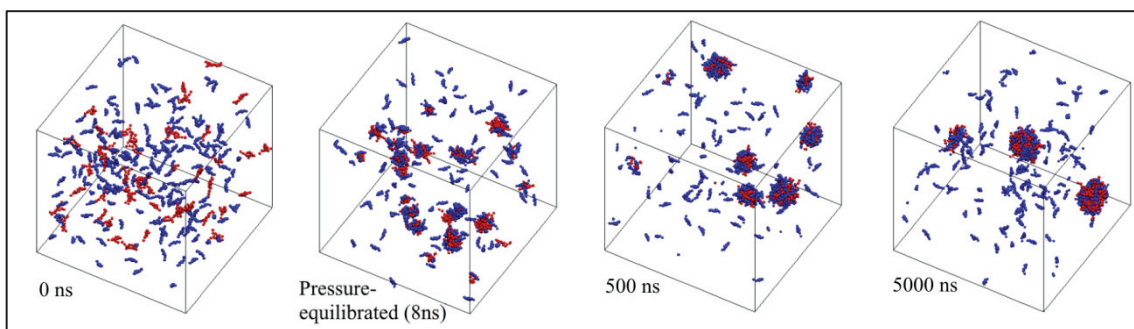
Figure 2.6. Snapshots from the trajectory of system D (Fed-16000 nm^3) showing the evolution of the self-assembly. Cholate and POPC molecules are colored in blue and red, respectively. Water molecules and ions are omitted for visual clarity.
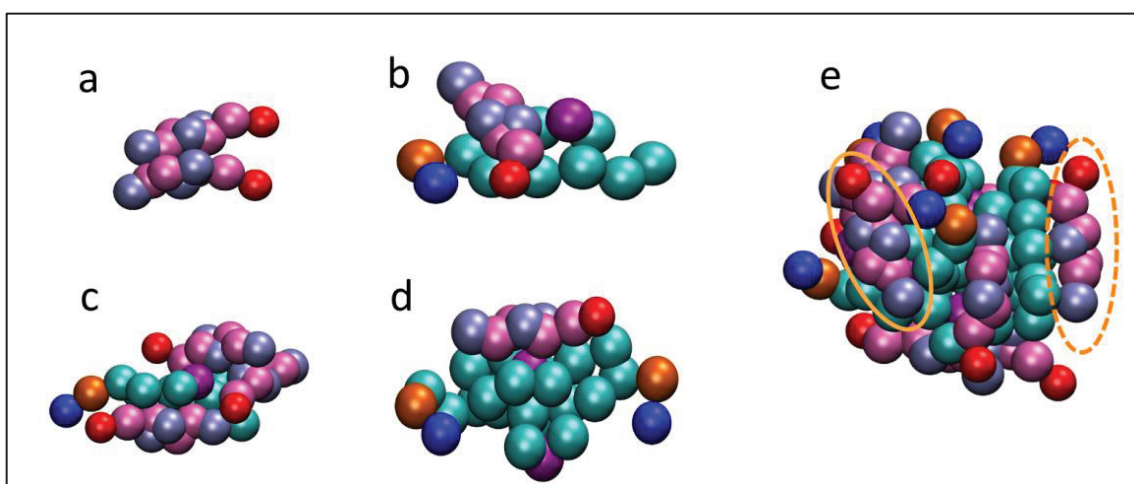
Figure 2.7. The representative aggregates that were formed during the simulation of system A (Fasted-8000 nm^3). The hydrophobic, hydrophilic and charged beads of cholates are colored in pink, ice blue and red, respectively. NC3$^+$ beads are colored in blue while PO4$^-$ beads are colored in orange. Glycerol and tail beads of POPCs are colored in cyan except for the bead with an intrinsic double bond, which is colored in purple.

The first aggregates in the earlier stages of the trajectory were formed by the neighboring CHOA (Figure 2.7-a) and CHOA-POPC (Figure 2.7-b) molecules. The dimers formed by parallel aligned cholates representing the majority of the population, as shown in Figure 2.7-a, result from the hydrophobic alignment of their steroid backbones. This configuration between bile salts has been reported several times (Haustein et al., 2014; Madenci & Egelhaaf, 2010; Sayyed-Ahmad et al., 2010; Turner et al., 2010; Verde & Frenkel, 2010). Figure 2.7-b shows a cross alignment of a POPC and a CHOA forming a dimer. This type of arrangement has also been reported between POPC and glycodeoxycholate (Birru, Warren, Headey, et al., 2017). The interaction

35

between them is mainly through the hydrophobic side of CHOA and the tails of POPC, as expected. Besides, an electrostatic interaction between the carboxylate and choline moieties of CHOA and POPC, respectively, seems to exist. Imminently, the aggregates became larger by joining of the free cholates. In Figure 2.7-c, a configuration involving a wrapped POPC tail by three CHOAs is shown. Note that the CHOAs exhibit different alignments with respect to POPC to ensure that the hydrophobic tail beads are effectively shielded from water. The strong affinity between POPC tail beads due to the hydrophobic effects resulted in aggregation of two or a few more POPC molecules during the early stages of simulations. An example arrangement between two POPC molecules aligned antiparallel to each other and a single CHOA trying to cover the tail beads is given in Figure 2.7-d. In the following time steps, those small aggregates fused in together to form larger clusters. The cluster shown in Figure 2.7-e, which is composed of 14 molecules in total, was formed by the fusion of the smaller aggregates including the ones in Figure 2.7-c,d. As the figure suggests, the micelle core is composed of POPC tail segments while the charged head beads protrude from the micelle surface into the aqueous phase. CHOAs, on the other hand, are arranged as wedges in different configurations on the micelle surface such that their hydrophilic sides are facing the solvent while trying to cover the POPC tails with their hydrophobic sides (circled molecule in Figure 2.7-e). Though, the opposite alignment (hydrophilic side facing the micelle core) was also occasionally possible (dash-circled molecule in Figure 2.7-e). Their alignment on the micelle surface was mostly flat (although not perfectly) as also suggested by the RDDs and the angle calculations (see Section 2.3.2.2 and 2.3.2.3). These morphological observations were also reported in other similar computational self-assembly studies involving bile salts and phospholipids (Birru, Warren, Han, et al., 2017; Haustein et al., 2014; S. J. Marrink & Mark, 2002; Prakash et al., 2012; Sayyed-Ahmad et al., 2010). Further findings on the morphological details of the mixed micelles are discussed in Section 2.3.2. Only the micelles with aggregation numbers that exhibit the largest cumulative probability after the equilibration point (i.e., 20, 32, 39 and 62 membered micelles for systems A, B, C, and D, respectively) were chosen for further analysis (Figure 2.8).
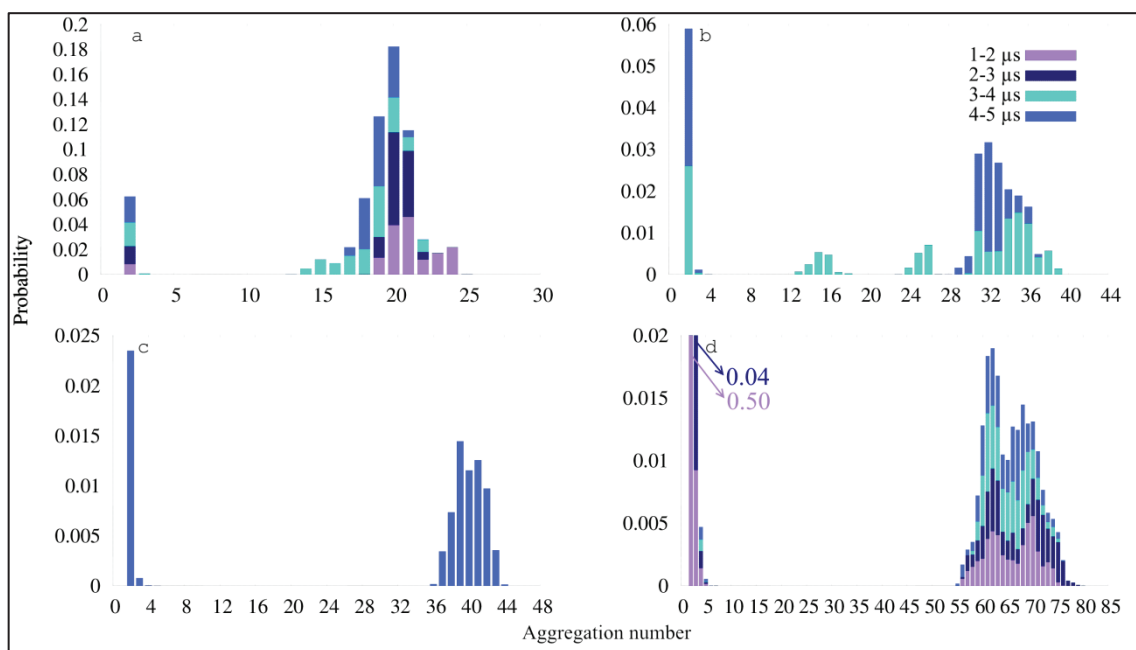
Figure 2.8. The cumulative probability distributions of aggregation numbers as a function of time (block-averaged over 1 μs intervals) after the corresponding equilibrium points for systems A, B, C, and D. The regions including larger aggregation numbers in part (d) are omitted for clarity.

2.3.2. Size Dependent Structural Characterization

Size dependent structural characterization of the mixed micelles were performed by calculating radius of gyration, principle moments of inertia and solvent accessible surface areas.

2.3.2.1. Size and Shape Properties

The radii of gyration (R_g) of the selected micelles were calculated to acquire an idea about the micelle sizes. Experimental studies have shown that micelle size is dependent on the total lipid concentration, the ratio of PL/BS in the medium, and the micellar PL/BS ratio; i.e. the ratio of PL to BS within the micelle (Nichols & Ozarowski, 1990). As mentioned before, the PL/BS ratio in the solution used in this study is 0.25 regardless of the total concentration, which rules out the assessment of the dependence of micellar properties on this factor. The micellar PL/BS ratios in our equilibrium micelles and the calculated R_g values are given in Table 2.2.

Table 2.2. Structural properties of the selected micelles: Radius of gyration (R_g); ratios of the principal moments of inertia, (I_1/I_2) and (I_2/I_3); total solvent accessible surface area (SASA); SASA per surfactant; the ratio of the hydrophilic SASA to hydrophobic SASA (Phi/Pho); and the average palmitoyl and oleoyl tail lengths of POPCs in the micelles.

System - Selected micelle	Numbers of CHOA:POPC molecules	Micellar POPC/CHOA Ratio	R_g (nm)	I_1/I_2	I_2/I_3	Total SASA (nm^2)	SASA per surfactant (nm^2)	Phi/ Pho	Average POPC tail lengths (nm)	
									Palmitoyl*	Oleoyl**
A - 20Fa	14:6	0.43	1.301±0.026	0.841±0.079	0.902±0.047	76.417 ±3.333	3.821	5.042	1.158±0.052	1.358±0.085
B - 32Fa	20:12	0.6	1.546±0.017	0.884±0.059	0.918±0.040	103.995±3.651	3.250	6.544	1.170±0.037	1.388±0.060
C - 39Fa	24:15	0.625	1.653±0.018	0.888±0.058	0.919±0.040	116.793±4.095	2.995	7.297	1.171±0.033	1.394±0.052
D - 62Fed	40:22	0.55	1.896±0.016	0.886±0.056	0.927±0.036	146.295±4.511	2.360	9.687	1.176±0.027	1.405±0.043

*The average palmitoyl tail length was calculated as the average distance between the C1A and C4A beads of POPCs over the corresponding equilibrium trajectory.

**The average oleoyl tail length was calculated as the average distance between the C1B and C5B beads of POPCs over the corresponding equilibrium trajectory.

First, the analysis of the mixed micelle at fed state (62-Fed) will be reported as it is considered to represent the true thermodynamic equilibrium structure fairly (Section 2.3.1). Its R_g was found to be 1.896±0.016 nm, which is in agreement with the literature. Mazer and coworkers (1980) reported that the hydrodynamic radii (R_h) of the mixed micelles changed between 1.8 and 3.5 nm when the PL/BS ratio in solution was smaller than 0.6. Similarly, Kossena et al (2003) reported an R_h value of 3.5 nm for both fasted and fed state mixed micelles where the PL/BS ratio in solution was 0.25. Schurtenberger et al. (1985) and Khoshakhlagh et al. (2014) determined an R_h of 2.4 nm when that ratio was equal to 0.3 and 0.25, respectively. For the sake of a fair comparison, one should keep in mind that R_h value for a spheroidal particle is greater than its R_g. More specifically, R_g/R_h ratio is 0.77 for a solid sphere (Tande, Wagner, Mackay, Hawker, & Jeong, 2001). As will be discussed below, the micelles of this chapter were found to be slightly ellipsoidal in shape. Therefore, it is believed that the R_g value determined for the 62-fed micelle reproduces the sizes reported in the literature fairly well.

The calculated R_g values for the fasted state equilibrium mixed micelles range from 1.301±0.026 nm to 1.653±0.018 nm with increasing aggregation numbers (Table 2). Once more, it should be noted that the equilibrated structures obtained from fasted state systems in this work do not completely characterize the corresponding true thermodynamic equilibrium state due to the limited system size issues (Section 2.3.1). Indeed, the experimental values reported for the radius of mixed micelles at fasted state concentrations range from 3.5 to 7.5 nm (Khoshakhlagh et al., 2014; Kossena et al., 2003; Mazer et al., 1980; Schurtenberger et al., 1985). On the other hand, Fatouros et al. (2007) reported an R_g of 2.5 ± 0.9 nm for a mixed micelle formed in a 5:1 mM mixture of BS:PL. The differences between the results reported in separate studies might be arising from the different types, amounts or micellar ratios of BS and PL, the experimental conditions and the methods used to determine the size of micelles. The compositions of the selected equilibrium micelles and the dependence of their size on aggregation number (N) were also analyzed (Table 2.2). Comparison of the fasted state systems suggests that at a fixed total lipids concentration and BS/PL ratio in solution, micelle size increases with increasing micellar POPC/CHOA ratio. Similar behavior was reported for cholate/DPPC mixed micelles by Haustein et al. (2014). The micellar ratio of PL/BS in the 62-fed micelle is also around 0.6. Finally, the R_g was found to be

linearly dependent on $N^{1/3}$ ($R^2 = 0.9962$, Figure 2.9-a) as expected for spheroidal micelles.
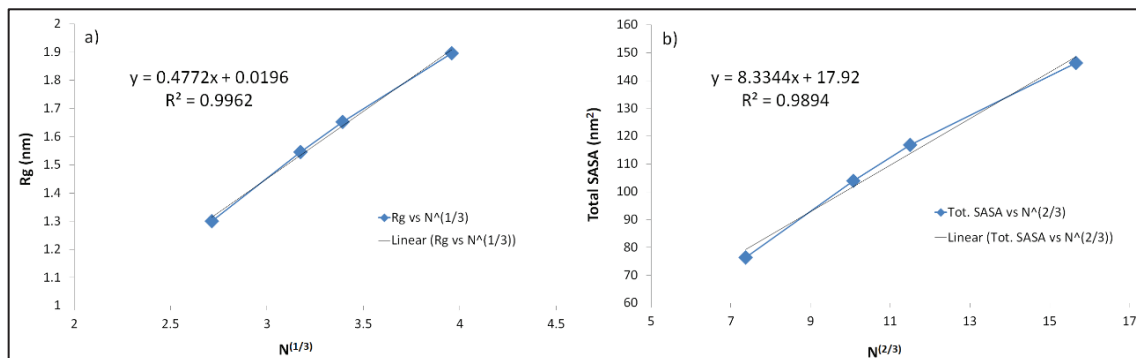
Figure 2.9. The relationships between **a)** the average radii of gyration (R_g) and aggregation number (N) to the power (1/3), **b)** total SASA and the aggregation number (N) to the power (2/3).

To characterize the shape of micelles, the ratios of three principal moments of inertia (I_1/I_2 and I_2/I_3) were calculated (where $I_1 \leq I_2 \leq I_3$). The ratios, I_1/I_2 and I_2/I_3, describe the micelle shapes; i.e., for spherical micelles, $I_1 \approx I_2 \approx I_3$ and $I_1/I_2 \approx I_2/I_3 \approx 1$; for disc-like micelles, $I_1 \approx I_2 \ll I_3$, and $I_1/I_2 \approx 1$ and $I_2/I_3 \approx 0$; for rod-like micelles, $I_1 \ll I_2 \approx I_3$, $I_1/I_2 \approx 0$ and $I_2/I_3 \approx 1$. As shown in Table 2.2, the average values for the ratios are close to, but smaller than 1. This indicates that the micelles are globular; not perfectly sphere, but slightly ellipsoidal in shape. Comparison of the values for each micelle suggests that the micelles are pretty similar in shape. It is only the smallest micelle (20-Fa), which seems to deviate more from spherical geometry. This must be due to the compositional differences rather than the micelle size for two reasons. Firstly, the ratios of the moments of inertia for the three largest micelles are very similar although their sizes are different, indicating no size dependence. Secondly, the micellar POPC/CHOA ratios in those micelles are similar (~0.6) while that of the smallest micelle is distinctive (0.43). Therefore, it must be this compositional difference, which led to a less spherical geometry in the smallest micelle. This behavior was observed also for DPC-CHOA micelles, which were shown to deviate from sphericity to a larger extent with increasing CHOA/DPC ratios (Sayyed-Ahmad et al., 2010). It is inferred that the dependence of the micelle shape on its composition is a result of its dependently changing flexibility, which is a function of the core fluidity. In the next section, it is shown that the core packing density of the POPC tails is the lowest in the smallest micelle and increases

with micelle size. Thus, the core fluidity is expected to be the highest in the smallest micelle resulting in more flexibility in shape. The latter can be inferred from the higher standard deviations of the corresponding I_1/I_2 and I_2/I_3 ratios in the smallest micelle compared to the others. All these differences prevailing, we should still note that they are small. It remains to be seen whether more significant differences would be observed for micelles covering a larger size range than the one studied in this work.

Another size dependent property is the solvent accessible surface area (SASA). The calculations were performed using a solvent probe of 0.56 nm in radius to mimic one MARTINI water bead, which represents four atomistic water molecules. Table 2.2 displays the total SASA, SASA per surfactant, and the ratio of the hydrophilic to hydrophobic SASA (Phi/Pho). The total SASA increased with micelle size as expected. For spheroidal micelles, it is expected that the total SASA is related linearly to $N^{2/3}$. This relationship was also observed for the micelles of this work to a good degree (R^2=0.9894, Figure 2.9-b). The small divergence might be due to that the micelles are not perfect spheres and their surfaces are rough (as it is seen in Figure 2.6 and Figure 2.7-e), which also contributes to the calculation of SASA. The contribution of the hydrophobic SASA to the total SASA is very small as understood from the high (and ever increasing) Phi/Pho ratios. As a higher Phi/Pho ratio means a more thermodynamically favorable organization of the hydrophilic and hydrophobic domains (Lebecque et al., 2017), it is inferred that as the micelles get larger they become more stable. This can be interpreted as evidence to the notion that hydrophobic effects are the main driving forces for the micellization. Finally, the decrease in total SASA per surfactant with increasing micelle size points to a denser surface packing of the molecules with size. This is also supported by the joint interpretation of the RDDs and angle measurement results (Section 2.3.2.2 and 2.3.2.3).

2.3.2.2. Radial Density Distributions

The local inner structure of the micelles and the distribution of ions and water molecules around them were investigated through RDDs. In Figure 2.10-a1, a general representation of the inner and surface organization of the molecules is depicted, which displays the RDDs of the specified moieties of POPC /CHOA, water molecules and ions with respect to the com of the micelle for 62-Fed system. It shows that the core is
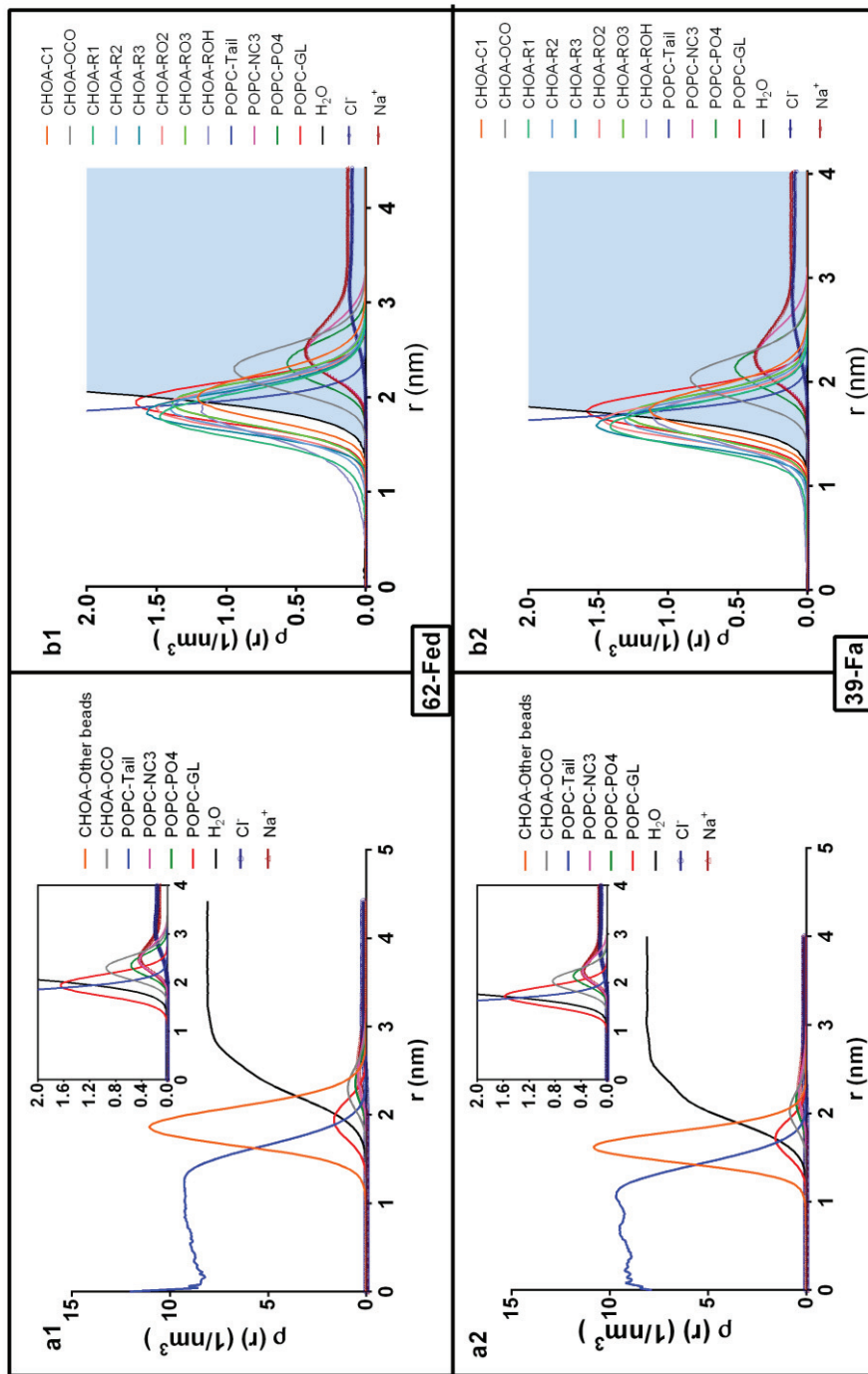
Figure 2.10. Radial density distributions (RDDs) ($\rho(r)$) of different moieties of the constituent molecules and ions with respect to center of mass of the micelles for the 62-Fed (1), 39-Fa (2) systems. a) RDDs of the specified moieties of CHOA (cholate) and POPC molecules. The close views of the interface regions are given in the insets, where all other beads except the OCO$^-$ bead of CHOA are omitted for clarity. b) The close views of the RDDs of the individual beads of CHOA molecules at the interface. RDDs of the surrounding Na$^+$ ($\triangle$), Cl$^-$ ($\circ$) ions and water ($-$) molecules are included in both graphs.
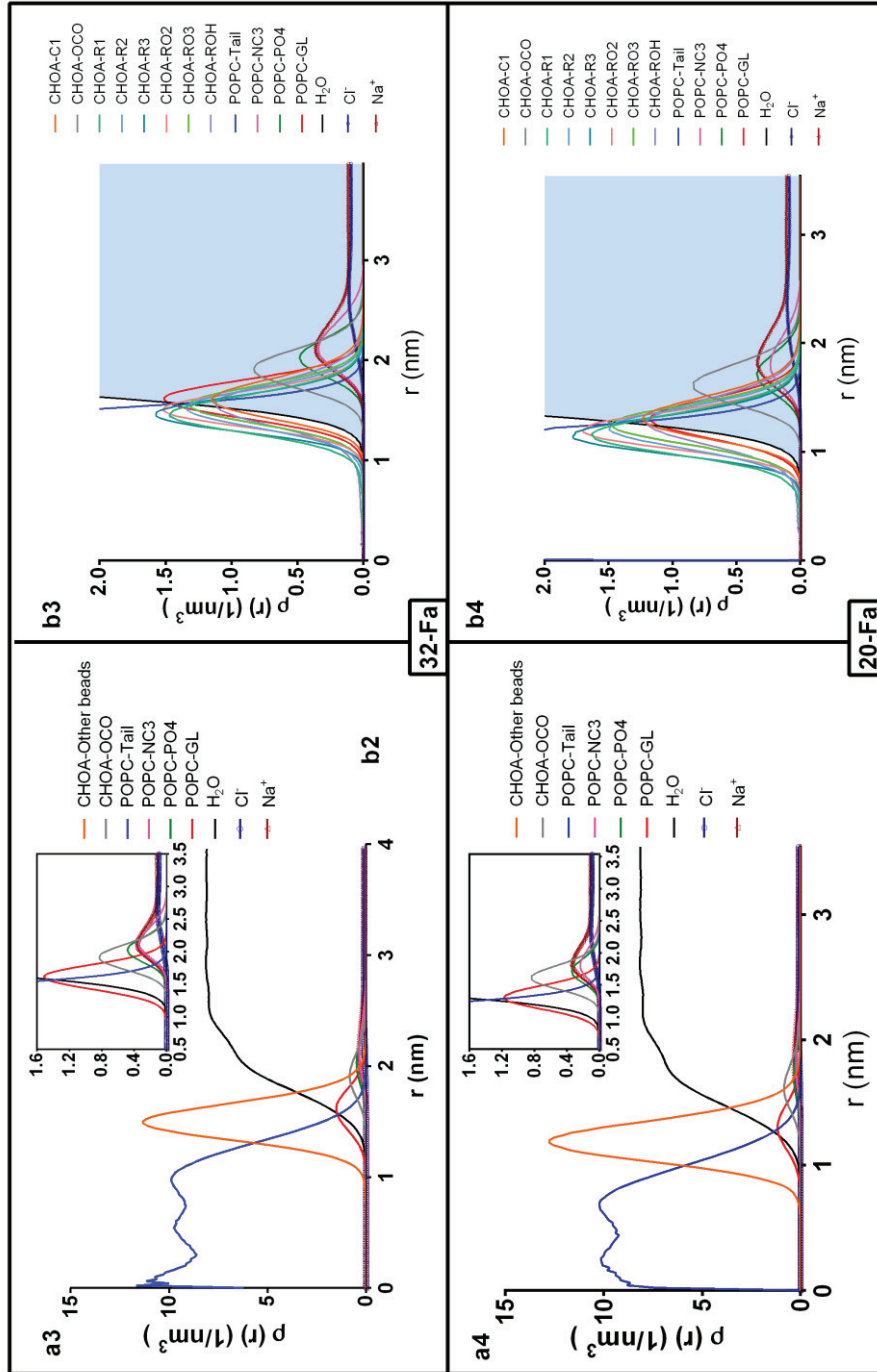
Figure 2.11. Radial density distributions (RDDs) ($\rho(r)$) of different moieties of the constituent molecules and ions with respect to center of mass of the micelles for the 32-Fa (3), and 20-Fa (4) systems. a) RDDs of the specified moieties of CHOA (cholate) and POPC molecules. The close views of the interface regions are given in the insets, where all other beads except the OCO⁻ bead of CHOA are omitted for clarity. b) The close views of the RDDs of the individual beads of CHOA molecules at the interface. RDDs of the surrounding Na⁺ (Δ), Cl⁻ (○) ions and water (-) molecules are included in both graphs.

occupied solely by POPC tails while CHOAs are located at the micelle surface. Water molecules, which solvate the head groups of CHOA, cannot diffuse into the micelle core. The inset figure shows the close view of the interface region. It is seen that the intermediate glycerol beads (GL) of POPCs are localized at the micelle surface where the water and POPC tail RDDs intersect each other (at 1.96 nm away from the center). The charged head groups (PO4$^-$ and NC3$^+$) protrude from the micelle surface and are in direct contact with water. Their orientation on the surface seems to be somewhat flat since the maxima of their RDDs are only ~0.1 nm away from each other. This is apparently smaller than the average distance between the choline and phosphate beads in a single POPC molecule, which was calculated as 0.455 nm. This is also supported by the average angle calculations between the PO4-NC3 vector on a POPC molecule and the micelle's surface normal (Figure 2.11-a). The protrusion of the negatively charged phosphate groups of POPCs into the aqueous medium is slightly (< 0.1 nm) further than that of the negatively charged carboxylate moieties of CHOAs. The presence of an ionic double layer around the micelle surface is also apparent. The first shell is comprised of Na$^+$ ions localized around the carboxylate and phosphate moieties of CHOAs and POPCs, respectively, coinciding with the location of NC3$^+$ groups of POPCs. This suggests that the Na$^+$ ions fill the left over space from the protruding choline moieties of POPCs over the micelle surface and help in screening the electrostatic repulsion between the negatively charged head groups of CHOAs and POPCs on the surface. The second shell of the double layer is formed by Cl$^-$ ions surrounding the members of the first shell. All of these general features were also reported in the atomistic simulations of Marrink and Mark (2002) and Sayyed-Ahmad et al. (2010) in which the mixed micelles of POPC-CHOA and DPC-CHOA were characterized, respectively. Therefore, we can say that the internal organizations of BSs and PLs are similar in the mixed micelles regardless of the chemistry. Furthermore, the ability of the MARTINI model in reproducing the structural features of dietary mixed micelles is demonstrated once more through this study.

More detailed information about the structuring of CHOAs within the micelle is obtained from Figure 2.10-b1, which shows the RDDs of each CHOA bead with respect to the com of the micelles. It is observed that the peaks corresponding to the beads of the sterol body are located almost at the same distance away from the micelle com except that the beads embodying the methyl groups (R1 and R3) seem to penetrate

deeper towards the core. This indicates that the sterol bodies are mainly oriented parallel at the surface with their hydrophilic faces being exposed to the aqueous environment, which is typical in mixed micelles of fully deprotonated bile salts and phospholipids (Birru, Warren, Han, et al., 2017; Haustein et al., 2014; S. J. Marrink & Mark, 2002; Sayyed-Ahmad et al., 2010; Suys et al., 2017). However, the widths of the distributions are not narrow enough to disregard the possibilities of different orientations. Especially, the end hydroxyl group of cholate (ROH bead) shows a wider distribution indicating a deeper penetration inside the micelle. Thus, it is inferred that the cholates are not always aligned flat on the micelle surface, but, occasionally, are able to adopt different orientations including more perpendicular ones. On the other hand, the RDD of the OCO$^-$ beads depicts a different orientation of the carboxylate groups at the micelle surface. They seem to protrude from the surface into the aqueous environment where they are completely solvated with water. This suggests that the carboxylate side chains of CHOAs are oriented such that they stick out from the surface, which gives a mashie-like shape to the molecules. These findings, which conform to the findings of others (S. J. Marrink & Mark, 2002; Sayyed-Ahmad et al., 2010), were also verified by the angle calculations of which the results are given in the next section. Figure 2.10-b1 also shows that the beads embodying the methyl groups (R1 and R3) are largely solvated by POPC tails, which reflects the importance of short-ranged van der Waals interactions between these moieties in maintaining the stability of micelles. Additionally, the interaction sites embodying the hydroxyl groups (RO3, RO2, ROH) seem to be located in very close proximity of the glycerol beads of POPCs. This feature was also reported in the atomistic simulations of Marrink and Mark (2002), which showed that the hydrogens of the hydroxyl groups of cholates spent substantial amount of their time (30-40 %) with forming H-bonds with the carbonyl oxygens of the glycerol moieties of POPC's. Therefore, it is clear that although H-bonding is under-represented in the MARTINI force field, associated structural details are yet sufficiently reproduced.

Comparison of the RDDs belonging to the other systems (Figure 2.10 and 2.11) indicates that the equilibrium organization of the constituent molecules, ions and the water molecules within/around a micelle is qualitatively the same regardless of the micelle size or initial concentrations in the solution. Small quantitative discrepancies exist due to the size effects; i.e. the maxima are shifted towards the core and the distributions become narrower as the micelle size decreases. On the other hand, the core

packing density seems to be affected by the micelle size and the micellar POPC amounts. This is inferred from the shapes of the RDDs corresponding to the POPC tails, which exhibit marked differences with increasing micelle size. For the smallest micelle (20-Fa), the foregoing RDD has peaks and valleys representing higher and lower density regions, respectively (Figure 2.11-4). Especially, the decaying density towards the com of the micelle is worth to mention. Several researchers reported lower densities towards the micelle core due to the steric repulsion of the tail ends, which is typical for phospholipid tails in fluid state (Bogusz, Venable, & Pastor, 2000; S. J. Marrink & Mark, 2002; Tieleman, van der Spoel, & Berendsen, 2000). However, as the micelle size increases the peaks and valleys become less prominent (Figure 2.10 and 2.11), and eventually they disappear for the largest micelle (62-Fed, Figure 2.10-a1). This suggests that the core packing gets more uniform with increasing micelle size. The reason behind can be clarified by an approximate calculation of the effective core volume per POPC molecule for each micelle. Assuming all the micelles are perfect spheres and roughly taking the core radius as the average distance between the micelle com and the GL beads of POPCs, it is seen that the effective core volume per POPC molecule diminishes as the micelle size increases. For instance, the average micelle com-GL bead distance in the smallest and the largest micelles are 1.30 nm, and 1.96 nm, respectively. Based on the aforementioned assumptions, these give effective volumes per POPC of 1.53 nm^3 and 1.43 nm^3 within the micelle core, respectively. Calculations on the intermediate size micelles also conform to the trend. Hence, the packing density of the POPC tails within the micelle core increases with increasing micelle size. Furthermore, below (Section 2.3.2.3), it is also shown that the orientation of the tails with respect to the radial vector, and, to a lesser extent, the conformations of the oleoyl tails change with micelle size. Therefore, it can be concluded that the increasing core packing density with increasing micelle size, which causes improved alignment of the tails with the radial direction (and barely more stretched oleoyl tails), results in more uniform distribution of the tails within the core.

2.3.2.3. Internal and Surface Orientations of the Molecules

The RDDs (Figure 2.10 and 2.11) showed that CHOAs are localized at the micelle surface. Therefore, the calculation of the average angle between a specified

vector on CHOAs and the radial direction would give information about the alignments of these molecules at the micelle surface. The calculations were performed for the whole CHOA molecule (represented by the vector connecting the OCO⁻ bead to the ROH bead) as well as for two parts of a molecule, where one part is the sterol body represented by the vector connecting the RO3 bead to ROH, and the remaining part represented by the vector connecting the OCO⁻ bead to RO3. The alignments of the short hydrophilic tail and the hydroxyl end of the sterol body were investigated separately through the vectors connecting the OCO⁻ bead to C1, and the R1 to ROH, respectively. The results are given in Figure 2.12-a for all the systems. Firstly, the average angle between the RO3-ROH vector on a CHOA molecule and the radial vector is observed to be in the range $86-94^{0}$, which suggests that the sterol bodies of the cholates are primarily oriented parallel to the micelle surface. This was inferred from the RDDs as well. However, the broad distributions also suggested that the molecules adopted more perpendicular orientations occasionally. This finding is also supported by the histograms of the observed angles between the vectors R1-ROH (or RO3-ROH) and the radial vector (Figure 2.12). Furthermore, the charged hydrophilic halves of CHOAs seem to adopt a tilted orientation with respect to the radial direction, which is inferred from the average angle between the OCO-RO3 vector and the radial vector ($\sim 120^{0}$). The average observed angle between the protruding short tail (OCO-C1) and the radial vector was also found to be $\sim 140^{0}$ regardless of the micelle size. All of these results together with the intramolecular average Type II angle values given in Figure 2.12-b ($\sim 145^{0}$ for OCO-RO3-ROH) suggest that the shape of the CHOA molecules is mashie-like with their sterol body aligned more or less parallel at the surface and their hydrophilic tail protruding into the aqueous environment with a tilt of $\sim 50^{0}$ from the surface. Similar findings were reported in resembling studies as well (Haustein et al., 2014; S. J. Marrink & Mark, 2002; Sayyed-Ahmad et al., 2010). Finally, it is observed that the orientation of CHOAs changes slightly with increasing micelle size. This is inferred from the increasing angles between the vectors OCO⁻ROH, RO3-ROH, R1-ROH and the radial vector with growing micelle size (Figure 2.12-a), which indicate that as the micelles get larger the CHOAs are sampling more perpendicular orientations with respect to the micelle surface. This might be a consequence of the decreasing surface area per surfactant with increasing micelle size (see Table 2.2); i.e. increased packing density at the micelle surface.
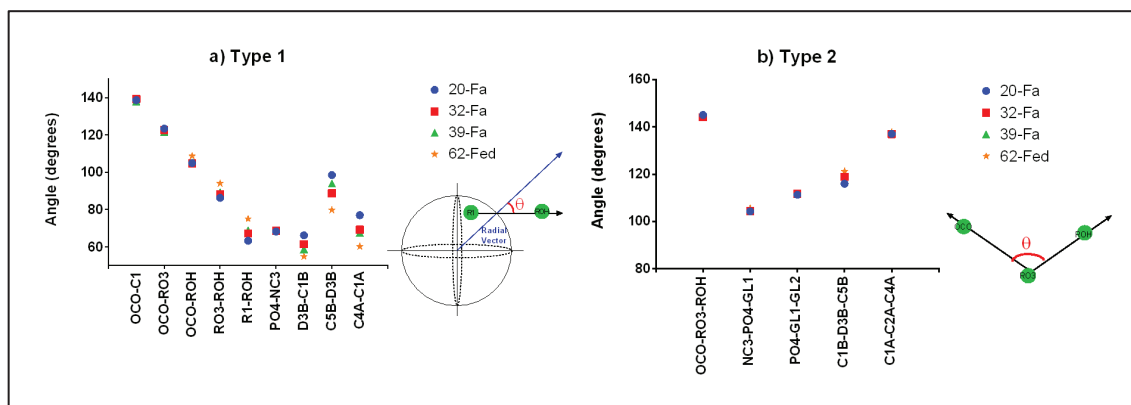
Figure 2.12. a) Type I average angles between a vector of two selected beads in a molecule and the local sphere normal (radial vector). The origin of each vector is the first specified bead; hence the direction of each vector is from the first to the second specified bead. The local sphere normal is the vector which connects the com of the micelle to the midpoint of the selected beads' positions as shown in the inset. b) Type II average angles between two vectors in a molecule. The origin of each vector is the middle-specified bead; hence the directions of the vectors are from the middle to the end beads as shown in the inset. The selected beads for angle calculations are given in x-axis (20-Fa: ●, 32-Fa: ■, 39-Fa: ▲, 62-Fed: ★).

Regarding the orientation of the head groups of POPCs at the surface, we can say that the findings from the RDDs are supported by Type I angle results. The average angle between the PO4-NC3 vector in a POPC molecule and the radial vector was found to be ~68^0 regardless of the micelle size (Figure 2.12-a), which indicates that the protruding head groups are principally aligned almost flat on the micelle surface. This type of orientation of the phosphate-choline head groups at the surface was also reported for simple micelles composed of lysophospholipids (Brocos et al., 2012). Nevertheless, the angle distribution histogram shows that miscellaneous orientations were practically possible (Figure 2.13-c). Figure 2.12-a also gives idea about the average orientations of the palmitoyl and the oleoyl tails of POPCs with respect to the radial direction. First of all, it is clear that the tails are not perfectly aligned with the radial direction as it was proposed by the classical idealized micelle models. Indeed, the disordered nature of the surfactant tails (in different types of micelles) has been demonstrated several times by MD simulations (Bogusz et al., 2000; Jójárt, Poša, et al., 2014; S. J. Marrink & Mark, 2002; Turner et al., 2010). It is clear that the orientations of the upper (D3B-C1B) and the lower (C5B-D3B) parts of the oleoyl tails are significantly different indicating the presence of a kick in the tail as expected due to the inherent double bond. Specifically, the average angle intrinsic to the oleoyl tail due to

48

the kick (Type II C1B-D3B-C5B angle) was found to be around 120^0 (Figure 2.12-b). Moreover, the distribution in the smallest micelle (20-Fa) exhibits a small shift towards lower angles (Figure 2.14-a). This, (as well as the decreasing average Type II C1B-D3B-C5B angles (Figure 2.12-b) and the decreasing oleoyl tail lengths in the core (the average distance between the C1B and C5B beads in a POPC molecule- see Table 2.2) with diminishing micelle size, indicate that the oleoyl tails of the POPCs are able to retain slightly more kinked conformations as the micelles get smaller.
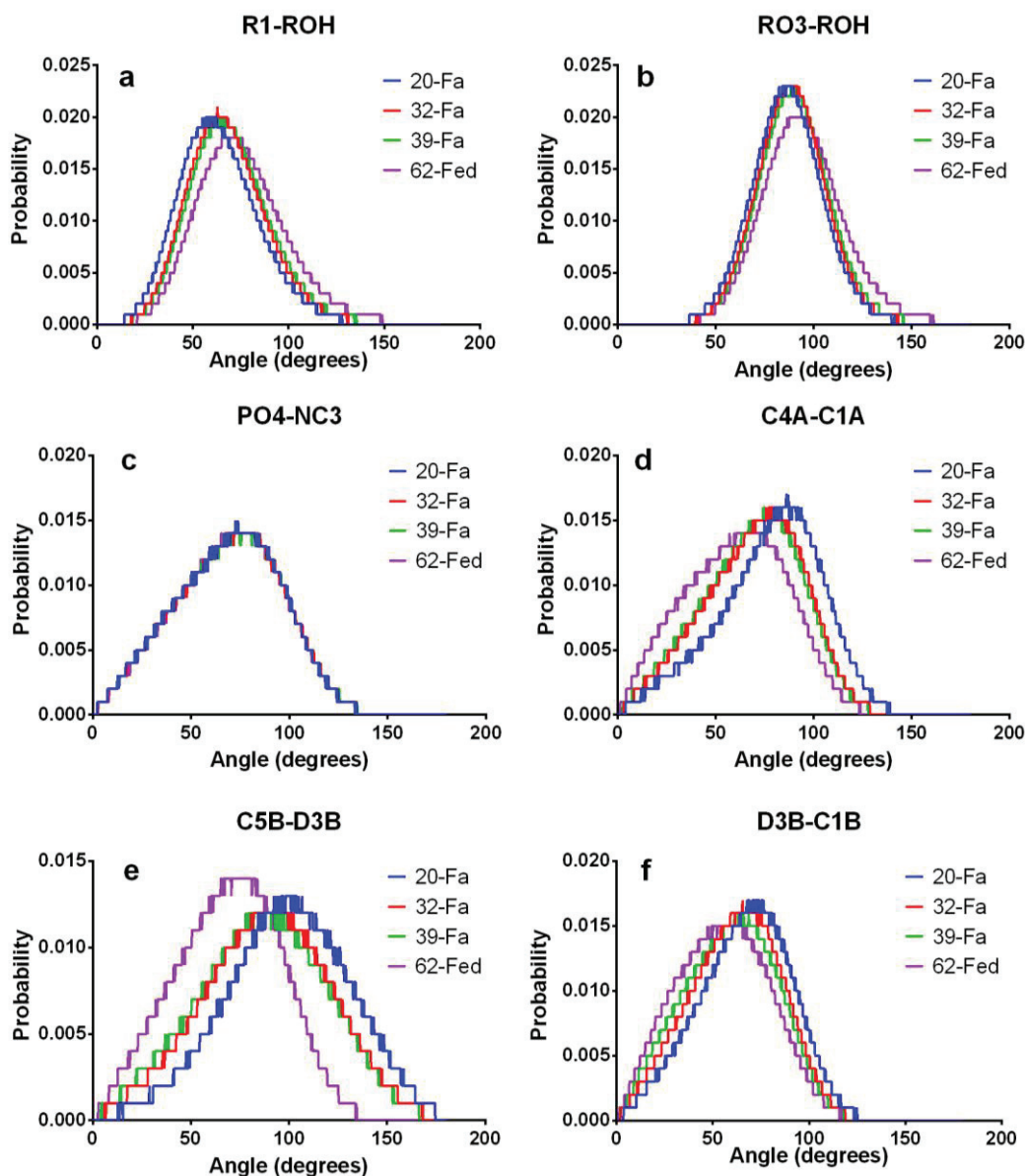
Figure 2.13. Selected Type I angle distribution histograms for cholate and POPC molecules in different micelles. The angles were calculated between a vector of two selected beads in a molecule and the local sphere normal. The origin of each vector is the first specified bead; hence the direction of each vector is from the first to the second specified bead. The local sphere normal is the vector which connects the com of the micelle to the midpoint of the selected beads' positions.

This must be due to the weakened packing constraints within the core with decreasing micelle size as discussed above in Section 2.3.2.2. In other words, each oleoyl tail has slightly more space to freely sample more kinked conformations as the effective volume per molecule within the core was found to increase with diminishing micelle size. Speaking of the palmitoyl tails, they seem to have sampled more stretched conformations compared to the oleoyl tails as the average C1A-C2A-C4A angle values (135^0, Figure 2.12-b) suggest. However, any remarkable conformational change in palmitoyl tails with increasing micelle size does not seem to occur since there is no evidence for such a change in the Type II C1A-C2A-C4A angle distribution histograms (Figure 2.14-b). Besides, the increase in the average tail length (the average distance between the C1A and C4A beads in a POPC molecule- see Table 2.2) with growing micelle size is very low (lower than 0.02 nm) to take into consideration. Another significant outcome from Figure 2.12-a is that although the tails of POPCs are not perfectly aligned along the radial direction, they become more capable of doing so as the micelles get larger. This is inferred from the diminishing average angles between the vectors D3B-C1B, C5B-D3B, C4A-C1A and the radial vector with increasing micelle size. This feature is even more significant in the corresponding angle distribution histograms, which exhibit marked shifts to lower angles with increasing size (Figure 2.14-d,e,f). Considering the above-mentioned observations on the intramolecular (Type II) angle distributions belonging to the tails and the average tail lengths, we can say that the increased alignment of POPC tails with radial direction is mainly due to their reorientation within the core imposed by the diminishing effective core volume per POPC molecule with increasing micelle size. The contribution of the slight extension of the oleoyl tails with increasing micelle size is thought to be minimal when the extent of increase in the tail length is taken into account. The improved alignment of both of the tails also resulted in denser and more uniform packing in the core as discussed before (Section 2.3.2.2). Though, the fluid nature of the core was not lost as the broadness of the distributions indicates (Figure 2.14-a,b). Finally, regardless of the micelle size, the distribution of the intramolecular NC3-PO4-GL1 angle was found to be bimodal (giving peaks at $\sim 60^0$ and $\sim 110^0$) (Figure 2.14-c), while the PO4-GL1-GL2 angle distribution was unimodal giving a peak at $\sim 110^0$ (Figure 2.14-d).
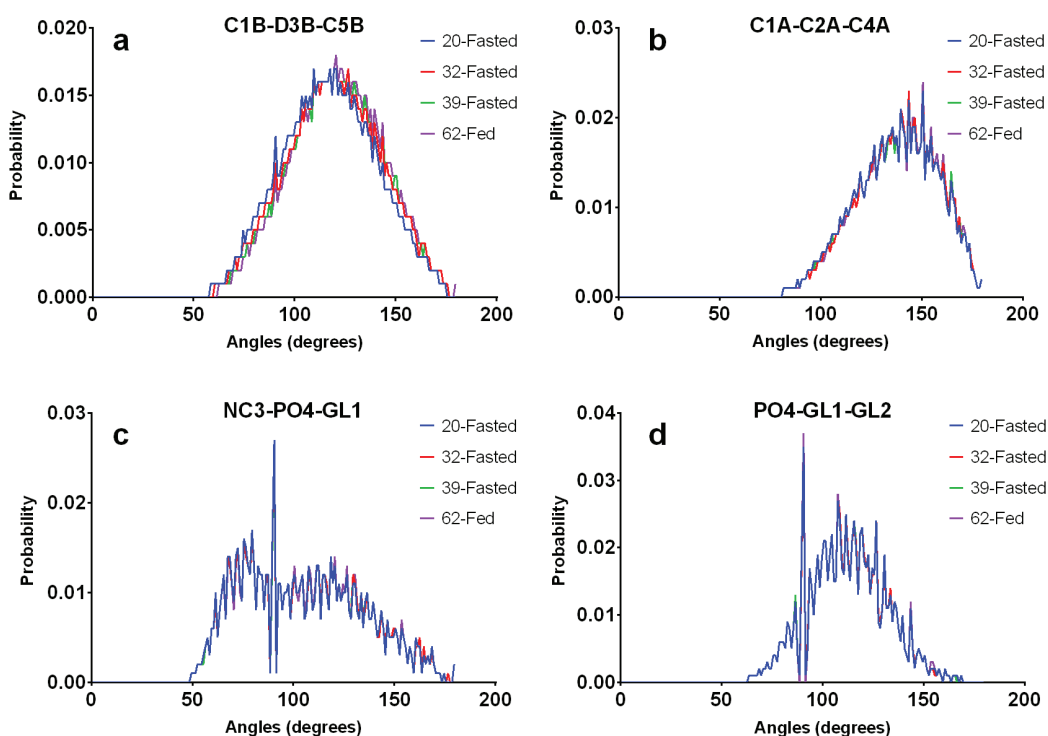
Figure 2.14. Intramolecular (Type II) angle distribution histograms for POPC molecules in different micelles. The angles were calculated between two vectors in a molecule. The origin of each vector is the middle-specified bead; hence the directions of the vectors are from the middle to the end beads.

2.4. Conclusions

The aims of the second chapter of the thesis study were to investigate the evolution of mixed micelle formation under physiological conditions in duodenum both at fasted and fed states and to analyze the structural properties of the equilibrium micelles as a function of size through coarse-grained molecular dynamics simulations. Cholate and POPC were used as model bile lipids. The analysis of the self-assembly processes showed that the micellization behavior was the same regardless of the total concentration of the bile lipids except that the equilibration was achieved the fastest under fed state concentrations. The spontaneous aggregations between the neighboring molecules were observed soon after the simulations were started. The initial stages were dominated by dimers of cholates and small clusters, which were principally simple micelles. During the course of the process, the small aggregates fused to form larger ones until stable mixed micelles were attained. It was observed that once the hydrophobic core was formed by POPC molecules they never left the micelle, thereafter which the micelle growth was continued only by the addition of unimers or dimers of

cholates. Cholates were continuously involved in a dynamic exchange between the micelles and the aqueous medium, which was responsible for the broadness of the equilibrium size distributions. The expected phase behavior of the coexistence of multiple mixed micelles with simple micelles and free cholates was attained at the end of fed state simulations only, which denotes a fair representation of the true thermodynamic equilibrium under fed state conditions. Despite the use of a CG model, the prohibitively limited time and length scales sampled were not sufficient to attain a representative true thermodynamic equilibrium system under fasted state concentrations. Therefore, a complete comparison of the equilibrium structures in both states was not possible. However, considering that the micellization behavior and the general aspects of the micelle morphologies were found to be independent of the total lipids concentration, the equilibrium micelles obtained in varying sizes in this study can be considered as transient structures that are formed in the duodenum under both fasted and fed states.

The structural analysis revealed that all of the micelles were slightly ellipsoidal regardless of the initial concentration. The shape was found to be dependent on the micellar composition rather than the size. The lower the micellar POPC/cholate ratio, the more flexibility in shape (resulting in rougher surfaces) and the more deviation from the spherical geometry were observed. The size of the equilibrium micelle obtained under fed state conforms to the experimental data from the literature. The R_g was found to be linearly dependent on the $(1/3)^{th}$ power of the aggregation number as expected for spheroidal micelles. The high and ever increasing ratios of the hydrophilic to hydrophobic SASAs indicate that thermodynamically more favorable organizations of molecules were attained with increasing micelle size. Furthermore, the decrease in the total SASA per surfactant with increasing micelle size indicates a denser surface packing of the molecules.

The internal structures of the equilibrium micelles were investigated by the help of RDDs and specific angle calculations. The general aspects of the morphology were found to be the same regardless of the total lipids concentration and micelle size. The general picture is such that the core is composed of POPC tails, the glycerol moieties lie on the surface and the charged phosphate and choline groups protrude from the surface to the surrounding medium where they are completely solvated with water. The cholates are located on the surface acting as wedges between the head groups of POPCs with

their hydrophobic faces primarily pointing towards the core. Their shape is mashie-like with their sterol backbones aligned more or less flat on the surface and the charged short tails protruding into the aqueous environment with a tilt from the surface. The micelles are surrounded by an ionic double shell where the Na^+ and Cl^- ions constitute the inner and the outer ones, respectively. Overall, the structures are flexible, and the bile lipids behave as in fluid state as suggested by the broadness of the RDDs and the angle distributions. The comparison of the results with those of other studies conducted with different bile lipids in the literature suggests that the morphologies of the duodenal mixed micelles are similar regardless of the chemistry. On the other hand, the results suggest that small differences might be observed for micelles of varying sizes due to changing packing constraints. For instance, the cholates were shown to sample slightly more perpendicular orientations at the surface with growing micelle size, which was attributed to the increasing packing density of the molecules at the surface. Besides, the core packing density of the POPC tails was found to increase with micelle size. The main consequence was an improvement in the alignments of POPC tails with radial direction. The overall effect was a more uniform density in the micelle core with increasing size. Whether or not more significant structural variations would be observed for micelles covering a larger size range than the one studied in this work remains to be seen.

The information gained by this part of the study sheds light on the mixed micelle formation in the duodenum under physiologically relevant concentrations and the morphology of the micelles at molecular level. The effects of the presence of different types of fatty acids to the formation mechanism and the micelle structure are explored in the next chapter.

CHAPTER 3

MIXED MICELLE FORMATION IN THE PRESENCE OF DIFFERENT TYPES OF FATTY ACIDS

3.1. Introduction

Triglycerides are the most abundant lipids in foods and the human body and they are responsible for 30% of calorie intake in the Western diet (German & Dillard, 2004; Smolin & Grosvenor, 2007). Triglycerides are formed by the fatty acids attached to the glycerol backbone. Fatty acids are the carbon chains with a carboxyl group (COOH) at one end and a methyl group (CH3) at the other end.

The length of the carbon chain and the double bonds present in the chain, affect the physical properties of fatty acids. The fatty acids are named according to their chain lengths as short- (4 to 7 carbons), medium- (8 to 12 carbons) and long- chain (greater than 12 carbons). If there is no double bond in the chain structure and all the carbon atoms are bonded to two hydrogen atoms, the fatty acids are called saturated fatty acids. The saturated fatty acids are mostly found in animal originated foods such as meat and dairy products. Palmitic (16:0) and stearic (18:0) acids are the most common saturated fatty acids in the human diet. If there is at least one double bond in the chain structure and not all the carbons are hydrogenated, the fatty acids are called unsaturated fatty acids. The number of double bonds specifies the degree of unsaturation. That is to say if there is one double bond in the structure it is called a monounsaturated fatty acid, and if there is more than one double bond in the structure it is called a polyunsaturated fatty acid. Unsaturated fatty acids are mainly found in plant-based foods in the human diet. Oleic (18:1) and linoleic (18:2) acids are the most abundant examples of mono- and polyunsaturated fatty acids, respectively.

Further categorization of the unsaturated fatty acids is based on the position of the double bond in the tail. For example, if the first double bond is located between the third and fourth carbons starting from the methyl group, the fatty acid is named as an omega-3 (ω-3) fatty acid. Similarly, if the first double bond is located between the sixth

and seventh carbons, it is named as an omega-6 (ω-6) fatty acid. Alpha-linoleic acid, eicosapentaenoic acid (EPA) and docosahexaenoic acid (DHA) are the most common examples of ω-3 fatty acids, while linoleic (18:2) acid is the main ω-6 fatty acid.

The positions of the hydrogen atoms in the double bond of fatty acid molecules also affect their physical properties. If the two hydrogen atoms are present at the same side of the double bond, the fatty acids are said to be in their *cis* configuration. This is the common configuration of the fatty acid double bonds in nature. On the contrary, if two hydrogen atoms are present at the opposite sides, the fatty acids are called *trans* fatty acids. Although the *trans* configurations are rarely observed in nature, the processes applied to the fatty acids such as hydrogenation and high temperatures increase their incidence.

Triglycerides are important energy sources for a human being. Besides their digestion products are the elements of cells and tissues and used for membrane synthesis and production of signaling compounds (German & Dillard, 2004). Health-related effects of fatty acids are also worth to mention. Most fatty acids are known to prevent diseases like atherosclerosis, obesity, cardiovascular diseases and certain types of cancer (Betz et al., 2010). Therefore, it is important to understand their digestion process.

Triglyceride digestion mainly occurs in the small intestine. However, a small amount can be digested in the stomach due to the lipase present here. In the small intestine, the secretions of bile aid the formation of small globular structures of lipids, which helps lipase to break them into fatty acids and monoglycerides. The digestion products of triglycerides, fatty acids, and monoglycerides, are solubilized in dietary mixed micelles with other lipophilic substances present in the small intestine such as cholesterol and vitamins. The formed mixed micelles diffuse from brush border mucosal cells and facilitate the absorption of lipophilic molecules. The unsolved part of the fatty acid molecules crystalizes and then is excreted in the feces. Therefore, they should necessarily join the mixed micelle structures to become bioavailable (Smolin & Grosvenor, 2007).

The morphologies of the mixed micelles composed of bile salts and phospholipids are reported to change in the presence of the digestion products of triglycerides. The mixed micelles of bile salts and phospholipids are in spherical form in

intestinal conditions. By the incorporation of fatty acids, micelle structures become swollen. The chain length of the fatty acid is believed to affect the amount of the increase in micelle size (Kossena et al., 2003; Phan et al., 2015). In the literature, long chain fatty acids are reported to increase the micelle size more than medium chain fatty acids do. The change in the micelle size also change their shape (Phan et al., 2015). The spherical shape of the micelles turns into more ellipsoidal in the presence of fatty acids. The increased amount of the hydrophobic domains results in the elongation of the micelle structures (Salentinig, Sagalowicz, Leser, Tedeschi, & Glatter, 2011). Further increase in the lipid concentration may lead to the formation of vesicles (Phan, Salentinig, Prestidge, & Boyd, 2014). Therefore, the concentration of fatty acids is another factor affecting the structure of mixed micelles. During the digestion of triglycerides, mixed micelles are reported to coexist with vesicles, especially when the majority of fatty acids are long chain (Fatouros, Walrand, Bergenstahl, & Müllertz, 2009; Kleberg, Jacobsen, Fatouros, & Müllertz, 2010; Kossena et al., 2003; Phan et al., 2014). The chain length of the fatty acids is reported to affect also the digestion time of the lipids. If there are larger amounts of long chain fatty acids in the triglyceride structure, longer time is required for their digestion (Salentinig et al., 2011). The bile salt concentration and the pH of the digestion media are other important factors affecting the shapes of the micelles with fatty acids (Fatouros, Deen, et al., 2007; Phan et al., 2014; Salentinig et al., 2011). The bile salts are responsible for the curvature effects and the lack of bile salts result with elongation of micelles and increase in the micelle size (Fatouros, Deen, et al., 2007; Rex P. Hjelm, Schteingart, Hofmann, & Thiyagarajan, 2000). The people suffer from bile salt deficiency also face the lack of fatty acid absorption due to the aforementioned situation (Werner, 2005). If the amount of bile salts in the small intestine is not sufficient, the excess fatty acids are crystallized and excreted from the body.

The presence of fatty acids in dietary mixed micelles is vital to increase the solubilization of other lipophilic nutrients and drugs. The presence of lipid digestion products in the media increases the solubility of the poorly water-soluble molecules. The amount of the increase depends on the level of hydrophobicity of the lipophilic molecule (Kleberg et al., 2010). Besides, the presence of lipids in the digestion media stimulates secretion of bile into the small intestine and increases the solubilization of lipophilic drugs and nutrients indirectly. Consequently, in the studies of drug

solubilization, the micelle structures in the presence of fatty acids have widely been studied. The micelles incorporating long chain fatty acids have been reported to solubilize larger amounts of hydrophobic drugs in *in vivo* studies. However, in some *in vitro* studies, the solubilization capacities of medium- and long-chain fatty acid micelles have been reported to be similar (Phan et al., 2014). The slower digestion of the long chain fatty acids provides more time for effective solubilization of the drugs in mixed micelles (Porter et al., 2004; Salentinig et al., 2011). Nevertheless, in some of the studies, the micelles with long chain fatty acids were reported to solubilize larger amounts of hydrophobic drugs due to their larger sizes compared to the micelles incorporating medium chain fatty acids (Kossena et al., 2003).
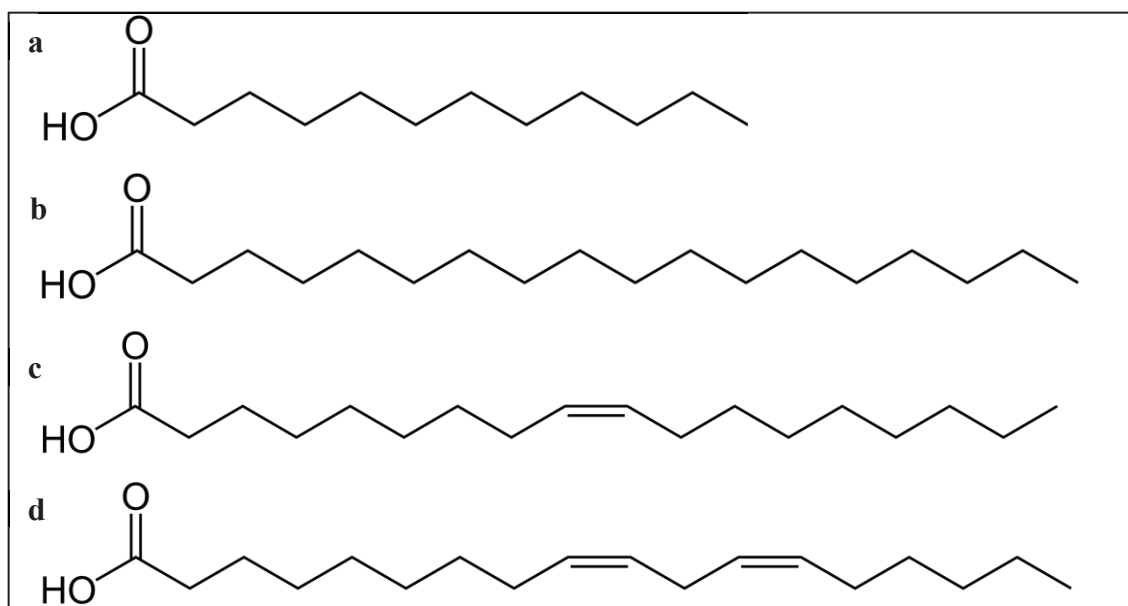
Figure 3.1. Chemical structures of a) Lauric, b) Stearic, c) Oleic and d) Linoleic acids

Browsing through the literature, one realizes that the experimental studies investigating the effects of the presence of different types of fatty acids on the mixed micelles have mainly focused on the size and shape properties, which were usually characterized via Cryo-TEM, dynamic light scattering (DLS), XRD, NMR, AFM, SANS etc. (Fatouros, Walrand, Bergenstahl, & Müllertz, 2009; Rex P. Hjelm et al., 2000; Kleberg et al., 2010; Müllertz, Fatouros, Smith, Vertzoni, & Reppas, 2012; Phan et al., 2013; Salentinig et al., 2011; Svard, Schurtenberger, Fontell, Joensson, & Lindman, 1988). However, a detailed cluster-specific examination of the internal structures or interactions within the micelles is missing due to the limitations of the current experimental methods. At this point, computational aproaches such as molecular

dynamics simulations may come to rescue. For instance, in the atomistic simulations of Turner et. al. (Turner et al., 2010), the inner local structure of the glycholate-oleic acid mixed micelles was investigated. For this purpose, the self-assembly of glycholate molecules at gallbladder concentration (100 mM) was simulated in the first place. The aggregation behavior of glycholate was also investigated. Following that, one of the equilibrium state micelles was selected and transferred to a medium mimicking the intestinal concentrations after which the oleic acid molecules were added to the system. After the equilibration of the system, size and inner organization of the micelles were analyzed. The effect of the addition of oleic acid in the bile salt micelles was analyzed by comparison of the structures with and without fatty acid molecules. In another atomistic study, the pH-dependent self-assembly behavior of lauric acid molecules was investigated (Morrow, Koenig, & Shen, 2012). Due to the different degrees of protonation of the fatty acid molecules at different pH values, the formed aggregated were in different shapes. Although this study showed the importance of the selected protonation situation of fatty acids in MD simulations, it did not give information about the aggregation of fatty acid molecules in the presence of bile extracts. Additionally, in the study of Birru et. al. (2017) the phase behavior of the gastrointestinal system at fed state in the presence of bile salts and digested phospholipid and fatty acids were investigated both with experimental methods and MD simulations. Moreover, the structures of the formed aggregates and solubilization of a lyophilic drug, danazol, within the micelles were inspected. The micelle sizes were reported to increase as a function of lipid concentration, and vesicles were observed after some point. The presence of digested lipids was said to enhance the drug solubility. At smaller lipid concentrations, danazol was reported to have crystallized while danazol solubility was increased with increasing lipid concentrations. The size and shape properties of the formed structures were compatible with the experimental results. The MD simulations provided information about the detailed inner structures and the localization of the drug within the micelles as well. Clulow et. al. (2017) investigated the structural differences of the aggregates present in the simulated intestinal fluids (SIF), which were prepared by different methods. They made use of both experimental methods and MD simulations in their study. They analyzed and compared the model intestinal fluids composed of only BSs as well as those with additional PLs and lipid digestion products. Their analysis involved the comparison of the size and shape properties of micelles formed in both the commercially prepared, and in-house prepared fluids with those

formed in the coarse-grained MD simulations. The results were found to be similar except the slight overestimation of ellipticity in the simulations due to the use of coarse-grained Martini force field.

In summary, to date, the experimental methods have been widely used to study the size and shape of dietary mixed micelles in the presence of different types of fatty acids. Besides, solubilization of some hydrophobic drugs and nutrients within those micelles were analyzed. The results only give information about the generic properties of the micelles like their size and shape, and their solubilization capacities. However, a cluster-specific characterization of the inner structures and aggregation mechanisms seem to be still missing. The computational studies conducted so far rather investigated the digestion media and some representative structures formed in presence of fatty acids. Yet, to the best of the author's knowledge, there is no study in the literature, which systematically investigated the mixed micelle structures in the presence of different types of fatty acids under physiological duodenal conditions. With this perspective, in the second part of the dissertation, it is aimed to characterize the duodenal self-assembly process in the presence of fatty acids, and the structural properties of the formed mixed micelles considering a variety of factors. The first factor is the concentration of bile lipids, which is presumed to affect the shapes and structures of the mixed micelles to a large extent. For this purpose, the simulation media have been constructed at both the fasted and fed state concentrations of CHOA and POPC molecules together with the addition of fatty acids at the same concentrations of bile salts. The second factor investigated is the chain length of fatty acids. Medium-chain Lauric acid (12:0) and long-chain Stearic acid (18:0) were used for this purpose. Finally, to see the effect of the degree of unsaturation, saturated (Stearic acid, 18:0), monounsaturated (Oleic acid, 18:1) and polyunsaturated (Linoleic acid, 18:2) fatty acids with the same chain length have been used. The structures of selected fatty acids can be found in Figure 3.1. Similar to the first part of the study, cholesterol molecules were not included in the systems because of their dilute concentrations in the small intestine originating from the gallbladder (Grundy & Metzger, 1972; Wilson & Rudel, 1994) and ineffectiveness on the micelle structure and dynamics at such dilute concentrations (SJ Marrink, 2004; Matsuoka et al., 2004; Suys et al., 2017). Furthermore, in order to keep the systems as simple as possible, monoglycerides of the fatty acid molecules were not included.

3.2. Methods

In the methods section, firstly the system details are given. Then the simulation procedure is explained in detail. the analysis methods. The methods used for the analyses are the same as described in Chapter 2 (see Section 2.2.3).

3.2.1. System Details

The concentrations of the constituent molecules in the systems have been chosen according to the state of digestion within the body. The concentrations of CHOA and POPC are equal to the concentrations in the first part of the study. Lauric acid (LA) and stearic acid (SA) were used as the representative saturated medium and long chain fatty acids, respectively. Oleic acid (OA) and linoleic acid (NA) were chosen as mono- and polyunsaturated long-chain fatty acids. To model the fasted (before digestion) and fed state (after digestion) conditions, the BS:PL:FA concentrations of 5:1.25:5 mM and 20:5:20 mM were used, respectively. The concentrations of the fatty acids were decided based on experimental studies in the literature (Fatouros, Walrand, Bergenstahl, & Mullertz, 2009; Salentinig et al., 2014).

Table 3.1. Number of molecules in the systems of self-assembly simulations at fasted and fed states.

	Fasted State (BS:PL:FA=5:1.25:5 mM)	Fed State (BS:PL:FA=20:5:20 mM)
CHOA	48	193
POPC	12	48
FA	48	193
Na^+	1541	1831
Cl^-	1445	1445
Water	~133000	~128000

BS: bile salt, PL: phospholipid, FA: fatty acid, CHOA: cholate, POPC: 1-palmitoyl-2-oleoyl-sn-glycero-3-phosphocholine.

The fatty acid molecules in the simulations were used in their deprotonated forms because the intestinal pH (~7) is greater than the pKa values of the fatty acids which vary between 4.8 to 6.5 (Bennett, Chen, Donnini, Groenhof, & Tieleman, 2013). To mimic the physiological conditions, 150 mM NaCl concentration was maintained by

addition of Na^+ and Cl^- ions to the media. Additional Na^+ ions were also used to neutralize the systems. The systems were solvated by a sufficient amount of water molecules. The size of each simulation box is 16000 nm^3, which has been shown to be large enough to avoid finite size effects in the first part of the study. The compositional details of the systems can be found in Table 3.1.

The coarse-grained (CG) MARTINI Force Field was used in the simulations. The previously proposed models for POPC, CHOA, lauric acid and stearic acid molecules were adopted (Siewert J Marrink et al., 2007; Sj Marrink, Vries, & Mark, 2004). The mappings of CHOA and POPC are the same as described in Chapter 2. The coarse-grained medium- and long-chain fatty acid molecules were modeled by 4 and 5 Martini beads, respectively. They consist of one charged head group (COO⁻) and 3 and 4 hydrophobic tail groups for LA and SA, respectively. The oleic and linoleic acids were modeled using the parameters of the hydrocarbon tails of DGDG (16:0-18:1-digalactosyl diacylglycerol) and DUPC (1,2-dilinoleoyl-sn-glycero-3-phosphocholine), respectively (de Jong et al., 2015). As all the fatty acids possess the same head group, the head group parameters of stearic acid were applied to those of oleic and linoleic acids as proposed in the literature (Janke, Bennett, & Tieleman, 2014; Risselada & Marrink, 2008). CG water molecules are comprised of four real water molecules and the CG beads of single atom ions are represented with their first hydration shell. The details of the CG structures of fatty acids are given in Figure 3.2.
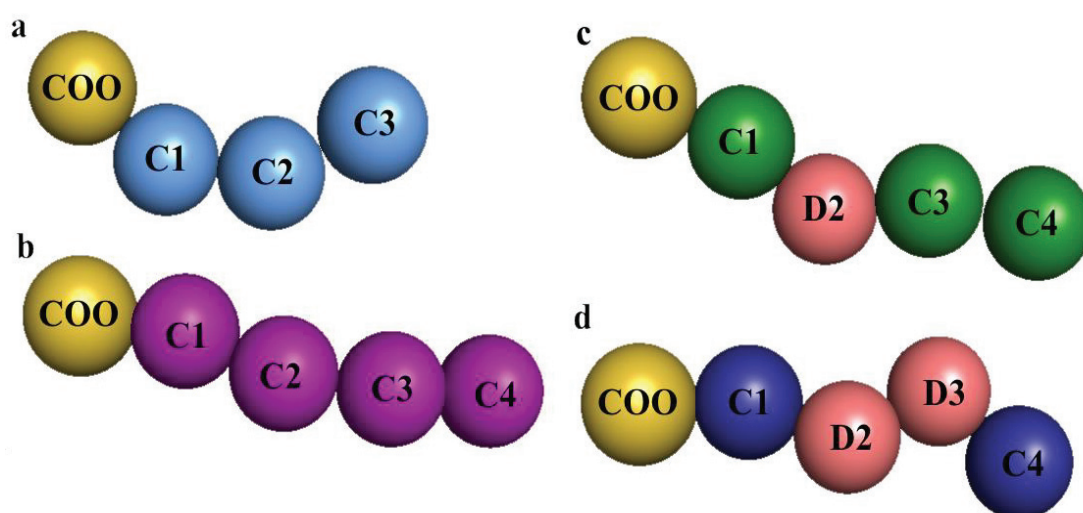
Figure 3.2. Coarse-grained structures of a) Lauric (light blue), b) Stearic (purple) c) Oleic (green) and d) Linoleic (dark blue) acids. The carboxylate groups and beads containing soluble bonds are colored yellow and salmon, respectively.

3.2.2. **Simulation** Procedure

The system setups were initiated by random placements of CHOA, POPC, and fatty acid molecules into the simulation boxes. The necessary configuration and topology files for CHOA, POPC, and saturated fatty acid molecules were taken from the Martini website (http://cgmartini.nl/index.php). The initial configuration files and the topologies of the unsaturated fatty acids were constructed using the corresponding configuration and topology files of DGDG and DUPC. Then the Na^+ and Cl^- ions were added randomly to the boxes to maintain the required NaCl concentration with additional Na^+ ions to neutralize the systems. Following that, the systems were solvated with Martini water molecules. Starting from that point, the procedure applied in the second chapter of the dissertation was used for simulations and the analyses (see Sections 2.2.2 & 2.2.3). The selections of the equilibrium micelle for further structural analyses were based on the corresponding cumulative probabilities of aggregation numbers; i.e., the micelle that was observed for the longest time in the trajectory (belonging to the production runs) was chosen for each system. Similar to the first part, each selected micelle was extracted from the final frame of its original trajectory and transferred to a smaller simulation box ful of equilibrated Martini water molecules. The concentrations of the free CHOA molecules in those simulation boxes were kept the same as those in the original simulation boxes in order not to disrupt the thermodynamic equilibrium conditions. The equilibration and production runs were performed for these small simulation boxes as previously described. The simulations were extended until a collection of time frames summing up to 500 ns in total was achieved for each system.

3.3. Results and Discussion

In the results and discussion section, firstly evolution of the micellization in presence of different fatty acid molecules is explained. Following that the structural characterization of the selected mixed micelles are investigated. The effect of the presence of different types of fatty acids on self-assembly process and the structural properties of the micelles are determined.

3.3.1. Evolution of the Mixed Micelle Formation in The Presence of Fatty Acids

The evolution of the micellization process was inspected for each system under fasted and fed states. The clustering was performed using a cut-off value of 0.6 nm as before. The time-dependent number of clusters and weight- (N_w) and number- (N_n) averaged aggregation numbers were calculated based on this cut-off in order to investigate the aggregation behaviors of the systems and to determine the equilibration points of the simulations.
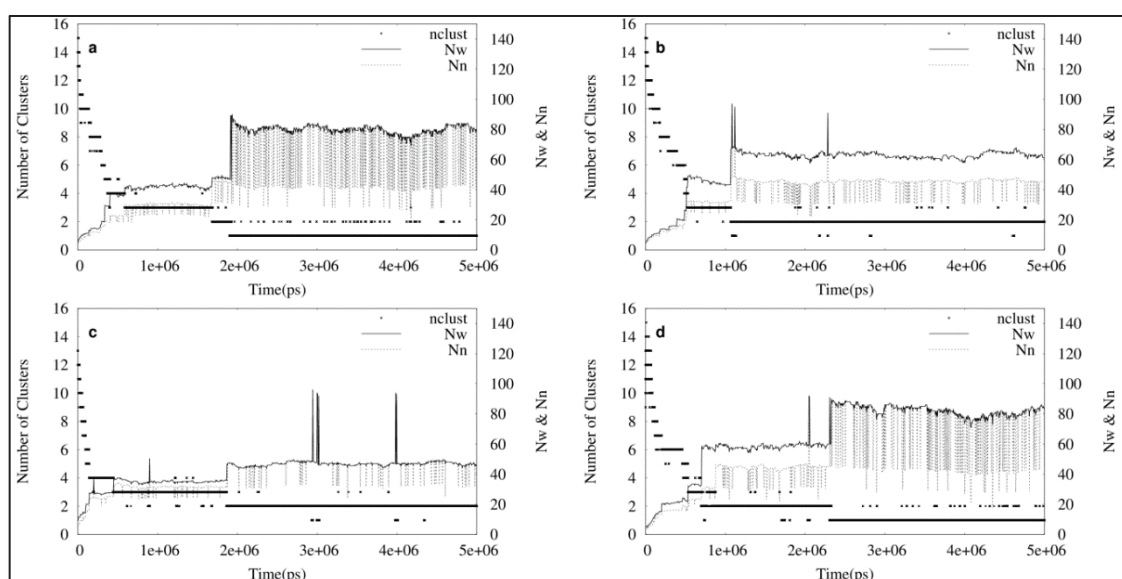
Figure 3.3. The time evolution of the number of clusters (left y-axis) and weight- (N_w) and number- (N_n) averaged aggregation numbers (right y-axis) for systems with a) Lauric, b) Stearic c) Oleic and d) Linoleic acids at <u>fasted state</u>. Results are given for each 5th ns of the trajectory (skipping the intermediate frames) for visual clarity. The numbers of clusters results were refined by excluding the clusters with two molecules.

The time evolution of N_w and N_n for systems at fasted and fed states are shown in Figure 3.3 and 3.4, respectively. The results are given for each 5th ns of the trajectory and the numbers of clusters of the aggregates composed of two molecules are omitted for visual clarity. As the systems are equilibrated with time, the numbers of clusters are expected to decrease while the average aggregation numbers are expected to increase. This expected behavior was observed in all the systems. The stepwise decrease in the number of clusters and increase in N_w & N_n values are the indicators of the fusion of smaller aggregates into larger ones. The points where after the results did not change

dramatically were chosen as the equilibration points of the simulations. For the simulations at fasted state, the equilibrium points were chosen as 1 μs for the system with stearic acid (SA), 2 μs for the systems with lauric (LA) and oleic acids (OA), and 2.5 μs for the system with linoleic acid (NA). At fasted state, the system with SA was equilibrated fastest. The number of cluster results showed that the systems with LA and NA resulted with single aggregates while the systems with SA and OA resulted in two final aggregates. The sharp increases observed in the N_w values of the systems with SA and OA represent the fusion moments of two smaller aggregates, which were clearly pretty unstable as they immediately broke into two again.
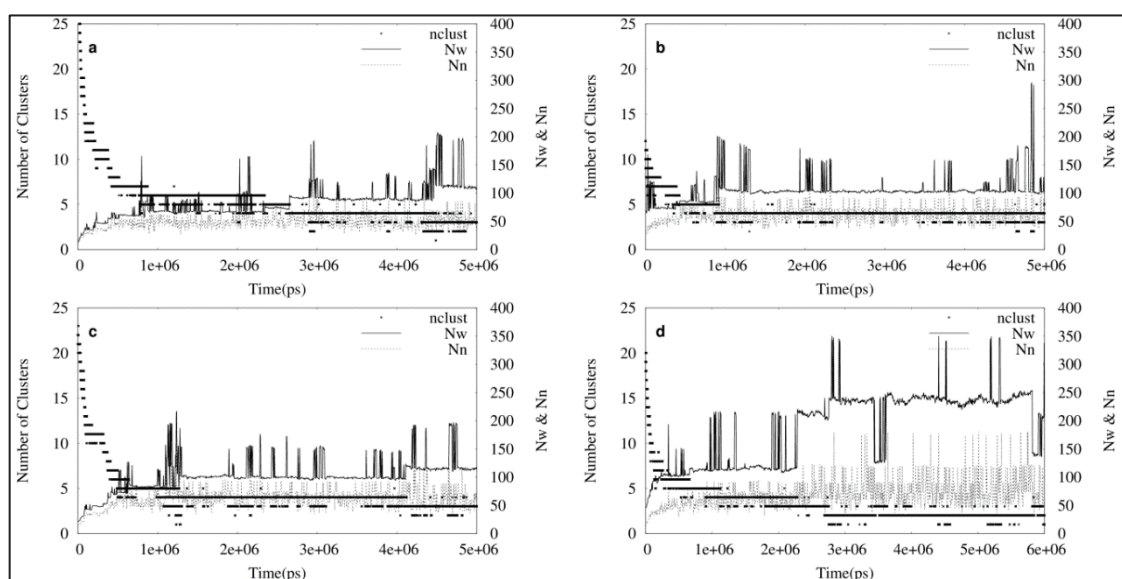
Figure 3.4. The time evolution of the number of clusters (left y-axis) and weight- (N_w) and number- (N_n) averaged aggregation numbers (right y-axis) for systems with a) Lauric, b) Stearic c) Oleic and d) Linoleic acids at <u>fed state</u>. Results are given for each 5th ns of the trajectory (skipping the intermediate frames) for visual clarity. The numbers of clusters results were refined by excluding the clusters with two molecules.

In the fed state, decision of the equilibration point of the simulations was more challenging due to the higher concentrations of the surfactant molecules resulting in the formation of higher numbers of aggregates. This is the expected phase behavior of the fed state duodenal medium as proposed by the literature (Kleberg et al., 2010). As a result, more frequent and closer approaches between the formed aggregates were observed. The more frequently seen sharp peaks in the N_w graphs indicates this situation. As the cut-off value chosen as the clustering criterion was 0.6 nm, any kind of approach equal to or smaller than this cut-off value between any beads of the

molecules belonging to different micelles were considered as a fusion moment of the two aggregates. However, whether or not that corresponds to a complete fusion of two or more aggregates into a stable micelle can be deduced from the time dependent behavior of N_w. If the increase in N_w is sustained for a long time, then a complete and stable fusion of the aggregates can be assumed. Therefore, it can be said that the frequently observed sharp peaks in N_w values in all the systems correspond to only the instances at which two or more aggregates are in close approach (≤ 0.6 nm), but not a complete fusion. Accordingly, the equilibration points of the systems with LA, SA, OA and NA were determined as ~4.5 µs, ~1 µs, ~4 µs, and ~3 µs, respectively. As clearly seen from the graphs, all the systems at fed state resulted with more than one mixed micelle structures (Figure 3.4).

The equilibration points of the simulations were also confirmed by the time-dependent hydrophobic SASA per molecule calculations. The SASA values were determined separately for different types of molecules. The plots can be found in Figures 3.7 & 3.6 for fasted and fed state systems, respectively. The point after which no more stable decrease in the hydrophobic SASA per POPC (or FA) was observed was considered as the equilibration point for each system. As expected, the equilibration points determined by both methods (the time-dependent hydrophobic SASA per molecule and the time-dependent N_w) agree with each other.

Although the mixed micelles obtained in each system were equilibrated structures, the attainment of true thermodynamic equilibrium states in these systems did not seem applicable due to the limited system size and computation times imposed by the available computational sources. In the literature, the presence of lipid digestion products has been reported to result in the formation of coexisting mixed micelles and vesicles both under the fasted and fed state conditions (Hemell, Staggers, & Carey, 1990; Kossena et al., 2003). The sizes of the aggregates depend on the concentration of the lipids present in the medium. However, in the present study, all the systems ended up only with coexisting simple and mixed micelle structures due to the limited system sizes. Unfortunately, these limitations do not let one to simulate a self-assembly process in which large vesicles (~70 nm) coexisting with mixed micelles are obtained unless a coarser-level simulation method is used. Nevertheless, the results obtained from these simulations still provide valuable insight into the mechanism of micellization.
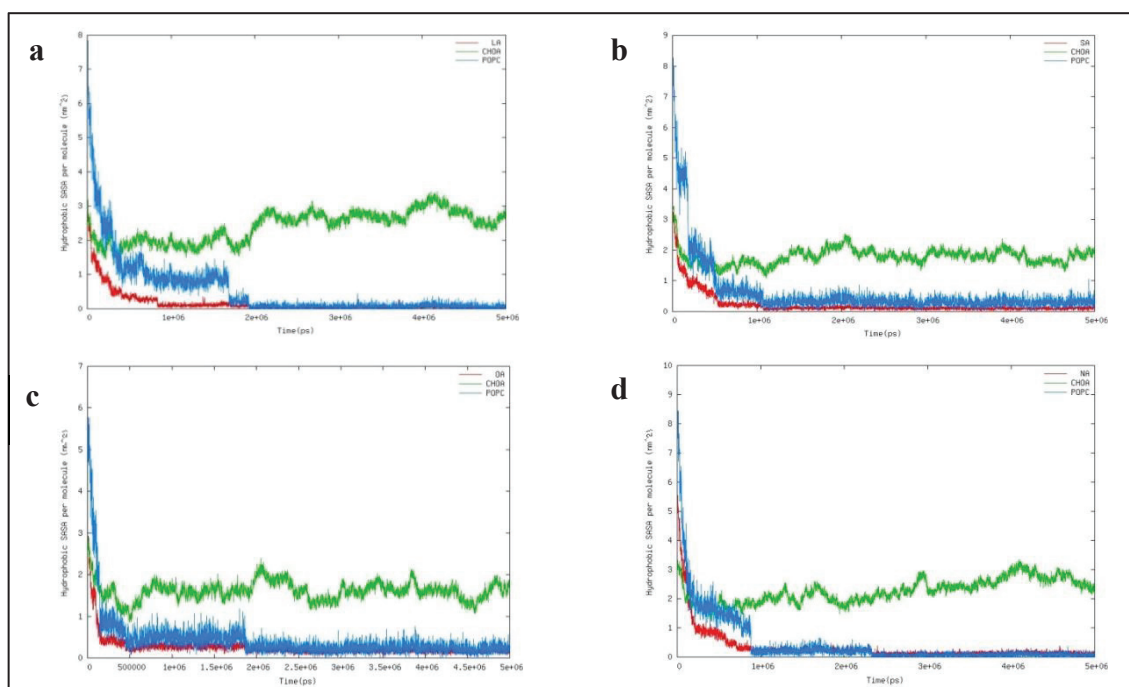
Figure 3.5. Time dependent hydrophobic SASA per molecule for systems with a) Lauric, b) Stearic c) Oleic and d) Linoleic acids at <u>fasted state</u>. Results are given for each half ns of the trajectory (skipping the intermediate frames) for visual clarity.
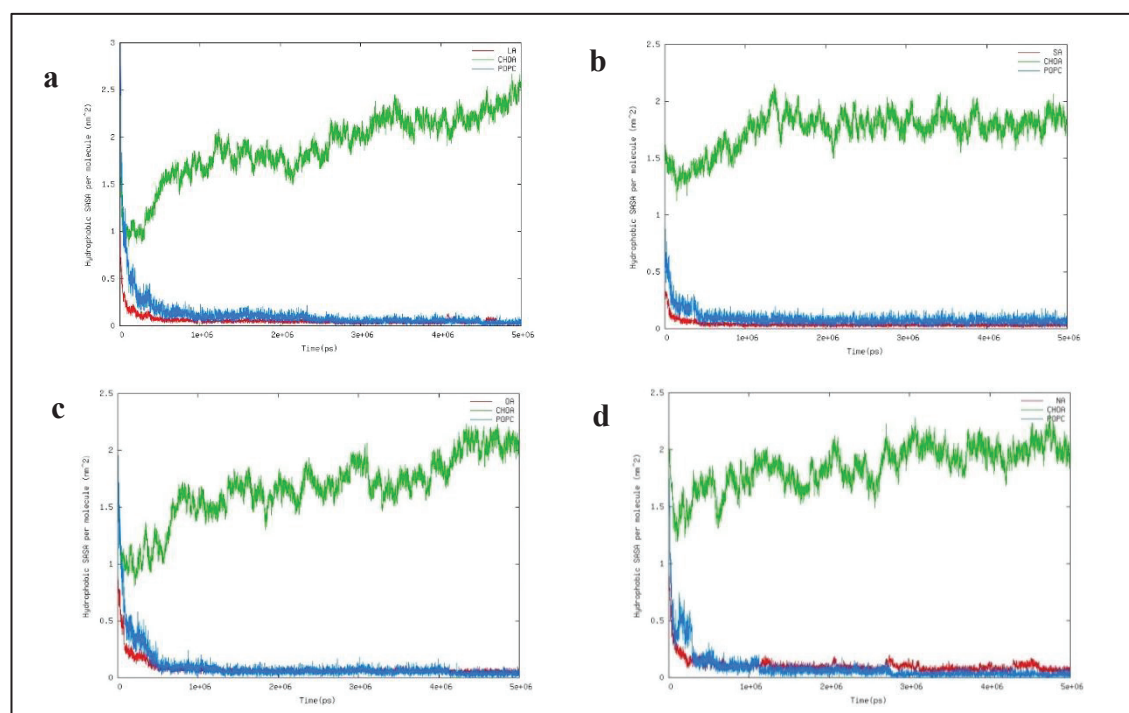
Figure 3.6. Time dependent hydrophobic SASA per molecule for systems with a) Lauric, b) Stearic c) Oleic and d) Linoleic acids at <u>fed state</u>. Results are given for each half ns of the trajectory (skipping the intermediate frames) for visual clarity.

Moreover, as mentioned in the literature and in Chapter 2, the structures formed during the digestion have a variety of sizes (Madenci & Egelhaaf, 2010; Phan et al., 2015; Xie et al., 2014). The smaller aggregates may join in together to form larger ones, or they may solubilize the hydrophobic nutraceuticals in the small intestine possessing a role in their digestion (Birru et al., 2014; Lebecque et al., 2017; Yao et al., 2014). Therefore, it is also important to analyze their structures (Fotouros, Walrand, Bergenstahl, & Mullertz, 2009).

The time-dependent hydrophobic SASA per molecule results also give information about the micellization behavior in each system. The hydrophobic moieties of the lipids in the media attempt to reduce their interaction with water molecules as proposed in the literature (Suys et al., 2017; Yao et al., 2014). The initial rapid decrease of hydrophobic SASA per surfactant in all of the fasted state self-assembly simulations indicates that the main driving force must be the hydrophobic effects. It is worth to mention that the initial rate of decrease in the hydrophobic SASA per molecule is greater in magnitude for POPCs compared to FAs suggesting that the initial aggregation kinetics is faster for POPCs. This can be explained by the fact that POPC tails occupy a larger volume (and surface area) owing to having two tails compared to FA tails, and therefore the driving force for their assembly is larger (considering that it would be energetically much more costly to break the structuring of water to make room for a POPC molecule than to make room for a FA molecule).

The time dependent micellization behaviors of the systems were also investigated by the help of cumulative probability distributions of the aggregation numbers as block-averaged values over 1 µs increments (Figure 3.7 & 3.8). The results indicate that the initial stages of the trajectories were dominated by small aggregates. In the course of simulations, larger micelles formed via fusion of smaller micelles. This characteristic behavior was observed for the systems both at fasted and fed state and with or without any fatty acid molecules. This behavior was also supported by the time dependent average aggregation number plots (Figure 3.3 and 3.4) as discussed above. According to the results of the systems at fasted state (Figure 3.7), the system with SA ended up with two mixed micelles, and smaller aggregates existed till the end of the trajectory. However, the system with OA had two micelle structures after the 2 µs of the trajectory with similar aggregation numbers. For the systems with LA and NA, the

systems resulted with single micellar structures. The compositions of the micelles selected for analysis and their accompanying structures can be found in Table 3.2.
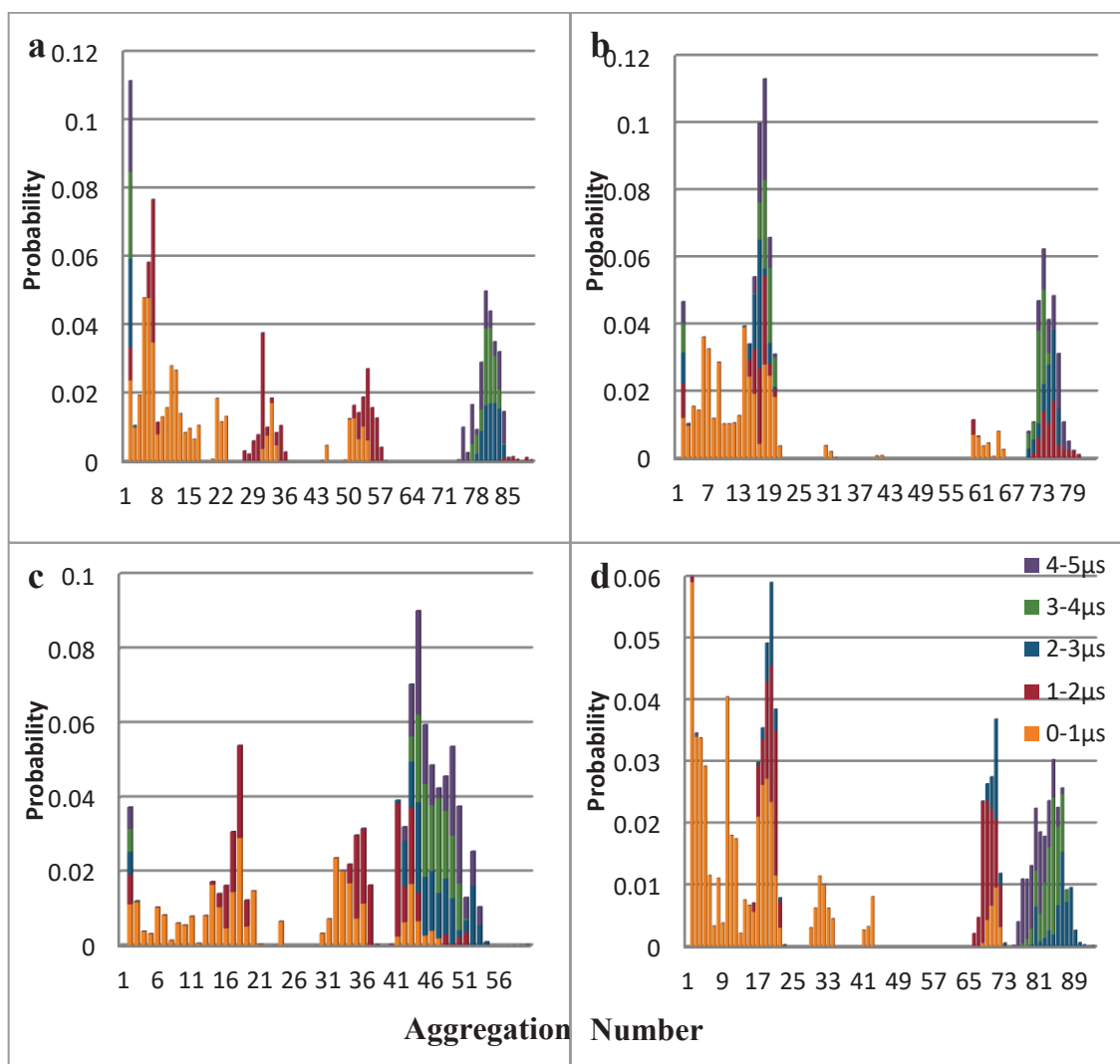
Figure 3.7. The cumulative probability distributions of aggregation numbers as a function of time (block-averaged over 1 μs intervals) for systems with a) Lauric, b) Stearic c) Oleic and d) Linoleic acids at <u>fasted state</u>.

The time dependent cumulative probability distributions of the systems at fed state can be found in Figure 3.8. The larger concentrations resulted in the formation of micelles with higher aggregation numbers. The numbers of aggregates were larger compared to the systems at fasted state as well. The systems ended up with at least two mixed micelles coexisting with simple micelles. Similar to the systems at fasted state, the trajectories were dominated by small aggregates at the beginning. Then, larger micelles started to form while smaller ones disappeared by time. The snapshots of the systems with Lauric acid at fasted and fed state are given as examples in Figure 3.9. At
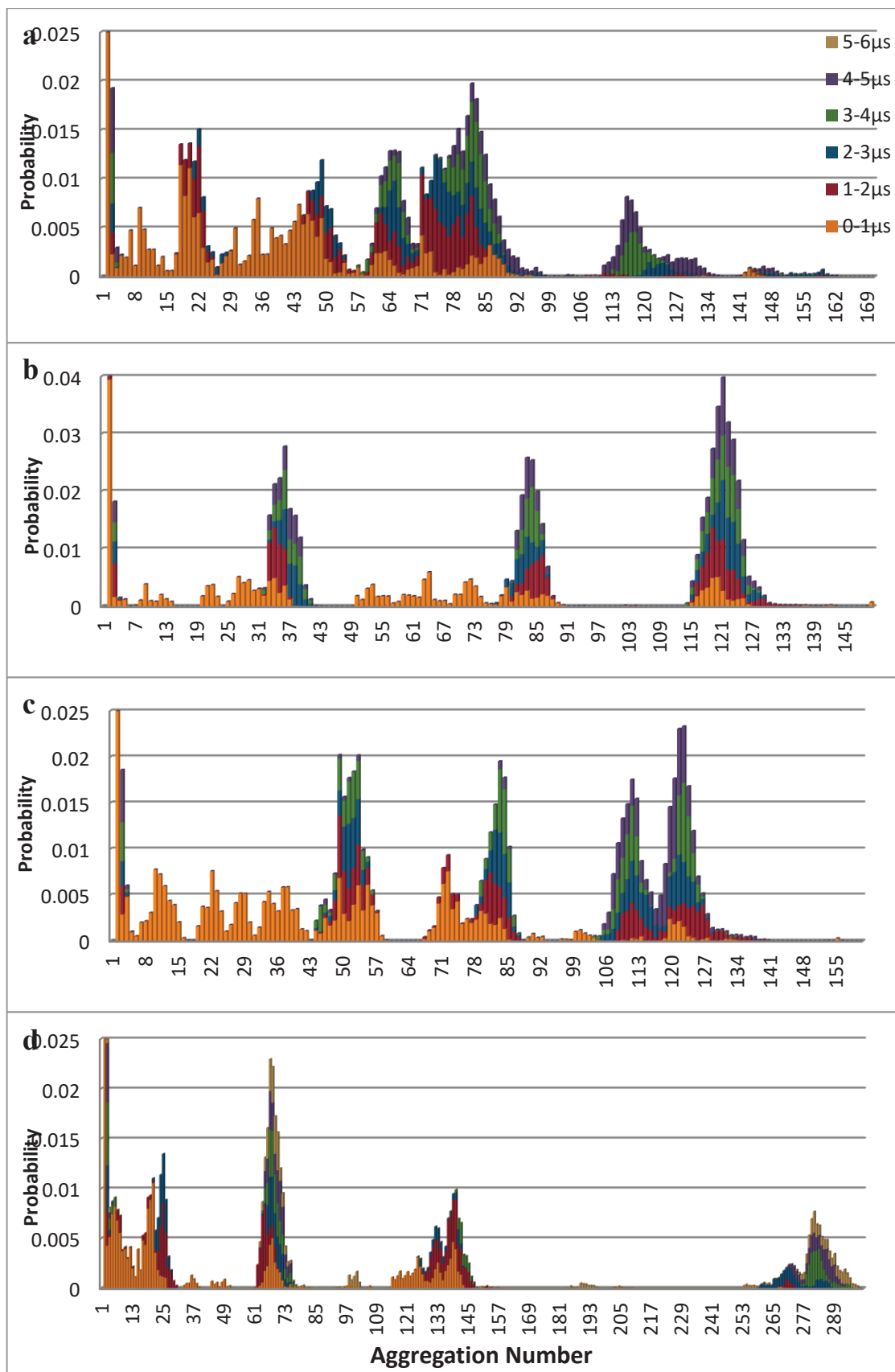
Figure 3.8. The cumulative probability distributions of aggregation numbers as a function of time (block-averaged over 1 μs intervals) for systems with a) Lauric, b) Stearic c) Oleic and d) Linoleic acids at fed state.

the first boxes, the random placement of the constituent molecules can be observed. After short pressure equilibration, the aggregates started to form. Following that, by the fusion of small aggregates larger micelles were formed. This characteristic behavior was valid for all the systems with different fatty acid molecules and concentrations. At fed state, all the systems ended up with more than one micelle of different aggregation numbers. After almost 1μs, smaller and larger aggregates exist till the end of the simulations in all the systems. Dimers were observed in all time intervals but for clarity, they were excluded from the plots. The difference in the probabilities of the micelles with similar aggregation numbers was originated from the exchange of CHOA molecules between the micelles and the surrounding media, which was also proved by visual inspections of the trajectories. The micelle with the highest cumulative probability and larger aggregation number after the equilibrium point was chosen for further analysis (Appendix 1&2). The aggregation numbers and compositions of selected micelles can be found in Table 3.2.
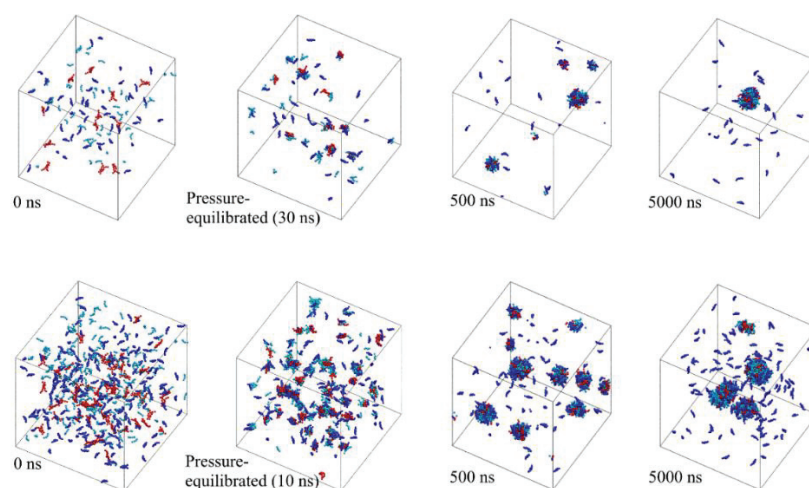
Figure 3.9. Snapshots from the trajectories of systems with lauric acid at fasted (above) and fed (below) states showing the evolution of self-assembly. Cholate, POPC and lauric acid molecules are colored in dark blue, red and light blue, respectively. Water molecules and ions are omitted for visual clarity.

To further characterize the micellization behavior, the average fractions of the constituent molecules in the micelles were calculated for each 1 μs interval of the trajectories via an in-house code written in Python language. Thus, the average percentages of CHOA, POPC, and FA molecules within the clusters of varying aggregation numbers were examined in time dependent manner. The probabilities of

Table 3.2. The compositions of the micelles observed at the end of the simulations in the presence of different fatty acid molecules

	Fasted State (BS:PL:FA=5:1.25:5 mM)						Fed State (BS:PL:FA=20:5:20 mM)											
	LA	SA		OA		NA	LA			SA				OA			NA	
Micelles	1	1	2	1	2	1	1	2	3	1	2	3	4	1	2	3	1	2
CHOA	20 (25%)	8 (47%)	23 (31%)	15 (34%)	17 (35%)	24 (29%)	26 (31%)	29 (25%)	30 (24%)	21 (55%)	30 (36%)	33 (27%)	38 (31%)	35 (32%)	38 (32%)	38 (31%)	26 (39%)	81 (29%)
POPC	12 (15%)	2 (12%)	10 (14%)	5 (11%)	7 (15%)	12 (14%)	16 (19%)	16 (14%)	19 (15%)	4 (11%)	13 (16%)	13 (11%)	18 (15%)	13 (11%)	17 (14%)	18 (15%)	10 (15%)	38 (14%)
FA	48 (60%)	7 (41%)	41 (55%)	24 (55%)	24 (50%)	48 (57%)	46 (54%)	71 (61%)	76 (61%)	13 (34%)	39 (48%)	75 (62%)	66 (54%)	63 (57%)	64 (54%)	66 (54%)	31 (46%)	162 (58%)
TOTAL	80*	17	74*	44*	48	84*	85	116*	125	38	82	121*	122	111	119	122*	67	281*

* Indicates the selected micelles for analyses. The values in the parenthesis are the percentages of the constituent molecules in the micelles.

incidence of the aggregates were not taken into account in the calculations; i.e., the average fractions were calculated for even an instantaneous appearance of an aggregate. The results are given in Figure 3.10 & 3.11 for fasted and fed state systems, respectively. At early stages (at 0-1 μs intervals), the simulation media consisted of clusters with a broad range of aggregation numbers as expected. The dimers, trimers, quartets, etc. of CHOAs, POPCs and FAs were present together with other small and larger mixed micelles in all the systems. The fractions of the constituent molecules seemed to vary for small micelles while they were more stable for larger ones. As the self-assembly proceeded, the fractions of the micelles with different aggregation numbers have evened out within the same trajectory. Generally, the micelles with consecutive aggregation numbers had CHOA fractions in increasing trend. This is due to the increase in the aggregation numbers by joining of CHOA molecules. A stepwise fusion of the smaller aggregates has been once more proven by the help of time dependent average fraction results of the constituent molecules. Moreover, no more mixed micelles composed only of CHOAs and FAs or CHOAs and POPCs existed as the simulations reached equilibrium; i.e., the equilibrium phases were composed of simple micelles of CHOAs coexisting with mixed micelles (with varying aggregation numbers) composed of CHOAs, POPCs and FAs. The reason for the exception in the system with NA at fed state (Figure 3.11-d) was due to an instantaneous appearance of a dimer composed of a CHOA and NA, which disappeared soon after its formation.

In the second chapter of the dissertation, it has been shown that once the POPC molecules joined the micelles, they never left them again. This behavior was also observed in the micelle structures in the presence of fatty acid molecules. However, it was observed that the fatty acid molecules occasionally left the micelles during the simulations. This was inferred from both the inspection of the time dependent fractions of the constituent molecules and visual inspection. However, the exchange of fatty acids with the surrounding media was not as frequent as the exchange of CHOA molecules. Fusion of smaller aggregates resulted in larger micelles of which the core was occupied by all the lipophilic moieties of POPCs and FAs.

The aggregation process in the simulation boxes was observed to have started between the neighboring molecules similar to the case encountered in the self-assembly of BSs and PLs in Chapter 2. The efforts of the FA tails trying to avoid the energetically unfavorable contacts with water molecules put them in various conformations. In Figure
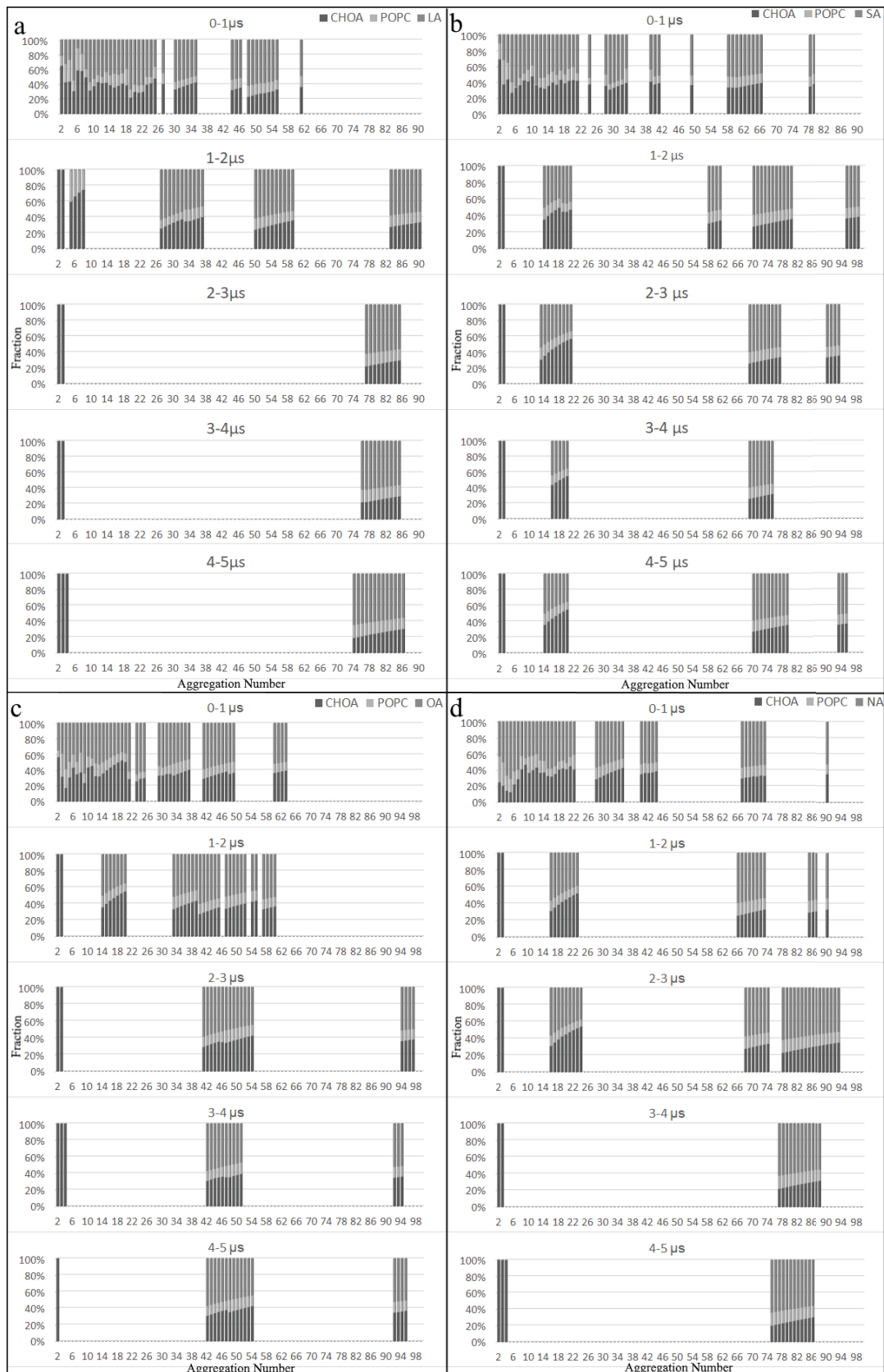
Figure 3.10. The average fractions of the constituent CHOA (yellow), POPC (red) and fatty acid molecules in the micelles with different aggregation numbers as a function of time for systems with a) Lauric (light blue), b) Stearic (purple) c) Oleic (green) and d) Linoleic (deep blue) acids at <u>fasted state</u>.
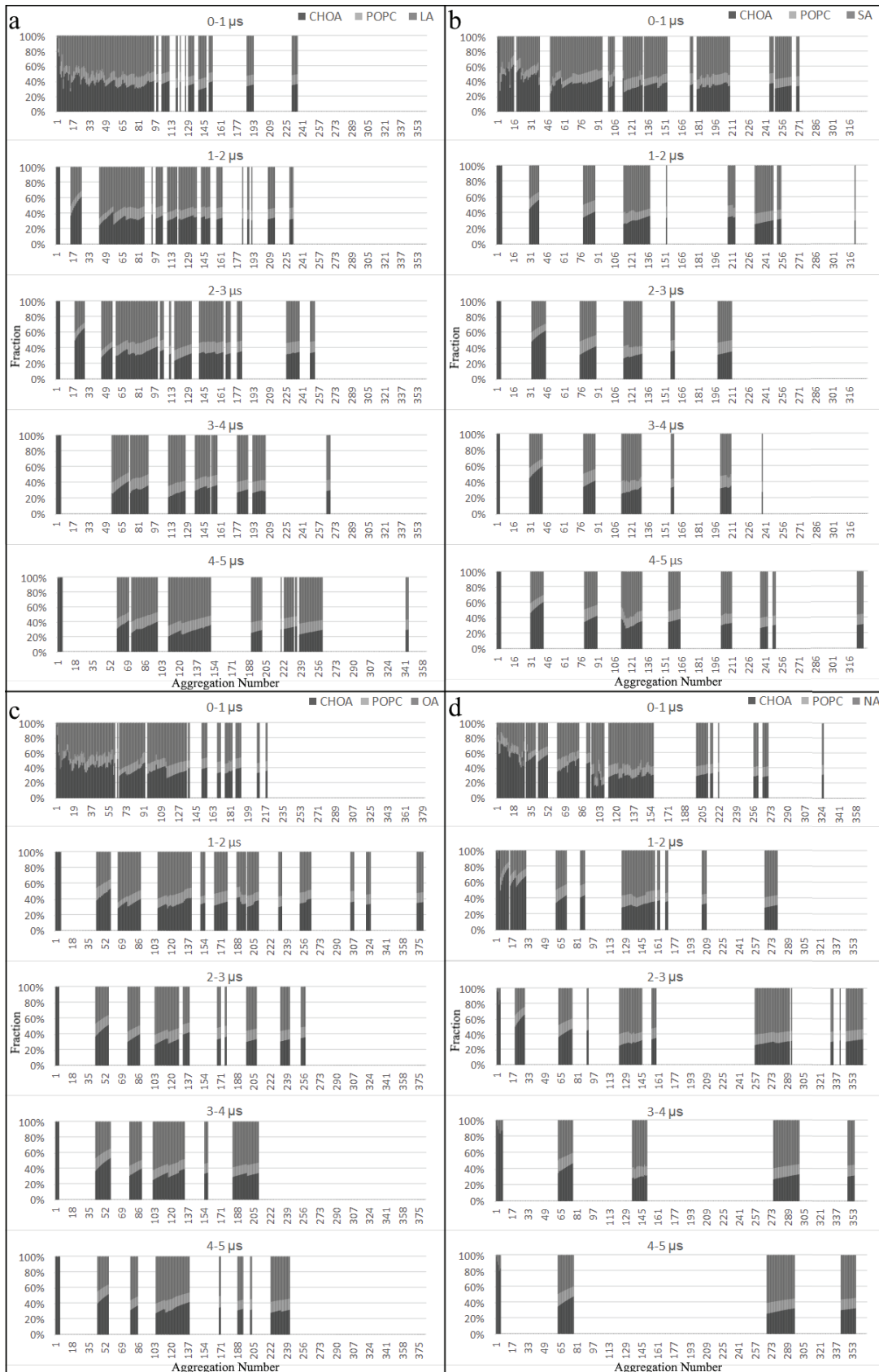
Figure 3.11. The average fractions of the constituent CHOA (yellow), POPC (red) and fatty acid molecules in the micelles with different aggregation numbers as a function of time for systems with a) Lauric (light blue), b) Stearic (purple) c) Oleic (green) and d) Linoleic (deep blue) acids at <u>fed state</u>.
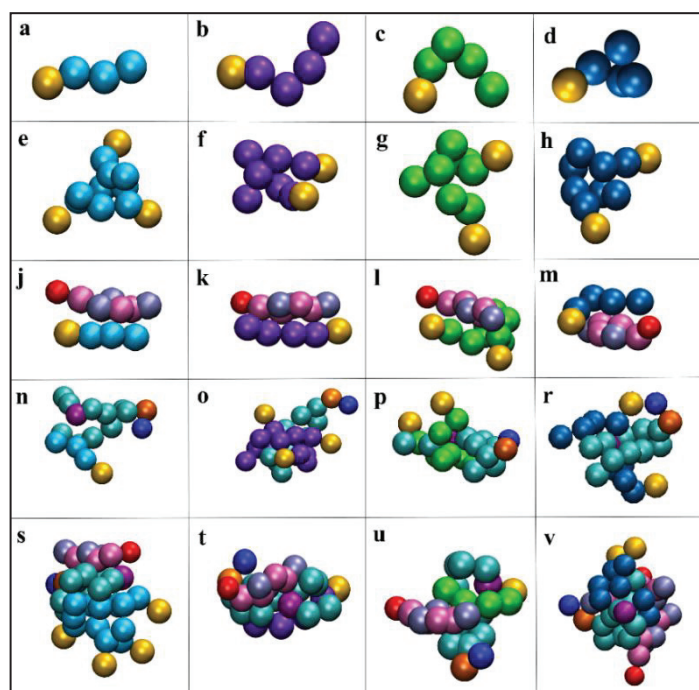
Figure 3.12. The representative aggregates that were formed during the simulation of systems with different fatty acids. The examples for monomers (a, b, c and d), dimers (e, f, g and h), and small aggregates of CHOA (cholate), POPC (1-palmitoyl-2-oleoyl-glycero-3-phosphocholine) and fatty acids (n to v) are given. The hydrophobic, hydrophilic and charged beads of CHOAs are colored in pink, ice blue and red, respectively. $NC3^+$ beads of POPCs are colored in blue while $PO4^-$ beads are colored in orange. Glycerol and tail beads of POPCs are colored in cyan except the bead with an intrinsic double bond, which is colored in purple. Head beads of fatty acids are colored in yellow and tail beads are colored according to fatty acid type; Lauric acid: light blue, Stearic acid: purple, Oleic acid: green and Linoleic acid: deep blue

3.12.a-d, free fatty acid molecules in the very early stages of the simulations are shown. It is clearly seen that due to the shorter chain length of lauric acid (Figure 3.12.a), it has a more rigid structure. By increasing chain length and the number of double bonds, the tails of the fatty acids seem to have gained more fluidity. For example, a linoleic acid tail folding over itself to minimize the contact area with water is demonstrated in Figure 3.12.d. Soon after the initiation of the simulations formation of small aggregates have been observed due to the hydrophobic interactions. The dimers of fatty acids were among those which were only observed at the very beginning of the trajectories (Figure 3.12.e-h). The small CHOA-FA aggregates were usually formed with the parallel alignment of the molecules due to the peculiar facial amphiphilic and rigid structure of CHOAs (Figure 3.12.j-m). The interactions are between the hydrophobic face of CHOA and the tail beads of fatty acids as expected. The representative POPC-FA aggregates

with different aggregation numbers can be found in Figure 3.12.n-r. The hydrophobic interactions between the tails of FAs and POPCs are apparent in all the structures. An occasional arrangement of the charged head groups of FAs and POPCs at the interface due to the strong electrostatic interactions in between is also exemplified in Figure 3.12.r. The joining of CHOAs to the aggregates resulted in similar structures as well (Figure 3.12.s-v). Therefore, it can be said all these observations support the notion that the main driving force of the micellization is the hydrophobic effects.

In summary, the inspection of the micellization behaviors of all the systems showed that the aggregation process was similar in all of them and independent of the fatty acids types and concentrations. The aggregation was observed to have started immediately between any neighboring molecules to shield the hydrophobic moieties from water. In the course of the simulations, the larger aggregates were formed with the fusion of smaller ones resulting in decreasing number of aggregates and increasing aggregation numbers with time. As the systems became more equilibrated, the compositions of the aggregates with a varying aggregation numbers were evened out. The dimers of CHOAs were formed at any time of the trajectories. Besides, the continuous exchange of CHOAs between the aqueous media and the micelles were observed in all the systems. Once the hydrophobic core of a micelle was formed by the POPC molecules, they always remained in the aggregates, which is similar to the case observed in the self-assembly of only BSs and PLs. On the contrary, fatty acid molecules were observed to leave the micelles occasionally, but not as frequently as CHOA molecules did. As the chain length and number of double bonds in the fatty acids increased, they had more freedom to adopt a variety of arrangements alone or within the micelles. Further structural analyses the results of which are given in Section 3.3.2.3 also support this finding.

3.3.2. Structural Characterization of Mixed Micelles in The Presence of Fatty Acids

The structural characterization of the mixed micelles in presence of different fatty acid molecules were performed by calculating radius of gyration, principle moments of inertia and solvent accessible surface areas.

3.3.2.1. Size and Shape Properties

The micelles with the highest cumulative probabilities and the higher aggregation numbers after the equilibrium points of the trajectories in each system were selected for further structural analyses. The analyzed micelles were named after the constituent fatty acid name and the status of being fasted or fed. For example, the selected micelles incorporating lauric acids at fasted and fed states were named as LA-Fa and LA-Fed, respectively. Additionally, the extra micelle analyzed in the presence of linoleic acid at fed state was named as NA-Fed-small. The total numbers of the molecules in the selected micelles were indicated with an asterisk in Table 3.2. The cross-sectional views of the selected micelles can be found in Figure 3.13.a-k. The selected micelle of the system with NA at fed state was observed to transform into many different shapes throughout the trajectory. Some of those shapes are given in Figure 3.13.j-l. This highly dynamic nature of the micelle prohibited the analysis of its internal arrangements via RDDs and certain types of angles (see sections 3.3.2.2 & 3.3.2.3). Instead, the smaller micelle in the equilibrated system was analyzed (Figure 3.13.h.) as it remained its stability in shape.

For structural characterization of the mixed micelles, the radii of gyration (R_g) of the selected micelles were calculated firstly. The results are given in Table 3.3. In the literature, the addition of fatty acids was reported to swell the micelles(Rex P Hjelm, 1992; Kossena et al., 2003; Phan et al., 2015). Hence the R_g values are expected to increase after the addition of fatty acid molecules to the micelles. The comparisons of the results of the systems with different fatty acids can be done with the help of Figure 3.14. According to the results, the addition of fatty acids to the media increased aggregation numbers for all the systems. The sizes of the selected aggregates grew by increasing aggregation numbers, except for the system with OA at fasted state. The micelle with OA has smaller aggregation number and R_g compared to the micelles incorporating other fatty acid types. Besides, it is observed that the OA-Fa micelle has a smaller smaller R_g compared to the micelle at fasted state without fatty acids (39-Fa) despite the fact that it has a larger aggregation number. This indicates that the OA-Fa micelle is denser than the 39-Fa micelle. The volume per lipid calculations also supports the higher density of the micelle with OA (volume per lipid=0.157 nm^3) compared to the micelle without fatty acids (volume per lipid=0.267 nm^3) at fasted state. The volume

per lipid values were calculated using the radii of gyration in three principal directions of the hydrophobic core. The volumes of the ellipsoidal cores were calculated in the first place, and then the results were divided to total number of POPC and FA molecules. The similar R_g results of the systems with LA and SA despite the different
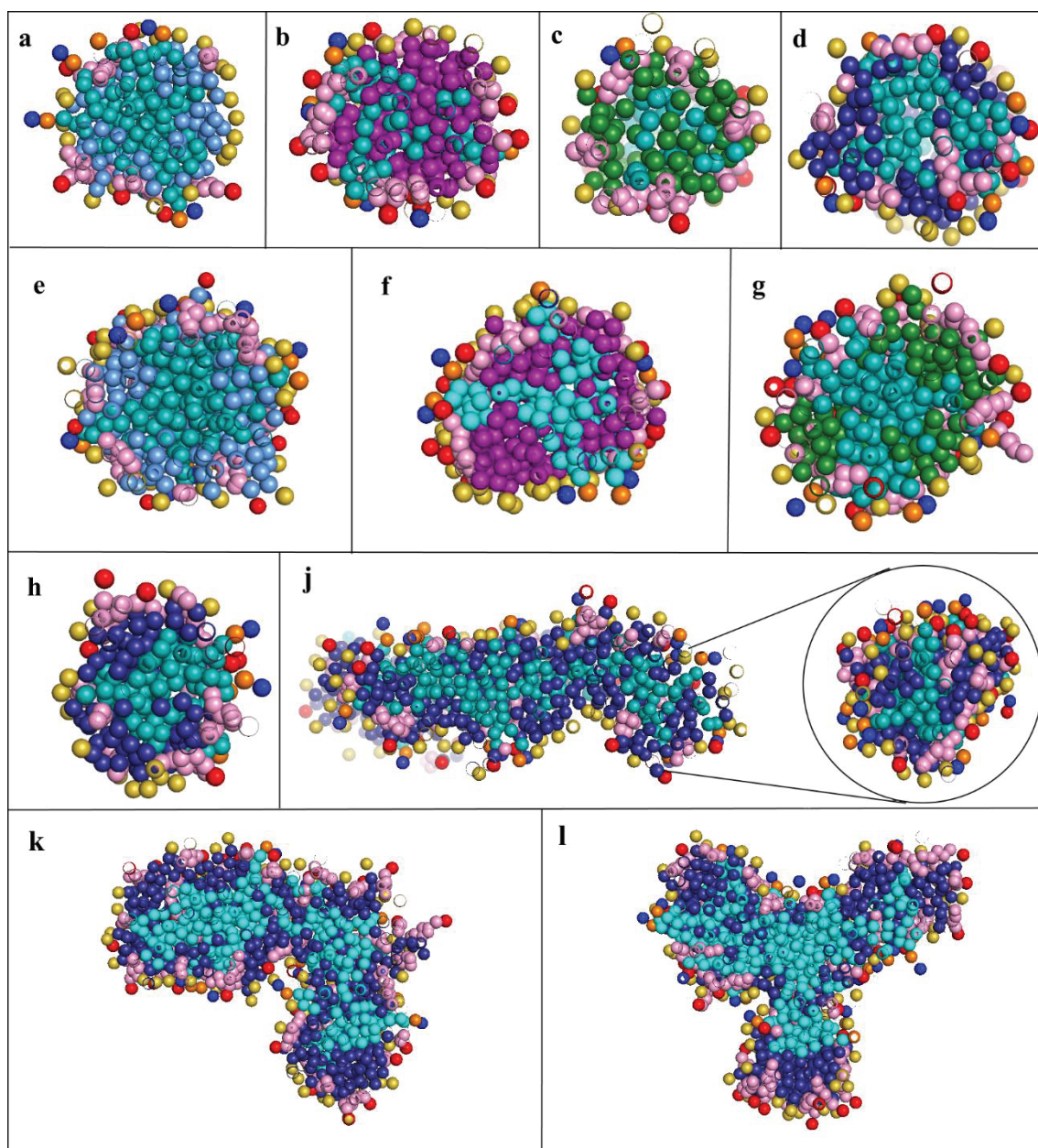
Figure 3.13. The cross-sectional views of the selected micelles of the systems at fasted (a, b, c & d) and fed (e, f, g, h, j, k & l) states. Different shapes of the micelle with NA at fed state can be found in parts h-l. The head bead and the remaining beads of CHOAs are colored in red and pink, respectively. $NC3^+$ beads are colored in blue while $PO4^-$ beads are colored in orange. Glycerol and tail beads of POPCs are colored in cyan. Head beads of fatty acids are colored in yellow and tail beads are colored according to fatty acid type; Lauric acid: light blue, Stearic acid: purple, Oleic acid: green and Linoleic acid: deep blue
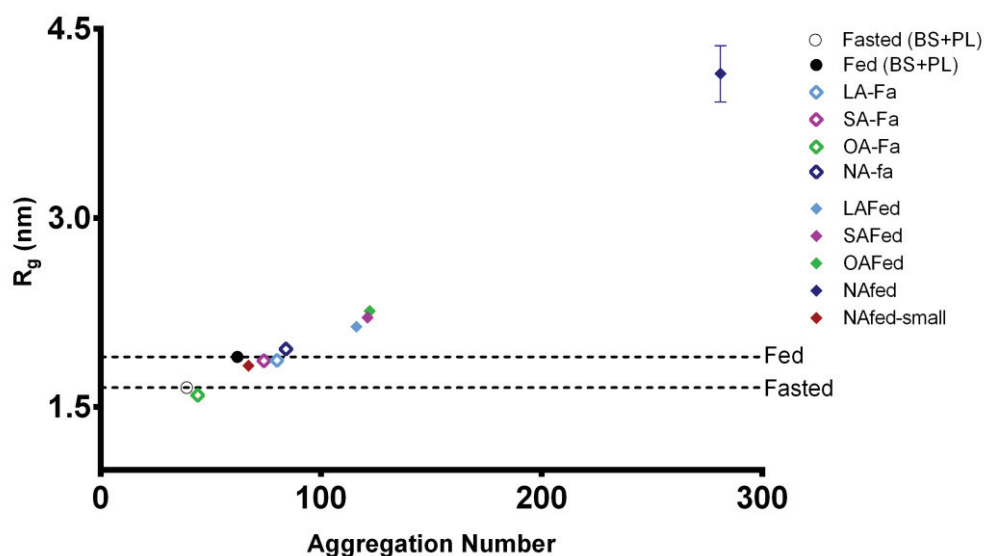
Figure 3.14. Radii of gyration of selected micelles at fasted (◇) and fed (◆) states with different fatty acids: Lauric acid: light blue, Stearic acid: purple, Oleic acid: green and Linoleic acid: deep blue. The R_g results of the systems without fatty acid molecules at fasted (○) and fed (●) states are also given and emphasized by dotted lines for ease of comparison.

aggregation numbers suggests that the micelle with LA has a denser structure. The volume per lipid calculations confirms this finding (Table 3.3.) as well. The longer chain of the SA prevented incorporation of fatty acid molecules into the micelles as many as LA molecules due to the increased steric effects. The R_g values of the micelles formed at fasted state vary between 1.593 to 1.959 nm in the present study. These values correspond to hydrodynamic radii (R_h) of 2.069 nm and 2.544 nm, respectively, based on the assumption that R_g/R_h ratio is 0.77 for a solid sphere (Tande et al., 2001). In the literature, the hydrodynamic radius of mixed micelles formed at the same fasted state conditions of bile acids (sodium taurodeoxycholate) and phospholipids (egg yolk lecithin) but with higher lipid concentrations were determined experimentally. The concentrations of selected caprylic/capric acids (60:40) (100 mM for fasted and fed state) as medium-chain and oleic acid (15 and 30 mM for fasted and fed states, respectively) as long-chain fatty acid molecules were higher compared to the present study and their monoglycerides were also included to the systems (FA:MG=2:1). As a consequence, the sizes (R_h) of the mixed micelles were found to be equal to 3.8 and 4.1 nm for the micelles with medium- and long-chain fatty acids at fasted state (Kossena et al., 2003). The micelles of oleic acid, monooleate, and cholylglycine or chenodeoxycholylglycine were reported to have sizes varying in the range of 20-30 angstroms depending on the lipid concentration (Rex P. Hjelm et al., 2000). According

to the study of Clulow et al. (2017), the micelles of sodium taurodeoxycholate (10 mM), soy lecithin (2 mM), glyceryl monooleate (5 mM) and sodium oleate (0.8 mM) had 44 angstroms of the radius. The concentrations of the lipid molecules in the present study were different from the studied concentrations in literature. Therefore, the exact comparison of the results was not possible. Nevertheless, the results are close to the given experimental values.

The R_g's of the selected micelles at fed state exhibit increasing trend with increasing chain length and number of double bonds. The more regular trend in the systems at fed state is probably due to the presence of larger amounts of free CHOA molecules in those systems. Therefore, the effects of chain length and the number of double bonds are observed more clearly. As stated in the literature, long-chain fatty acids swell the micelles more than the medium-chain fatty acids (Kossena et al., 2003; Phan et al., 2015; Porter et al., 2004; Salentinig et al., 2011). Besides, the presence of double bonds further increased the micelle size. This can be clearly seen by the comparison of R_g results of micelles SA-Fed and OA-Fed. The aggregation numbers of those two micelles were almost equal but the size of the OA-Fed micelles was larger due to the double bond present in the fatty acid structure. Despite the larger size of OA-Fed micelle, its hydrophobic core was denser than the SA-Fed micelle because of the larger amounts of POPC molecules solubilized within that micelle (see Table 3.3.). Moreover, in the presence of long-chain polyunsaturated linoleic acid, the micelles underwent a transition from ellipsoid to rod-like shape. This situation may be explained by both the larger volume occupied by the tails of the fatty acid molecules in the presence of double bond and the curvature effects. More than one double bond resulted in increased steric effects and higher fluidity of the molecules. Therefore, larger amounts of CHOAs were required to protect the hydrophobic moieties from water, and this process resulted in the elongation of micelles. This behavior has been reported in the literature before (Rex P. Hjelm et al., 2000; Salentinig et al., 2011). The R_g result of NA-Fed-small micelle was smaller due to its smaller aggregation number. Here, the presence of double bond in the system resulted in increased density (volume per lipid=0.177 nm^3) compared to BS+PL micelles (volume per lipid=0.272 nm^3) like the OA-Fa micelle.

Table 3.3. Structural properties of the selected micelles: Radius of gyration (R_g); ratios of the principal moments of inertia, (I_1/I_2) and (I_2/I_3); total solvent accessible surface area (SASA); SASA per surfactant; the ratio of the hydrophilic SASA to hydrophobic SASA (Phi/Pho), volume per lipid in micelle core and concentration of free CHOA molecules in the media

System	Numbers of total molecules (CHOA:POPC:FA)	Micellar Lipid/CHOA ratio	R_g (nm)	I_1/I_2	I_2/I_3	Total SASA (nm²)	Phi/Pho	SASA per surfactant (nm²)	Volume per lipid in the micelle core	Concentration of free CHOAs (mM)
LA-Fa	80 (20:12:48)	3.00	1.869±0.028	0.866±0.069	0.916±0.042	141.341±4.714	16.347	1.767	0.078	2.81
SA-Fa	74 (23:10:41)	2.22	1.864±0.018	0.878±0.062	0.923±0.038	140.686±3.722	14.064	1.901	0.154	1.67
OA-Fa	44 (15:5:24)	1.93	1.593±0.033	0.840±0.080	0.894±0.051	105.966±3.452	8.508	2.408	0.157	1.45
NA-Fa	84 (24:12:48)	2.50	1.959±0.033	0.854±0.076	0.906±0.046	155.979±4.424	11.400	1.857	0.168	2.52
LA-Fed	116 (29:16:71)	3.00	2.137±0.037	0.789±0.102	0.896±0.049	173.806±5.351	18.561	1.498	0.143	8.61
SA-Fed	121 (33:13:75)	2.67	2.208±0.032	0.782±0.096	0.892±0.052	182.979±5.076	18.283	1.512	0.186	6.88
OA-Fed	122 (38:18:66)	2.21	2.261±0.034	0.764±0.097	0.900±0.048	194.122±5.807	14.631	1.591	0.179	6.94
NA-Fed	281 (81:38:66)	2.47	4.144±0.223	0.245±0.097	0.937±0.053	397.730±10.569	13.483	1.415	-	7.71
NA-Fed-small	67 (26:10:31)	1.64	1.826±0.023	0.862±0.069	0.915±0.042	137.069±4.445	9.87	2.046	0.177	7.71

According to Table 3.3, the R_g values of the systems at fed state vary between 2.14 to 4.14 nm corresponding to R_h values of 2.78 and 5.38nm, respectively. In the previously mentioned study of Kossena et al. (Kossena et al., 2003), the hydrodynamic radius values of the micelles were reported as 3.8 and 4.1 nm for medium- and long-chain fatty acids at fed state, which were equal to the results of the fasted state. In the study of Phan et. al. (2015), the exact same concentrations of bile salt (sodium taurodeoxycholate), phospholipid (DOPC) and different types of saturated fatty acids (C_8, C_{12} or C_{14}) were used. The micelle sizes were reported to increase by increasing chain length of fatty acids and reached up to 30 angstroms. The diameter of the micelles composed of bile extract (15 mM), lecithin (3.75 mM) and oleic acid (10 mM) with its monooleate (5 mM) was measured as 5 nm (Kleberg et al., 2010). Therefore, the results of the systems at fed state are compatible with the literature.

To characterize the shape of micelles, the ratios of three principal moments of inertia (I_1/I_2 and I_2/I_3) were calculated (where $I_1 \leq I_2 \leq I_3$). The results are presented in Table 3.3. At fasted state, the ratios, I_1/I_2 and I_2/I_3, were almost equal, but the ones with OA were somewhat smaller. The ratios were smaller than 1, but close to each other in value. Therefore, the micelles can be considered as slightly ellipsoidal in shape, which is also supported by the visual inspection (Figure 3.13.a-d).However, smaller values for the ratios, I_1/I_2 and I_2/I_3 were obtained under fed state indicating that the micelles became more ellipsoidal in shape with increasing concentrations. Moreover, there was a clear correlation between the fatty acid characteristics and the micelle shape under fed state concentrations. The micelles became more ellipsoidal in shape as the degree of unsaturation of the fatty acids increased such that one of the micelles with NA adopted even a rod-like shape. Although the average ratios of the principal moment of inertia results showed us the micelle with NA in rod-like shape, visual inspection of the system revealed the presence of many different shapes in the subjected micelle. The presence of multiple double bonds in that system increased the volume hydrophobic moieties and initiated shape transition. The increase in the lipid concentration, which also reduces the BS/Lipid ratio, was reported to cause a shape transition in the literature (Birru, Warren, Han, et al., 2017; Rex P. Hjelm et al., 2000; Phan et al., 2014; Salentinig et al., 2011). Still smaller mixed micelles also existed in the media as suggested in the literature (Kossena et al., 2003; Staggers, Hernell, Stafford, & Carey, 1990). The shape of the smaller micelle was ellipsoidal similar to the other systems. In general, the addition of

fatty acid molecules to the media resulted in divergence from the spherical shape as proposed in the literature (Clulow et al., 2017; Phan et al., 2015). The higher concentration and unsaturation level increased the amount of transformation from spheroidal to ellipsoidal shape. However, no significant difference was observed between the shapes of the micelles with medium- and long-chain fatty acid molecules.
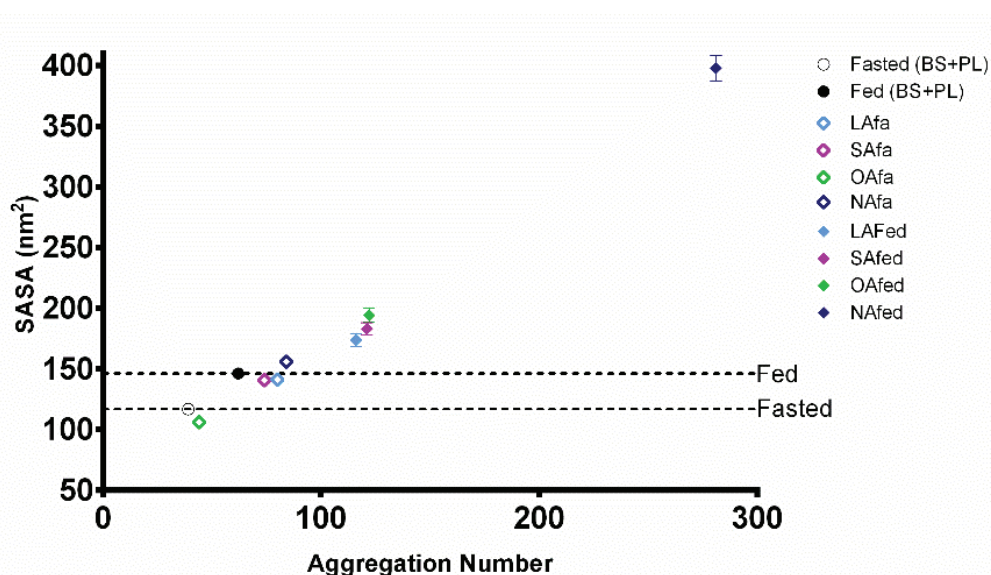
Figure 3.15. SASA results of selected micelles at fasted (◇) and fed (◆) states with different fatty acids: Lauric acid: light blue, Stearic acid: purple, Oleic acid: green and Linoleic acid: deep blue. The SASA results of the systems without fatty acid molecules at fasted (○) and fed (●) states are also given and emphasized by dotted lines for ease of comparison.

Solvent accessible surface areas (SASA) of the micelles in the presence of different fatty acids were also examined. The calculations were performed using a solvent probe of 0.56 nm in radius to mimic one MARTINI water bead, which represents four atomistic water molecules. Table 3.3 displays the total SASA, SASA per surfactant, and the ratio of the hydrophilic to hydrophobic SASA (Phi/Pho). In the systems without fatty acid molecules, SASA values increased with increasing micelle size. The correlation between SASA and R_g results was also observed for the systems with fatty acids (Figure 3.15). On the contrary, the size dependence of Phi/Pho ratio was diminished by incorporation of fatty acids to the micelle structures. The micelles composed only of CHOA and POPC were reported to have higher Phi/Pho ratios with increasing micelle size in the second chapter of the dissertation, and thus more stable structures were obtained. The smallest OA-Fa micelle conformed to this size dependent trend as it had the smallest Phi/Pho ratio. However, the increased chain length and

unsaturation showed different effects at fasted state. On the other hand, increasing chain length and the number of double bonds reduced the Phi/Pho ratio at fed state and so the stability of the micelles. Lastly, the SASA per surfactant results were examined. The slightly smaller SASA per surfactant in the LA-Fa micelle than in the similar sized SA-Fa micelle can be interpreted as an indicator of a slightly denser surface packing in the latter. The RDD results also supported the denser structure of the system with LA-Fa (see section 3.3.2.2). At fed state, SASA per surfactant values were increased regularly by increasing micelle size.

3.3.2.2. Radial Density Distribution

The inner structures of the micelles and the distributions of the surrounding water molecules and ions were investigated by the help of RDDs of selected beads in a molecule with respect to the center of mass (com) of the micelles. The results of the systems at fasted and fed states are given in Figure 3.16&17.a-d, respectively. Note that due to the different shapes of the selected micelle with NA at fed state, the RDDs of the constituent molecules could not be analyzed. Therefore, to have an idea about the inner structuring of the micelles in the presence of linoleic acid, the RDDs of the spheroidal NA-Fed-small micelle were calculated. On the left side of the figures, the RDDs of the head, glycerol and tail beads of POPC molecules, head and tail groups of fatty acid molecules and charged OCO^- and one representative bead (R3) of CHOA molecules are given with surrounding water molecules and ions. These plots give information about general placements of the molecules which are slightly different from the micelles of CHOA and POPC molecules. In detail, the charged beads of constituent molecules are placed on the micelle surface and fully solvated while the hydrophobic tail groups form the core. The charged beads of each type of molecules are placed on the surface. The $NC3^+$ beads of POPC molecules are placed slightly further from (~ 0.1 nm) the $PO4^-$ beads, similar to the systems without fatty acids. This, and also the angle results between the PO4-NC3 vector and micelle's surface normal (section 3.3.2.3) show the preservation of protruded head groups of POPC molecules. In the micelles without fatty acids molecules, $PO4^-$ and OCO^- beads were placed almost at the same distance. In contrast, in the presence of fatty acids, OCO^- bead of CHOAs are closer (~0.6 nm) to the micelle surface than $PO4^-$ beads in systems with LA, SA and OA at fasted state. In

NA-Fa and NA-Fed-small micelles, the maxima of RDDs of OCO$^-$ beads are placed at the same distance from the micelle com. The charged COO$^-$ beads of fatty acid molecules are placed slightly closer to the micelle surface compared to the charged beads of other molecules. The glycerol bead of POPC molecules are positioned at the micelle-water interface. However, the incorporation of fatty acids in the micelles seems to have shifted their positions towards water molecules. Finally, the fatty acid micelles are surrounded with the double layer of Na$^+$ and Cl$^-$ ions. The Na$^+$ ions are preferentially localized around the negatively charged beads of CHOA, POPC, and fatty acids and fill the space between them as in the micelles of BS+PL. Then the Cl$^-$ ions form a second shell around them. Overall, it can be said that the local arrangements of the constituent molecules within the micelles (except the small differences for charged beads) and the ions surrounding them are similar in general regardless of the presence of fatty acid molecules. The results are compatible with the previous chapter and the studies of BS+PL micelles proposed in the literature (S. J. Marrink & Mark, 2002; Sayyed-Ahmad et al., 2010).

To gain more detailed information about the arrangement of CHOA molecules within the micelles, RDDs of individual CHOA beads were calculated. The plots are placed in the middle parts of Figure 3.16&17.a-d. CHOA molecules are placed on the micelle surfaces as in the case of micelles composed of CHOA and POPC. The beads forming the sterol backbone are placed almost at the same distance. R1 and R3 beads, which contain methyl groups, are slightly closer to the core because of their hydrophobic structures. According to these results, CHOA molecules are placed flatly on the micelle surface exposing their hydrophilic groups to the water as indicated in the literature and in the second chapter of the study (Birru, Warren, Headey, et al., 2017; Haustein et al., 2014; S. J. Marrink & Mark, 2002; Sayyed-Ahmad et al., 2010; Suys et al., 2017). Each bead of CHOA molecules seems to be somehow interacting with water molecules. The layer of Na$^+$ ions around the OCO$^-$ beads is obvious. The carboxylate groups are completely solvated and placed further away from the rest of the CHOA molecules. This typical behavior of the CHOAs confirms their wedge-like presence on the micelle surface as repeatedly shown in the literature (S. J. Marrink & Mark, 2002; Sayyed-Ahmad et al., 2010; Turner et al., 2010). The presence of fatty acids did not affect the characteristic conformation of CHOAs on the micelle surface. However, the width of the RDD peaks of CHOA molecules exhibited some differences. The addition

of NA at fasted state resulted in broader RDD peaks, while any fatty acid exhibited the same effect at fed state. This broadness indicates the freedom of CHOA molecules on micelle surface to have different alignments. It is clearly seen that some of the beads (especially the ROH bead) even penetrated into the micelle cores. This indicates that, occasionally CHOAs have also adopted more perpendicular alignments on the micelle surface with increasing micelle size.

Table 3.4. The average distances (nm) of fatty acid and POPC palmitoyl and oleoyl tails

Distances (nm) /Micelles	Fatty acid tail (C1-C3/4)	POPC-palmitoyl tail (C1A-C4A)	POPC-oleoyl tail (C1B-C5B)
LA-Fa	0.835±0.014	1.191±0.037	1.428±0.057
SA-Fa	1.190±0.020	1.189±0.040	1.426±0.062
OA-Fa	1.117±0.028	1.179±0.058	1.399±0.091
NA-Fa	0.991±0.027	1.199±0.037	1.443±0.056
LA-Fed	0.837±0.011	1.200±0.032	1.447±0.049
SA-Fed	1.195±0.015	1.200±0.035	1.460±0.053
OA-Fed	1.129±0.017	1.201±0.030	1.450±0.046
NA-Fed	1.002±0.015	1.201±0.021	1.443±0.032

The investigation of the detailed structuring of POPCs within the micelles showed that the tail beads form the micelle core. However, incorporation of fatty acid molecules in the micelles seems to disorder the tail groups of POPCs resulting in the formation of a modest shoulder in the corresponding RDDs especially at fasted state. The reason that this effect is more apparent in fasted state micelles must be their smaller sizes; i.e., the FA molecules are able to occupy regions close to the core more readily with decreasing micelle size as shown by the corresponding RDDs. Among all the fasted state micelles incorporating FAs, the size of the formed shoulder is the smallest in LA-Fa micelle indicating that POPC tails are influenced the least from the presence of LAs. This is, of course, due to their shorter chain length. The effect of the incorporation of fatty acids on POPC tails can also be verified by POPC tail length calculations (Table 3.4). Shorter tail lengths of the POPC molecules at fasted state, especially for LA-Fa, SA-Fa and OA-Fa micelles, were due to the distraction of them by fatty acid molecules. Still, the POPC tail groups had the highest probability to be in
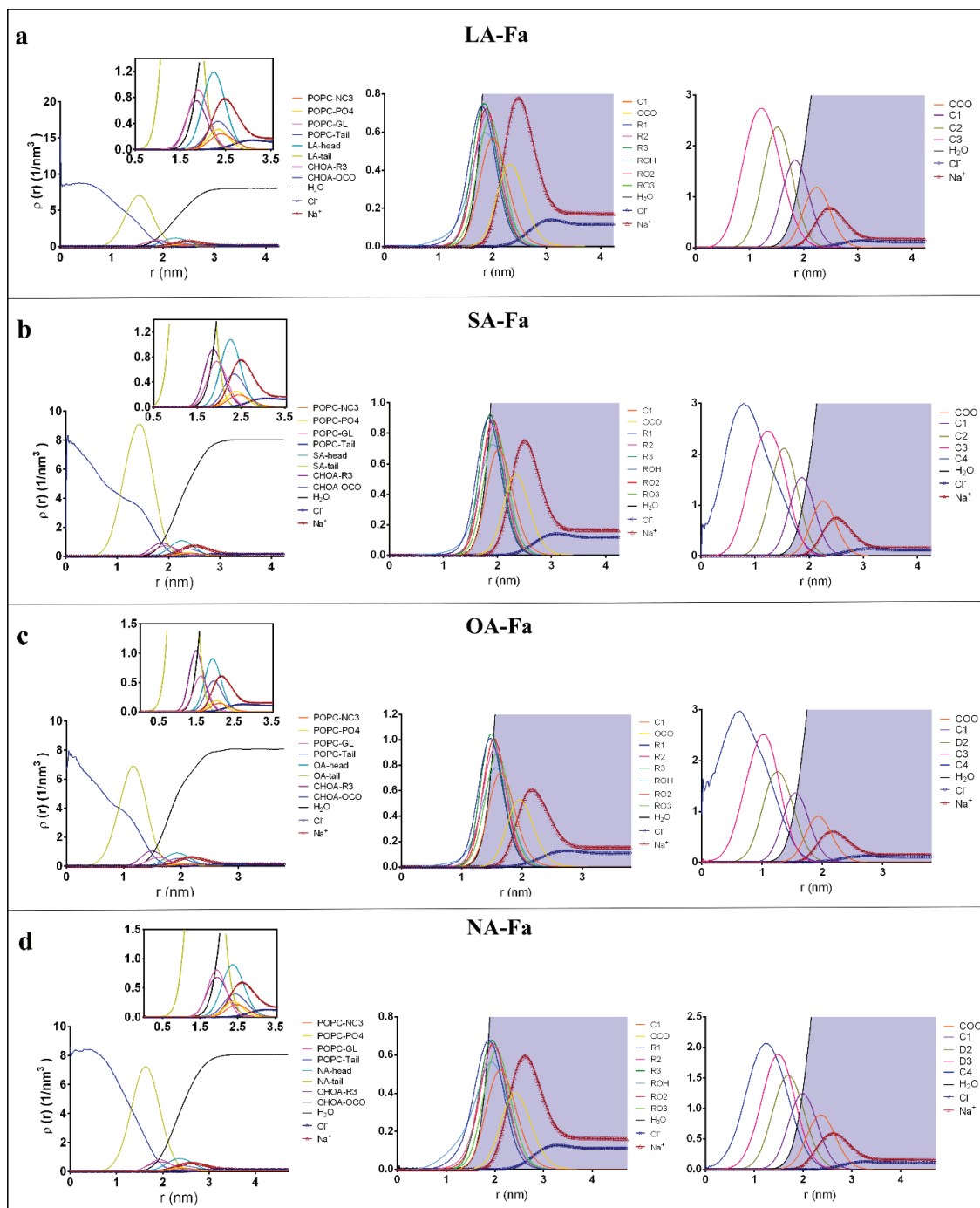
Figure 3.16. Radial density distributions (RDDs) ($\rho(r)$) of different moieties of the constituent molecules and ions with respect to the center of mass of the micelles for the (a) LA-Fa, (b) SA-Fa, (c) OA-Fa and (d) NA-Fa systems. RDDs of the specified moieties of CHOA (cholate), POPC and fatty acid molecules are given on the left. The close views of the interface regions are given in the insets, where all other beads except the OCO⁻ and R3 beads of CHOA and tail beads of POPC are omitted for clarity. The close views of the RDDs of the individual beads of CHOA and fatty acid molecules are given in the middle and on the right, respectively. RDDs of the surrounding Na⁺ (Δ), Cl⁻ (○) ions and water (-) molecules are included in both graphs
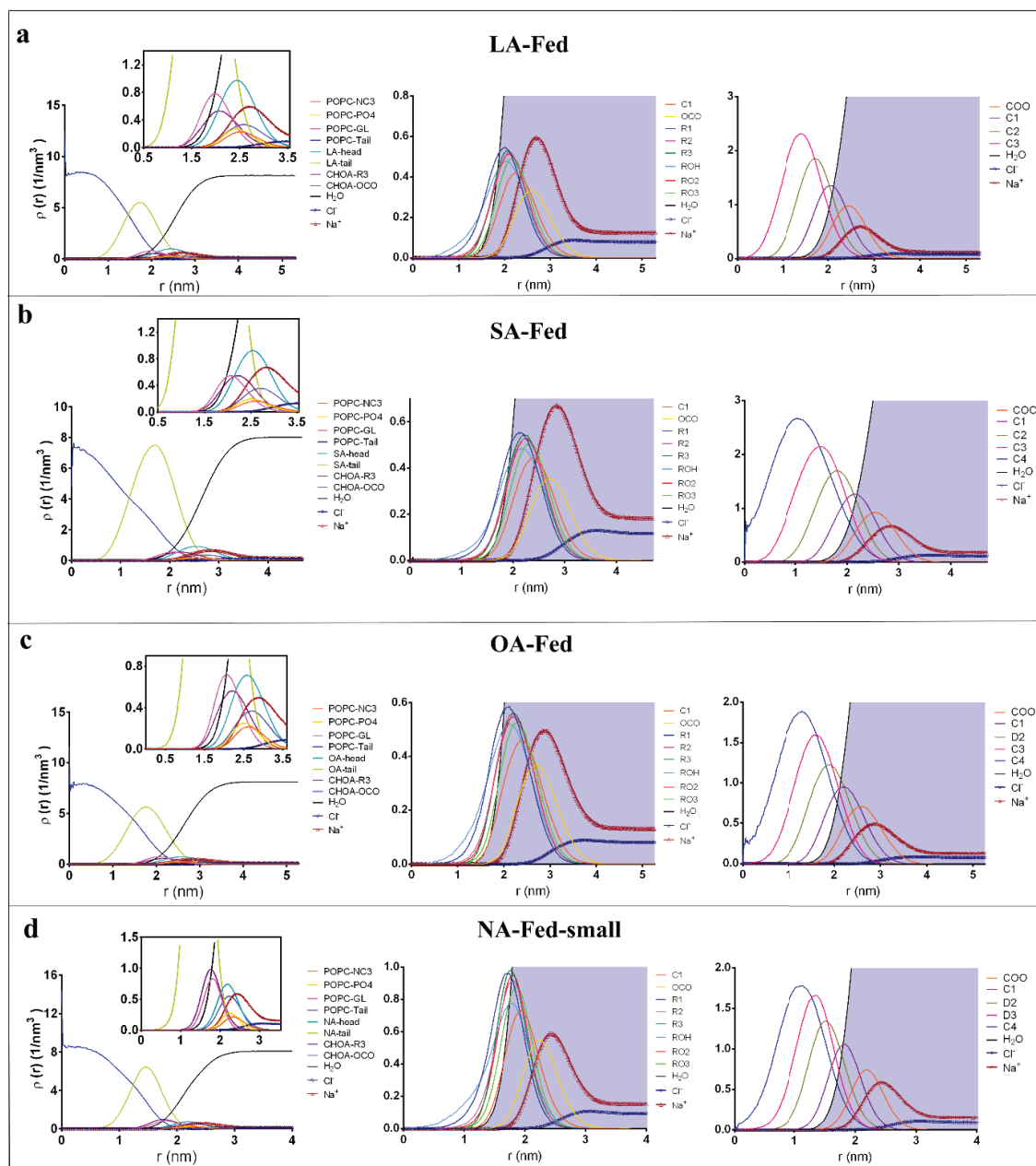
Figure 3.17. Radial density distributions (RDDs) ($\rho(r)$) of different moieties of the constituent molecules and ions with respect to the center of mass of the micelles for the (a) LA-Fed, (b) SA-Fed, (c) OA-Fed and (d) NA-Fed systems. RDDs of the specified moieties of CHOA (cholate), POPC and fatty acid molecules are given on the left. The close views of the interface regions are given in the insets, where all other beads except the OCO⁻ and R3 beads of CHOA and tail beads of POPC are omitted for clarity. The close views of the RDDs of the individual beads of CHOA and fatty acid molecules are given in the middle and on the right, respectively. RDDs of the surrounding Na$^+$ (Δ), Cl$^-$ (○) ions and water (-) molecules are included in both graphs

the micelle core which can be clearly seen from the cross-sectional pictures of the micelles also (Figure 3.13). Another observation is that the size dependence of micelle core density and the improved alignment of POPC tails disappeared with the incorporation of fatty acids. Instead, the presence of double bonds in the FA tails and the chain length seem to affect the core density and alignment of molecules. The system, LA-Fa has the highest core density (see Table 3.3). The more rigid structure of LA compared to other fatty acids used in the present study, due to its shorter chain length and saturated nature, resulted with increased density in the hydrophobic core of the micelle. For LA-Fed micelle, the increasing concentration decreases the core density because of having a larger size compared to micelles of fasted state. The increasing chain length and unsaturation level increase the volume per lipid in fasted and fed state situations. The POPC tail RDDs and core density results obtained by the volume per lipid calculations are correlated. In the angle results, the increasing angles between the vectors of POPC tail groups and micelle surface normal with decreasing core density support the above-mentioned situation.

According to the consecutive RDD results of individual fatty acid beads (right-hand side of Figure 3.16&17.a-d), independent of their concentrations, fatty acid molecules are placed in the micelles with their last tail beads pointing towards the micelle core. This type of arrangement of the fatty acid beads was reported before in the study of Turner at al. (2010a). The fourth tail bead, if present, is the closest one to the micelle center and occasionally placed in the core of micelles with SA and OA. The larger size of the NA-Fa micelle decreases the density of the molecules in the core. As a consequence, the probability of the last tail bead of NA at the micelle center is smaller compared to other micelles with fatty acids. The higher volume per lipid results for NA-Fa also supports that finding (Table 3.3.). Although the fatty acids were shown to be placed pointing towards the micelle core, their alignment in the core are further analyzed in section 3.3.2.3 by the help of angle results.

3.3.2.3. Internal and Surface Orientations of the Molecules

The internal and surface orientations of the constituent molecules were investigated by calculating average angles between selected vectors in a molecule. Type I: The angle between a vector which is formed by two selected beads on a molecule and

the radial vector (calculated as the vector from the com of the micelle to the midpoint of the selected beads' positions) (see inset of Figure 3.18-a); and, Type II: The angle between two vectors in a molecule denoted by 3 beads in total, of which the middle bead is the origin of both vectors and the remaining ones indicate their directions (see inset of Figure 3.18-b). The latter gives information about the conformations of the molecules within the micelles. Note that Type I angle calculations for the NA-Fed micelle were not conducted due to the micelle's highly unstable shape.

As shown with the RDD results given in the previous section, CHOA molecules are placed on the micelle surface similar to the CHOA+POPC micelles. To get detailed information about their alignment on the surface, the average angle between a specified vector on CHOAs and the radial direction was calculated. The two parts of CHOA molecules represented by the vectors from OCO$^-$ to RO3 and from RO3 to ROH were used to characterize the alignment of sterol backbone. The vectors of short tail (OCO$^-$-C1) and the hydroxyl end of the sterol body (R1-ROH) were calculated to gain further information about the orientation of CHOAs on the surface. Additionally, the vector of whole CHOA (OCO$^-$-ROH) was calculated. The results are given in Figure 3.18.a&c. First of all, the angle between the vector RO3-ROH and the radial vector range between 90 and 100^0, which proves the flat alignment of the sterol body on the micelles surface. The angles are larger compared to the systems without fatty acids (86-94^0). The smallest angle is observed for the systems OA-Fa and NA-Fed, which have the smallest sizes. By increasing micelle size, the angle also increases pointing to slightly more perpendicular alignments of CHOAs. The angle between the vector R1-ROH and the radial direction increases with increasing micelle size. Although the average angle results propose typically flat alignment of the CHOAs on the surface, both the histogram plots (Figure 3.19&20) and the RDD results show that different alignments are also possible. The second part of the CHOA molecules, (OCO$^-$-RO3 vector) seems to exhibit larger angles (125^0) with the radial vector compared to the micelles without fatty acids (120^0). This suggests the tilted orientations of CHOAs are still observed after the incorporation of fatty acids to the micelles. Moreover, the increased angles indicate slightly more perpendicular alignments of CHOAs on the surface, as proposed in RDD results. To further characterize this behavior, the angle between the short tails (OCO$^-$-C1) and radial vector was calculated. According to the results, the presence of fatty

acids also results in an increase in the protrusion of OCO⁻ beads from the surface (as the average angles are decreased from ~145 to ~139⁰).
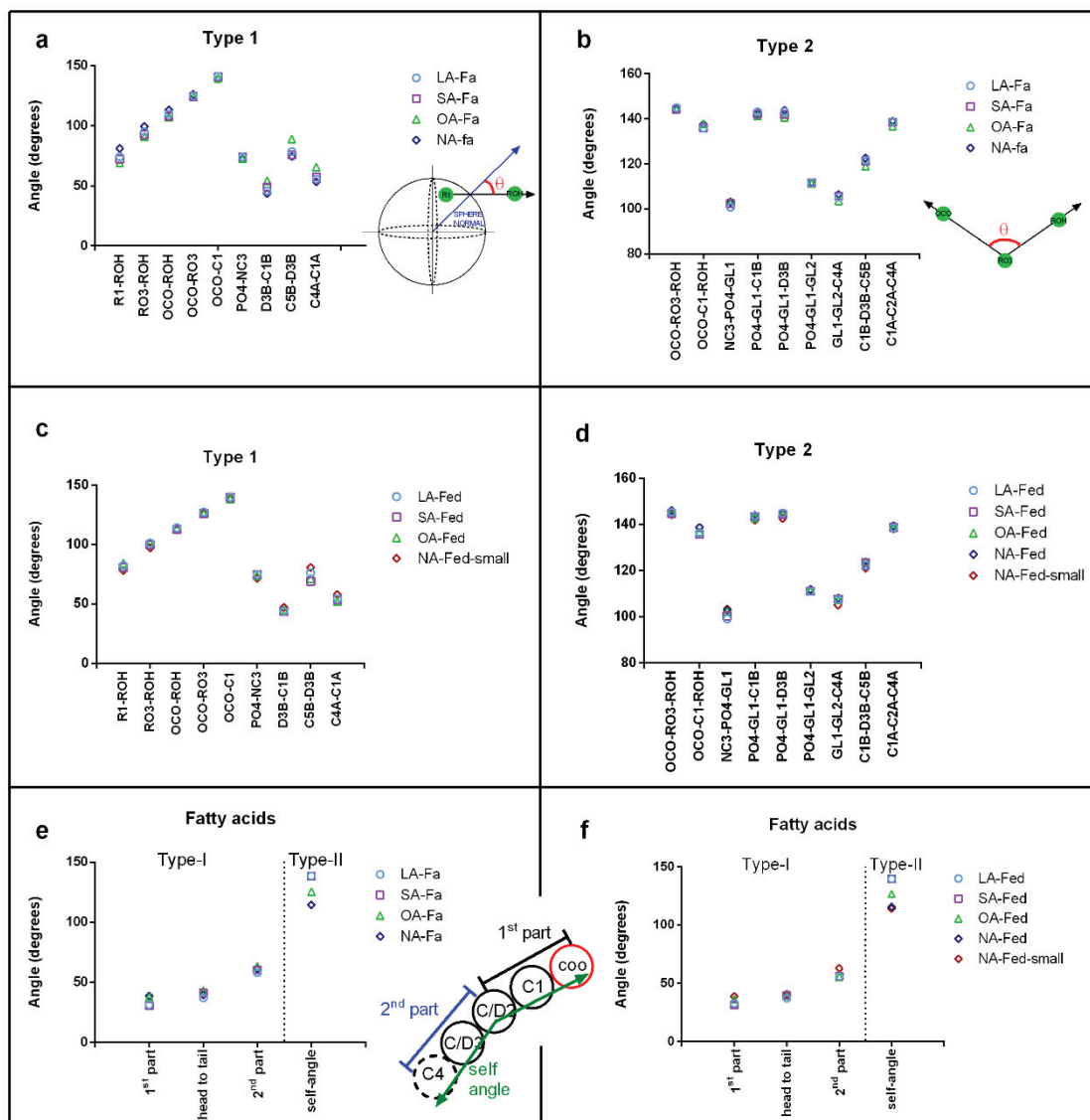
Figure 3.18. Type I average angles between a vector of two selected beads in a molecule and the local sphere normal (radial vector) at a) fasted and c) fed states. The origin of each vector is the first specified bead; hence the direction of each vector is from the first to the second specified bead. The local sphere normal is the vector which connects the com of the micelle to the midpoint of the selected beads' positions as shown in the inset of a. Type II average angles between two vectors in a molecule at b) fasted and d) fed states. The origin of each vector is the middle specified bead; hence the directions of the vectors are from the middle to the end beads as shown in the inset b. The Type I and Type II average angles of fatty acid molecules at e) fasted and f) fed states. The vectors on fatty acid molecules are shown in the inset e. The selected beads for angle calculations are given in x-axis (LA: ○, SA: □, OA: △, NA: ◇).

To examine the orientations of POPC molecules, Type I and II average angles for head and tail groups were analyzed separately. The results of Type I angle between the PO4-NC3 vector and the radial direction support the RDD results, which indicated the placement of these two beads almost flat on the surface. Compared to the systems without fatty acids (~68°) the larger angles observed for this vector in BS+PL+FA micelles (~74°) is the indicator of a more flattened conformation. Nevertheless, the histogram results show that a variety of conformations are sampled by the charged head groups of POPCs occasionally (Figure 3.19&20) independent of the micelle size or composition. The orientations of tail groups with respect to the radial direction are analyzed by the help of Figure 3.18.a-c. First of all, varying values of average angles for different parts of the tails prove that the micelle core is much less ordered compared to what was proposed in the classical idealized micelle models once more. The fluid interior of the micelles with different surfactants was reported to be disordered in the literature (S. J. Marrink & Mark, 2002; Turner et al., 2010). The angles between the tails and the radial direction show size-dependent behavior. The larger angle for the smaller micelles indicates more disordered alignment within the micelles. Despite the similar sizes of LA-Fa and SA-Fa micelles, the difference in the Type I angle results of POPC tail groups is obvious. Due to the shorter chain length LA, the packing of POPC tail beads within the LA-Fa micelles is less affected by the presence of FAs. Thus, the alignment of the POPC tails with the radial vector is better (smaller Type I angles) compared to the case in SA-Fa micelle. The extra tail bead of SA causes a disturbance in the packing of POPC tails within the core due to the increased steric effects. This is why the alignment of POPC tails with the radial direction is weakened (larger Type I angles) in the SA-Fa micelle. However, at fed state, the micelles grow in size and this effect disappears. These observations also support the interpretations made on the RDD results, which were based on the comparison of shoulders formed in the plots of POPC tail groups. Another observation is that the intramolecular angle in the oleoyl tail of POPCs is the smallest, which indicates a stronger kick within the tail, for the OA-Fa micelle while there are no significant differences for the remaining fasted state micelles. This is also supported by the average distance calculations for the oleoyl tails (Table 3.4.); i.e., the shorter oleoyl tail length in the OA-Fa micelle indicates a stronger kick within the tail. However, the fact that this effect disappears for the fed state micelles indicates that this is solely due to the micelle size. Therefore, one can say that the oleoyl

tails are able to sample wider conformations more freely as long as the micelle size is large enough so that there is enough space within the core.
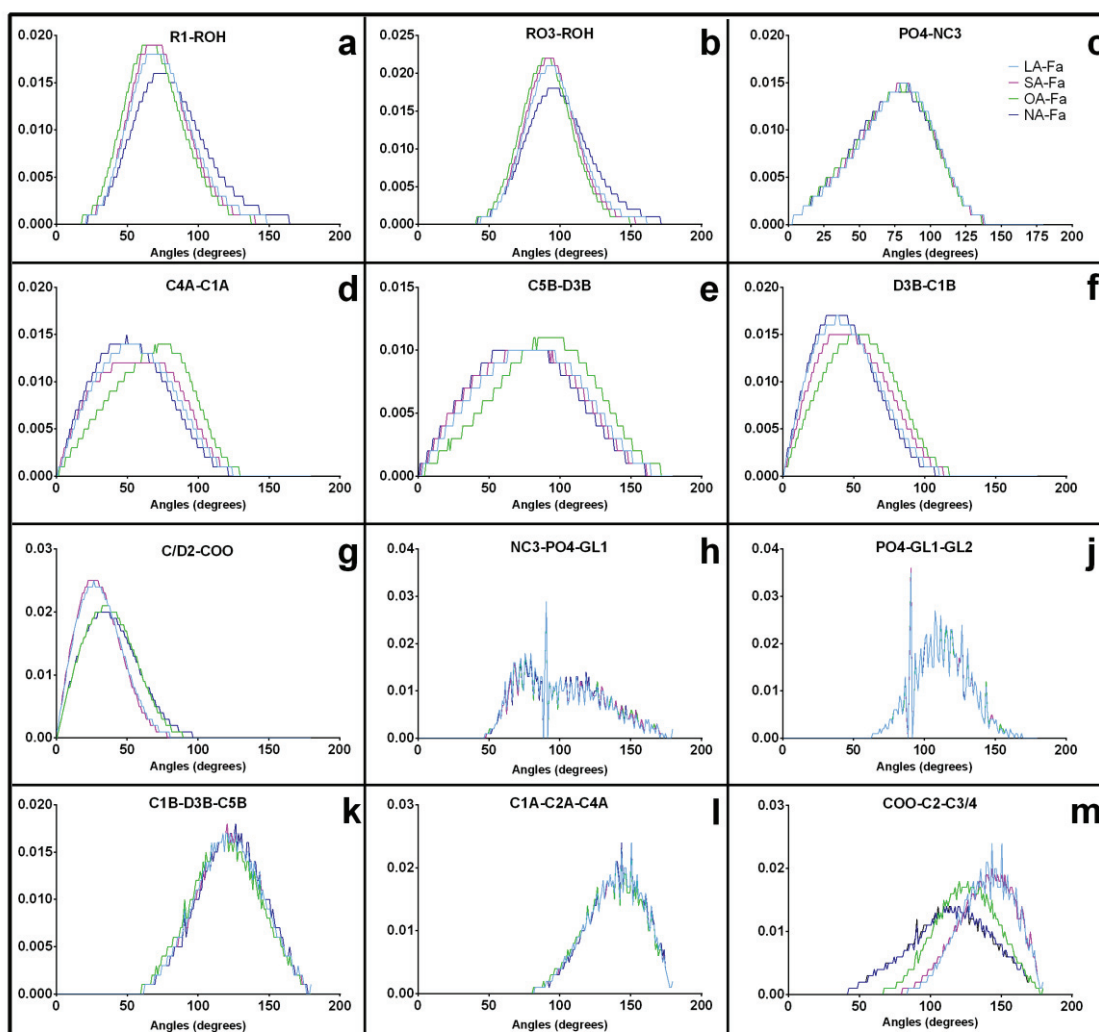
Figure 3.19. Selected Type I angle (a-g) distribution histograms for cholate, POPC and fatty acid molecules in different micelles at <u>fasted state</u>. The angles were calculated between a vector of two selected beads in a molecule and the local sphere normal. The origin of each vector is the first specified bead; hence the direction of each vector is from the first to the second specified bead. The local sphere normal is the vector which connects the com of the micelle to the midpoint of the selected beads' positions. Intramolecular (Type II) (h-m) angle distribution histograms for POPC and fatty acid molecules in different micelles at <u>fasted state</u>. The angles were calculated between two vectors in a molecule. The origin of each vector is the middle specified bead; hence the directions of the vectors are from the middle to the end beads.

Finally, the orientations of fatty acid molecules within the micelles was analyzed by the help of Figure 3.18.e and f. Type I angles were calculated for the whole, first and
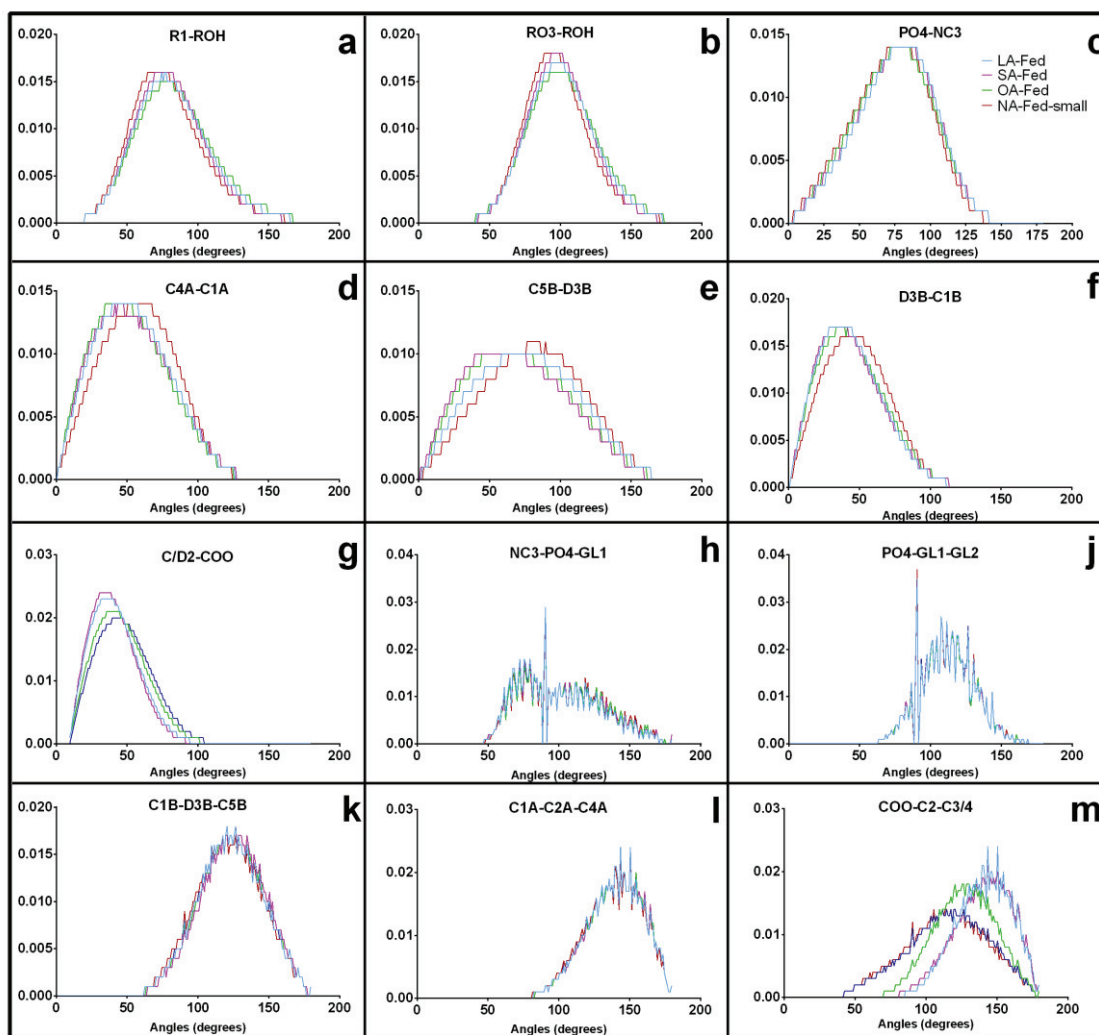
Figure 3.20. Selected Type I angle (a-g) distribution histograms for cholate, POPC and fatty acid molecules in different micelles at <u>fed state</u>. The angles were calculated between a vector of two selected beads in a molecule and the local sphere normal. The origin of each vector is the first specified bead; hence the direction of each vector is from the first to the second specified bead. The local sphere normal is the vector which connects the com of the micelle to the midpoint of the selected beads' positions. Intramolecular (Type II) (h-m) angle distribution histograms for POPC and fatty acid molecules in different micelles at <u>fed state</u>. The angles were calculated between two vectors in a molecule. The origin of each vector is the middle specified bead; hence the directions of the vectors are from the middle to the end beads.

the second part of the molecules. According to the results, the first parts of the fatty acids, which include the carboxylate group, are more weakly aligned with the radial direction in the OA-Fa, NA-Fa, OA-Fed and NA-Fed micelles due to the double bonds present in the fatty acids. This situation is more clearly observed in the corresponding histograms given in Figure 3.19 and Figure 3.20. The angles for the second parts of the

94

FA tails do not seem to exhibit different results for systems neither at fasted nor fed states. The effect of the double bonds on the FA tail conformations was also confirmed via Type II angles. As clearly seen from Figure 3.18.e&f, independent of the micelle size, as the degree of unsaturation increases, the intramolecular self-angle within the FA tail decreases. This is due to the increasing number of kicks within the FA tails with increasing number of double bonds resulting in a larger number of segments bending over themselves.

3.4. Conclusion

The aim of the third chapter of the dissertation was to characterize the self-assembly process and structural properties of the dietary mixed micelles in the presence of different types of fatty acids under both fasted and fed state concentrations. In order to observe the effect of fatty acid chain length, lauric acid and stearic acids were studied, while oleic acid and linoleic acids were studied to see the effects of degree of unsaturation.

The self-assembly process did not show any differences depending on the fatty acid type. The micellization started between any type of neighboring molecules. Initially, smaller micelles with varying fractions of constituent molecules dominated the systems. In the course of simulations, larger micelles with more similar compositions were formed via fusion of smaller ones. Similar to the mixed micelles of CHOA and POPC, once the phospholipid molecules were solubilized within the micelles, they never left them. However, fatty acid molecules occasionally left mixed micelles and joined to the unsteady small aggregates. The exchange of CHOA molecules between the micelles and the surrounding media existed throughout the trajectories. Together with the exchange of FA molecules, they were responsible for the broadness of aggregation numbers of the micelles. The exchange of the molecules was more frequent and larger in number under the fed state concentrations.

The structural properties of the micelles were affected by the addition of fatty acids. The micelles became swollen by the incorporation of FAs, except for the micelle with oleic acid at fasted state. The correlation between the micelle size and fatty acid characteristics was not clear at fasted state. However, micelle sizes increased with increasing chain length and degree of unsaturation at fed state as suggested in the

experimental studies. Indeed, the micelle with linoleic acid at fed state underwent shape transitions and a rod-like micelle coexisting with a smaller spheroidal micelle was obtained eventually. In contrast to the case in micelles of CHOA+POPC, the Phi/Pho ratio decreased with increasing micelle size in the presence of different fatty acids. The incorporation of fatty acids in the mixed micelles resulted in more ellipsoidal shapes when compared to the micelles composed only of CHOAs and POPCs. The higher lipids concentration under fed state also increased the degree of ellipticity. On the other hand, fatty acid characteristics did not have an impact the micelle shapes except the rod-like micelle incorporating NA at fed state.

The internal structures of the mixed micelles were investigated via RDD and specific angle calculations. General aspects of the morphologies were found to be similar regardless of concentration of the type of fatty acids. The micelle cores were occupied by POPC tails like in CHOA+POPC micelles. The incorporation of fatty acids to the micelles disturbed the POPC molecules, especially when the micelle size was smaller. POPC molecules became more relaxed in the core with increasing micelle size. The charged groups of fatty acid molecules were placed on the micelle surface and their tails pointing through the micelle core. Still they were not parallel to the radial axis. The most important factor affecting the alignments of POPC and fatty acid molecules in the core was the micelle size. Also, fatty acid characteristics affected the alignment of these molecules in the core. The increased chain length and number of double bonds resulted with more disordered alignment of the FA tails through the radial direction. The surface morphology was also affected by joining of fatty acid molecules. Charged POPC head groups became more flattened on the surface while the glycerol moieties were more shifted towards water. CHOA molecules were slightly more perpendicular on the surface compared to CHOA+POPC micelles and as the micelle size increased, they became more perpendicular. The protrusion of the OCO^- beads from the surface was also increased due to the size effects. Therefore, their mashie-like structure was preserved. The ionic double layer composed of Na^+ and Cl^- ions was also present around the surface.

CHAPTER 4

SOLUBILIZATOIN OF *β*-CAROTENE IN DIETARY MIXED MICELLES IN THE PRESENCE OF DIFFERENT TYPES OF FATTY ACID

4.1. Introduction

Carotenoids are natural colorants that are responsible for the yellow to deep-red colors in nature. More than 700 types of carotenoids have been identified. (Maiani et al., 2009). The main food sources of carotenoids are yellow and orange fruits and vegetables and dark-green, leafy vegetables. Almost 50 types of carotenoids are consumed by humans and can be metabolized within the body. The main carotenoids found in human blood are *β*-carotene, *β*-cryptoxanthin, *α*-carotene, lycopene, lutein, and zeaxanthin (Maiani et al., 2009; O'Neill et al., 2001). Because of its extensive consumption by humans, its many health benefits, and its wide use as a supplement, *β*-carotene was chosen as a representative carotenoid in the present study.

β-carotene molecules are dicyclic fat-soluble pigments that are formed by covalently bonded isoprene units ($C_{40}H_{56}$). The two *β*-ionone rings at the ends are responsible for the vitamin A activity of *β*-carotenes. In addition to their vitamin A activity, they are important for their antioxidant properties. The double bonds in their structures behave as singlet oxygen quenchers and free radical scavengers; they protect cell membranes from the damages of free radicals (Rao & Rao, 2007; Smolin & Grosvenor, 2007). In the literature, they are reported to have protective effects on certain types of cancers, such as lung, prostate, cervical, stomach, pancreatic, and colorectal (Betz et al., 2010; Namitha & Negi, 2010). Additionally, their intake prevents eye diseases and vision weakness due to macular degeneration and cataracts (Betz et al., 2010; Smolin & Grosvenor, 2007).

Despite the many health benefits of *β*-carotene molecules, the bioavailability of *β*-carotene molecules in the human body is limited due to their hydrophobic structure. The steps *β*-carotene molecules follow to become bioavailable begins with their release

from the food matrix. They then join the mixed micelles in the small intestine. The intestinal cells absorb carotenoids as solubilized in dietary mixed micelles. In the intestinal cells, *β*-carotenes join to the structure of chylomicrons. The secreted chylomicrons transport the carotenoids to the blood (Desmarchelier & Borel, 2017; O'Sullivan et al., 2008). Therefore, solubilization of *β*-carotenes in the mixed micelles of the small intestine called as a key step that affects their bioavailability.

In the literature, the presence of lipids in the media is reported to promote the bioavailability of *β*-carotene. Lipids enhance the bioavailability in several ways. First, they provide a media for the solubilization of *β*-carotenes after their release from the food matrix. Second, they stimulate the secretion of bile and lipases from the liver, contributing to mixed micelle formation. Third, the increased amount of fat in the food matrix postpones the gastric emptying and increases the rate of lipid digestion. Consequently, the liberation of lipid digestion products increased with the increase of the solubilization rate in mixed micelles with other lipophilic particles in the media. Fourth, the uptake of lipid digestion products by enterocytes stimulates the assembly and basolateral secretion of chylomicrons for the transfer of lipophilic particles, such as *β*-carotenes to lymph (Kopec & Failla, 2018). According to the perspective of the present thesis, the effects of fatty acids on dietary mixed micelles and the solubilization of the *β*-carotenes within them were under question.

The experimental studies widely investigated the effects of lipids with different characteristics on the bioavailability of *β*-carotenes. In the in vitro studies, scientists usually added oils with selected characteristics to the food matrix and applied in vitro digestion methods to the samples. Then they determined the amount of micellized *β*-carotene, (i.e., bioaccessibility). One study investigated the effect of triglycerides and different types of fatty acids on *β*-carotene bioaccessibility. The study reported that the presence of triglycerides increased the amount of micellization. The short-chain fatty acids did not significantly affect the bioaccessibility, but medium- and long-chain saturated and unsaturated fatty acids had promoting effects. The C12-16 fatty acids were found less effective on bioaccessibility by increasing chain lengths due to their increased melting points (which are hotter than 37ºC). The unsaturated fatty acids had more positive effects than saturated ones. Even so, the increasing unsaturation level for long-chain (18C) fatty acids was reported as decreasing the bioaccessibility of *β*-carotenes (Nagao et al., 2013). The lower efficiency of polyunsaturated fatty acids was

reported in other studies (R. Lakshminarayana, Raju, Keshava Prakash, & Baskaran, 2009; Rangaswamy Lakshminarayana & Baskaran, 2013). Similarly, Huo et al. (2007) confirmed the greater positive effect of long-chain triglycerides on bioaccessibility and unsaturation, while no significant difference was reported between mono- and poly-unsaturated fatty acids. The studies that tested fat and vegetable oils reported higher bioaccessibility for the oils rich in unsaturated fatty acids (Chitchumroonchokchai, Schwartz, & Failla, 2004; Failla et al., 2014).

Although some studies reported that increasing triglyceride amounts increased the bioaccessibility of β-carotenes, some in vivo and in vitro studies showed that excess lipid may be unnecessary. The bioavailability was reported to be enhanced by the addition of lipids to the media, but no significant difference was observed between samples containing low and high fat (Hedrén et al., 2002; Hornero-Méndez & Mínguez-Mosquera, 2007; Roodenburg, Leenen, Hof, Weststrate, & Tijburg, 2000). Conflicting results were also reported that claimed a greater amount of fat is necessary to increase the bioavailability (Brown et al., 2004). The different experimental conditions, the lipid types and amounts used, the different contents and amounts of the food matrix, or the discrepancies related to the host may be the reason for the contradictions.

The incorporation of β-carotenes to edible excipient emulsions, or nanoemulsions, is a common method used for increasing bioaccessibility. The effects of different types of lipids present in the nanoemulsions also have promoting effects on β-carotene bioaccessibility. The use of long-chain triglycerides in the nanoemulsions was reported to have more significant effects on increasing the micellization of β-carotenes compared to the use of medium-chain triglycerides (Liu et al., 2015; Qian, Decker, Xiao, & McClements, 2012; Salvia-Trujillo, Qian, Martín-Belloso, & McClements, 2013).

The studies investigating the effects of different lipid types on the bioavailability of β-carotenes provide valuable information. A consistent finding is that the micellization of β-carotenes is a key step for its bioavailability. Although able to define the important factors that affect this phenomenon, experimental studies remain insufficient for explaining the mechanism behind the solubilization process and the detailed investigation of formed micelle structures. Therefore, we investigated the solubilization of β-carotenes in dietary mixed micelles at the molecular level with

molecular dynamics simulations. Among the various possibilities, the fatty acids with different unsaturation levels and chain lengths were selected for testing at different concentration levels representing fasted and fed states in the duodenum. To avoid complications from human metabolisms and food-related differences, all the lipids assumed to underwent lipolysis, which results in the presence of fatty acids in the media. In the third part of the thesis study, we placed β-carotene molecules in the media that contained pre-formed mixed micelles. By doing so, we eliminated the factors related to the release of the β-carotene from the lipid phase in the digestive system.

4.2. Methods

In the methods section, firstly the system details are given. Then the simulation procedure is explained in detail. the analysis methods. The methods used for the analyses are the same as described in Chapter 2 (see Section 2.2.3).

4.2.1. System Details

The solubilization of β-carotene molecules was investigated using pre-formed selected micelles (see chapter 3). The selected micelles were comprised of POPC, cholate, and fatty acid molecules at fasted and fed state physiological conditions. To see the effect of the fatty acid type on the solubilization of β-carotene molecules, fatty acids with different chain lengths and unsaturation levels were used (e.g., lauric (12:0), stearic (18:0), oleic (18:2), and linoleic (18:3) acids). The micelles that had the highest cumulative probability after the equilibration of the systems were selected for analysis in chapter 2. The subjected selected micelles were transferred to a smaller simulation box. The box volume was chosen considering the sizes of the selected micelles. To avoid the side effects of periodic boundary conditions and to prevent structures interacting with their mirror images, a box size larger than the diameter of micelles plus the double of long-term interaction cutoff (1.2 nm) was used as suggested in GROMACS manual (Apol et al. 2010). Additional CHOA molecules were included to maintain the intermicellar concentration in the original simulation boxes. The determined numbers of β-carotene molecules were included in the boxes (see section 4.3.1). The required amount of Na^+ and Cl^- ions were used to achieve the 150 mM NaCl concentration and neutralize the systems. Finally, the systems were solvated using

Martini water molecules. The number of constituent molecules present in each system and the selected micelles are in Table 4.1. One, two, or three *β*-carotene molecules were added to each simulation box.

Table 4.1. Number of molecules for each simulation box and micelle

	Number of molecules in the micelle				Number of free molecules in the system				Box volume ($\sim nm^3$)
	CHOA	POPC	FA	Total	CHOA	Na$^+$	Cl$^-$	Water	
LA-fa	20	12	48	80	2	190	120	11124	1425
SA-fa	23	10	41	74	2	222	156	14191	1805
OA-fa	15	5	24	44	1	130	90	8737	1110
NA-fa	24	12	48	84	3	251	176	14097	1810
LA-fed	29	16	71	116	5	195	90	8555	1140
SA-fed	33	13	75	121	10	431	313	17516	2280
OA-fed	38	18	66	122	13	393	276	19459	2510
NA-fed	81	38	162	281	27	797	527	43570	5600

The coarse-grained (CG) MARTINI Force Field was used in the simulations. The previously proposed models for POPC and CHOA molecules (Siewert J Marrink et al., 2007; SJ Marrink, 2004) were adopted for this study. POPC and CHOA are represented by 13 and 8 beads, respectively. There are two charged beads on the POPC head group representing the choline and the phosphate groups. Two beads of intermediate hydrophilicity are used to represent the glycerol ester moiety, and the remaining nine beads are hydrophobic tail beads. CHOA is modeled by six beads, mapped on a 3:1 basis, forming the sterol body and two beads representing the short tail, including the charged COO$^-$ group. Previously described models were used for lauric and stearic acids. Coarse-grained medium- and long-chain fatty acid molecules were modeled by four and five Martini beads, respectively. They consisted of one charged head group (COO$^-$) and three and four hydrophobic tail groups for LA and SA, respectively. Unsaturated fatty acid molecules, oleic and linoleic acids, were modeled using the hydrocarbon tails of DGDG (16:0-18:1-digalactosyl diacylglycerol) and DUPC (1,2-dilinoleoyl-sn-glycero-3-phosphocholine), respectively (de Jong et al., 2015). Therefore, the head group parameters of stearic acid were applied to the head groups of oleic and linoleic acids, as proposed in the literature (Janke et al., 2014;

Risselada & Marrink, 2008). The previously provided model for *β*-carotene molecules was used in the present study (de Jong et al., 2015; Van Eerden et al., 2017). According to this model, the *β*-carotene molecule was represented by 10 Martini beads. The three beads were in ring structures at both ends of the molecule and connected by four intermediate beads, preserving the characteristic symmetrical structure. For the head groups, 3:1 mapping was applied while 4:1 mapping was used for intermediate particles. A coarse-grained *β*-carotene molecule can be found in Figure 4.1. CG water molecules are comprised of four real water molecules and the CG beads of single atom ions are represented with their first hydration shell.
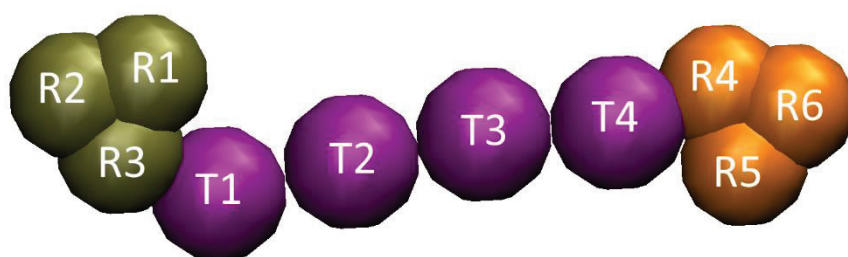
Figure 4.1. Coarse-grained structure of the *β*-carotene molecule. Olive-green and orange beads representing two head groups, purple beads are representing the intermediate beads.

4.2.2. Simulation Procedure

The selected micelles from chapter 3 of the study were placed in smaller simulation boxes. After random placement of required amounts of *β*-carotene and other constituent molecules, the systems were solvated by Martini water molecules. Next, a small energy minimization and pressure equilibrations were performed, as described in chapter 2. After the systems were pressure equilibrated to the desired volumes, production runs were conducted (see 2.2.2 and 2.2.3). The systems were run for at least 5 μs, including equilibration and production runs. The micelles that were stable for the longest time after the equilibration were chosen for structural analysis. The time frames containing the selected micelles were extracted. At least 1.5 μs trajectories were collected for each system, except for the systems with NA at fed state. The highly dynamic nature of the subjected micelles prevents the collection of the desired amounts of trajectories and at least ~500 ns time frames were collected for those micelles. If the runs did not allow collection of the desired amount of trajectory, the simulations were extended. The extracted time frames were then concatenated, and these final trajectories

were used for structural analysis such as radii of gyration, solvent accessible surface area, and radial density distributions.

4.3. Results and Discussion

In the results and discussion section, firstly evolution of the micellization in presence of different fatty acid molecules and different number of BCRs are explained. Following that the structural characterization of the selected mixed micelles are investigated.

4.3.1. Addition of *β*-carotene Molecules to the Systems

Due to *β*-carotenes' highly hydrophobic nature, their solubilization in polar solvents is highly restricted. Therefore, the amount to add to the simulation media is important. To decide the proper number of *β*-carotenes to involve, preliminary simulations were performed for all systems. In those simulations, varying amounts of up to 50 molecules of *β*-carotene were added to the systems. The simulations were performed at least for 3 μs as described in section 2.2.2. The preliminary simulations showed that all *β*-carotene molecules were incorporated into micelles, regardless of the amounts. Incorporation of hydrophobic *β*-carotene molecules into the micelles was thermodynamically the most favorable situation due to the lack of other lipophilic media. This result gave us valuable information about their solubilization within intestinal mixed micelles. If there were no other lipophilic media in the small intestine, the *β*-carotene molecules preferred to join mixed micelle structures despite their high concentrations. In the literature it is reported that *β*-carotene molecules are more readily solvated in undigested lipid particles before joining the micelles (Gleize et al., 2013). Therefore, it can be concluded that the complete digestion of lipids after consumption greatly affects *β*-carotene bioaccessibility. The food matrix also affects the extent of lipid digestion with the release of *β*-carotene molecules, as suggested in the literature (Borel, 2003; Desmarchelier & Borel, 2017; Gleize et al., 2013; Parker, 1996). The presence of lipids in the media is reported to enhance the bioaccessibility of *β*-carotenes by delaying gastric emptying. The longer durations were stated to increase the release of fatty acids and bile, and consequently increased *β*-carotene solubilization within the mixed micelles (Kopec & Failla, 2018). Additionally, the necessity of *β*-carotene

molecules to come in contact with mixed micelles for solubilization was reported in the literature (Gleize et al., 2013). Due to the small sizes of the simulation boxes, the solubilization occurred quickly. Although there was only one micelle in the systems, it is clear that an increased amount of mixed micelles would enhance β-carotene solubility by both increasing the probability of contact with mixed micelles and increasing the solubilization capacity.

After the solubilization of all β-carotene molecules in the mixed micelles, the maximum number of β-carotene molecules that did not dramatically change the number of free CHOA molecules was decided to be used because the number of free CHOAs in the media was limited, and there were only single mixed-micelle structures in the systems. It is important not to alter the equilibrium between the free CHOAs and the ones in mixed micelles to avoid misleading results. For that purpose, the average number of free CHOA molecules in the systems after the incorporation of β-carotenes into the micelles was calculated. The average CHOA molecules were compared to the free CHOA molecules at the beginning of the simulations, which represent the inter-micellar concentration in original simulation boxes from Chapter 3. The results are given in Figures 4.2 and 4.3 for fasted and fed state systems, respectively. The common number that did not have a significant effect was chosen as the maximum and was equal to 3 considering the standard deviations of the number of free CHOA molecules (see Figures 4.2 and 4.3). The number of free CHOA molecules could not be preserved in the system with NA at fed state due to the highly unstable nature of these micelles. The micelles were divided at some time steps, and at those points the free CHOA molecules in the media attached to the surfaces of the divided micelles to shield the hydrophobic core of the micelles from the water. As a consequence, the free CHOA concentration in the media was reduced. One, two, and three β-carotene molecules were added to investigate their solubilization in the micelles before division.

Figure 4.2. Average number of free CHOA molecules in the systems with different fatty acids for different numbers of *β*-carotene molecules <u>at fasted state</u>. The red lines are representing the required number of free CHOAs to maintain the intermicellar concentrations in original simulation boxes.
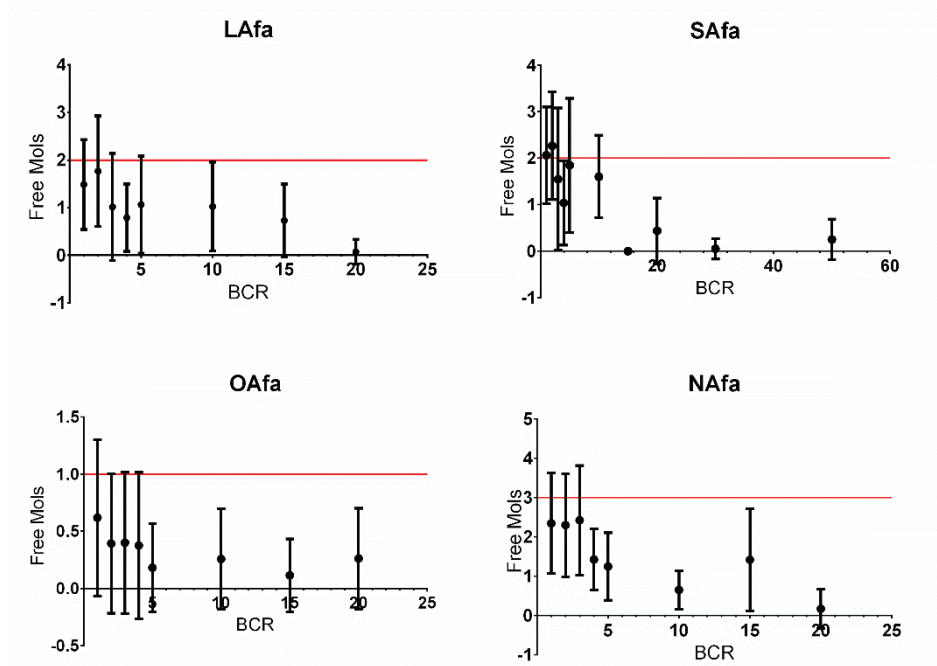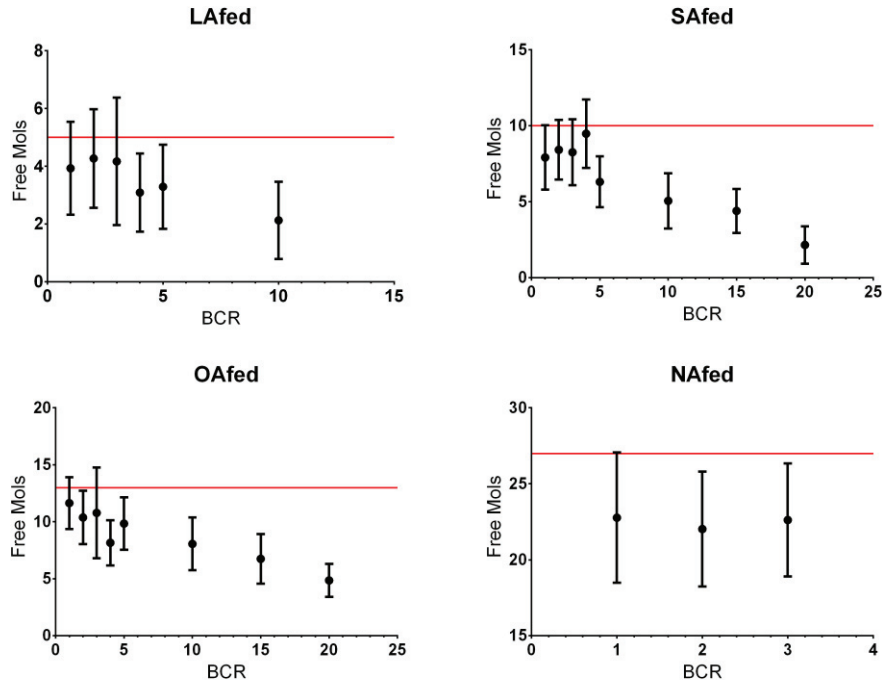

Figure 4.3. Average number of free CHOA molecules in the systems with different fatty acids for different numbers of *β*-carotene molecules <u>at fed state</u>. The red lines are representing the required number of free CHOAs to maintain the intermicellar concentrations in original simulation boxes.

4.3.2. Equilibration of the Systems

β-carotene molecules were incorporated into the micelle structures quickly due to their hydrophobic nature and the small size of simulation boxes. The solubilization process began from any beads of BCR molecules. The closest head or intermediate bead to the mixed micelles started to interact with the molecules on the surface. After this, BCRs moved through the micelle core. In the presence of multiple BCR molecules, they joined to the micelles either separately or together. In the latter case, they formed small aggregates in the solvent phase and then were incorporated into the micelles. After the solubilization of all BCRs into the mixed micelles, the equilibration points of the systems were analyzed. For this purpose, the time dependent radial distribution functions (RDF) of the selected groups in the micelles were calculated. Due to their highly hydrophobic nature, BCRs were expected to be placed in the hydrophobic core of the micelles and to interact with the tail beads of POPC and fatty acid molecules. (This is proved by the structural analysis of the micelles. See section 4.3.4.) Therefore, RDFs of head groups of BCRs (R1, R2, R3, R4, R5, and R6) with respect to the last tail beads of POPC (C5B) and fatty acid (C3/4) molecules were calculated. The RDF results were expected to be similar for different time spans when the systems were stabilized. According to the results, systems were equilibrated quickly following the incorporation of all BCRs. The only observed difference was in the first 500 ns of the trajectories for all systems at fasted and fed states. The quick equilibration was due to the addition of small amounts of BCRs and the use of pre-equilibrated micelles from the previous steps. Since the results were the same for all systems, the RDF plots are shown for only the systems containing three BCRs with different fatty acids in Appendix 3 and 4 for systems at fasted and fed states, respectively. Thus, the structural analyses of the micelles were conducted over the trajectory excluding the first 500 ns following the incorporation of all BCRs into the micelles.

4.3.3. Selection of the Micelles

The selection of micelles was done using cumulative probability distribution results. The cumulative probability distributions of the micelles provided information about the frequency of existence of micelles throughout the simulations. The micelles with the highest probability of occurring after the equilibration of the systems were

chosen for further structural analyses. The probability plots for all the systems are shown in Appendices 5–10. According to the cumulative probability plots, the number of molecules in the micelles changed during the trajectory. This was mainly due to the exchange of CHOA molecules with the surrounding media. Fatty acid molecules rarely left micelles, but if they did, they immediately turned back to the micelle structures. Simulations belonging to some of the systems were extended until the required amounts of time frames (adding up to 1.5 µs) were collected.
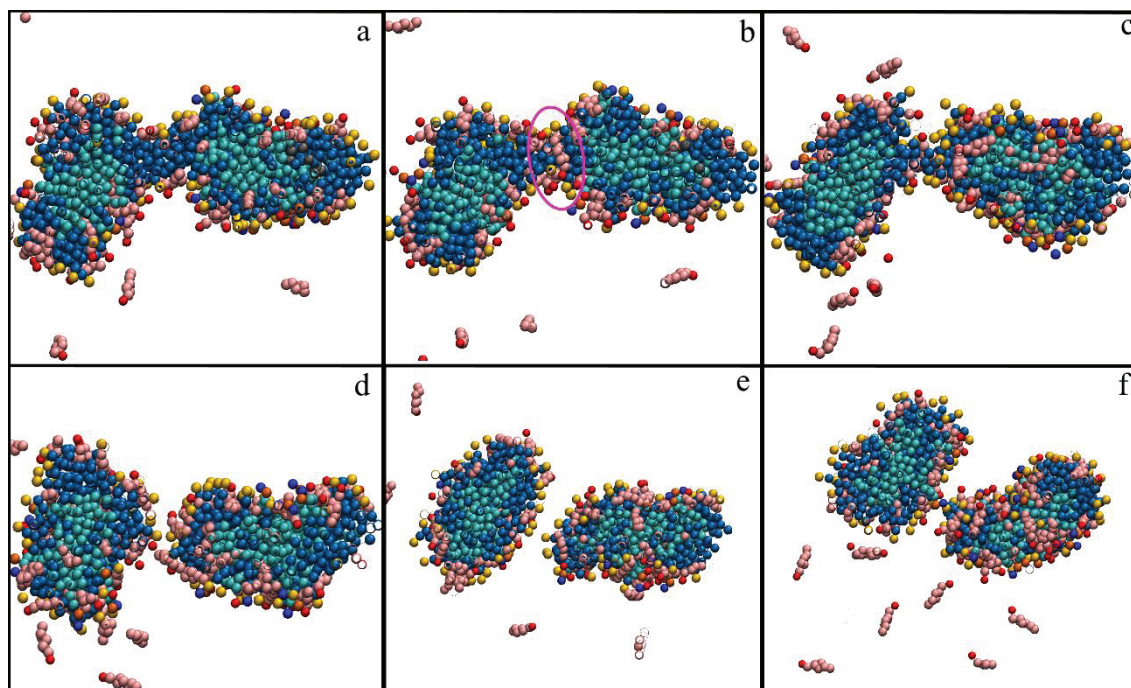
Figure 4.4. Detailed cross-sectional snapshots describing the division process for micelle with linoleic acid and one *β*-carotene molecule at fed state. a, b, c, d, e and f are the consecutive snapshots of the division process. The circle in b) shows the incorporation of the cholates to the thinner part of the micelle. Head and other groups of CHOA molecules are colored in red and pink; the NC3, PO4 and tail beads of POPCs are colored in blue, orange and cyan; head and tail beads of linoleic acid are colored in yellow and dark blue, respectively. Water and ions are not shown for clarity.

The systems with NA at fed state showed different behavior compared to the other systems. The highly unstable and larger micelles in those systems were divided into two at some time steps. The details of the division process can be seen from the cross-sectional snapshots of the micelles in Figure 4.4. Before the division, POPC molecules were separated into two different regions in the micelle structure, and the micelle became thinner at the point where fatty acid molecules are mostly present

(Figure 4.4.a). The CHOA molecules then started to join to the thinner part of the micelle as shown with a circle in Figure 4.4.b. Next, the fatty acid molecules moved away from each other (Figure 4.4.d), and the separation occurred (Figure 4.4.e). The micelles either stood apart (Figure 4.4.f) or interacted with each other throughout the trajectory. This process usually ended with the fusion of two smaller structures. Therefore, the formed smaller micelles were not stable and were not chosen for further structural analysis despite their high cumulative probabilities.

Table 4.2. The compositions of the selected micelles for further analysis in the presence of different numbers of β-carotene molecules at fasted and fed states

	LA-Fa			SA-Fa			OA-Fa			NA-Fa		
	1	2	3	1	2	3	1	2	3	1	2	3
CHOA	20	21	21	23	23	24	16	16	16	25	25	25
POPC	12	12	12	10	10	10	5	5	5	12	12	12
FA	48	48	48	41	41	41	24	24	24	48	48	48
BCR	1	2	3	1	2	3	1	2	3	1	2	3
Total lipid	61	62	63	52	53	54	30	31	32	61	62	63
Lipid/CHOA	3.05	2.95	3.0	2.26	2.30	2.25	1.88	1.94	2.00	2.44	2.48	2.52
TOTAL	81	83	84	75	76	78	46	47	48	86	87	88
	LA-Fed			SA-Fed			OA-Fed			NA-Fed		
	1	2	3	1	2	3	1	2	3	1	2	3
CHOA	29	30	31	34	35	34	39	41	40	80	84	84
POPC	16	16	16	13	13	13	18	18	18	38	38	38
FA	71	71	71	75	75	75	66	66	66	162	162	162
BCR	1	2	3	1	2	3	1	2	3	1	2	3
Total lipid	88	89	90	89	90	91	85	86	87	201	202	203
Lipid/CHOA	3.03	2.97	2.90	2.62	2.57	2.68	2.18	2.09	2.18	2.51	2.40	2.42
TOTAL	117	119	121	123	125	125	124	127	127	281	286	287

The micelles chosen for further structural analyses are listed in Table 4.2 with their compositions. The representative cross-sectional snapshots are in Figure 4.5. The only change was observed in the number of CHOA molecules present in the micelles. At fasted state, incorporation of a single BCR molecule to the micelle did not affect micelle composition. However, two and three BCR molecules increased the volume of the hydrophobic core to a point at which the CHOAs were not enough to cover the

micelle surface. Therefore, one additional CHOA molecule joined to the micelle structure. The need for extra CHOA was seen when three BCR molecules were added to the micelles of SA-Fa. Due to the larger chain length of stearic acid, the micelle size was greater than the LA-Fa micelle, and hence the micelles could tolerate two BCR molecules without changing their compositions. For the micelles of OA-Fa and NA-Fa,

	LA-Fa	SA-Fa	OA-Fa	NA-Fa
1BCR				
2 BCR				
3 BCR				
	LA-Fed	SA-Fed	OA-Fed	NA-Fed
1BCR				
2 BCR				
3 BCR				
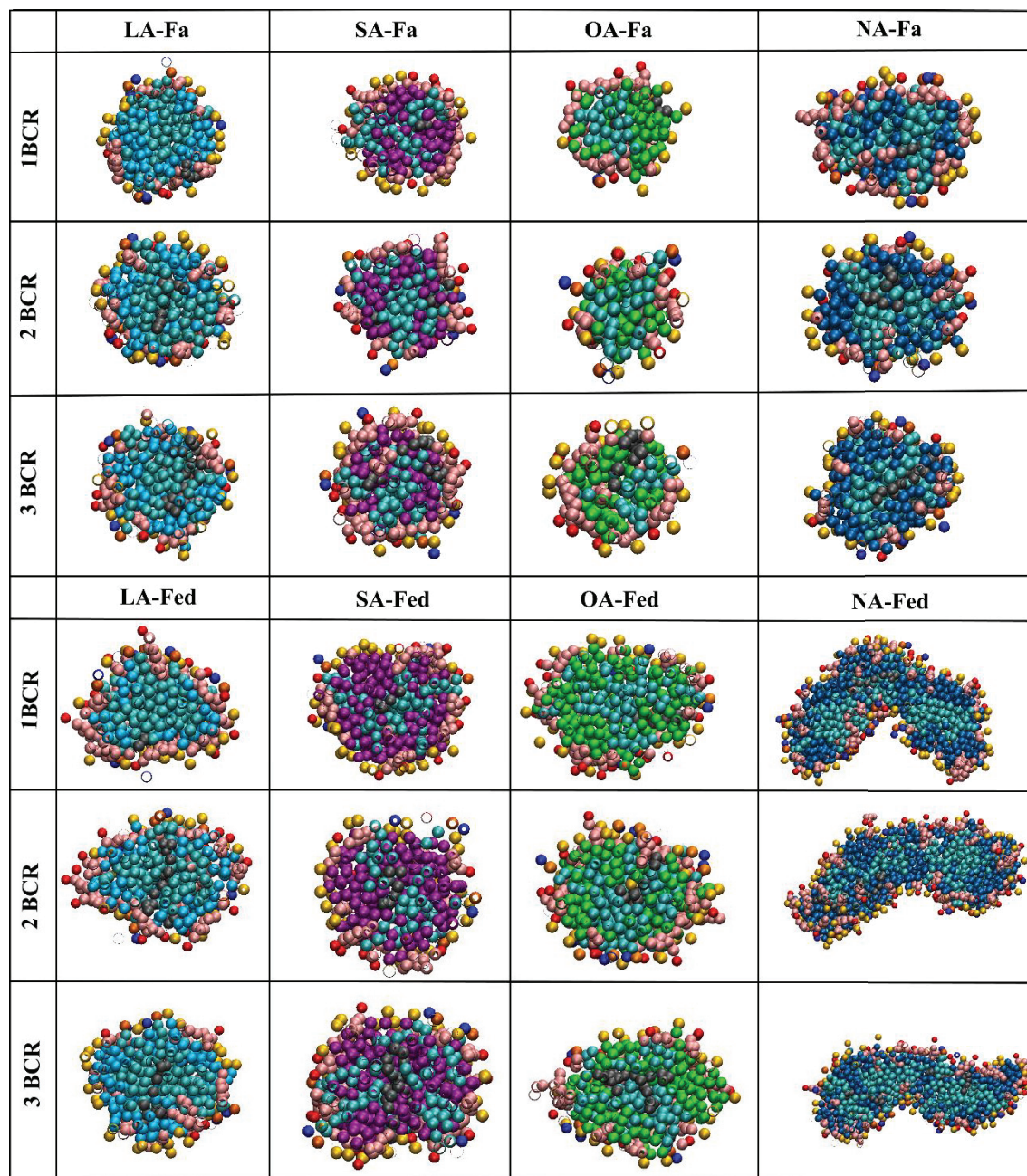
Figure 4.5. Representative cross-sectional snapshots of selected micelles for all systems. Each molecule is colored differently: head and other groups of CHOA molecules are colored in red and pink; the $NC3^+$, $PO4^-$ and tail beads of POPCs are colored in blue, orange and cyan; head beads of fatty acids are colored in yellow, respectively. Tail groups of each fatty acid molecules colored differently: LA: light blue, SA: purple, OA: green, NA: dark blue.

the incorporation of BCR molecules to the micelles increased the number of CHOAs independent of BCR amount. Smaller core densities of those micelles, due to the double bonds present in the fatty acid tails, gave more space to BCR molecules in the micelle. Consequently, the increased amount of BCR molecules did not change the number of CHOAs in the micelles. For the LA-Fed micelle, the amount of CHOA molecules was increased by one each time a single BCR molecule joined the micelle. For the micelles of SA-Fed and OA-Fed, the joining of up to three BCR molecules resulted in the increased number of CHOA molecules. However, the micelles released one CHOA when three BCR molecules were present in the core. The rod-like micelle of the NA-Fed system exhibited different behaviors. The incorporation of one BCR reduced the number of CHOAs while two and three BCRs increased the number. Similar to the case in the system without BCRs, the shape of the micelles transitioned, which resulted in more frequently changing number of CHOA molecules. Thus, the presence of more than one BCR increased the need for CHOA molecules on the surface. The longer micelle size of those systems resulted in thinner micelles, and the swelling of micelles after incorporation of two or three BCRs required more CHOAs to shield hydrophobic moieties from the water.

4.3.4. Structural Characterization of Mixed Micelles in the Presence of *β*-carotene Molecules

The structural characterization of the mixed micelles in presence of different fatty acid molecules were performed by calculating radius of gyration, principle moments of inertia and solvent accessible surface areas.

4.3.4.1. Size and Shape Properties

As explained in the previous section, the micelles with the highest cumulative probability after the equilibration points of the trajectories were selected for further structural analysis. To start with, radii of gyration of the selected micelles were calculated to obtain information about micelle sizes. The results are provided in Table 4.3 and Figure 4.6. Due to the large molecule size of *β*-carotene, the micelles should be large enough for incorporation (Yao et al., 2014). The mixed micelles with fatty acids were large enough for the solubilization of *β*-carotene molecules in the present study.

Generally speaking, small micelles (of fasted state) were swollen with the incorporation of BCRs while no significant swelling effect was observed in large micelles (of fed state) with the exception of SA-Fed micelle. The latter is attributed to the rigid structure of long SA tails; i.e., the packing constraints due to the allocation of multiple BCRs within the core cannot be as easily overcome as they have been in the presence of less rigid FAs. In addition, the large β-carotene molecules reduced the micelle core packing density of the micelles compared to the ones without due to the increased effects of steric interactions (Table 4.3).

Figure 4.6. Radii of gyration of selected micelles at fasted ($\diamond$) and fed ($\blacklozenge$) states with different fatty acids: Lauric acid: light blue, Stearic acid: purple, Oleic acid: green and Linoleic acid: deep blue. The different number of β-carotenes are shown by different shapes: 1 BCR: $\circ$, 2 BCR: $\varnothing$, 3 BCR: $\square$. The results are indicated with the shape frames for fasted and filled shapes for fed states.

In the literature, β-carotene molecules were reported as interacting strongly with POPC molecules in the core (Kotake-Nara, Yonekura, & Nagao, 2015; Yonekura, Tsuzuki, & Nagao, 2006). According to the results obtained in this study, the BCR molecules interacted with both fatty acid and POPC molecules within the core (see sections 4.3.4.2 - 3). A comparison of the sizes of the micelles obtained in this study to those of the literature is not possible, unfortunately. In the literature, the bioaccessibility studies were usually performed using food-born carotenoids instead of pure ones. The food matrix used in the studies contains other components that have a significant effect on micellization behavior.
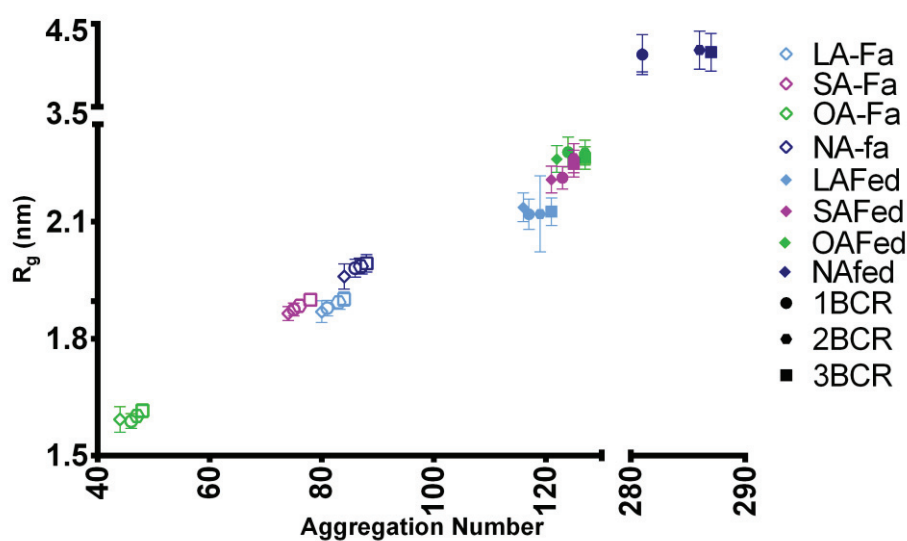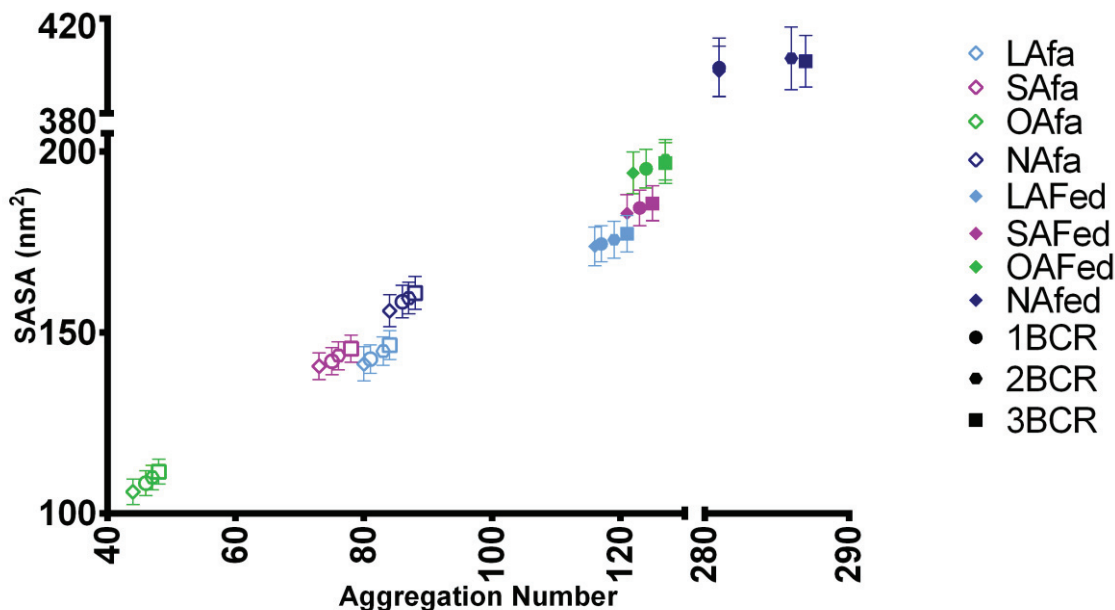
Figure 4.7. Solvent accessible surface areas (SASA) of selected micelles at fasted ($\diamond$) and fed ($\blacklozenge$) states with different fatty acids: Lauric acid: light blue, Stearic acid: purple, Oleic acid: green and Linoleic acid: deep blue. The different number of β-carotenes are shown by different shapes: 1 BCR: $\circ$, 2 BCR: $\circ$, 3 BCR: $\square$. The results are indicated with the shape frames for fasted and filled shapes for fed states.

To characterize the shape of micelles, the ratios of three principal moments of inertia (I_1/I_2 and I_2/I_3) were calculated (where $I_1 \leq I_2 \leq I_3$). The results are presented in Table 4.3. According to results, the incorporation of up to three BCR molecules did not affect the micelle shapes at fasted state. The average ratio results were close to but less than 1, similar to the micelles without BCR molecules. The slightly more ellipsoidal structure of an OA-Fa micelle disappeared with the incorporation of BCRs. However, at fed state, the I_1/I_2 and I_2/I_3 ratios increased slightly with the incorporation of BCR molecules. However, the number of BCRs did not dramatically change the shape. The ratios of the moment of inertia results and visual inspection of the micelles (see Figure 4.5) revealed that the micelles, both at fasted and fed states, were slightly ellipsoidal, except for the NA-Fed micelles. The NA-Fed micelles were still rod-like in shape according to I_1/I_2 and I_2/I_3 ratios. Even so, the dynamic structure and shape transition of the micelles were observed after the addition of BCRs. Moreover, the micelles underwent fission in certain time frames, as explained previously. In the literature, the incorporation of pure β-carotene molecules into intestinal mixed micelles in the presence of fatty acids was expected to not change micelle shape due to the small amounts. The shape of the micelles, however, could not be detected due to the

112

sensitivity of *β*-carotene molecules to the X-Ray (Aizawa et al., 2017). In the present study, this hypothesis was proved by calculating average I_1/I_2 and I_2/I_3 ratios. The slightly ellipsoidal shapes of dietary mixed micelles in the presence of fatty acids were not changed considerably after incorporation of BCRs.

Solvent accessible surface areas (SASA) of micelles were calculated after the incorporation of *β*-carotene molecules. The results are in Table 4.3. and Figure 4.7. As the number of BCRs in the micelles increased, the SASA of the micelles were also increased. The incremental increase followed aggregation number dependent behavior within micelles of the same fatty acids at fasted or fed state. However, the SASA results of the micelles of LA-Fa and SA-Fa were similar despite their different aggregation numbers. As described in the previous chapter, the larger chain length of the stearic acid resulted in larger micelles size, and thus SASA, despite the smaller aggregation number. Similarly, the micelles of LA-Fa3, NA-Fed, or LA-Fed3, SA-Fed, and OA-Fed had the same or very similar aggregation numbers but different SASA values. The differences were caused by both longer chain length and the unsaturated structure of fatty acid molecules. The correlation between the SASA and R_g results was weakened after the incorporation of BCR molecules to the micelle structures. At fasted state, the correlation was preserved for the micelles with LA, SA, and NA. The OA-Fa micelle size was reduced after incorporation of one BCR molecule while the SASA was increased. This situation indicates an increased surface roughness of the OA-Fa1 micelle. The angle results of CHOA molecules revealed that the molecules were placed more flatly on the micelles surface after incorporation of one BCR molecule. However, the charged head groups of POPC and FA molecules became more aligned with the radial axis, which indicates the more protruded location on the surface. Therefore, the increase in SASA is attributed mainly to an increase in the surface roughness due to the charged head groups of POPC and OA molecules (see section 4.3.4.3). Similarly, by increasing the number of BCRs, the size of micelles with LA-Fed became smaller while their SASA became larger. This situation indicates an increased roughness on the surface after the addition of BCRs. The same aspect occurred for the micelles with SA and OA-fed micelles with two and three BCRs. The increased number of BCRs increased the SASA while the sizes were similar for the micelles of SA- or OA-fed. The incorporation of BCR to the micelles increased the volume of the hydrophobic core of the micelles. BCR molecules

Table 4.3. Structural properties of the selected micelles: Radius of gyration (R_g); ratios of the principal moments of inertia, (I_1/I_2) and (I_2/I_3); total solvent accessible surface area (SASA); SASA per surfactant; the ratio of the hydrophilic SASA to hydrophobic SASA (Phi/Pho), and volume per lipid in micelle core

	Numbers of CHOA:POPC:FA molecules	Micellar Lipid/CHOA ratio	Rg (nm)	l_1/l_2	l_2/l_3	Total SASA (nm²)	Phi/pho	SASA per surfactant (nm²)	Volume per lipid in the micelle core
LA-Fa1	20:12:48	3.05	1.878±0.020	0.868±0.067	0.919±0.040	142.691±3.925	16.00	1.762	0.246
LA-Fa2	21:12:48	2.95	1.893±0.018	0.873±0.066	0.918±0.040	144.835±3.887	15.43	1.745	0.248
LA-Fa3	21:12:48	3.00	1.901±0.019	0.875±0.064	0.920±0.040	146.506±4.015	14.94	1.744	0.247
SA-Fa1	23:10:41	2.26	1.875±0.016	0.881±0.061	0.922±0.038	142.055±3.777	13.13	1.894	0.287
SA-Fa2	23:10:41	2.30	1.885±0.017	0.880±0.061	0.922±0.038	143.565±3.826	12.62	1.889	0.286
SA-Fa3	24:10:41	2.25	1.900±0.016	0.879±0.061	0.920±0.039	145.477±3.742	12.31	1.865	0.287
OA-Fa1	16:5:24	1.88	1.588±0.019	0.871±0.067	0.915±0.042	108.375±3.415	8.24	2.356	0.302
OA-Fa2	16:5:24	1.94	1.602±0.018	0.870±0.067	0.916±0.042	109.905±3.387	7.69	2.338	0.300
OA-Fa3	16:5:24	2.00	1.615±0.018	0.871±0.066	0.915±0.041	111.517±3.450	7.19	2.323	0.298
NA-Fa1	25:12:48	2.44	1.981±0.023	0.854±0.073	0.914±0.042	158.322±4.500	11.16	1.841	0.288
NA-Fa2	25:12:48	2.48	1.986±0.020	0.861±0.070	0.914±0.420	159.527±4.319	11.02	1.834	0.286
NA-Fa3	25:12:48	2.52	1.993±0.022	0.866±0.069	0.916±0.041	160.907±4.559	10.86	1.828	0.284
LA-Fed1	29:16:71	3.03	2.119 ±0.039	0.803±0.095	0.899±0.048	174.500±4.951	18.99	1.491	0.243
LA-Fed2	30:16:71	2.97	2.120±0.038	0.812±0.091	0.902±0.048	175.638±5.086	18.75	1.476	0.241
LA-Fed3	31:16:71	2.90	2.126±0.035	0.825±0.083	0.900±0.049	177.245±5.046	18.79	1.465	0.240
SA-Fed1	34:13:75	2.62	2.213±0.029	0.803±0.090	0.897±0.049	184.424±4.891	18.55	1.499	0.273
SA-Fed2	35:13:75	2.57	2.263±0.037	0.828±0.084	0.899±0.048	185.780±4.840	18.38	1.486	0.290
SA-Fed3	34:13:75	2.68	2.249±0.035	0.841±0.079	0.902±0.047	185.692±4.884	18.58	1.486	0.282
OA-Fed1	39:18:66	2.18	2.279±0.038	0.801±0.092	0.896±0.050	195.287±5.303	15.06	1.575	0.312
OA-Fed2	41:18:66	2.09	2.277±0.032	0.794±0.094	0.897±0.049	197.732±5.559	14.91	1.557	0.308
OA-Fed3	40:18:66	2.18	2.263±0.029	0.822±0.086	0.907±0.049	196.853±5.642	15.06	1.550	0.300
NA-Fed1	80:38:162	2.51	4.129±0.239	0.241±0.792	0.947±0.039	399.341±12.358	13.30	1.421	-
NA-Fed2	84:38:162	2.40	4.184±0.229	0.234±0.087	0.948±0.044	403.278±13.246	13.27	1.410	-
NA-Fed3	84:38:162	2.42	4.157±0.225	0.235±0.073	0.944±0.039	401.967±10.885	13.41	1.401	-

occupied the center of the micelle and pushed POPC and fatty acid molecules through the micelle surface when there was a large number of BCR molecules combined with a sufficient number of free CHOA molecules. Therefore, the head groups became more protruded on the surface depending on the core density of the micelles (i.e., if the core density was higher, the protrusion on the surface was also larger).

4.3.4.2. Radial Density Distributions

The inner structuring of the micelles after the incorporation of β-carotene molecules was investigated using the radial density distributions (RDD) of selected beads in a molecule with respect to the center of mass (com) of the micelles. The RDDs of surrounding water molecules and ions were calculated to obtain information about their distribution around the micelles. The results of the systems at fasted and fed states are in Figure 4.8-15. Due to the different shapes of the selected micelles with NA at fed state, the RDDs of the constituent molecules could not be analyzed. In the first column of the plots, the RDDs of the head, glycerol and tail beads of POPC molecules, head and tail groups of fatty acid molecules and charged OCO$^-$ and one representative bead (R3) of CHOA molecules are given with surrounding water molecules and ions with respect to micelle center of mass. The inset figures provide closer views of the micelle-water interfaces. General information about the micelle structures can be obtained by using the plots 4.8-15.a, e, j. Independent of the numbers of constituent molecules, the general internal structuring of the micelles was similar. The hydrophobic tail beads of fatty acid and POPC molecules and whole BCR molecules formed the core. The CHOAs and charged moieties of each molecule were placed on the micelle surface and interacted with the ion double layer. The Na$^+$ ions formed the first shell around the micelle. Their interaction with negatively charged beads formed the majority of the ions on the surface. The second shell formed by Cl$^-$ ions also interacted with both Na$^+$ ions and PO4$^+$ beads of POPCs. The PO4$^+$ beads were placed 0.1 nm further away from the NC3$^-$ beads when BCRs were involved, similar to the micelles without BCRs (see section 3.3.2.2). In conjunction with the angle results between the PO4-NC3 and radial vectors, the protruded arrangement of POPC head groups on the surface were preserved. However, the extension of protrusion varied in different systems (see 4.3.4.3). The distance of the OCO$^-$ bead from the micelle core was larger than the PO4$^-$ beads for the micelles without BCR molecules. However, the distance between OCO$^-$ and PO4$^-$ beads

decreased when BCRs were incorporated into the micelles. This result points out to changes to the surface roughness of the micelles. A further discussion of their alignment on the surface is conducted in angle results (see 4.3.4.3).

The detailed information on CHOA molecule arrangements can be obtained from the second column of RDD plots (Figure 4.8-15.b, f, k). The RDD results for each bead of CHOA molecule exhibited minor differences by the addition of BCR molecules. Therefore, their general arrangement on the surface was similar to the micelles without BCR molecules. All CHOA beads, except the C1 and the charged OCO^- beads, were placed at the same distance from the micelle core. However, the R1 and R3 beads that contain methyl groups were slightly closer to the core. Therefore, CHOA molecules preserved their flat alignment on the surface with their hydrophobic groups facing the hydrophobic micelle core, as proposed in the literature (Prakash &and Gorfe 2013; S. J. Marrink and Mark 2002; Sayyed-Ahmad, Lichtenberger, and Gorfe 2010). The charged beads were still tilted with varying extents as described previously. Typical wedge-like alignment of CHOA on the micelle surface in the presence of different molecules was also reported (S. J. Marrink & Mark, 2002; Sayyed-Ahmad et al., 2010; Turner et al., 2010). Even so, the broader RDDs of micelles, especially for ROH beads, at fed state and NA-Fa indicated the CHOA may occasionally sample different alignments and may penetrate into the micelle core. The interaction of OCO^- with the NA^+ shell and each bead with water molecules were still discernable.

The detailed structuring of POPC molecules within the micelles was investigated with help of the RDDs of tail, glycerol, and head beads with respect to the com of micelles (Figure 4.8-15.a, e, and j). Similar to other micelles studied in this work, the tail groups of POPCs were placed in the micelle core. The presence of other lipophilic molecules in the core affected their alignment (i.e., fatty acid molecules disordered POPC tail groups), as reported in Chapter 3. For the micelles with LA, the disturbance decreased after incorporation of one BCR. However, by increasing number of BCRs, the shoulder in the corresponding RDD plots reappeared. This is also supported by the calculations of the average POPC tail lengths, which showed that incorporation of one BCR into the micelle resulted in more extended tail conformations while additional BCRs resulted in the opposite situation (Table 4.4.). The probability of POPC tail groups being in the core decreased with increasing numbers of BCR molecules. This behavior was also observed for the micelles of SA-Fa, OA-Fa, and SA-

Fed. At NA-Fa, LA-Fed and OA-Fed micelles there was no shoulder in the RDD plots of POPC tail groups. However, POPC tails were partially swept away from the micelle center with increasing numbers of BCRs. The absence of the last tail bead in LA and the presence of double bonds in OA and NA provided larger space in the micelle center for incorporation of BCR molecules. Therefore, the probability that the POPC tails occupy the core was reduced. The most obvious effect of increased numbers of BCRs was observed as increased levels of self-interaction between the BCRs in the micelle core. Despite separately dissolving in the micelle core, BCRs came together in different conformations, they occupied the micelle center, and pushed the remaining molecules towards the surface. The increased distance between the two head beads (R2-R6) of BCR molecules within the same type of micelle was due to this strong interaction (Table 4.4). As their amount was increased, they became flatter in the micelle core.

Table 4.4. The average distances (nm) of fatty acid and POPC palmitoyl and oleoyl tails and β-carotene molecules

Distances (nm) /Micelles	POPC palmitoyl tail (C1A-C4A)	POPC oleoyl tail (C1B-C5B)	Fatty acid tail (C1-C3/4)	β-carotene molecules (R2-R6)
LA-Fa	1.191±0.037	1.428±0.057	0.835±0.014	-
LA-Fa1	1.192±0.063	1.431±0.057	0.837±0.013	2.033±0.408
LA-Fa2	1.191±0.036	1.430±0.057	0.836±0.013	2.067±0.284
LA-Fa3	1.189±0.036	1.425±0.057	0.836±0.013	2.079±0.236
SA-Fa	1.189±0.040	1.426±0.062	1.190±0.020	-
SA-Fa1	1.202±0.035	1.458±0.054	1.197±0.015	2.158±0.360
SA-Fa2	1.188±0.040	1.425±0.063	1.191±0.020	2.036±0.287
SA-Fa3	1.187±0.040	1.425±0.062	1.190±0.020	2.042±0.232
OA-Fa	1.179±0.058	1.399±0.091	1.117±0.028	-
OA-Fa1	1.181±0.057	1.407±0.088	1.118±0.028	1.933±0.399
OA-Fa2	1.181±0.057	1.406±0.089	1.118±0.028	1.934±0.283
OA-Fa3	1.181±0.056	1.407±0.089	1.118±0.028	1.936±0.236
NA-Fa	1.199±0.037	1.443±0.056	0.991±0.027	-
NA-Fa1	1.198±0.036	1.442±0.056	0.990±0.027	2.078±0.409
NA-Fa2	1.197±0.036	1.439±0.056	0.988±0.027	2.110±0.271
NA-Fa3	1.195±0.036	1.437±0.057	0.985±0.028	2.120±0.228
LA-Fed	1.200±0.032	1.447±0.049	0.837±0.011	-
LA-Fed1	1.200±0.031	1.446±0.049	0.838±0.011	2.131±0.380
LA-Fed2	1.196±0.032	1.438±0.049	0.836±0.011	2.128±0.280
LA-Fed3	1.194±0.032	1.435±0.049	0.835±0.011	2.154±0.218
SA-Fed	1.200±0.035	1.460±0.053	1.195±0.015	-
SA-Fed1	1.202±0.035	1.458±0.054	1.197±0.015	2.158±0.360
SA-Fed2	1.199±0.035	1.451±0.054	1.195±0.014	2.158±0.266
SA-Fed3	1.196±0.035	1.443±0.054	1.195±0.015	2.142±0.233
OA-Fed	1.201±0.030	1.450±0.046	1.129±0.017	-
OA-Fed1	1.202±0.030	1.453±0.045	1.129±0.016	2.152±0.355
OA-Fed2	1.197±0.030	1.447±0.046	1.127±0.017	2.160±0.267
OA-Fed3	1.196±0.030	1.443±0.046	1.127±0.017	2.160±0.221
NA-Fed	1.201±0.021	1.443±0.032	1.002±0.015	-
NA-Fed1	1.204±0.021	1.449±0.032	1.005±0.015	2.161±0.367
NA-Fed2	1.201±0.021	1.445±0.032	1.003±0.015	2.167±0.252
NA-Fed3	1.202±0.021	1.446±0.032	1.003±0.015	2.174±0.214

Figure 4.8. RDDs ($\rho(r)$) of different moieties of the constituent molecules and ions with respect to the com of the micelles for the micelles of LA-Fa with different number of BCRs. RDDs of the specified moieties of CHOA, POPC, and LA molecules are given on the left (a, e, j). The close views of the interface regions are given in the insets, where all other beads except the OCO$^-$ and R3 beads of CHOA and tail beads of POPC are omitted for clarity. The close views of the RDDs of the individual beads of CHOA (b, f, k), LA (c, g, m) and BCR (d, h, n) molecules are given also. RDDs of the surrounding Na$^+$, Cl$^-$ ions and water molecules are included in both graphs.

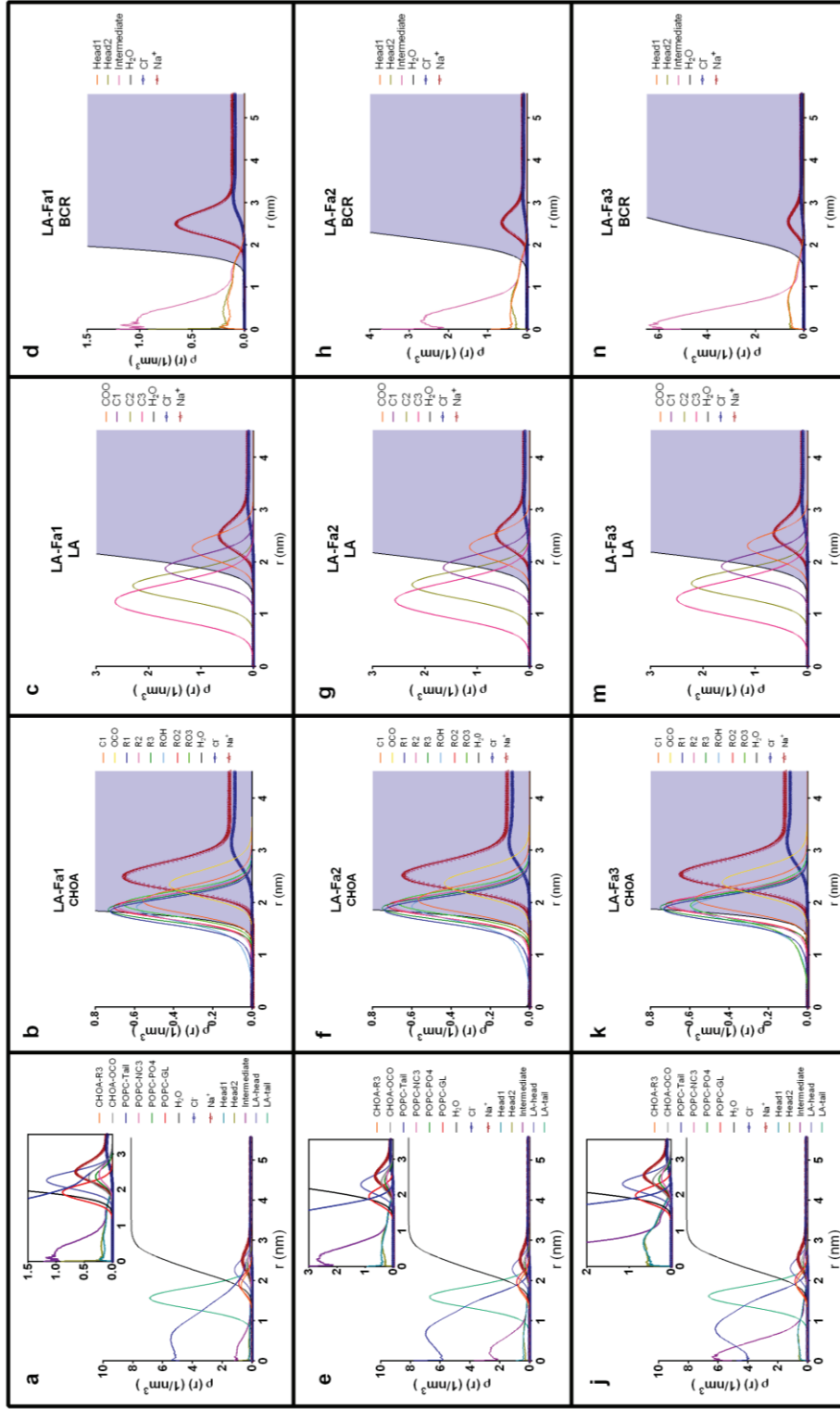Figure 4.9. RDDs ($\rho(r)$) of different moieties of the constituent molecules and ions with respect to the com of the micelles for the micelles of SA-Fa with different number of BCRs. RDDs of the specified moieties of CHOA, POPC, and SA molecules are given on the left (a, e, j). The close views of the interface regions are given in the insets, where all other beads except the OCO⁻ and R3 beads of CHOA and tail beads of POPC are omitted for clarity. The close views of the RDDs of the individual beads of CHOA (b, f, k), SA (c, g, m) and BCR (d, h, n) molecules are given also. RDDs of the surrounding Na⁺, Cl⁻ ions and water molecules are included in both graphs
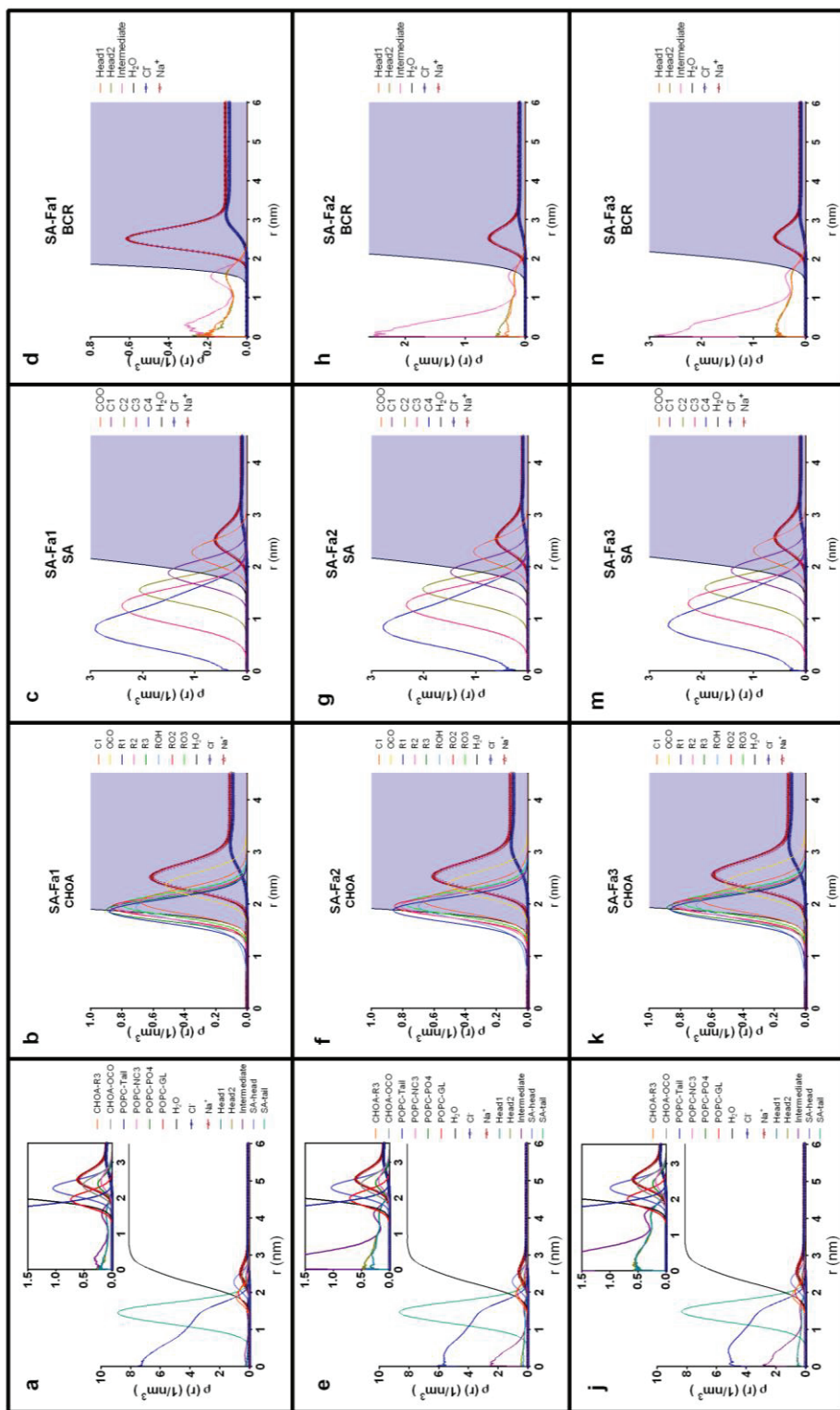
119

Figure 4.10. RDDs ($\rho(r)$) of different moieties of the constituent molecules and ions with respect to the com of the micelles for the micelles of OA-Fa with different number of BCRs. RDDs of the specified moieties of CHOA, POPC, and OA molecules are given on the left (a, e, j). The close views of the interface regions are given in the insets, where all other beads except the OCO$^-$ and R3 beads of CHOA and tail beads of POPC are omitted for clarity. The close views of the RDDs of the individual beads of CHOA (b, f, k), OA (c, g, m) and BCR (d, h, n) molecules are given also. RDDs of the surrounding Na$^+$, Cl$^-$ ions and water molecules are included in both graphs
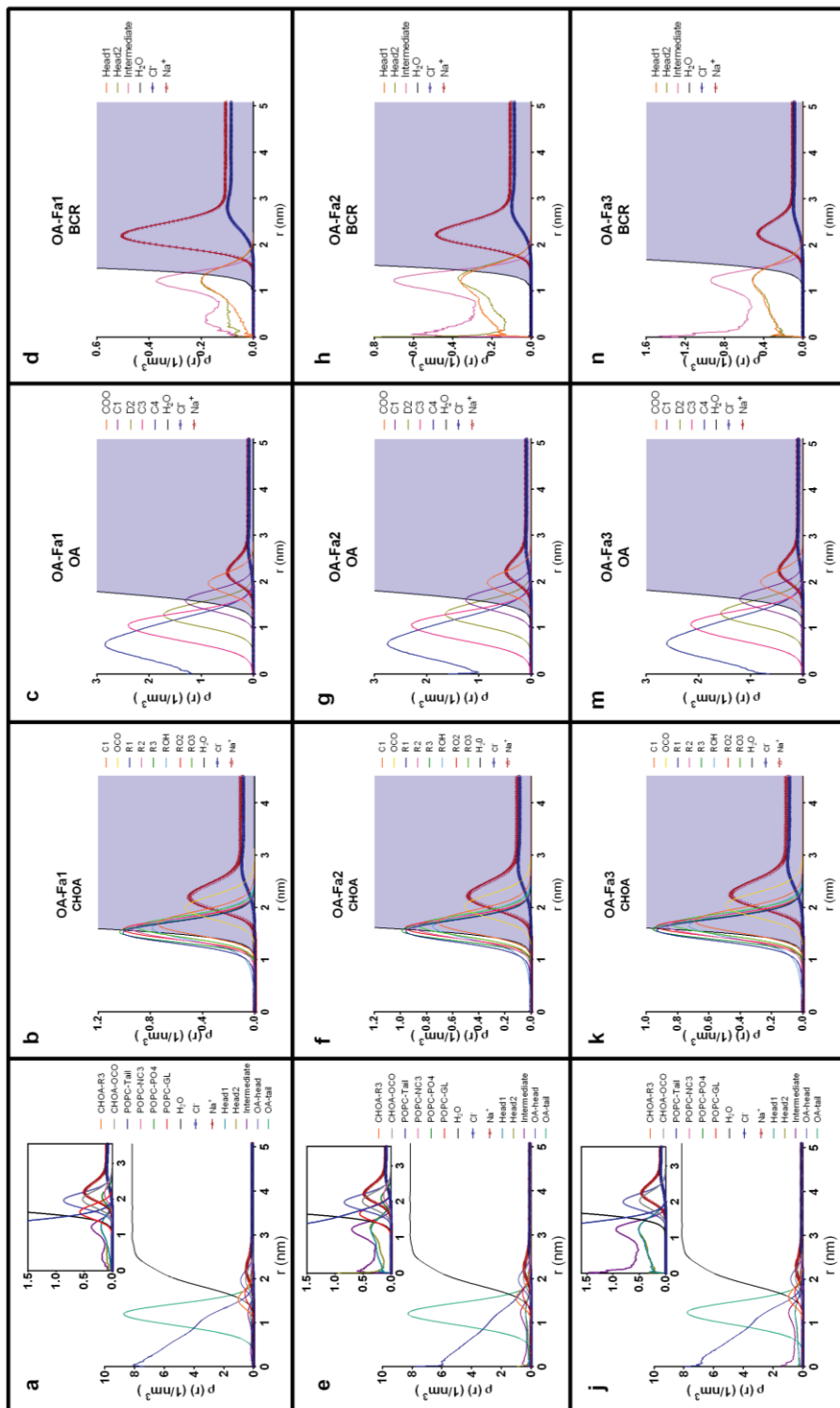
Figure 4.11. RDDs ($\rho(r)$) of different moieties of the constituent molecules and ions with respect to the com of the micelles for the micelles of NA-Fa with different number of BCRs. RDDs of the specified moieties of CHOA, POPC, and NA molecules are given on the left (a, e, j). The close views of the interface regions are given in the insets, where all other beads except the OCO⁻ and R3 beads of CHOA and tail beads of POPC are omitted for clarity. The close views of the RDDs of the individual beads of CHOA (b, f, k), NA (c, g, m) and BCR (d, h, n) molecules are given also. RDDs of the surrounding Na^+, Cl^- ions and water molecules are included in both graphs
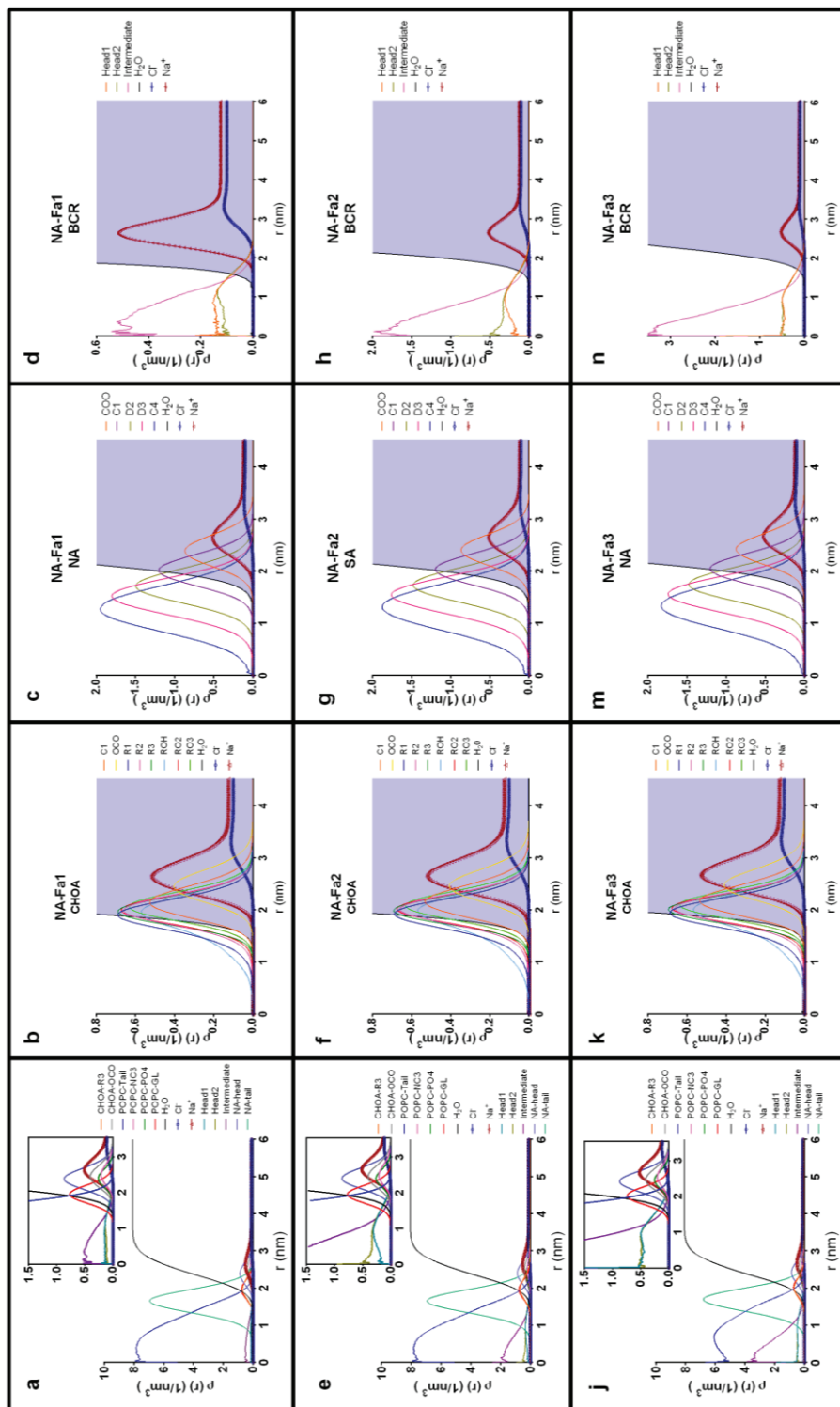
Figure 4.12. RDDs ($\rho(r)$) of different moieties of the constituent molecules and ions with respect to the com of the micelles for the micelles of LA-Fed with different number of BCRs. RDDs of the specified moieties of CHOA, POPC, and LA molecules are given on the left (a, e, j). The close views of the interface regions are given in the insets, where all other beads except the OCO⁻ and R3 beads of CHOA and tail beads of POPC are omitted for clarity. The close views of the RDDs of the individual beads of CHOA (b, f, k), LA (c, g, m) and BCR (d, h, n) molecules are given also. RDDs of the surrounding Na⁺, Cl⁻ ions and water molecules are included in both graphs

122

Figure 4.13. RDDs ($\rho(r)$) of different moieties of the constituent molecules and ions with respect to the com of the micelles for the micelles of SA-Fed with different number of BCRs. RDDs of the specified moieties of CHOA, POPC, and SA molecules are given on the left (a, e, j). The close views of the interface regions are given in the insets, where all other beads except the OCO⁻ and R3 beads of CHOA and tail beads of POPC are omitted for clarity. The close views of the RDDs of the individual beads of CHOA (b, f, k), SA (c, g, m) and BCR (d, h, n) molecules are given also. RDDs of the surrounding Na⁺, Cl⁻ ions and water molecules are included in both graphs
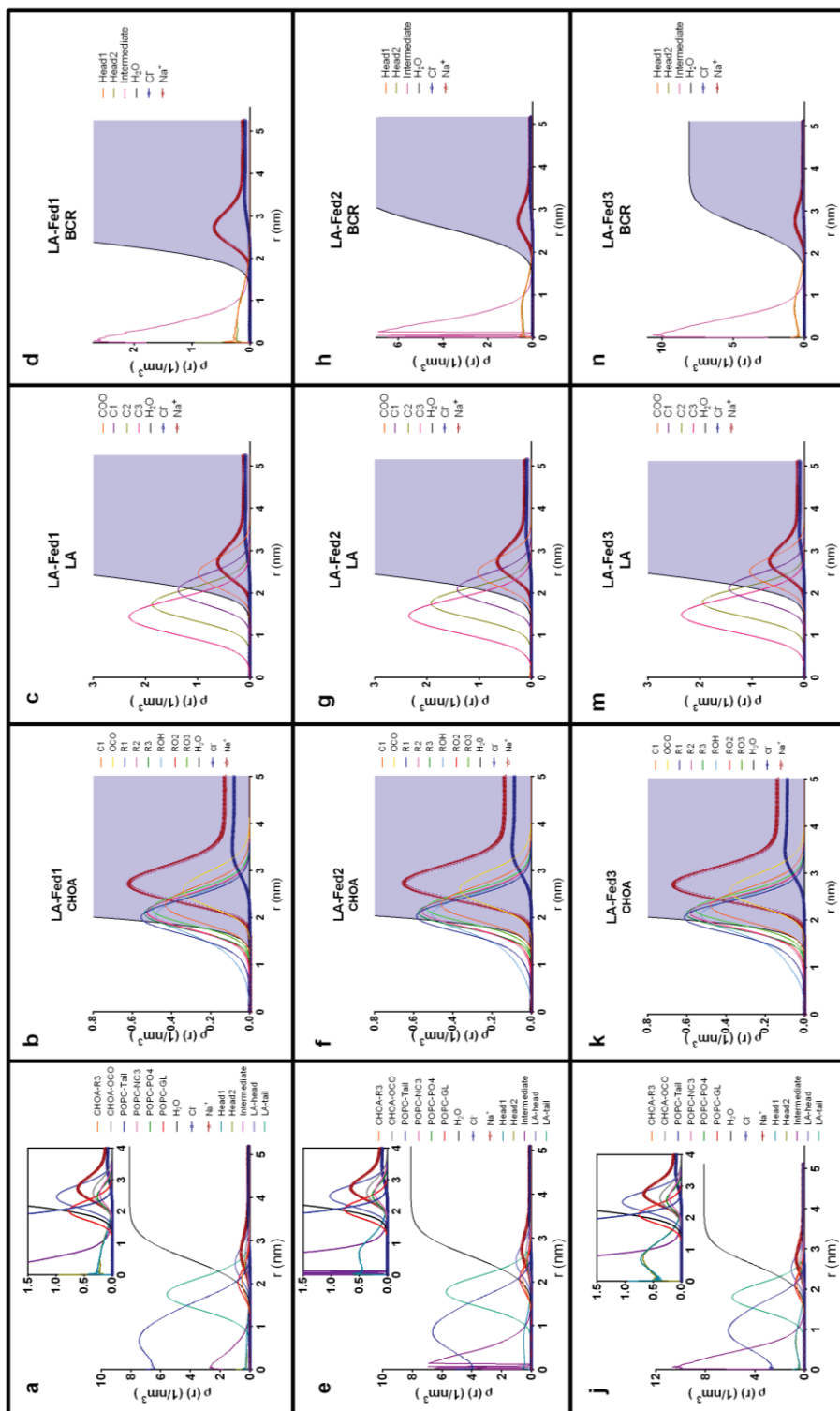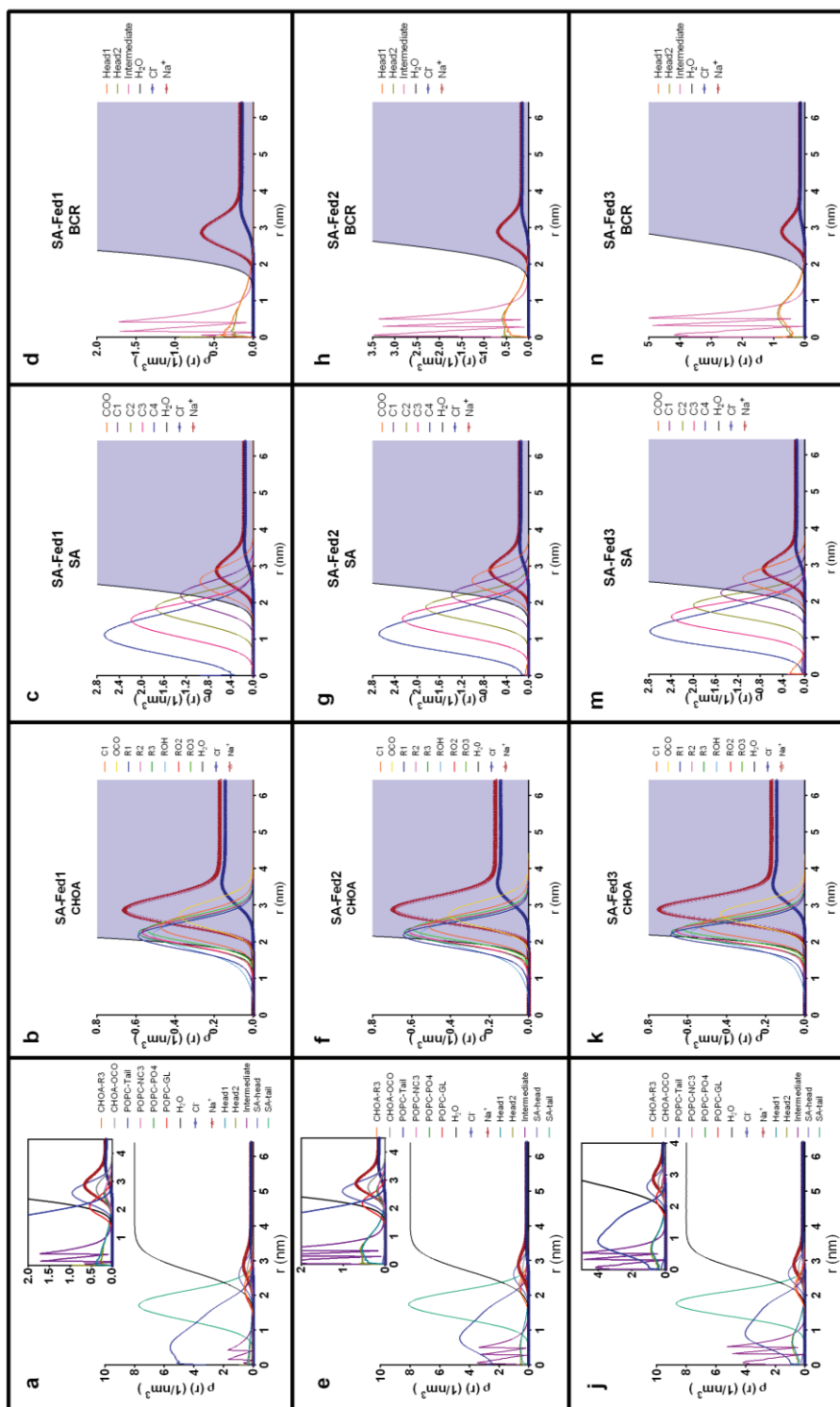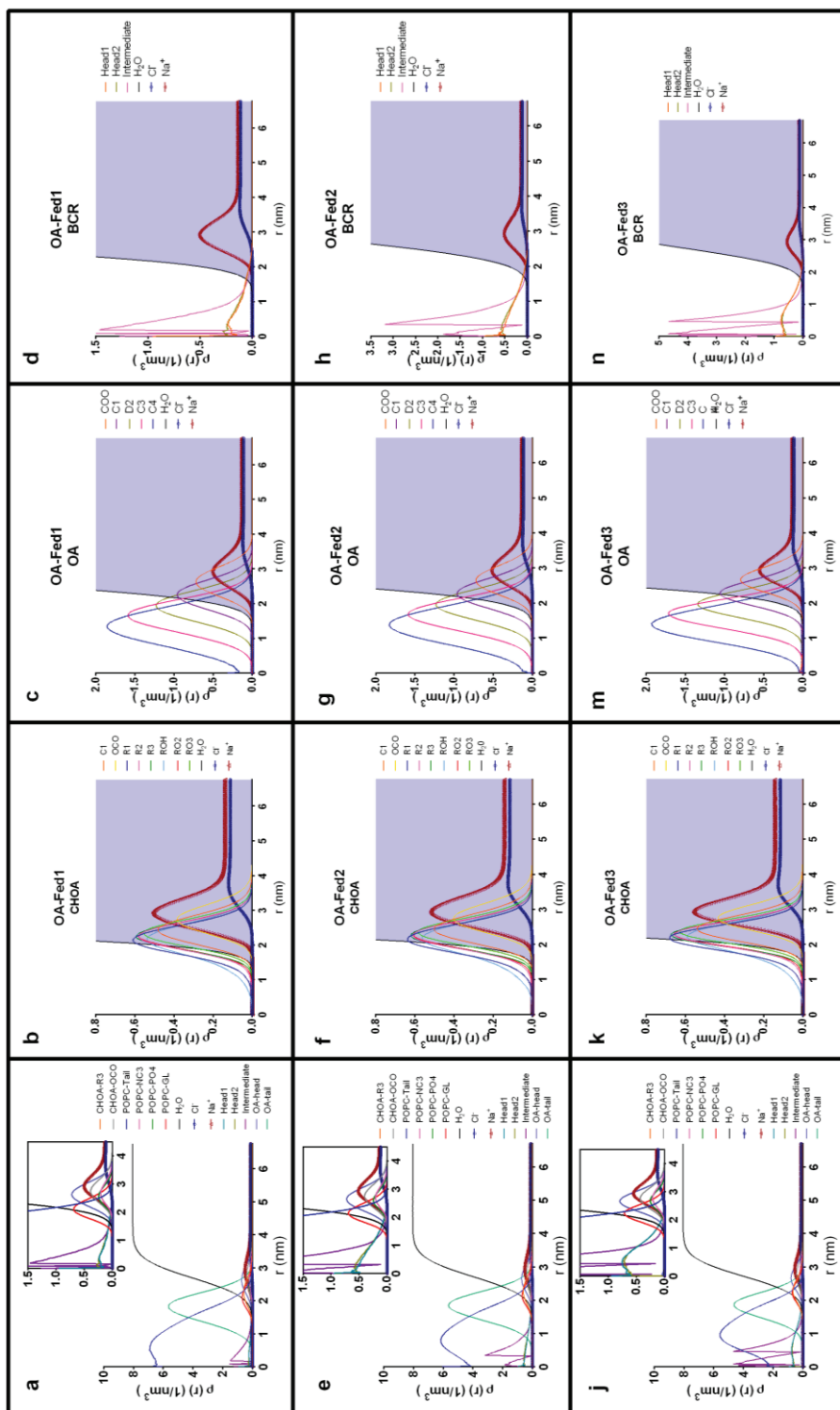
Figure 4.14. RDDs ($\rho(r)$) of different moieties of the constituent molecules and ions with respect to the com of the micelles for the micelles of OA-Fed with different number of BCRs. RDDs of the specified moieties of CHOA, POPC, and OA molecules are given on the left (a, e, j). The close views of the interface regions are given in the insets, where all other beads except the OCO⁻ and R3 beads of CHOA and tail beads of POPC are omitted for clarity. The close views of the RDDs of the individual beads of CHOA (b, f, k), OA (c, g, m) and BCR (d, h, n) molecules are given also. RDDs of the surrounding Na⁺, Cl⁻ ions and water molecules are included in both graphs

The RDDs of each bead of fatty acid molecule with respect to the com of micelles are in Figure 4.8-15.c, g, m. The general arrangement of fatty acid molecules was similar to the micelles without BCRs. The charged head beads were placed on the surface, and the consecutive tail beads were located towards the core. The medium-chain fatty acids were not present in the micelle center (LA-Fa and LA-Fed). Although the RDD plots were similar to the ones without BCRs, the average distances between the consecutive tail beads increased with the addition of one BCR, while they decreased with additional incorporation of BCRs. In the long-chain SA-Fa, SA-Fed, and OA-Fed micelles, additional last tail beads were occasionally present in the micelle center. It is also worth to notice that the probability of the fatty acid head bead's being at the center in the SA-Fed3 system is not zero. Visual inspection of the system revealed a stearic acid molecule, situated between BCR molecules, was interacting with the molecules. The increased amount of BCRs reduced the probability of fatty acid's presence at the core. The interaction of BCRs with fatty acid molecules in the core is revealed by this result and also by the result that a decrease in fatty acid tail lengths is observed with increasing the number of BCR molecules (Table 4.4).

Finally, the RDD results for two-head and intermediate groups of β-carotene molecules were examined with respect to micelle center of mass (Figure 4.8-15.d, h, n). According to the results, BCR molecules try to position themselves in the micelle core as much as possible. The probability of intermediate beads being at the core was higher compared to that of the head beads. Additionally, the head groups did not behave differently as expected due to the symmetrical structure of BCR molecules. Although the BCRs were placed in the micelle core, they occasionally interacted with water molecules, especially when the micelle size was smaller. The RDD results of systems LA-Fa and NA-Fa were similar and represented the above-mentioned arrangement of BCRs in the micelle. However, there were small discrepancies between the results of other micelles. Even if the defined general arrangement remained consistent, the probability of BCR molecules being in the micelle center or almost 1 nm further away was almost equal. The longer chain-length and saturated structure of SA resulted in a more rigid structure and the last tail bead was occasionally placed at the center together with POPC tail groups. As the number of BCRs increased, their probability of being located at the core increased, which was reflected as decreases in the probabilities of POPC and SA tails being in the center. Similar behavior was observed for two-headed

RDD plots of OA-Fa micelles. The probability of BCRS' being almost 1 nm farther away from the center was higher due to the smaller micelle size. The increased number of BCRs increased the probability of being at the micelle center. At fed state, the probability of intermediate beads being at the core was much higher compared to the head beads. The larger sizes and lower core densities at fed state allowed BCRs to more readily be placed in the micelle center. The sharp peaks in the RDD plots of LA-Fed, SA-Fed, and OA-Fed micelles were due to the highly dynamic behavior of the BCRs within the micelles. The detailed orientation of BCRs within the micelles was examined in the angle results (see section 4.3.4.3). The RDD and angle results were also verified by visual inspection of the systems.

4.3.4.3. Internal and Surface Orientations of the Molecules

The internal and surface orientations of the micelles were investigated by means of average angle calculations between selected vectors in a molecule. Type I angle represents the angle between a vector that is formed by two selected beads on a molecule and the radial vector, calculated as the vector from the com of the micelle to the midpoint of the positions of selected beads (see inset of Figure 4.15.a). Type II angle represents the angle between two vectors in a molecule denoted by three beads in total, of which the middle bead is the origin of both vectors and the remaining beads indicate their directions (see inset of Figure 4.15.b). The latter provides information on the conformations of the molecules within the micelles.

The results of RDD calculations demonstrated that CHOA molecules were placed on the micelle surface facing the water with their hydrophilic face. The OCO^- beads were more protruded compared to other beads in all micelles. The orientations of CHOAs on the surface were studied by means of angle calculations of selected vectors. The results are given in Figures 4.15.a and b. The incorporation of BCRs to the micelles did not make a significant difference on their alignments. Overall, the CHOAs preserved their wedge-like shape with their sterol body mostly aligned flatly on the surface and their charged head group protruding from the surface. The characteristic shape of bile acids was reported in the presence of different molecules, such as drugs, fatty acids, or different phospholipids (Haustein et al., 2014; S. J. Marrink & Mark, 2002; Sayyed-Ahmad et al., 2010; Turner et al., 2010). Besides, increasing numbers of

BCR molecules did not affect their alignment as well as the alignment of any charged head groups of the other constituent molecules (Appendix 10-14).
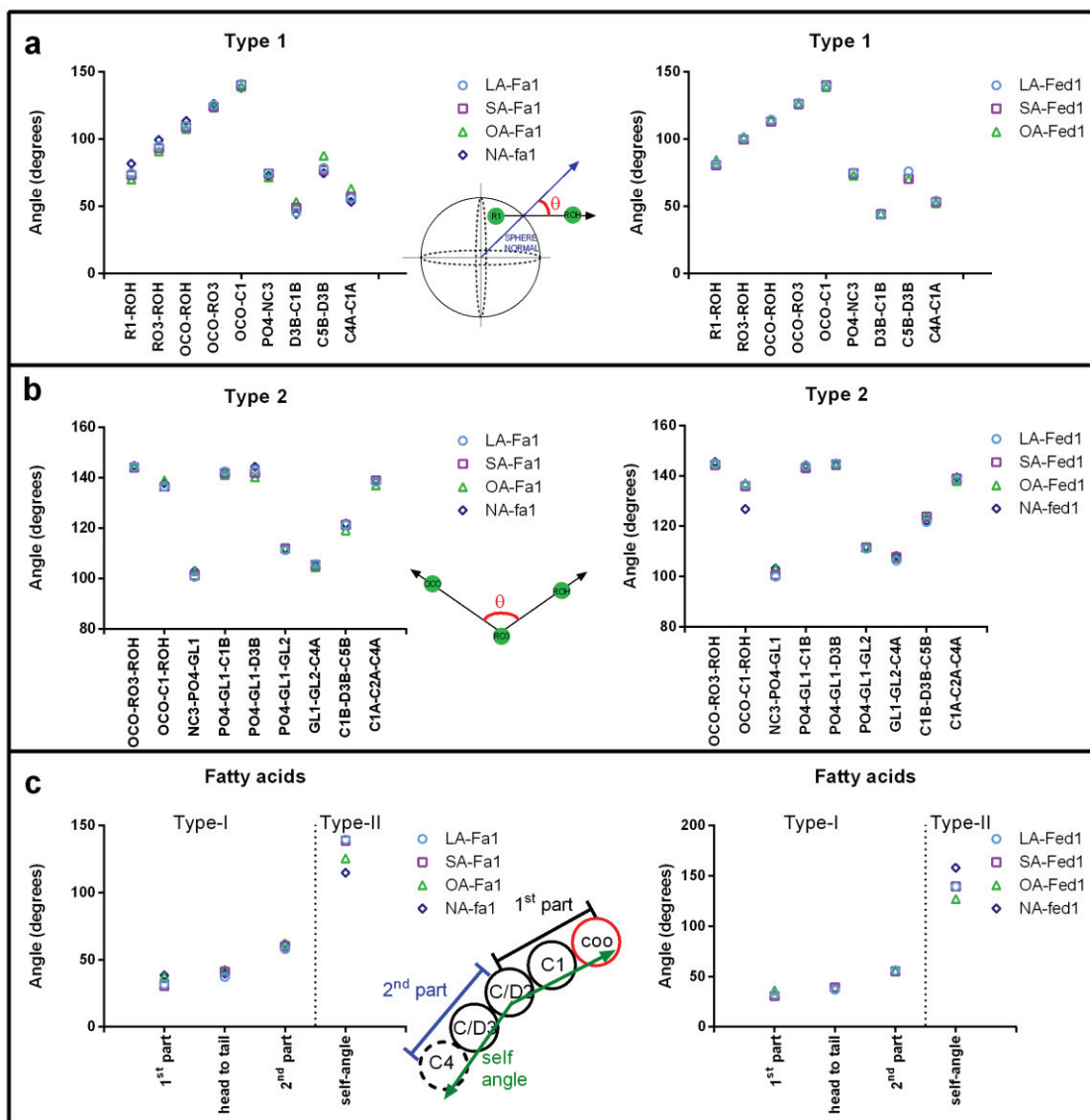
Figure 4.15. a) Type I average angles between a vector of two selected beads in a molecule and the local sphere normal (radial vector) at fasted (left) and fed (right) states. The origin of each vector is the first specified bead; hence the direction of each vector is from the first to the second specified bead. The local sphere normal is the vector which connects the com of the micelle to the midpoint of the selected beads' positions as shown in the inset of a. b) Type II average angles between two vectors in a molecule at fasted (left) and fed (right) states. The origin of each vector is the middle specified bead; hence the directions of the vectors are from the middle to the end beads as shown in the inset b. c) The Type I and Type II average angles of fatty acid molecules at fasted (left) and fed (right) states. The vectors on fatty acid molecules are shown in the inset e. The selected beads for angle calculations are given in x-axis (LA: ○, SA: □, OA: △, NA: ◇).

Type I and Type II angles of POPC and FA acid molecules were almost identical to the average angle results of the micelles without BCR molecules (see Appendix 10 and 11). Therefore, solubilization of BCRs only slightly changed the orientation of constituent molecules. The reader should see Section 3.3.2.3 for detailed orientations of POPC and fatty acid molecules within the micelles.
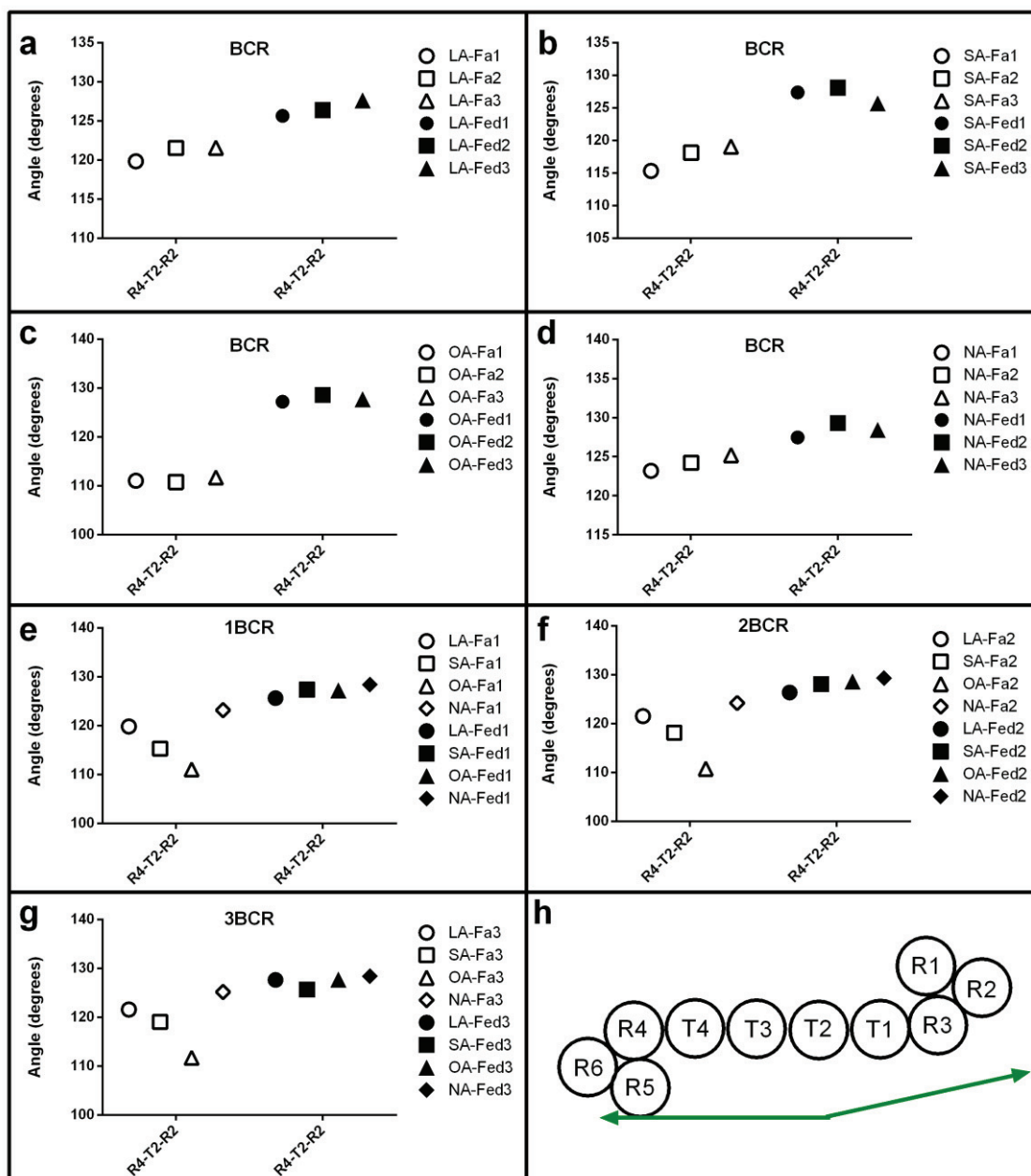

Figure 4.16. Type II average angles between two vectors in a molecule at fasted and fed states. The angle results were calculated for different number of BCR (a, b, c and d) and different types of fatty acid molecules (e, f and g). A representative BCR molecule is given in h.

In the micelle core, the BCR molecules were highly dynamic and in strong interaction with other moieties and each other. To understand the effect of these interactions on the conformation of BCR molecules, the average Type II angles (R4-T2-R2) were calculated. The selected angle varied between 110-125^0, depending on the micelle sizes at fasted state after the addition of one BCR molecule (Figure 4.16). As the micelle size increased, the angle increased. By increasing the number of BCRs, the difference between the angles was reduced. Moreover, at fed state, no difference was observed depending on fatty acid type (~127^0) while the increased number of BCR molecules slightly increased the angle (~129^0). The Type II angle results demonstrated that BCR molecules were not aligned perfectly flat in the micelle core. Instead, they adopted moderately bent conformations to different degrees depending on the micelle size at fasted state; i.e., they sampled more bent conformations with decreasing micelle size. On the other hand, such dependence was not observed at fed state, because the micelles were large enough to accommodate all BCRs more freely. Furthermore, all R4-T2-R2 angles were almost identical regardless of the fatty acid type and number of BCRs in the fed state micelles. Therefore, it can be said that the micelle size is the dominant effect in determining the conformation of BCRs within the micelles.

A more detailed investigation of the BCR conformations was done by calculating the bending angles (Type II) between the vectors of consecutive beads. The results for fasted and fed states are in separate columns in Figure 4.17. According to the results, the ranges of the calculated angles involving the head beads had smaller widths as expected due to the presence of rigid sterol moieties (R4 and R3). The varying average angle for the vectors including head beads did not follow a discernable pattern. However, the size-dependent behavior of the intermediate section of the BCRs (the region at which the self-bending occurred) (T3-T2-T1 and T4-T3-T2 angles) was clear at fasted state, as shown in the first column of the results. In the smaller sized OA-Fa micelles, the BCRs were more bent. The angles got larger as the micelle size increased. The highest values were reached in the NA-Fa micelles. The increase in the number of BCRs resulted in either increasing or decreasing angles within the same type of micelles at fasted states. However, at fed state, the size dependency of the BCR bending was not observed, similar to R4-T2-R2 angle results.
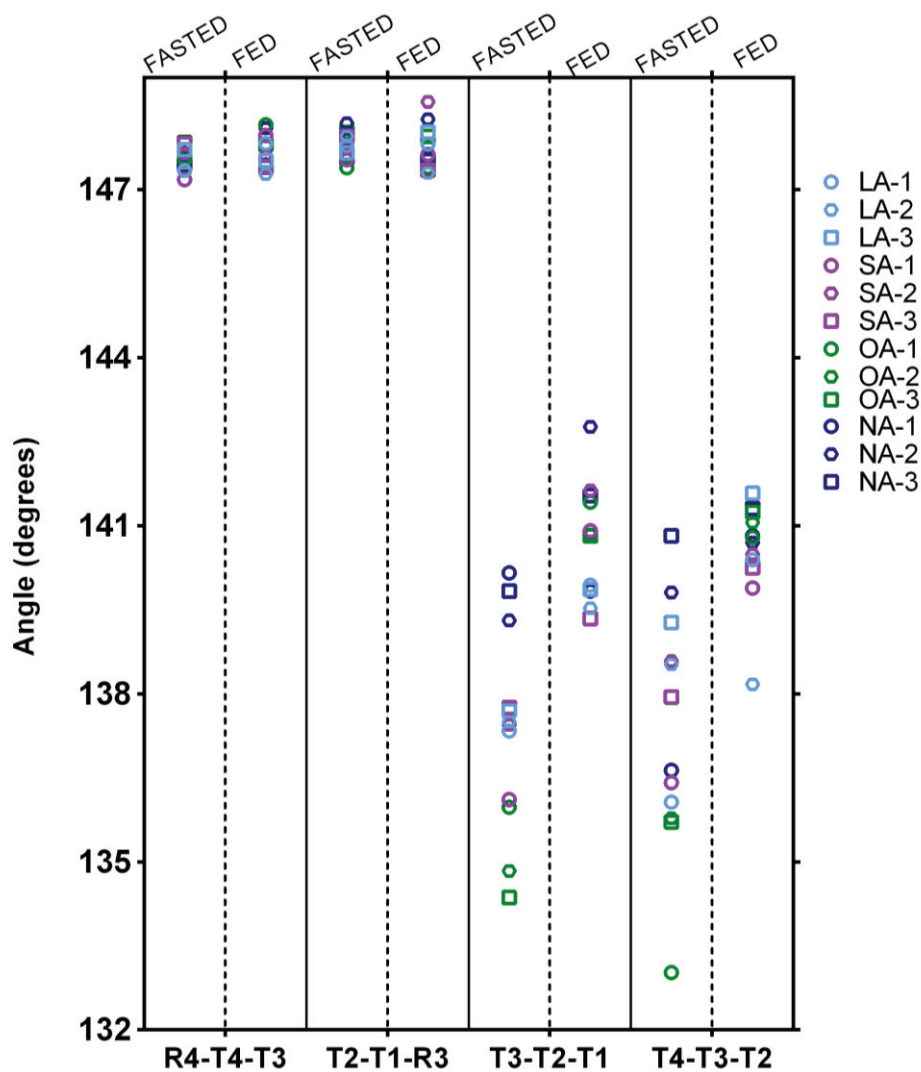
Figure 4.17. Type II average angles between two vectors in a BCR molecule in the micelles with different fatty acids and numbers of BCRs. The selected beads for angle calculations are given in x-axis. (LA: ○, SA: □, OA: △, NA: ◇).
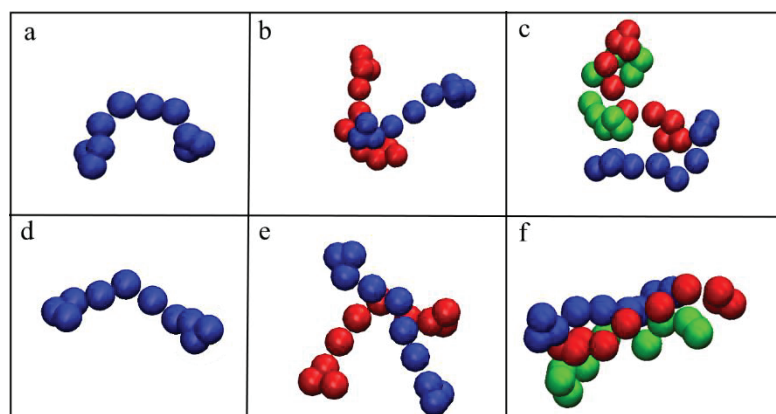

Figure 4.18. Representative alignments of a) single b) two and c) three BCR molecules in the micelles with oleic acid at fasted (top) and fed (below) states. Each BCR residue was colored differently.

130

The representative orientations of BCRs found in OA-Fa and OA-Fed micelles are provided in Figure 4.18. Visual inspection of the BCR molecules also confirmed the Type II angle results. Due to the smaller size of OA-Fa micelles, BCR molecules adopted more bent conformations compared to those in the fed state micelles. Incorporation of more BCRs into the micelles resulted in slightly more stretched conformations in fasted state systems (smaller micelles), while a significant difference in their conformations was not observed in fed state systems (large micelles). The last but not the least, it was observed that increasing interactions between the BCR molecules with increasing numbers of BCRs in the micelles resulted in a stacked packing of flattened molecules on top of each other as long as the micelle size was large enough to allow for it (Figure 4.18.f.).

4.4.   Conclusion

The aim of the fourth chapter of the dissertation was to characterize the solubilization of β-carotenes in dietary mixed micelles and investigate the structural properties of the micelles at molecular level. For that purpose, the mixed micelles formed in Chapter 3 with different fatty acid molecules at two different physiological conditions, i.e. fasted and fed states, were used. The preliminary simulations that were conducted to determine the appropriate amounts of β-carotenes to be incorporated to the systems showed that, irrespective of the concentration, all of the β-carotenes were preferentially solubilized within the micelles leaving no crystallized clusters behind. This was due to the absence of undigested lipid phase or partially digested food matrix in the simulation media. However, the incorporation of such large amounts of β-carotenes in the dietary mixed micelles would never take place in actuality, because their release from the lipid phase (or the food matrix) into the aqueous intestinal medium is usually in limited amounts. Hence, the solubilization of 1, 2 and 3 β-carotene molecules within the selected micelles was simulated separately in order to investigate also the interactions between β-carotenes within the micelles. The solubilization of the β-carotenes started from any intermediate or head bead. Following the incorporation, they moved through the micelle core. Independent of the micelle type, the equilibration of the micelles was fast. The micelles kept exchanging cholate molecules with the surrounding media.

The solubilization of the β-carotenes resulted with different effects on micelle sizes. The sizes were designated by the equilibrium between the micelle size before incorporation of β-carotenes and the core density. For the micelles at fasted state, the sizes were observed to increase for lauric, stearic and linoleic acid micelles by the incorporation of β-carotenes. However, the small-sized oleic acid micelle became smaller after incorporation of a single β-carotene molecule. A similar effect was observed for lauric, oleic and linoleic acid micelles at fed state. This must be because the less rigid nature of the unsaturated FA tails, owing to the presence of double bonds, allowed a better adaptation to the packing constraints within the micelles, and thus shrinkage in size. However, the rigid structure of stearic acid because of its long and saturated tail groups did not allow such an adaptation to the packing constrains resulting in increased micelle size with increasing numbers of β-carotene molecules. The reason that a similar increase in size was not observed for lauric acid micelles might be due their shorter chain length. That is to say, the tails were not long enough to reach the micelle cores where the β-carotenes were mostly found (as proved by RDDs), so they did not have a significant role in the packing of β-carotenes. The slightly ellipsoidal shapes of the micelles were preserved after the incorporation of β-carotene molecules. The solvent accessible surface areas of the micelles increased with increasing numbers of β-carotene molecules, and consequently their correlation with the radii of gyration results was lost. This points to the effect of β-carotene incorporation on the surface roughness of the micelles.

The investigation of the detailed inner structuring of the micelles showed that the general arrangement of the molecules in the micelles did not change drastically. The cholate molecules preserved their wedge-like shapes on the surface between the charged head beads of POPC and fatty acid molecules. Fatty acids were placed such that their tails point towards the micelle core. Fatty acid tails formed the core of the micelles together with POPC tails and β-carotene molecules. The incorporation of β-carotenes mostly affected POPC tails and last tail beads of fatty acids. The mentioned groups and β-carotene had a competitive behavior in the core in order to be placed at the center. Due to their large size and highly hydrophobic nature, β-carotene molecules were mostly placed at the core trying to push other molecules through the surface. This effect resulted in increased surface roughness due to the protrusion of POPC and fatty acid head groups in small micelles and the micelles with stearic acid because of its saturated

long-chain. The orientations of the molecules in the micelle core were only slightly affected from the incorporation of *β*-carotene molecules. *β*-carotene molecules were highly dynamic in shape due to the competition between the other molecules and *β*-carotene molecules in the core. Besides, in small-sized micelles, they adopted more bent conformations to avoid water. However, with increasing numbers of molecules, their probability to be placed at the core increased due to the strong interaction between each other. Additionally, they became more flattened in the micelle core with increasing numbers.

CHAPTER 5

CONCLUSION

The aim of this dissertation was to systematically investigate the factors modulating the solubilization of β-carotene molecules in dietary mixed micelles through coarse-grained molecular dynamics computer simulations. For this purpose, the study was divided into three main parts. In the first part, the self-assembly of bile acid (cholate) and phospholipid (POPC) molecules into dietary mixed micelles was investigated under the fasted and fed state physiological conditions of the duodenum. In the second part, the effects of different types of fatty acids on the micellization process and micelle structures were investigated. In order to observe the effect of fatty acid chain length, lauric acid and stearic acids were studied, while oleic acid and linoleic acids were studied to see the effects of the degree of unsaturation. Finally, in the third part, the solubilization of β-carotene molecules in the selected pre-formed micelles was conducted. In order to analyze the effect of interactions between β-carotenes, 1, 2 and 3 β-carotene molecules were added to the systems.

The mixed micelles of cholate, POPC and fatty acids (when included) were formed by the self-aggregation of constituent molecules. The simulations revealed that the micellization behavior was the same regardless of the total concentration of the bile lipids and fatty acids. The micellization started between any types of neighboring surfactants. The initial stages were dominated by dimers of cholates and small clusters. In the presence of fatty acid molecules, smaller micelles had varying fractions of constituent molecules. In the course of simulations, larger micelles with similar compositions were formed via fusion of smaller ones. It was observed that once the hydrophobic core was formed by POPC molecules they never left the micelle. However, fatty acid molecules occasionally left mixed micelles and joined the unsteady small aggregates. Cholates were continuously involved in a dynamic exchange between the micelles and the aqueous medium. Despite the use of a CG model, the prohibitively limited time and length scales sampled were not sufficient to attain a representative true thermodynamic equilibrium system under fasted state concentrations. Therefore, a complete comparison of the equilibrium structures in both states was not possible. However, the equilibrium micelles obtained in varying sizes in this study can be

considered as transient structures that are formed in the duodenum under both fasted and fed states. The solubilization of the β-carotenes started from any intermediate or head bead. Following their incorporation, they moved through the micelle core. Due to the absence of undigested lipid phase or a partially digested food matrix, all β-carotenes were preferentially solubilized within the micelles. This result proves the importance of the matrix that β-carotenes are ingested with and the completion of lipid digestion in the gastrointestinal tract.

The structural analysis revealed that all of the micelles composed of cholate and POPC were spheroidal (slightly ellipsoidal) in shape. The incorporation of fatty acids into the mixed micelles resulted in an increase in the deviation from the spherical geometry. The higher lipids concentration under fed state also increased the degree of ellipticity. On the other hand, fatty acid characteristics did not have an impact the micelle shapes except the rod-like micelle incorporating linoleic acid at fed state. Solubilization of β-carotene molecules in the pre-formed micelles did not have a significant effect on the micelle shapes.

The size of the equilibrium micelle of cholate and POPC obtained under fed state conforms to the experimental data from the literature. The micelles became swollen by the incorporation of fatty acids, except for the micelle with oleic acid at fasted state. The correlation between the micelle size and fatty acid characteristics was not clear at fasted state. However, micelle sizes increased with increasing chain length and degree of unsaturation at fed state as suggested in the experimental studies. The solubilization of the β-carotene molecules in the mixed micelles induced different impacts on the micelle sizes. The sizes were designated by the equilibrium between the micelle size before the incorporation of β-carotenes and the core density. Additionally, the presence of additional free CHOA in the media influenced the final size. For the micelles at fasted state, the sizes were increased for lauric, stearic and linoleic acid micelles by the addition of β-carotenes. However, the small-sized oleic acid micelle became smaller after incorporation of a single β-carotene. A similar effect was observed for lauric, oleic and linoleic acid micelles at fed state. The shrinkage in size with the incorporation of unsaturated fatty acids into the micelles were attributed to the presence of double bonds, which decreases the rigidity of the tails so that they are more ready to adopt the packing requirements within the micelle core. However, the rigid structure of stearic acid because of its long and saturated tail groups resulted in increased micelle

135

size with increasing numbers of *β*-carotene molecules. On the contrary, the reason that a shrinkage in size was observed for lauric acid micelles might be due their shorter chain length. That is to say, the tails were not long enough to reach the micelle cores where the *β*-carotenes were mostly found, so they did not have a significant role in the packing of *β*-carotenes

The internal structures of the equilibrium micelles were investigated by the help of radial density distributions (RDDs) and specific angle calculations. The general aspects of the morphology were found to be similar for all micelles. The general picture is such that the hydrophobic core is composed of POPC and fatty acid tails and *β*-carotenes (when included), the glycerol moieties lie on the surface and the charged phosphate and choline groups of POPCs together with carboxylate group of fatty acids protrude from the surface to the surrounding medium where they are completely solvated with water. The cholates are located on the surface acting as wedges between the head groups of POPCs and fatty acids (when present) with their hydrophobic faces primarily pointing towards the core. Their shape is mashie-like with their sterol backbones aligned more or less flat on the surface and the charged short tails protruding into the aqueous environment with a tilt from the surface. The micelles are surrounded by an ionic double shell where the Na+ and Cl- ions constitute the inner and the outer ones, respectively. Overall, the micelles are flexible in shape, and the bile lipids behave as in fluid state as suggested by the broadness of the RDDs and the angle distributions. The results suggest that small differences might be observed for micelles of varying sizes due to changing packing constraints. For instance, the cholates were shown to sample slightly more perpendicular orientations at the surface with growing micelle size, which was attributed to the increasing packing density of the molecules at the surface before solubilization of *β*-carotenes. However, incorporation of *β*-carotenes increased core volume and cholates became moderately flatter. An improved alignment of POPC tails with radial direction was observed with increasing size for cholate and POPC micelles. The incorporation of fatty acids to the micelles effected the POPC tail alignments molecules, especially when the micelle size was smaller. The charged groups of fatty acid molecules were placed on the micelle surface and their tails pointing towards the micelle core. Still, they were not completely aligned parallel to the radial axis. The increased chain length and number of double bonds resulted with the more disordered alignment of the FA tails through the radial direction. The surface

morphology was also affected by joining of fatty acid molecules. Charged POPC head groups became more flattened on the surface while the glycerol moieties shifted towards the aqueous environment due to the increased amounts of hydrophobic parts to shield from water molecules. The β-carotene molecules were located essentially at the micelle center following their solubilization. They pushed POPC and long chain fatty acid molecules from the center towards the surface. This effect resulted with increased surface roughness due to the protrusion of POPC and fatty acid head groups in small micelles and the micelles with stearic acid because of its saturated long-chain. The overall results indicate a competition between the POPC and fatty acid tails and β-carotene molecules for the occupation of the micelle core. The orientations of the molecules in the micelle core were only slightly affected from incorporation of β-carotene molecules. The β-carotenes were highly dynamic in shape and did not adopt a completely flat conformation in the micelle core. Besides, in the small-sized micelles, they adopted even more bent conformations. Additionally, the probability of the β-carotene molecules to be located at the core was increased with increasing numbers of these molecules, due to the strong interaction in between. Moreover, they exhibited flatter conformations in the micelle core with increasing numbers of β-carotenes.

In conclusion, this study provides important knowledge about the micellization mechanisms in the upper intestinal medium under physiological conditions, the effects of different types of fatty acids on these mechanisms and the structural properties of the dietary micelles as well as the solubilization of β-carotene molecules within them. This knowledge is believed to be useful in the design of effective delivery systems for β-carotene in future studies. The study can be improved by performing atomistic simulations on the back-mapped structures of the selected micelles into atomistic resolution in order to investigate the contributions of different types of interactions (like H-bonding, electrostatic, van der Waals) more deeply. Furthermore, the mixed micelles can be used to investigate the solubilization of other types of nutraceuticals. The parameters affecting the bioaccesibilities of β-carotene molecules such as the coexistence of different types of carotenoids or additional food matrix components such as pectin can be the subject of further studies.

REFERENCES

Aizawa, H., Ichikawa, S., Kotake-Nara, E., & Nagao, A. (2017). Effects of a lysophosphatidylcholine and a phosphatidylcholine on the morphology of taurocholic acid-based mixed micelles as determined by small-angle X-ray scattering. *Journal of Dispersion Science and Technology*, 1–7. https://doi.org/10.1080/01932691.2017.1380529

Allen, M. P., & Tildesley, D. J. (1989). *Computer simulation of liquids*. Oxford: Oxford University Press.

Apol, E., Apostolov, R., Berendsen, H. J. C., Buuren, A., Bjelkmar, P., Drunen, R. van, Freenstra, A., Groenhof, G., Kasson, P., Larsson, P., Meulenhoff, P., Murtola, T., P´all, S., Pronk, S., Schulz, R., Shirts, M., Sijbers, A., Tieleman, P., Hess, B., Spoel, D., & Lindahl, E. (2010). *Gromacs User Manual- version 4.5.4*.

Arleth, L., Roskilde, D.-, Egelhaaf, S. U., Schurtenberger, P., & Pedersen, J. S. (2003). Growth Behavior of Mixed Wormlike Micelles : a Small-Angle Scattering Study of the Lecithin - Bile Salt System, (9), 4402–4410.

Arunkumar, R., Harish Prashanth, K. V., & Baskaran, V. (2013). Promising interaction between nanoencapsulated lutein with low molecular weight chitosan: characterization and bioavailability of lutein in vitro and in vivo. *Food Chemistry*, *141*(1), 327–37. https://doi.org/10.1016/j.foodchem.2013.02.108

Bennett, W. F. D., Chen, A. W., Donnini, S., Groenhof, G., & Tieleman, D. P. (2013). Constant pH simulations with the coarse-grained MARTINI model — Application to oleic acid aggregates. *Canadian Journal of Chemistry*, *91*(April), 839–846. https://doi.org/10.1139/cjc-2013-0010

Berendsen, H. J. C., Postma, J. P. M., Gunsteren, W. F. Van, Dinola, A., & Haak, J. R. (1984). Molecular dynamics with coupling to an external bath. *Journal of Chemical Physics*, *3684*(1984). https://doi.org/10.1063/1.448118

Betz, J. M., Blackman, M. R., & Levine, M. (2010). *Encyclopedia of Dietary Supplements*. *Health (San Francisco)*. https://doi.org/10.1201/b13959

Birru, W. A., Warren, D. B., Han, S., Benameur, H., Porter, C. J. H., Pouton, C. W., & Chalmers, D. K. (2017). Computational Models of the Gastrointestinal Environment. 2. Phase Behavior and Drug Solubilization Capacity of a Type I

Lipid-Based Drug Formulation after Digestion. *Molecular Pharmaceutics*, *14*(3), 580–592. https://doi.org/10.1021/acs.molpharmaceut.6b00887

Birru, W. A., Warren, D. B., Headey, S. J., Benameur, H., Porter, C. J. H., Pouton, C. W., & Chalmers, D. K. (2017). Computational Models of the Gastrointestinal Environment. 1. The Effect of Digestion on the Phase Behavior of Intestinal Fluids. *Molecular Pharmaceutics*, *14*(3), 566–579. https://doi.org/10.1021/acs.molpharmaceut.6b00888

Birru, W. A., Warren, D. B., Ibrahim, A., Williams, H. D., Benameur, H., Porter, C. J. H., Chalmers, D. C., & Pouton, C. W. (2014). Digestion of phospholipids after secretion of bile into the duodenum changes the phase behavior of bile components. *Molecular Pharmaceutics*, *11*(8), 2825–2834. https://doi.org/10.1021/mp500193g

Bogusz, S., Venable, R. M., & Pastor, R. W. (2000). Molecular Dynamics Simulations of Octyl Glucoside Micelles : Structural Properties, (Md), 5462–5470.

Borel, P. (2003). Factors Affecting Intestinal Absorption of Highly Lipophilic Food Microconstituents (Fat-Soluble Vitamins , Carotenoids and Phytosterols). *Clinical Chemistry and Laboratory Medicine : CCLM / FESCC*, *41*(8), 979–994.

Brocos, P., Mendoza-Espinosa, P., Castillo, R., Mas-Oliva, J., & Piñeiro, Á. (2012). Multiscale molecular dynamics simulations of micelles: coarse-grain for self-assembly and atomic resolution for finer details. *Soft Matter*, *8*(34), 9005. https://doi.org/10.1039/c2sm25877c

Brown, M. J., Ferruzzi, M. G., Nguyen, M. L., Cooper, D. A., Eldridge, A. L., Schwartz, S. J., & White, W. S. (2004). Carotenoid bioavailability is higher from salads ingested with full-fat than with fat-reduced salad dressings as measured with electrochemical detection. *American Journal of Clinical Nutrition*, *80*(2), 396–403. https://doi.org/80/2/396 [pii]

Castenmiller, J. J., & West, C. E. (1998). Bioavailability and bioconversion of carotenoids. *Annual Review of Nutrition*, *18*, 19–38. https://doi.org/10.1146/annurev.nutr.18.1.19

Charman, W. N., Porter, C. J. H., Mithani, S., & Dressman, J. B. (1997). Physicochemical and Physiological Mechanisms for the Effects of Food on Drug Absorption : The Role of Lipids and pH. *The Journal of Pharmaceutical Sciences*, *86*(3), 269–282.

Chitchumroonchokchai, C., Schwartz, S. J., & Failla, M. L. (2004). Assessment of lutein bioavailability from meals and a supplement using simulated digestion and caco-2 human intestinal cells. *The Journal of Nutrition*, *134*(9), 2280–2286. https://doi.org/134/9/2280 [pii]

Clulow, A. J., Parrow, A., Hawley, A., Khan, J., Pham, A. C., Larsson, P., Bergström, C. A. S., & Boyd, B. J. (2017). Characterization of Solubilizing Nanoaggregates Present in Different Versions of Simulated Intestinal Fluid. *Journal of Physical Chemistry B*, *121*(48), 10869–10881. https://doi.org/10.1021/acs.jpcb.7b08622

Cohen, D. E., Thurston, G. M., Chamberlin, R. A., Benedek, G. B., & Carey, M. C. (1998). Laser light scattering evidence for a common wormlike growth structure of mixed micelles in bile salt- and straight-chain detergent- phosphatidylcholine aqueous systems: Relevance to the micellar structure of bile. *Biochemistry*, *37*(42), 14798–14814. https://doi.org/10.1021/bi980182y

Coreta-Gomes, F. M., Vaz, W. L. C., Wasielewski, E., Geraldes, C. F. G., & Moreno, M. J. (2016). Quantification of cholesterol solubilized in dietary micelles: Dependence on human bile salt variability and the presence of dietary food ingredients. *Langmuir*, *32*(18), 4564–4574. https://doi.org/10.1021/acs.langmuir.6b00723

Daily, M. D., Olsen, B. N., Schlesinger, P. H., Ory, D. S., & Baker, N. A. (2014). Improved Coarse-Grained Modeling of Cholesterol-Containing Lipid Bilayers. *Journal of Chemical Theory and Computation*, *10*, 2137–2150.

de Jong, D. H., Liguori, N., van den Berg, T., Arnarez, C., Periole, X., & Marrink, S. J. (2015). Atomistic and Coarse Grain Topologies for the Cofactors Associated with the Photosystem II Core Complex. *The Journal of Physical Chemistry. B*, *119*(25), 7791–7803. https://doi.org/10.1021/acs.jpcb.5b00809

Desmarchelier, C., & Borel, P. (2017). Overview of carotenoid bioavailability determinants: From dietary factors to host genetic variations. *Trends in Food Science and Technology*, *69*, 270–280. https://doi.org/10.1016/j.tifs.2017.03.002

Doucet, J.-P., & Weber, J. (1997). *Computer-Aided Molecular Design: Theory and Applications*. Academic Press.

Elbe, J. H. von, & Schwartz, S. J. (1996). *Colorants*. (R. F. Owen, Ed.), *Food Chemistry* (Third eddi). New York: Marcel Dekker. https://doi.org/10.1016/0260-8774(88)90055-6

Failla, M. L., Chitchumronchokchai, C., Ferruzzi, M. G., Goltz, S. R., & Campbell, W. W. (2014). Unsaturated fatty acids promote bioaccessibility and basolateral secretion of carotenoids and α-tocopherol by Caco-2 cells. *Food & Function*, *5*(6), 1101–1112. https://doi.org/10.1039/c3fo60599j

Fatouros, D. G., Bergenstahl, B., & Mullertz, A. (2007). Morphological observations on a lipid-based drug delivery system during in vitro digestion. *European Journal of Pharmaceutical Sciences*, *31*(2), 85–94. https://doi.org/10.1016/j.ejps.2007.02.009

Fatouros, D. G., Deen, G. R., Arleth, L., Bergenstahl, B., Nielsen, F. S., Pedersen, J. S., & Mullertz, A. (2007). Structural development of self nano emulsifying drug delivery systems (SNEDDS) during in vitro lipid digestion monitored by Small-angle X-ray scattering. *Pharmaceutical Research*, *24*(10), 1844–1853. https://doi.org/10.1007/s11095-007-9304-6

Fatouros, D. G., Walrand, I., Bergenstahl, B., & Mullertz, A. (2009). Physicochemical Characterization of Simulated Intestinal Fed-State Fluids Containing Lyso-Phosphatidylcholine and Cholesterol, (August), 47–50.

Fatouros, D. G., Walrand, I., Bergenstahl, B., & Müllertz, A. (2009). Colloidal structures in media simulating intestinal fed state conditions with and without lipolysis products. *Pharmaceutical Research*, *26*(2), 361–74. https://doi.org/10.1007/s11095-008-9750-9

Fernández-García, E., Mínguez-Mosquera, M. I., & Pérez-Gálvez, A. (2007). Changes in composition of the lipid matrix produce a differential incorporation of carotenoids in micelles. Interaction effect of cholesterol and oil. *Innovative Food Science & Emerging Technologies*, *8*(3), 379–384. https://doi.org/10.1016/j.ifset.2007.03.016

Fotouros, D. G., Walrand, I., Bergenstahl, B., & Mullertz, A. (2009). Physicochemical Characterization of Simulated Intestinal Fed-State Fluids Containing Lyso-Phosphatidylcholine and Cholesterol. *Dissolution Technologies*, (August), 47–50.

Frenkel, D., & Smith, B. (2002). *Understanding Molecular Simulations*. Academic Press.

German, J. B., & Dillard, C. J. (2004). Saturated fats : what dietary intake ? *American Journal of Clinical Nutrition*, *80*(February), 550–559.

Gleize, B., Tourniaire, F., Depezay, L., Bott, R., Nowicki, M., Albino, L., Lairon, D.,

Kesse-Guyot, E., Galan, P., Hercberg, S., & Borel, P. (2013). Effect of type of TAG fatty acids on lutein and zeaxanthin bioavailability. *The British Journal of Nutrition*, *110*(1), 1–10. https://doi.org/10.1017/S0007114512004813

Gorusupudi, A., & Vallikannan, B. (2012). Glycolipids improve lutein bioavailability and accumulation in eyes in mice. *European Journal of Lipid Science and Technology*, *114*(7), 710–717. https://doi.org/10.1002/ejlt.201100183

Grundy, S. M., & Metzger, A. L. (1972). A Physiological Method for Estimation of Hepatic Secretion of Biliary Lipids in Man. *Gastroenterology*, *62*(6), 1200–1217. https://doi.org/10.1016/S0016-5085(72)80089-1

Haustein, M., Schiller, P., Wahab, M., & Mögel, H.-J. (2014). Computer Simulations of the Formation of Bile Salt Micelles and Bile Salt/DPPC Mixed Micelles in Aqueous Solutions. *Journal of Solution Chemistry*, *43*(9–10), 1755–1770. https://doi.org/10.1007/s10953-014-0239-3

Hedrén, E., Diaz, V., & Svanberg, U. (2002). Estimation of carotenoid accessibility from carrots determined by an in vitro digestion method. *European Journal of Clinical Nutrition*, *56*(5), 425–30. https://doi.org/10.1038/sj.ejcn.1601329

Hemell, O., Staggers, J. E., & Carey, M. C. (1990). Digestion and Absorption . 2 . Phase Analysis and Aggregation States of Luminal Lipids during Duodenal Fat Digestion in Healthy Adult Human Beings

Hess, B., Kutzner, C., Van Der Spoel, D., & Lindahl, E. (2008). GRGMACS 4: Algorithms for highly efficient, load-balanced, and scalable molecular simulation. *Journal of Chemical Theory and Computation*, *4*(3), 435–447. https://doi.org/10.1021/ct700301q

Hildebrand, A., Neubert, R., Garidel, P., & Blume, A. (2002). Bile salt induced solubilization of synthetic phosphatidylcholine vesicles studied by isothermal titration calorimetry. *Langmuir*, *18*(7), 2836–2847. https://doi.org/10.1021/la011421c

Hjelm, R. P. (1992). Organization of phosphatidylcholine and bile salt in rodlike mixed micelles, 8653–8661. https://doi.org/10.1021/j100200a080

Hjelm, R. P., Alkan, M. H., & Thiyagarajan, P. (1990). Small-Angle Neutron Scattering Studies of Mixed Bile Salt-Lecithin Colloids. *Molecular Crystals and Liquid Crystals Incorporating Nonlinear Optics*, *180*(1), 155–164.

Hjelm, R. P., Schteingart, C. D., Hofmann, A. F., & Thiyagarajan, P. (2000). Structure of Conjugated Bile Salt−Fatty Acid−Monoglyceride Mixed Colloids: Studies by Small-Angle Neutron Scattering. *The Journal of Physical Chemistry B*, *104*(2), 197–211. https://doi.org/10.1021/jp992157n

Holden, J. M., Eldridge, A. L., Beecher, G. R., Buzzard, I. M., Bhagwat, S., Davis, C. S., Douglass, L. W., Gebhardt, S., Haytowitz, D., & Schakel, S. (1999). Carotenoid Content of U . S . Foods : An Update of the Database. *Journal of Food Composition and Analysis*, *12*, 169–196.

Hornero-Méndez, D., & Mínguez-Mosquera, M. I. (2007). Bioaccessibility of carotenes from carrots: Effect of cooking and addition of oil. *Innovative Food Science & Emerging Technologies*, *8*(3), 407–412. https://doi.org/10.1016/j.ifset.2007.03.014

Huo, T., Ferruzzi, M. G., Schwartz, S. J., & Failla, M. L. (2007). Impact of fatty acyl composition and quantity of triglycerides on bioaccessibility of dietary carotenoids. *Journal of Agricultural and Food Chemistry*, *55*(22), 8950–8957. https://doi.org/10.1021/jf071687a

Janke, J. J., Bennett, W. F. D., & Tieleman, D. P. (2014). Oleic acid phase behavior from molecular dynamics simulations. *Langmuir : The ACS Journal of Surfaces and Colloids*, *30*(35), 10661–7. https://doi.org/10.1021/la501962n

Jójárt, B., Poša, M., Fiser, B., Szőri, M., Farkaš, Z., & Viskolcz, B. (2014). Mixed Micelles of Sodium Cholate and Sodium Dodecylsulphate 1:1 Binary Mixture at Different Temperatures – Experimental and Theoretical Investigations. *PLoS ONE*, *9*(7), e102114. https://doi.org/10.1371/journal.pone.0102114

Jójárt, B., Viskolcz, B., Poša, M., & Fejer, S. N. (2014). Global optimization of cholic acid aggregates. *Journal of Chemical Physics*, *140*(14). https://doi.org/10.1063/1.4869832

Khoshakhlagh, P., Johnson, R., Nawroth, T., Langguth, P., Schmueser, L., Hellmann, N., Decker, H., & Szekely, N. K. (2014). Nanoparticle structure development in the gastro-intestinal model fluid FaSSIF mod6.5 from several phospholipids at various water content relevant for oral drug administration. *European Journal of Lipid Science and Technology*, *116*(9), 1155–1166. https://doi.org/10.1002/ejlt.201400066

Kleberg, K., Jacobsen, F., Fatouros, D. G., & Müllertz, A. (2010). Biorelevant Media Simulating Fed State Intestinal Fluids: Colloid Phase Characterization and Impact on Solubilization Capacity. *Journal of Pharmaceutical Sciences*, *99*(8), 3522-3532.

Knockaert, G., Lemmens, L., Van Buggenhout, S., Hendrickx, M., & Van Loey, A. (2012). Changes in β-carotene bioaccessibility and concentration during processing of carrot puree. *Food Chemistry*, *133*(1), 60–67. https://doi.org/10.1016/j.foodchem.2011.12.066

Kopec, R. E., & Failla, M. L. (2018). Recent advances in the bioaccessibility and bioavailability of carotenoids and effects of other dietary lipophiles. *Journal of Food Composition and Analysis*, *68*(May 2017), 16–30. https://doi.org/10.1016/j.jfca.2017.06.008

Kossena, G. A., Boyd, B. J., Porter, C. J. H., & Charman, W. N. (2003). Separation and characterization of the colloidal phases produced on digestion of common formulation lipids and assessment of their impact on the apparent solubility of selected poorly water-soluble drugs. *Journal of Pharmaceutical Sciences*, *92*(3), 634–648. https://doi.org/10.1002/jps.10329

Kotake-Nara, E., Yonekura, L., & Nagao, A. (2015). Glyceroglycolipids Affect Uptake of Carotenoids Solubilized in Mixed Micelles by Human Intestinal Caco-2 Cells. *Lipids*, *50*(9), 847–860. https://doi.org/10.1007/s11745-015-4033-9

Kraft, J. F., Vestergaard, M., Schiøtt, B., & Thøgersen, L. (2012). Modeling the self-assembly and stability of DHPC micelles using atomic resolution and coarse grained MD simulations. *Journal of Chemical Theory and Computation*, *8*(5), 1556–1569. https://doi.org/10.1021/ct200921u

Lakshminarayana, R., & Baskaran, V. (2013). Influence of olive oil on the bioavailability of carotenoids. *European Journal of Lipid Science and Technology*, *115*(10), 1085–1093. https://doi.org/10.1002/ejlt.201200254

Lakshminarayana, R., Raju, M., Keshava Prakash, M. N., & Baskaran, V. (2009). Phospholipid, oleic acid micelles and dietary olive oil influence the lutein absorption and activity of antioxidant enzymes in rats. *Lipids*, *44*(9), 799–806. https://doi.org/10.1007/s11745-009-3328-0

Leach, A. R. (2001). Molecular modelling principles and applications (Second Edd). New York: Prentice Hall.

Lebecque, S., Crowet, J.-M., Nasir, M. N., Deleu, M., & Lins, L. (2017). Molecular dynamics study of micelles properties according to their size. *J. Phys. Chem. B*, *72*, 6–15. https://doi.org/10.1016/j.jmgm.2016.12.007

Lin, T. L., Chen, S. H., Gabriel, N. E., & Roberts, M. F. (1986). Use of Small-Angle Neutron Scattering To Determine the Structure and Interaction of Dihexanoylphosphatidylcholine Micelles. *Journal of the American Chemical Society*, *108*(12), 3499–3507. https://doi.org/10.1021/ja00272a055

Liu, X., Bi, J., Xiao, H., & McClements, D. J. (2015). Increasing Carotenoid Bioaccessibility from Yellow Peppers Using Excipient Emulsions: Impact of Lipid Type and Thermal Processing. *Journal of Agricultural and Food Chemistry*, *63*(38), 8534–8543. https://doi.org/10.1021/acs.jafc.5b04217

Madenci, D., & Egelhaaf, S. U. (2010). Self-assembly in aqueous bile salt solutions. *Current Opinion in Colloid and Interface Science*, *15*(1–2), 109–115. https://doi.org/10.1016/j.cocis.2009.11.010

Madenci, D., Salonen, A., Schurtenberger, P., Pedersen, J. S., & Egelhaaf, S. U. (2011). Simple model for the growth behaviour of mixed lecithin-bile salt micelles. *Physical Chemistry Chemical Physics*, *13*(8), 3171–3178. https://doi.org/10.1039/c0cp01700k

Maiani, G., Caston, M. J. P., Catasta, G., Toti, E., Cambrodon, I. G., Bysted, A., Granado-Lorencio, F., Olmedilla-Alonso, B., Knuthsen, P., Valoti, M., Böhm, V., Mayer-Miebach, E., Behsnilian, D., & Schlemmer, U. (2009). Carotenoids: Actual knowledge on food sources, intakes, stability and bioavailability and their protective role in humans. *Molecular Nutrition and Food Research*, *53*(SUPPL. 2), 194–218. https://doi.org/10.1002/mnfr.200800053

Marisiddaiah, R., Rangaswamy, L., & Vallikannan, B. (2011). Single oral dose of micellar β -carotene containing phospholipids improves carotene metabolism and plasma lipids in vitamin A-deficient rats. *European Journal of Nutrition*, *50*(7), 531–541. https://doi.org/10.1007/s00394-010-0160-5

Markina, A. A., Ivanov, V. A., Komarov, P. V., Khokhlov, A. R., & Tung, S. H. (2017). Self-Assembly of Lecithin and Bile Salt in the Presence of Inorganic Salt in Water: Mesoscale Computer Simulation. *Journal of Physical Chemistry B*, *121*(33), 7878–7888. https://doi.org/10.1021/acs.jpcb.7b04566

Marrink, S.-J., Fuhrmans, M., Risselada, H. J., & Periole, X. (2009). *The MARTINI Force Field*. (G. A. Voth, Ed.), *CoarseGraining of Condensed Phase and Biomolecular Systems*. CRC Press. https://doi.org/10.1201/9781420059564

Marrink, S. (2004). Molecular dynamics simulation of cholesterol nucleation in mixed micelles modelling human bile. *Gallstones: Pathogenesis and Treatment*, 98–105.

Marrink, S. J., & Mark, a. E. (2002). Molecular Dynamics Simulations of Mixed Micelles Modeling Human Bile. *Biochemistry*, *41*(17), 5375–5382. https://doi.org/10.1021/bi015613i

Marrink, S. J., Risselada, H. J., Yefimov, S., Tieleman, D. P., & Vries, A. H. De. (2007). The MARTINI Force Field : Coarse Grained Model for Biomolecular Simulations, *111*(June), 7812–7824. https://doi.org/10.1021/jp071097f

Marrink, S. J., & Tieleman, D. P. (2013). Perspective on the Martini model. *Chemical Society Reviews*, *42*(16), 6801–22. https://doi.org/10.1039/c3cs60093a

Marrink, S., Vries, A. De, & Mark, A. (2004). Coarse grained model for semiquantitative lipid simulations. *The Journal of Physical Chemistry B*, 750–760. https://doi.org/10.1021/jp036508g

Matsuoka, K., Maeda, M., & Moroi, Y. (2004). Characteristics of conjugate bile salt–phosphatidylcholine–cholesterol–water systems. *Colloids and Surfaces B: Biointerfaces*, *33*(2), 101–109. https://doi.org/10.1016/j.colsurfb.2003.09.002

Matsuoka, K., Rie, E., Yui, S., Honda, C., & Endo, K. (2012). Competitive solubilization of cholesterol and ??-sitosterol with changing biliary lipid compositions in model intestinal solution. *Chemistry and Physics of Lipids*, *165*(1), 7–14. https://doi.org/10.1016/j.chemphyslip.2011.10.004

Mazer, N. A., Benedek, G. B., & Carey, M. C. (1980). Quasielastic Light-Scattering Studies of Aqueous Biliary Lipid Systems. Mixed Micelle Formation in Bile Salt-Lecithin Solutions. *Biochemistry*, *19*(4), 601–615. https://doi.org/10.1021/bi00545a001

Morrow, B. H., Koenig, P. H., & Shen, J. K. (2012). Atomistic simulations of pH-dependent self-assembly of micelle and bilayer from fatty acids. *Journal of Chemical Physics*, *137*(19). https://doi.org/10.1063/1.4766313

Müllertz, A., Fatouros, D. G., Smith, J. R., Vertzoni, M., & Reppas, C. (2012). Insights into intermediate phases of human intestinal fluids visualized by atomic force microscopy and cryo-transmission electron microscopy ex vivo. *Molecular Pharmaceutics*, *9*(2), 237–47. https://doi.org/10.1021/mp200286x

Murkovic, M., Gams, K., Draxl, S., & Pfannhauser, W. (2000). Development of an Austrian carotenoid database. *Journal of Food Composition and Analysis*, *13*(4), 435–440. https://doi.org/10.1006/jfca.2000.0909

Nagao, A., During, A., Hoshino, C., Terao, J., & Olson, J. A. (1996). Stoichiometric conversion of all trans-β-carotene to retinal by pig intestinal extract. *Archives of Biochemistry and Biophysics*, *328*(1), 57–63. https://doi.org/10.1006/abbi.1996.0142

Nagao, A., Kotake-Nara, E., & Hase, M. (2013). Effects of fats and oils on the bioaccessibility of carotenoids and vitamin E in vegetables. *Bioscience, Biotechnology, and Biochemistry*, *77*(5), 1055–60. https://doi.org/10.1271/bbb.130025

Namitha, K. K., & Negi, P. S. (2010). Chemistry and biotechnology of carotenoids. *Critical Reviews in Food Science and Nutrition*, *50*(8), 1040–8398. https://doi.org/10.1080/10408398.2010.499811

Nichols, J. W., & Ozarowski, J. (1990). Sizing of Lecithin-Bile Salt Mixed Micelles by Size-Exclusion High-Performance Liquid Chromatography. *Biochemistry*, *29*(19), 4600–4606. https://doi.org/10.1021/bi00471a014

O'Neill, M. E., Carroll, Y., Corridan, B., Olmedilla, B., Granado, F., Blanco, I., Berg, H., Hininger, I., Rousell, A. M., Chopra, M., Southon, S., & Thurnham, D. I. (2001). A European carotenoid database to assess carotenoid intakes and its use in a five-country comparative study. *British Journal of Nutrition*, *85*(04), 499. https://doi.org/10.1079/BJN2000284

O'Sullivan, L., Ryan, L., Aherne, S. A., & O'Brien, N. M. (2008). Cellular transport of lutein is greater from uncooked rather than cooked spinach irrespective of whether it is fresh, frozen, or canned. *Nutrition Research (New York, N.Y.)*, *28*(8), 532–8. https://doi.org/10.1016/j.nutres.2008.05.011

Parker, R. S. (1996). Transport of Carotenoids. *The FASEB Journal*, *10*(5), 542–551. Retrieved from http://www.fasebj.org/content/10/5/542.short

Pártay, L. B., Jedlovszky, P., & Sega, M. (2007). Molecular aggregates in aqueous solutions of bile acid salts. Molecular dynamics simulation study. *The Journal of Physical Chemistry. B*, *111*(33), 9886–96. https://doi.org/10.1021/jp072974k

Pártay, L. B., Sega, M., & Jedlovszky, P. (2007). Morphology of bile salt micelles as studied by computer simulation methods. *Langmuir : The ACS Journal of Surfaces and Colloids*, *23*(24), 12322–8. https://doi.org/10.1021/la701749u

Pârtay, L. B., Sega, M., & Jedlovszky, P. (2008). Counterion binding in the aqueous

solutions of bile acid salts, as studied by computer simulation methods. *Langmuir*, *24*(19), 10729–10736. https://doi.org/10.1021/la801352d

Periole, X., & Marrink, S. (2013). *Biomolecular Simulations* (Vol. 924). https://doi.org/10.1007/978-1-62703-017-5

Phan, S., Hawley, A., Mulet, X., Waddington, L., Prestidge, C. A., & Boyd, B. J. (2013). Structural aspects of digestion of medium chain triglycerides studied in real time using sSAXS and Cryo-TEM. *Pharmaceutical Research*, *30*(12), 3088–3100. https://doi.org/10.1007/s11095-013-1108-2

Phan, S., Salentinig, S., Gilbert, E., Darwish, T. A., Hawley, A., Nixon-Luke, R., Bryant, G., & Boyd, B. J. (2015). Disposition and crystallization of saturated fatty acid in mixed micelles of relevance to lipid digestion. *Journal of Colloid and Interface Science*, *449*, 160–166. https://doi.org/10.1016/j.jcis.2014.11.026

Phan, S., Salentinig, S., Prestidge, C. A., & Boyd, B. J. (2014). Self-assembled structures formed during lipid digestion: Characterization and implications for oral lipid-based drug delivery systems. *Drug Delivery and Translational Research*, *4*(3), 275–294. https://doi.org/10.1007/s13346-013-0168-5

Porter, C. J. H., Kaukonen, A. M., Taillardat-Bertschinger, A., Boyd, B. J., O'Connor, J. M., Edwards, G. A., & Charman, W. N. (2004). Use of in Vitro Lipid Digestion Data to Explain the in Vivo Performance of Triglyceride-Based Oral Lipid Formulations of Poorly Water-Soluble Drugs: Studies with Halofantrine. *Journal of Pharmaceutical Sciences*, *93*(5), 1110–1121. https://doi.org/10.1002/jps.20039

Prakash, P., & Gorfe, A. a. (2013). Phosphatidylcholine attenuates aggregation of nonsteroidal anti-inflammatory drugs with bile acid. *Biochemistry*, *52*(42), 7461–7469. https://doi.org/10.1021/bi400723r

Prakash, P., Sayyed-Ahmad, A., Zhou, Y., Volk, D. E., Gorenstein, D. G., Dial, E., Lichtenberger, L. M., & Gorfe, A. a. (2012). Aggregation behavior of ibuprofen, cholic acid and dodecylphosphocholine micelles. *Biochimica et Biophysica Acta*, *1818*(12), 3040–7. https://doi.org/10.1016/j.bbamem.2012.07.029

Qian, C., Decker, E. A., Xiao, H., & McClements, D. J. (2012). Nanoemulsion delivery systems: Influence of carrier oil on β-carotene bioaccessibility. *Food Chemistry*, *135*(3), 1440–1447. https://doi.org/10.1016/j.foodchem.2012.06.047

Rao, a V, & Rao, L. G. (2007). Carotenoids and human health. *Pharmacological*

Research : The Official Journal of the Italian Pharmacological Society, *55*(3), 207–16. https://doi.org/10.1016/j.phrs.2007.01.012

Rezhdo, O., Di Maio, S., Le, P., Littrell, K. C., Carrier, R. L., & Chen, S. H. (2017). Characterization of colloidal structures during intestinal lipolysis using small-angle neutron scattering. *Journal of Colloid and Interface Science*, *499*, 189–201. https://doi.org/10.1016/j.jcis.2017.03.109

Rich, G. T., Bailey, A. L., Faulks, R. M., Parker, M. L., Wickham, M. S. J., & Fillery-Travis, A. (2003). Solubilization of carotenoids from carrot juice and spinach in lipid phases: I. Modeling the gastric lumen. *Lipids*, *38*(9), 933–945. https://doi.org/10.1007/s11745-003-1147-0

Risselada, H. J., & Marrink, S. J. (2008). The molecular face of lipid rafts in model membranes. *Proceedings of the National Academy of Sciences of the United States of America*, *105*(45), 17367–72. https://doi.org/10.1073/pnas.0807527105

Roodenburg, A. J. C., Leenen, R., Hof, K. H. Van, Weststrate, J. A., & Tijburg, L. B. M. (2000). Amount of fat in the diet affects bioavailability of lutein esters but not of a-carotene , b -carotene , and vitamin E in humans. *American Journal of Clinical Nutrition*, *71*(April), 1187–1193.

Rozner, S., Shalev, D. E., Shames, A. I., Ottaviani, M. F., Aserin, A., & Garti, N. (2010). Do food microemulsions and dietary mixed micelles interact? *Colloids and Surfaces. B, Biointerfaces*, *77*(1), 22–30. https://doi.org/10.1016/j.colsurfb.2009.12.026

Saini, R. K., Nile, S. H., & Park, S. W. (2015). Carotenoids from fruits and vegetables: Chemistry, analysis, occurrence, bioavailability and biological activities. *Food Research International*, *76*, 735–750. https://doi.org/10.1016/j.foodres.2015.07.047

Salentinig, S., Phan, S., Darwish, T. a, Kirby, N., Boyd, B. J., & Gilbert, E. P. (2014). pH-responsive micelles based on caprylic acid. *Langmuir : The ACS Journal of Surfaces and Colloids*, *30*(25), 7296–303. https://doi.org/10.1021/la500835e

Salentinig, S., Sagalowicz, L., Leser, M. E., Tedeschi, C., & Glatter, O. (2011). Transitions in the internal structure of lipid droplets during fat digestion. *Soft Matter*, *7*(2), 650–661. https://doi.org/10.1039/c0sm00491j

Salvia-Trujillo, L., Qian, C., Martín-Belloso, O., & McClements, D. J. (2013).

Modulating β-carotene bioaccessibility by controlling oil composition and concentration in edible nanoemulsions. *Food Chemistry*, *139*(1–4), 878–84. https://doi.org/10.1016/j.foodchem.2013.02.024

Sanders, S. A., & Panagiotopoulos, A. Z. (2010). Micellization behavior of coarse grained surfactant models. *Journal of Chemical Physics*, *132*(11). https://doi.org/10.1063/1.3358354

Sayyed-Ahmad, A., Lichtenberger, L. M., & Gorfe, A. a. (2010). Structure and dynamics of cholic acid and dodecylphosphocholine-cholic acid aggregates. *Langmuir : The ACS Journal of Surfaces and Colloids*, *26*(16), 13407–14. https://doi.org/10.1021/la102106t

Schersten, T. (1973). Formation of Lithogenic Bile in Man. *Digestion*, *9*, 540–553.

Schurtenberger, P., Mazer, N., & Kanzig, W. (1985). Micelle to Vesicle Transition in Aqueous Solutions of Bile Salt and Lecithin. *Journal of Phyical Chemistry*, *89*(6), 1042–1049. https://doi.org/10.1021/j100252a031

Sek, L., Porter, C. J. H., Kaukonen, A. M., & Charman, W. N. (2002). Evaluation of the in-vitro digestion profiles of long and medium chain glycerides and the phase behaviour of their lipolytic products. *The Journal of Pharmacy and Pharmacology*, *54*(1), 29–41. Retrieved from http://www.ncbi.nlm.nih.gov/pubmed/11833493

Smolin, L. A., & Grosvenor, M. B. (2007). *Nutrition Science & Applications* (Second Edi). United States of America.

Socaciu, C. (2008). *Food Colorants Chemical and Functional Properties*. https://doi.org/10.1201/9781420031713.ch1

Staggers, J. E., Hernell, O., Stafford, R. J., & Carey, M. C. (1990). Physical-chemical behavior of dietary and biliary lipids during intestinal digestion and absorption. 1. Phase behavior and aggregation states of model lipid systems patterned after aqueous duodenal contents of healthy adult human beings. *Biochemistry*, *29*(8), 2028–40. Retrieved from http://www.ncbi.nlm.nih.gov/pubmed/2328237

Suys, E. J. A., Warren, D. B., Porter, C. J. H., Benameur, H., Pouton, C. W., & Chalmers, D. K. (2017). Computational Models of the Intestinal Environment. 3. the Impact of Cholesterol Content and pH on Mixed Micelle Colloids. *Molecular Pharmaceutics*, *14*(11), 3684–3697. https://doi.org/10.1021/acs.molpharmaceut.7b00446

Svard, M., Schurtenberger, P., Fontell, K., Joensson, B., & Lindman, B. (1988). Micelles, vesicles, and liquid crystals in the monoolein-sodium taurocholate-water system: phase behavior, NMR, self-diffusion, and quasi-elastic light scattering studies. *The Journal of Physical Chemistry*, *92*(8), 2261–2270. https://doi.org/10.1021/j100319a034

Sy, C., Gleize, B., Dangles, O., Landrier, J.-F., Veyrat, C. C., & Borel, P. (2012). Effects of physicochemical properties of carotenoids on their bioaccessibility, intestinal cell uptake, and blood and tissue concentrations. *Molecular Nutrition & Food Research*, *56*(9), 1385–97. https://doi.org/10.1002/mnfr.201200041

Tande, B. M., Wagner, N. J., Mackay, M. E., Hawker, C. J., & Jeong, M. (2001). Viscosimetric, hydrodynamic, and conformational properties of dendrimers and dendrons. *Macromolecules*, *34*(24), 8580–8585. https://doi.org/10.1021/ma011265g

Tieleman, D. P., van der Spoel, D., & Berendsen, H. J. C. (2000). Molecular Dynamics Simulations of Dodecylphosphocholine Micelles at Three Different Aggregate Sizes: Micellar Structure and Chain Relaxation. *The Journal of Physical Chemistry B*, *104*(27), 6380–6388. https://doi.org/10.1021/jp001268f

Turner, D. C., Yin, F., Kindt, J. T., & Zhang, H. (2010). Molecular dynamics simulations of glycocholate-oleic acid mixed micelle assembly. *Langmuir : The ACS Journal of Surfaces and Colloids*, *26*(7), 4687–92. https://doi.org/10.1021/la903573m

Van Buggenhout, S., Alminger, M., Lemmens, L., Colle, I., Knockaert, G., Moelants, K., Van Loey, A. & Hendrickx, M. (2010). In vitro approaches to estimate the effect of food processing on carotenoid bioavailability need thorough understanding of process induced microstructural changes. *Trends in Food Science & Technology*, *21*(12), 607–618. https://doi.org/10.1016/j.tifs.2010.09.010

Van Eerden, F. J., Van Den Berg, T., Frederix, P. W. J. M., De Jong, D. H., Periole, X., & Marrink, S. J. (2017). Molecular Dynamics of Photosystem II Embedded in the Thylakoid Membrane. *Journal of Physical Chemistry B*, *121*(15), 3237–3249. https://doi.org/10.1021/acs.jpcb.6b06865

Verde, A. V., & Frenkel, D. (2010). Simulation study of micelle formation by bile salts. *Soft Matter*, *6*(16), 3815. https://doi.org/10.1039/c0sm00011f

Vila Verde, A., & Frenkel, D. (2016). Kinetics of formation of bile salt micelles from coarse-grained Langevin dynamics simulations. *Soft Matter*, *12*(23), 5172–5179.

Warren, D. B., Chalmers, D. K., Hutchison, K., Dang, W., & Pouton, C. W. (2006). Molecular dynamics simulations of spontaneous bile salt aggregation. *Colloids and Surfaces A: Physicochemical and Engineering Aspects*, *280*(1–3), 182–193. https://doi.org/10.1016/j.colsurfa.2006.02.009

Werner, A. (2005). *University of Groningen Essential fatty acid absorption and metabolism in hepatic disorders Werner, Anniek*. University of Groningen.

Wilson, M. D., & Rudel, L. L. (1994). Review of cholesterol absorption with emphasis on dietary and biliary cholesterol. *Journal of Lipid Research*, *35*(6), 943–955.

Xia, Z., McClements, D. J., & Xiao, H. (2017). Influence of Lipid Content in a Corn Oil Preparation on the Bioaccessibility of β-Carotene: A Comparison of Low-Fat and High-Fat Samples. *Journal of Food Science*, *82*(2), 373–379. https://doi.org/10.1111/1750-3841.13599

Xie, X., Cardot, J. M., Garrait, G., Thery, V., El-Hajji, M., & Beyssac, E. (2014). Micelle dynamic simulation and physicochemical characterization of biorelevant media to reflect gastrointestinal environment in fasted and fed states. *European Journal of Pharmaceutics and Biopharmaceutics*, *88*(2), 565–573. https://doi.org/10.1016/j.ejpb.2014.05.020

Yao, M., Xiao, H., & McClements, D. J. (2014). Delivery of lipophilic bioactives: assembly, disassembly, and reassembly of lipid nanoparticles. *Annual Review of Food Science and Technology*, *5*, 53–81. https://doi.org/10.1146/annurev-food-072913-100350

Yonekura, L., & Nagao, A. (2007). Intestinal absorption of dietary carotenoids. *Molecular Nutrition & Food Research*, *51*(1), 107–15. https://doi.org/10.1002/mnfr.200600145

Yonekura, L., Tsuzuki, W., & Nagao, A. (2006). Acyl moieties modulate the effects of phospholipids on β-carotene uptake by Caco-2 cells. *Lipids*, *41*(7), 629–636. https://doi.org/10.1007/s11745-006-5013-x
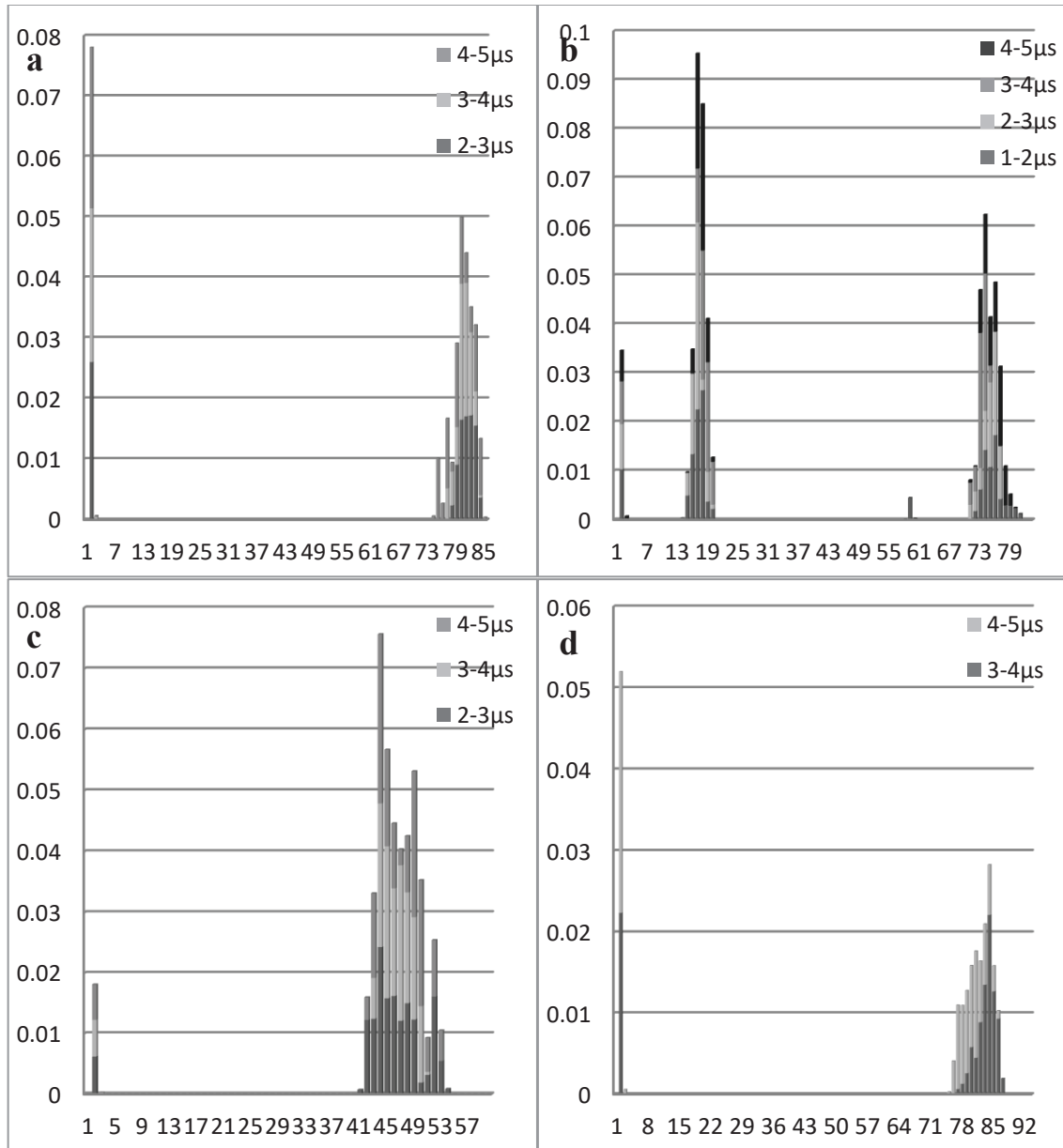
ADDITIONAL DATA

Figure A.1. Cumulative probability distributions of aggregation numbers as a function of time (block-averaged over 1 μs intervals) after the equilibration of the with a) Lauric, b) Stearic, c) Oleic and d) Linoleic acids <u>at fasted state</u>.

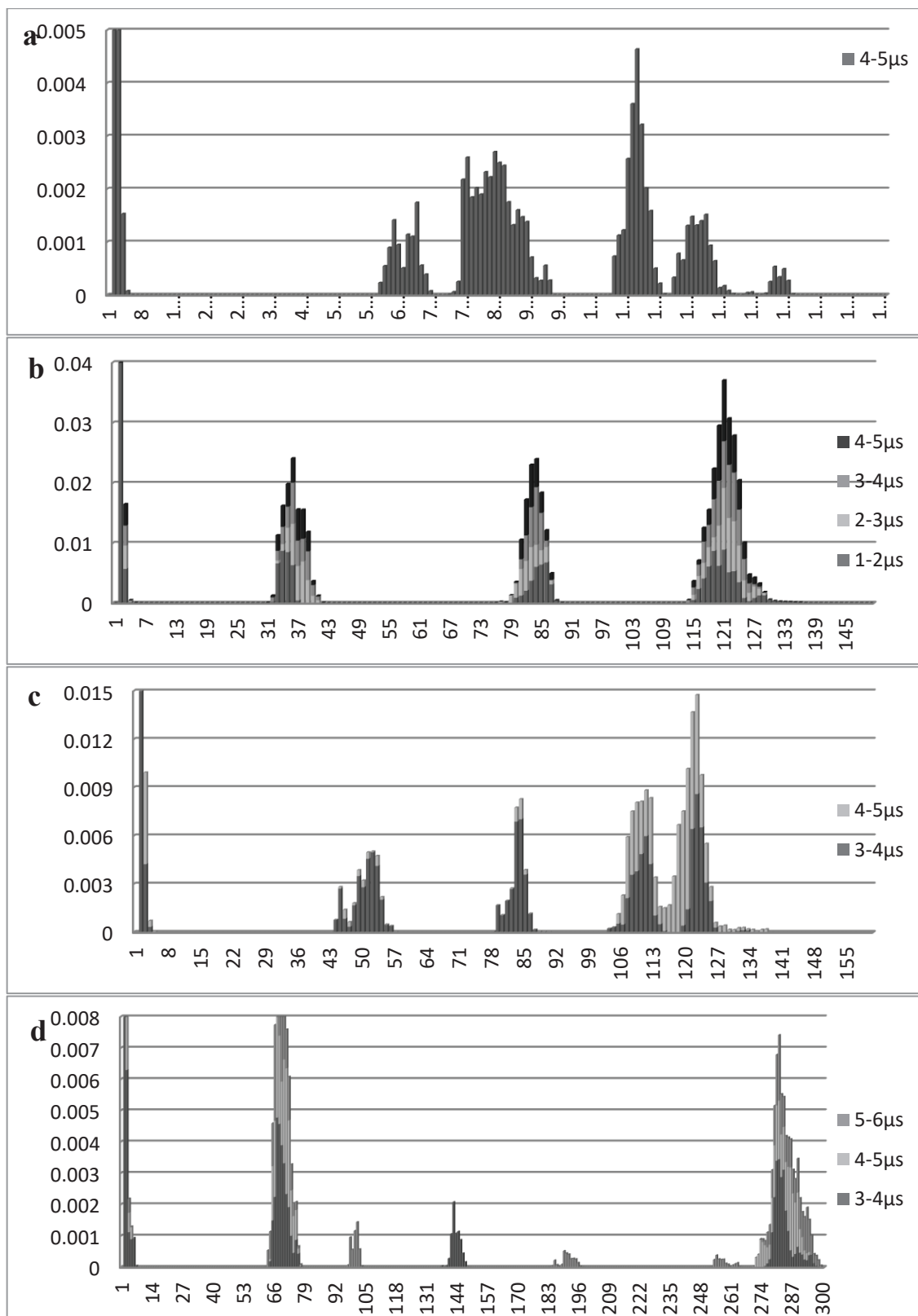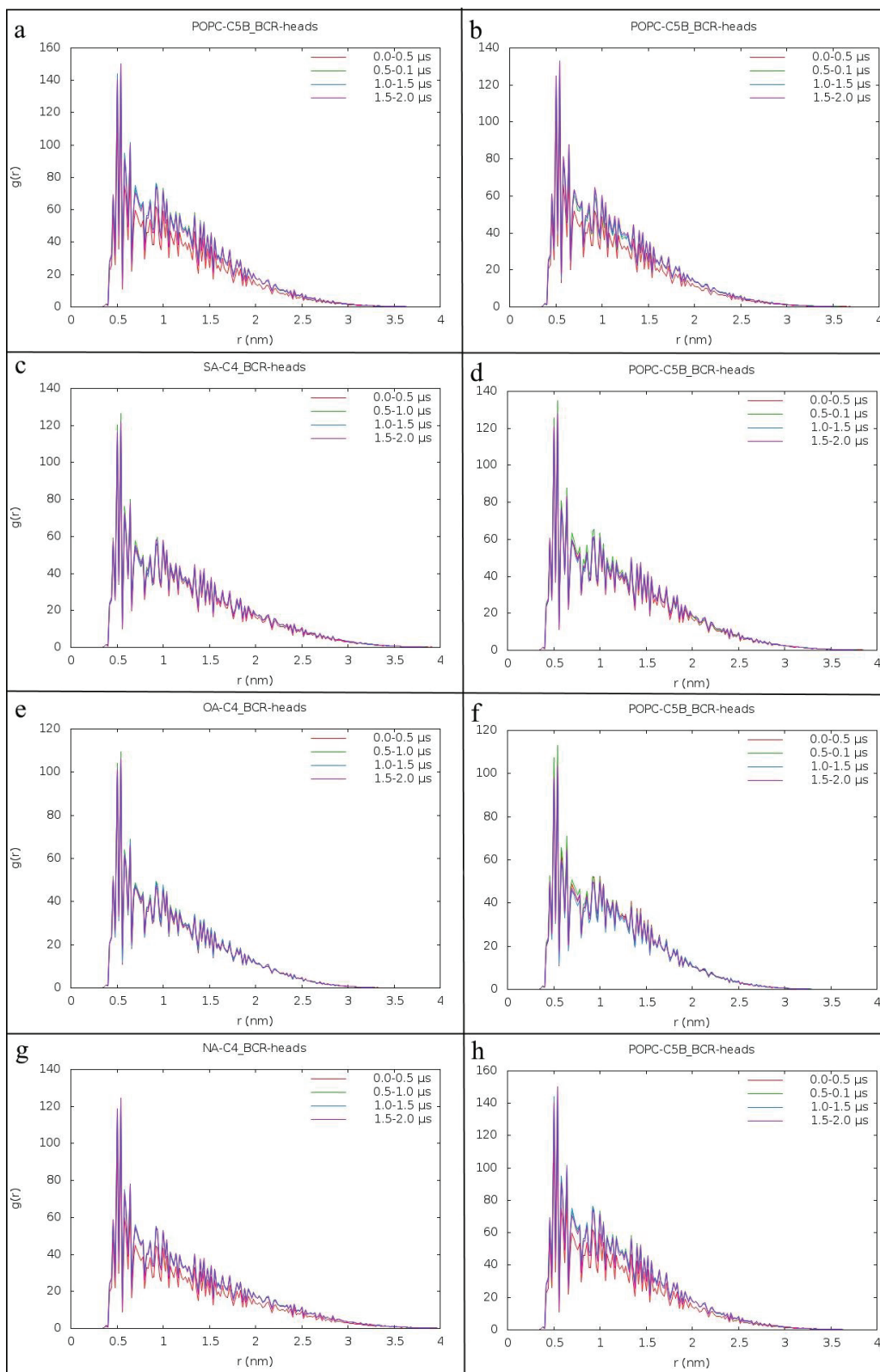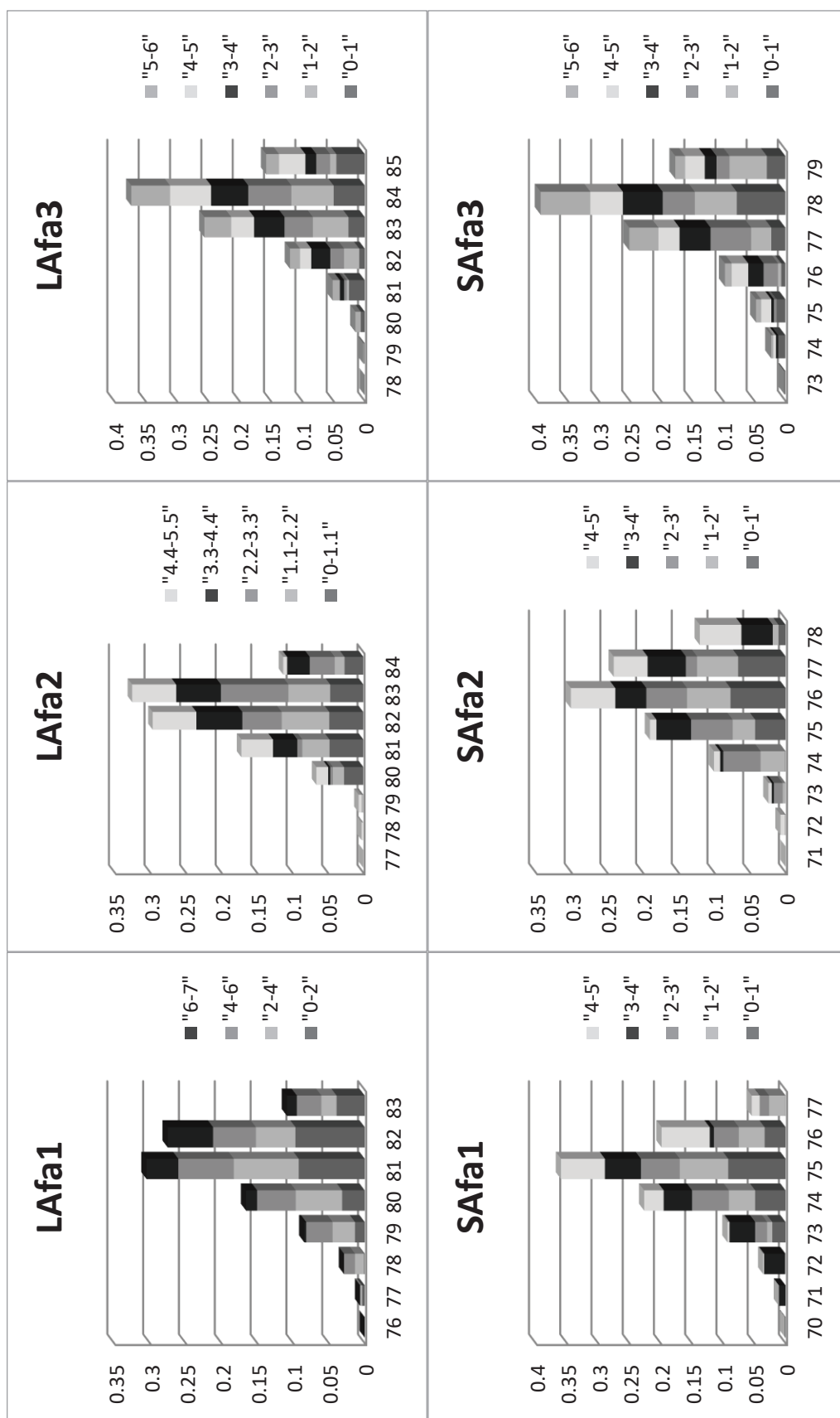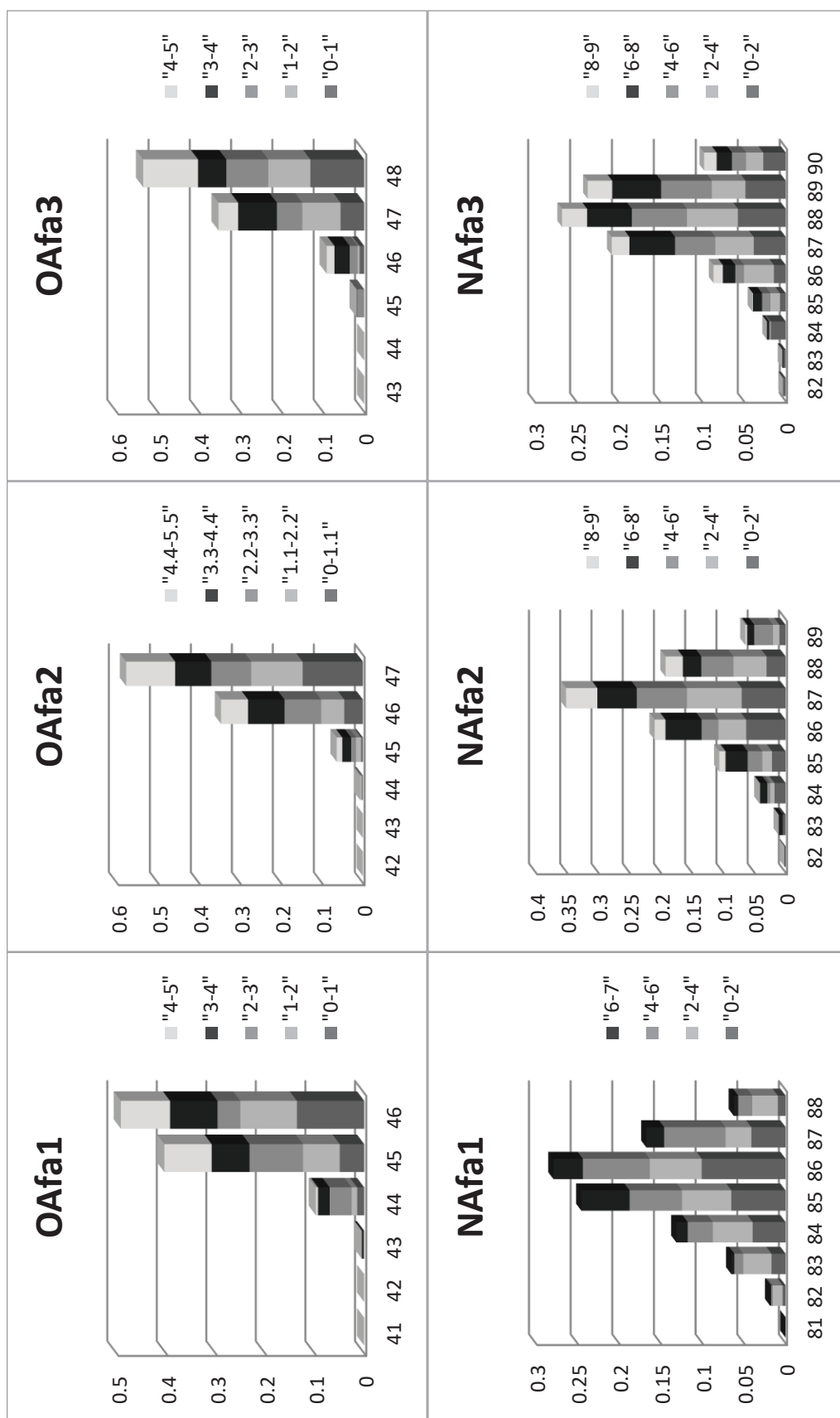Figure A.2. Cumulative probability distributions of aggregation numbers as a function of time (block-averaged over 1 µs intervals) after the equilibration of the with a) Lauric, b) Stearic, c) Oleic and d) Linoleic acids at fed state.

Figure A.3. RDFs of BCR head beads with respect to the tail beads of fatty acid (C3/4-on the right) and POPC (C5B bead-on the left) molecules for each 500ns of the trajectories with 3 (bottom) *β*-carotene molecules for systems LA (a, b), SA (c, d), OA(e, f) and NA (f, g) at <u>fasted state</u>
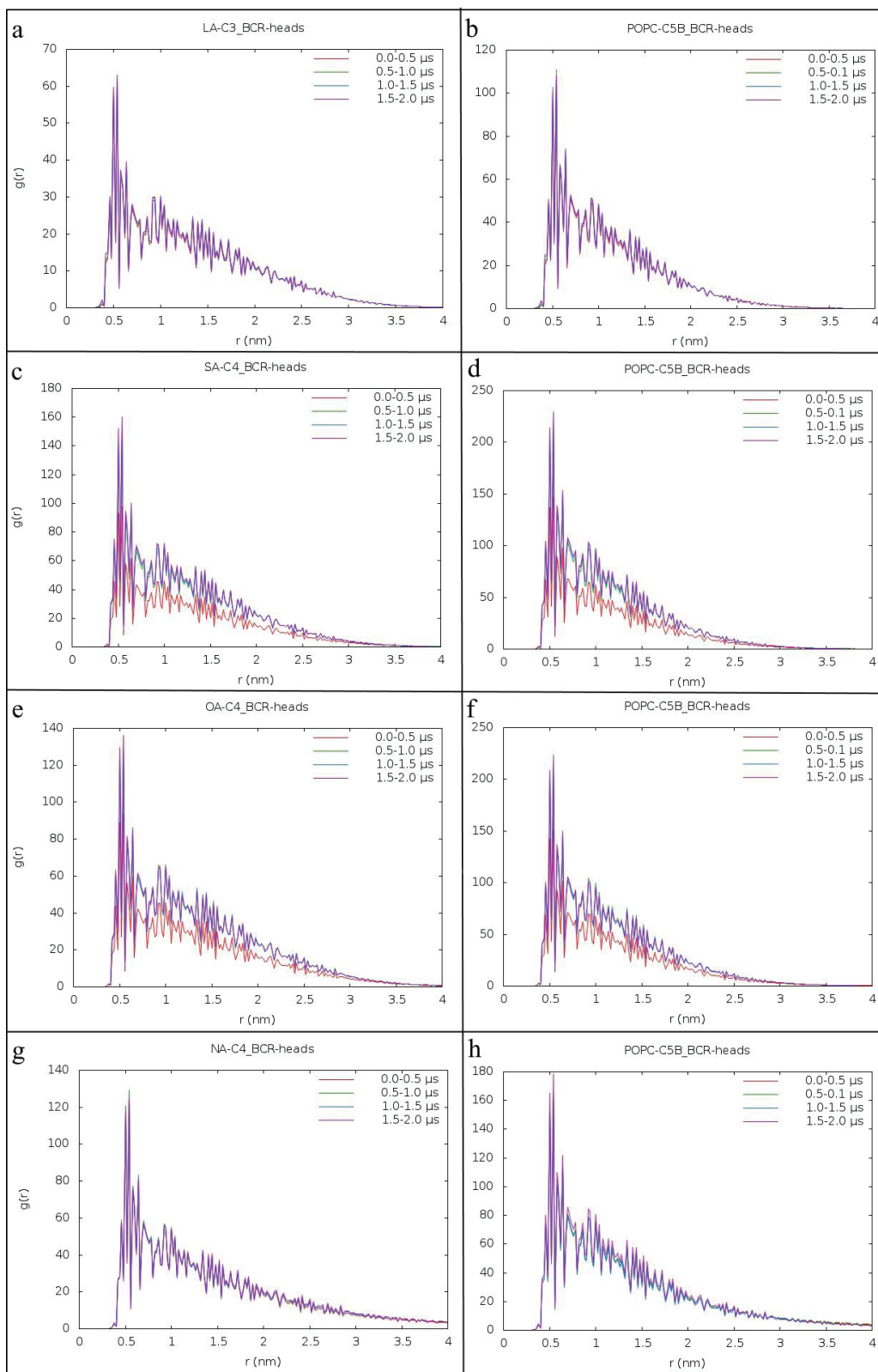
Figure A.4. RDFs of BCR head beads with respect to the tail beads of fatty acid (C3/4-on the right) and POPC (C5B bead-on the left) molecules for each 500ns of the trajectories with 3 (bottom) β-carotene molecules for systems LA (a, b), SA (c, d), OA(e, f) and NA (f, g) at <u>fed state</u>
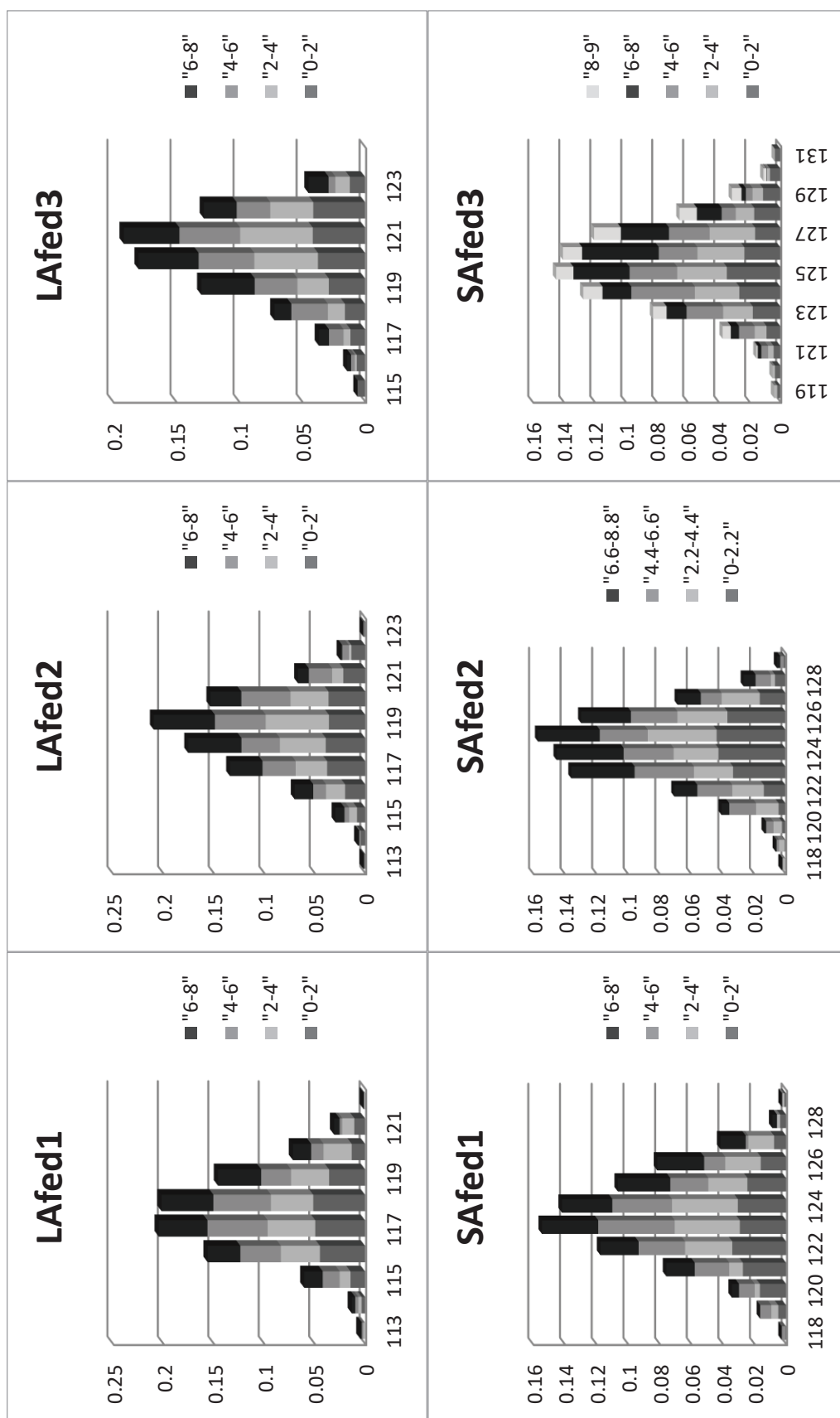
Figure A.5. Cumulative probability distributions of aggregation numbers as a function of time (block-averaged over 1 or 2 µs intervals) for systems with Lauric (a, b, c) and Stearic (d, e, f) acids in presence of 1, 2 and 3 β-carotene molecules at fasted state.
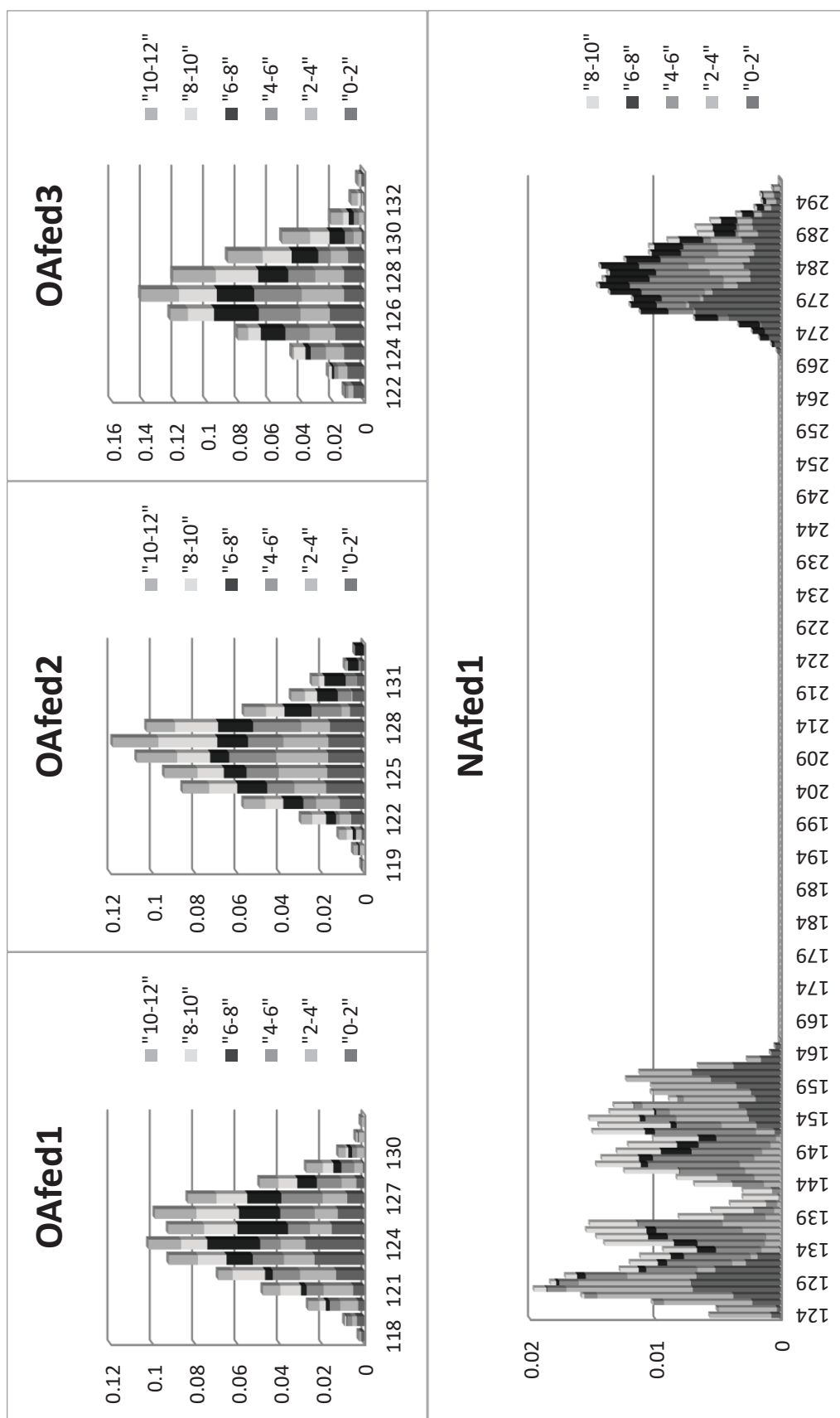
157

Figure A.6. Cumulative probability distributions of aggregation numbers as a function of time (block-averaged over 1 or 2 μs intervals) for systems with Oleic (a, b, c) and Linoleic (d, e, f) acids in presence of 1, 2 and 3 β-carotene molecules at fasted state.

158

Figure A.7. Cumulative probability distributions of aggregation numbers as a function of time (block-averaged over 1 or 2 μs intervals) for systems with Lauric (a, b, c) and Stearic (d, e, f) acids in presence of 1, 2 and 3 β-carotene molecules at <u>fed state</u>.

Figure A.8. Cumulative probability distributions of aggregation numbers as a function of time (block-averaged over 2 μs intervals) for systems with Oleic (a, b, c) and Linoleic (d, e, f) acids in presence of 1, 2 and 3 β-carotene molecules at fed state.
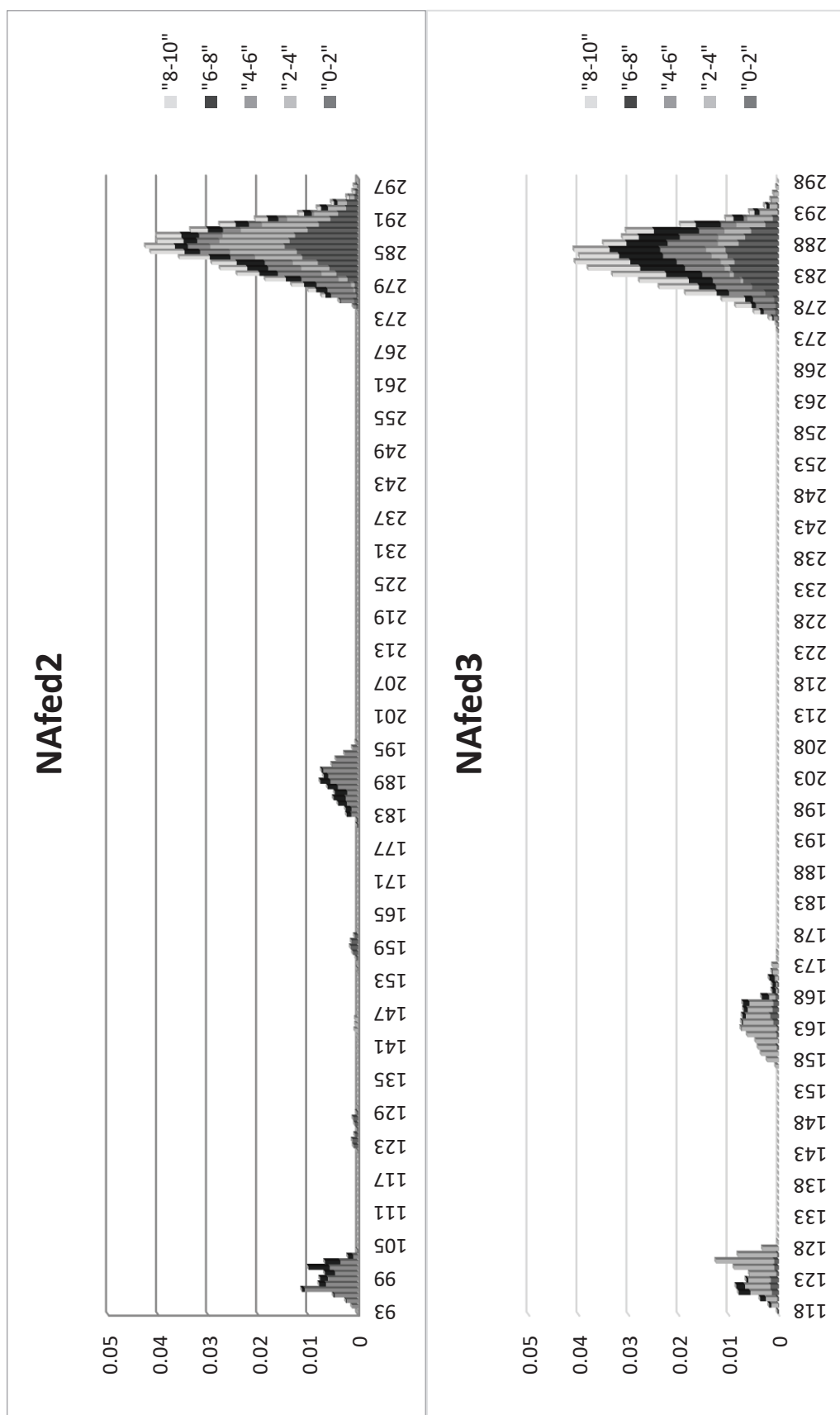
Figure A.9. Cumulative probability distributions of aggregation numbers as a function of time (block-averaged over 2 μs intervals) for systems with Oleic (a, b, c) and Linoleic (d, e, f) acids in presence of 1, 2 and 3 *β*-carotene molecules at <u>fed state</u>.
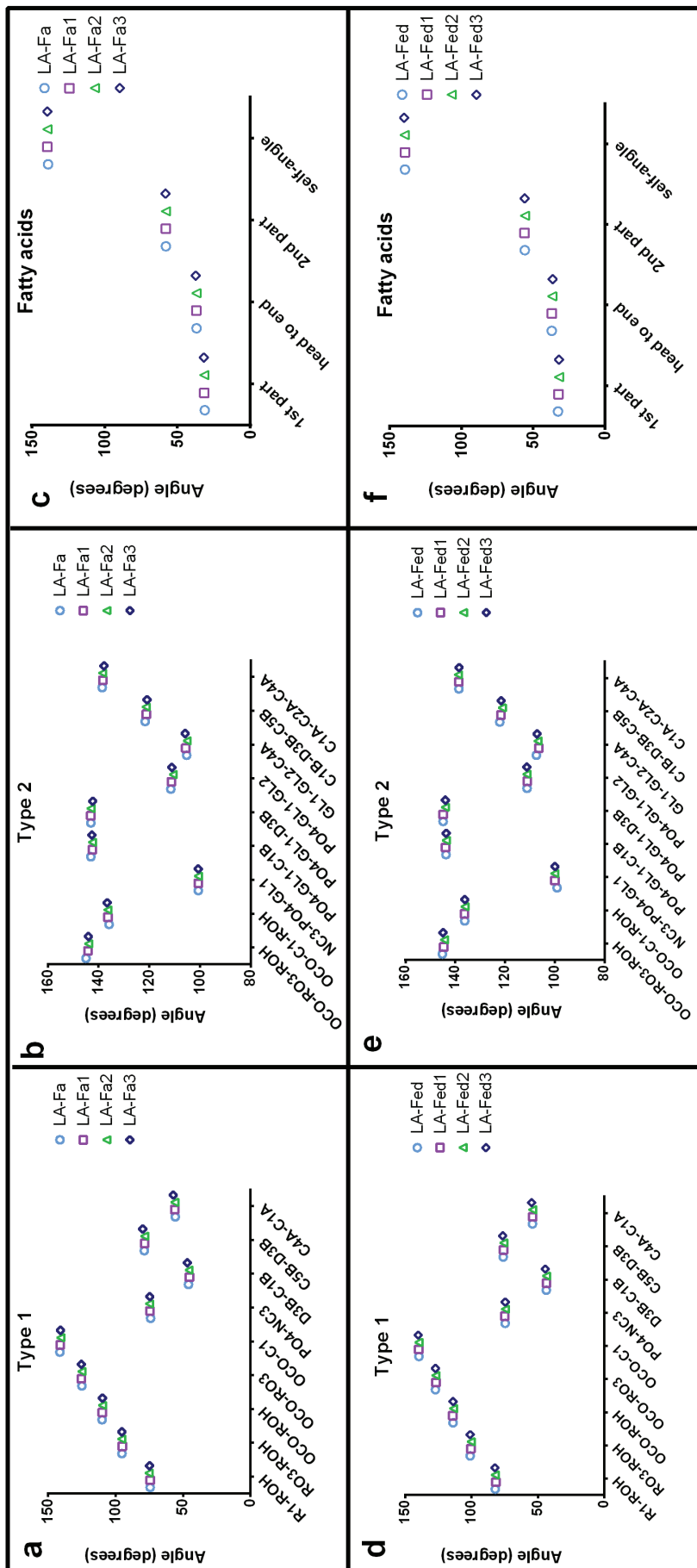
Figure A.10. Type I average angles between a vector of two selected beads in a molecule and the local sphere normal (radial vector) at fasted (a) and fed (d) states. The origin of each vector is the first specified bead; hence the direction of each vector is from the first to the second specified bead. The local sphere normal is the vector which connects the com of the micelle to the midpoint of the selected beads' positions. Type II average angles between two vectors in a molecule at fasted (b) and fed (e) states. The origin of each vector is the middle specified bead; hence the directions of the vectors are from the middle to the end beads. The Type I and Type II average angles of fatty acid molecules at fasted (c) and fed (f) states (Fatty acid: Lauric acid, No-BCR: ○, 1 BCRs: □, 2 BCRs: △, 3 BCRs: ◇).
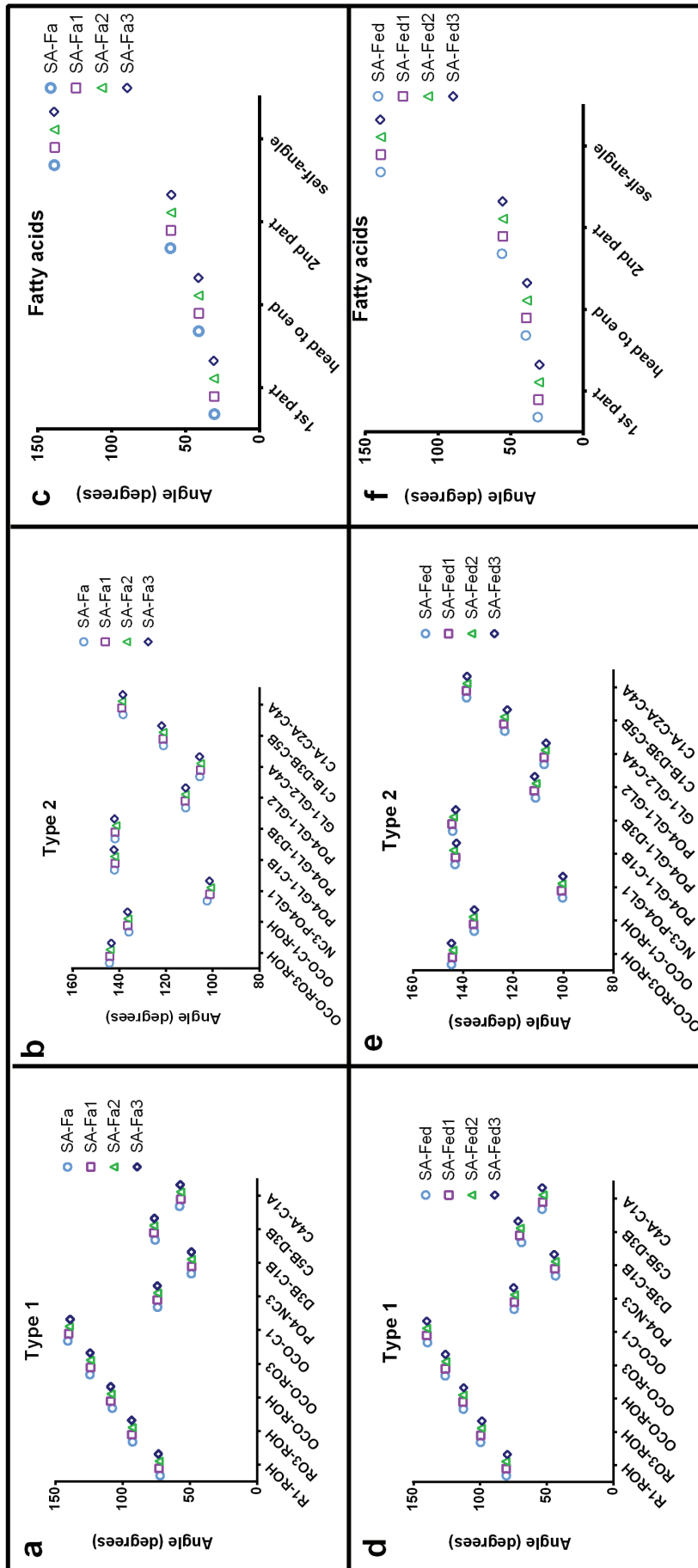
Figure A.11. Type I average angles between a vector of two selected beads in a molecule and the local sphere normal (radial vector) at fasted (a) and fed (d) states. The origin of each vector is the first specified bead; hence the direction of each vector is from the first to the second specified bead. The local sphere normal is the vector which connects the com of the micelle to the midpoint of the selected beads' positions. Type II average angles between two vectors in a molecule at fasted (b) and fed (e) states. The origin of each vector is the middle-specified bead; hence the directions of the vectors are from the middle to the end beads. The Type I and Type II average angles of fatty acid molecules at fasted (c) and fed (f) states (Fatty acid: Stearic acid, No-BCR: ○, 1 BCRs: ◇, 2 BCRs: □, 3 BCRs: △).
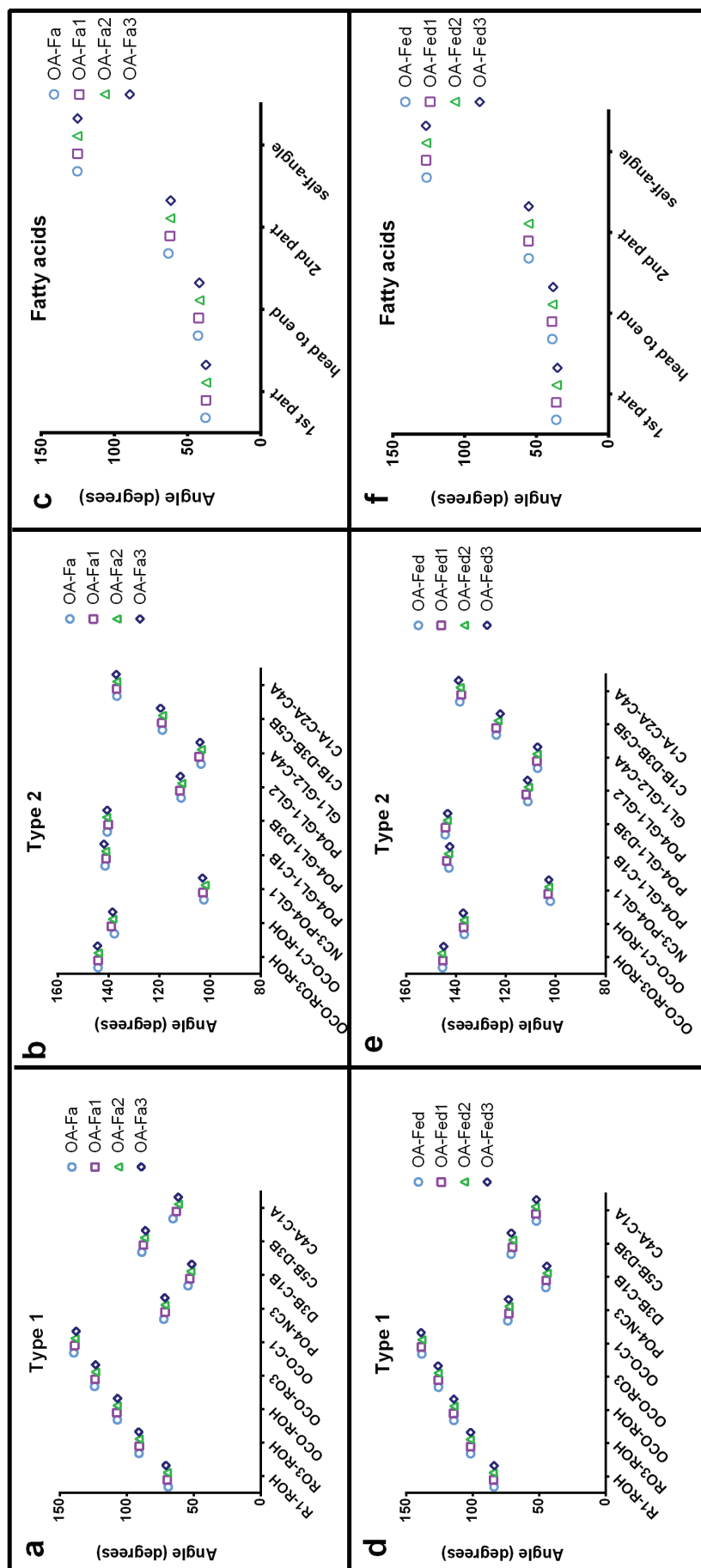
Figure A.12. Type I average angles between a vector of two selected beads in a molecule and the local sphere normal (radial vector) at fasted (a) and fed (d) states. The origin of each vector is the first specified bead; hence the direction of each vector is from the first to the second specified bead. The local sphere normal is the vector which connects the com of the micelle to the midpoint of the selected beads' positions. Type II average angles between two vectors in a molecule at fasted (b) and fed (e) states. The origin of each vector is the middle specified bead; hence the directions of the vectors are from the middle to the end beads. The Type I and Type II average angles of fatty acid molecules at fasted (c) and fed (f) states (Fatty acid: Oleic acid, No-BCR: ○, 1 BCRs: □, 2 BCRs: △, 3 BCRs: ◇).
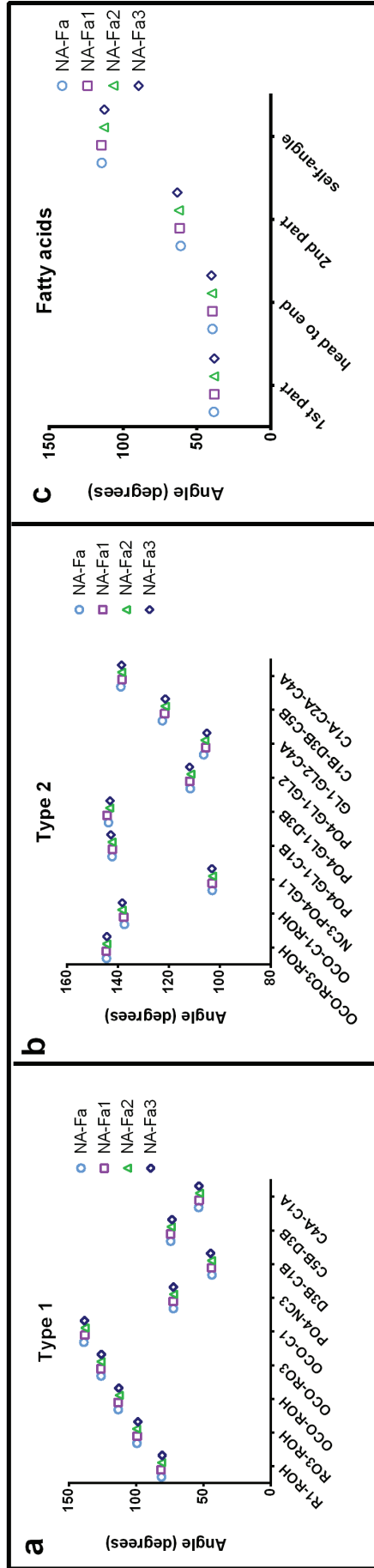
Figure A.13. Type I average angles between a vector of two selected beads in a molecule and the local sphere normal (radial vector) at fasted (a) state. The origin of each vector is the first specified bead; hence the direction of each vector is from the first to the second specified bead. The local sphere normal is the vector which connects the com of the micelle to the midpoint of the selected beads' positions. Type II average angles between two vectors in a molecule at fasted (b) state. The origin of each vector is the middle specified bead; hence the directions of the vectors are from the middle to the end beads. The Type I and Type II average angles of fatty acid molecules at fasted (c) state (Fatty acid: Linoleic acid, No-BCR: ○, 1 BCRs: □, 2 BCRs: △, 3 BCRs: ◇).

Table A.114. Type I average angles between the head groups of CHOA, POPC and fatty acid molecules and the radial axis of the micelles in the presence of different fatty acid molecules and different numbers of BCRs

Micelles	OCO-C1	PO4-NC3	COO-C2
LA-Fa1	140.947	74.574	31.579
LA-Fa2	140.674	75.068	31.579
LA-FA3	140.725	74.638	31.828
SA-Fa1	140.244	74.372	30.607
SA-Fa2	140.076	74.361	30.978
SA-FA3	139.136	74.350	31.040
OA-Fa1	138.990	71.607	37.465
OA-Fa2	138.931	71.888	37.517
OA-Fa3	137.841	71.740	37.463
NA-Fa1	138.137	72.515	38.304
NA-Fa2	138.230	72.355	38.503
NA-Fa3	138.462	72.400	38.263
LA-Fed1	139.868	74.985	32.283
LA-Fed2	139.955	74.649	32.000
LA-Fed3	140.291	74.740	31.907
SA-Fed1	140.062	74.424	30.802
SA-Fed2	140.255	74.375	30.605
SA-Fed3	140.122	75.072	30.161
OA-Fed1	138.643	72.825	36.399
OA-Fed2	138.448	73.052	36.217
OA-Fed3	138.767	73.151	35.576

VITA

Name, Surname: Esra TUNÇER
Date of Birth : 21.05.1987
Place of Birth : Demirci / MANİSA

Education

2012 Master of Science (M.Sc.) Ege University, Department of Food Engineering.
2010 Bachelor of Science (B.Sc.) Ankara University, Department of Food Engineering.

Academic Work Experience:

Research Assistant, Trakya University, Department of Food Engineering, continues - 2018
Research Assistant, İzmir Institute of Technology, Department of Food Engineering 2014–2007

Scientific Articles Published in International Journals:

Özdestan, Ö., Kaçar, E., Keşkeoğlu, H. and Üren, A., 2013. Development of a New Extraction Method for Heterocyclic Aromatic Amines Determination in Cooked Meatballs. Food Analytical Methods, 10.1007/s12161-013-9607-7.